

# **BULGARIAN CHEMICAL COMMUNICATIONS**

**2016** Volume 48 / Number 3

*Journal of the Chemical Institutes  
of the Bulgarian Academy of Sciences  
and of the Union of Chemists in Bulgaria*



## Mechanism of hydrogen transfer from 1-methylbutyl peroxide to hydroxyl radical

S. Q. Zhou\*, H. W. Kuai, Y. X. Gu, W. Zhou, A. P. Li

Faculty of Chemical Engineering, Huaiyin Institute of Technology, Huai'an, 223003, P. R. China

Received November 4, 2014, Accepted December 28, 2015

The density functional theory method was used to study the mechanism for the hydrogen transfer from 1-methylbutyl peroxide [ $n\text{-C}_3\text{H}_7\text{CH}(\text{CH}_3)\text{OOH}$ ] to hydroxyl radical. The B3LYP method was used in conjunction with the 6-311++G\*\* basis set. The geometrical configurations of reactants, products and transition states were fully optimized on the potential energy surfaces. The activation energies for the hydrogen transfer are in the range from 0.37 to 7.9 kJ/mol. The results suggest that the alkyl  $\beta\text{-H}$  is the easiest to transfer in view of both thermodynamics and kinetics. On the contrary, the  $\gamma\text{-H}$  transfer requires larger activation energy compared to  $\alpha\text{-}$  and  $\beta\text{-H}$ . All three types of hydrogen transfers become much easier in the presence of hydroxyl radical compared to the intramolecular hydrogen transfer, which is in good agreement with the experimental fact that the emulsification of diesel oil and water results in improved combustion properties.

**Keywords:** 1-Methylbutyl peroxide, Hydroxyl radical, Intermolecular hydrogen-atom transfer, Density functional theory.

### INTRODUCTION

The diesel engine is still one of the most fuel-efficient combustion engines at present [1-4]. Diesel emulsion is considered one of the possible alternative fuels for curtailing the emission pollution of combustion equipment such as diesel engines and large power boilers [5-8]. Emulsion fuels are defined as emulsions of water in fuel with the typical composition of 5–20% of water, surfactant and based fuel such as kerosene or diesel. It is consistently proven that emulsion fuels significantly lower emissions of hydrocarbons, carbon monoxide/dioxide and especially hazardous nitrous oxides and particulate matters [9-12].

Diesel oil primarily consists of hydrocarbons with  $n\text{-alkanes}$  being the dominant components. It converts to self-ignited peroxides of hydrocarbons prior to complete combustion. The easiness of formation of hydrocarbon peroxides determines whether or not the engine is knocking. Of all types of peroxides, the di-peroxyl hydrocarbons have been believed to be the precursors of the final products carbon oxide and water. These di-peroxyl hydrocarbons are expected to play an important role in eliminating the diesel engine knocking. The key steps to produce di-peroxyl hydrocarbons are the intramolecular hydrogen-atom transfer reactions [13-16]. However, on the condition of water existing, the hydroxyl radical that is produced from water takes part in the process of the formation of di-peroxyl hydrocarbons (Fig. 1). Hydroxyl radical

assimilates a hydrogen atom from the mono-peroxyl hydrocarbon. The process yields the formation of a carbon radical. Once the products of alkyl radicals come into being, they are easy to further react with oxygen to produce di-peroxyl hydrocarbons. Here, 1-methylbutyl peroxide was used as the computational model of hydrocarbon peroxide.

The main objective of this work is to explore energies and mechanisms for the hydroxyl assimilating a hydrogen from 1-methylbutyl peroxide [synonym, 2-pentyl peroxide, chemical formula  $n\text{-C}_3\text{H}_7\text{CH}(\text{CH}_3)\text{OOH}$ ] as a computational model.

### COMPUTATIONAL METHODS

The molecular structures and energies of the reaction stationary points were calculated with the density functional theory (DFT) B3LYP technique [17-19]. Unrestricted wave function was employed for the open-shell systems. The geometries of all species (reactants, transition states and products) were optimized at the B3LYP/6-311++G\*\* level. The corresponding vibration frequencies were calculated at the same level. All located transition states exhibited one normal imaginary frequency with a transition vector corresponding to the motion of a H-atom during the intermolecular H-atom-transfer process. All calculations were performed with Gaussian 03 package of programs [20].

\* To whom all correspondence should be sent:  
E-mail: zhousuqin7803@sina.com

## RESULTS AND DISCUSSION

*Structures and geometries*

Fig. 2 shows the optimized geometries of the transition states. The imaginary frequencies of TS1, TS2, TS3 and TS4 are  $-446.16$ ,  $-257.60$ ,  $-823.85$  and  $-240.27$   $\text{cm}^{-1}$ , respectively. The vibrational normal modes of the four transition states correspond to the wagging of a hydrogen atom towards the hydroxyl radical. On going from the reactant to TS, one of the C–H bonds elongates toward the hydroxyl radical. The O $\cdots$ H lengths of partially formed water moiety in TS1, TS2, TS3 and TS4 are 1.412 Å, 1.460 Å, 1.333 Å and 1.444 Å, respectively. The lengths of the C–H bonds associated with the transfer of a H atom are 1.188 Å, 1.167 Å, 1.211 Å and 1.172 Å, for TS1, TS2, TS3 and TS4, respectively. The lengths of these C–H bonds are increased by about 10% compared to their corresponding C–H bond lengths in the reactants. The structure of TS2 differs more from that of its product than that of the other three TS. However, there is a six-membered ring with an intramolecular hydrogen bond in TS2, which attributes it with lower activation energy as discussed below.

*Change of energy*

The hydroxyl radical approaches the alkyl hydrogen atoms, resulting in the formation of TS1-TS4. Table 1 collects the total energies, zero point vibrational energies and relative energies at the B3LYP/6-311++G\*\* level. The relative energy, after being corrected for the zero point vibrational energy, refers to the corresponding reactant, i.e., the complex of 1-methylbutyl peroxide and hydroxyl radical. The relative energy is the energy barrier needed to be overcome during the intermolecular hydrogen transfer reaction. As can be seen from Table 1 and Fig. 3, for  $\alpha$ -H, the methylene hydrogen is energetically favorable to be transferred in comparison with methyl hydrogen. In other words, the  $\alpha$ -H transfer from methylene to hydroxyl results in the largest energy release. All four reactions are firstly endothermic to overcome the energy barrier from the reactants to the transition states. But these reactions are exothermic from the reactants to the products. The activation energy of 0.37 kJ/mol for reaction (2) is the lowest one, that is, the alkyl  $\beta$ -H is the easiest to transfer. The  $\beta$ -H transfer is a favorable process in view of both thermodynamics and kinetics. On the contrary, the reaction (4) of alkyl  $\gamma$ -H transfer requires the largest activation energy. Table 1 also lists the relative energies of the transition states for the

corresponding intrahydrogen transfers.  $\beta$ -H is the easiest to transfer in the process of intramolecular hydrogen transfer in comparison with  $\alpha$ -H and  $\gamma$ -H. Notably,  $\beta$ -H is also the easiest to transfer assisted by hydroxyl in comparison of  $\alpha$ -H and  $\gamma$ -H. However, all types of H transfer become much easier in the presence of hydroxyl radical. This finding can explain the fact that the combustion of diesel oil is accelerated by the addition of small amounts of water.

*Atomic Mulliken charge and spin density*

As can be seen from Table 2, the Mulliken charges on C<sub>3</sub>, C<sub>2</sub>, C<sub>5</sub> and C<sub>1</sub> atoms for TS1, TS2, TS3 and TS4, respectively, decrease (more negatively charged) in comparison with those of the reactant. However, their corresponding charges on C<sub>3</sub>, C<sub>2</sub>, C<sub>5</sub> and C<sub>1</sub> atoms increase on going from reactant to products. It is interesting to note that the C<sub>3</sub> and C<sub>2</sub> atoms, for P1 and P2, respectively, are positively charged with 0.3 a.u.; on the contrary, the C<sub>5</sub> and C<sub>1</sub> atoms, for P3 and P4, respectively, are negatively charged with  $-0.4$  a.u. This large difference of charges is due to the C<sub>5</sub> and C<sub>1</sub> atoms being at the end of the carbon chain. There are less hyper-conjugation effects between the single electron on the end carbon and its neighbor C-H bond. More electron charges (negative charges) are built up on O<sub>7</sub> on going from reactants to products. And much more electron charges (negative charges) are built up on O<sub>8</sub> on going from reactants to products.

The electrons on the transferred hydrogen atoms are attracted by the hydroxyl oxygen atom in the reaction process. On going from the reactants to their corresponding TS1-TS4, the Mulliken charges on the transferred H<sub>11</sub> atom increase dramatically, since its electrons are shared by both neighbor carbon and oxygen atoms. On going from the TS1-TS3 to their corresponding products P1-P3, the Mulliken charges on the transferred H<sub>11</sub> atom decrease just slightly. Although the electronegativity of oxygen is larger than that of carbon, the transferred H<sub>11</sub> atom is closer to carbon than to oxygen.

Table 3 lists the spin densities of hydroxyl atoms, transferred hydrogen atom and its neighbor carbon. The total spin density of hydroxyl for the reactant is 1.0 a.u. However, on going from reactant to TS1-TS4, the spin densities of hydroxyl oxygen atoms decrease by about 0.3 a.u., but those of the carbon atoms increase from near zero to 0.3-0.4 a.u. This indicates that a hydrogen atom is partially transferred from carbon to hydroxyl oxygen.

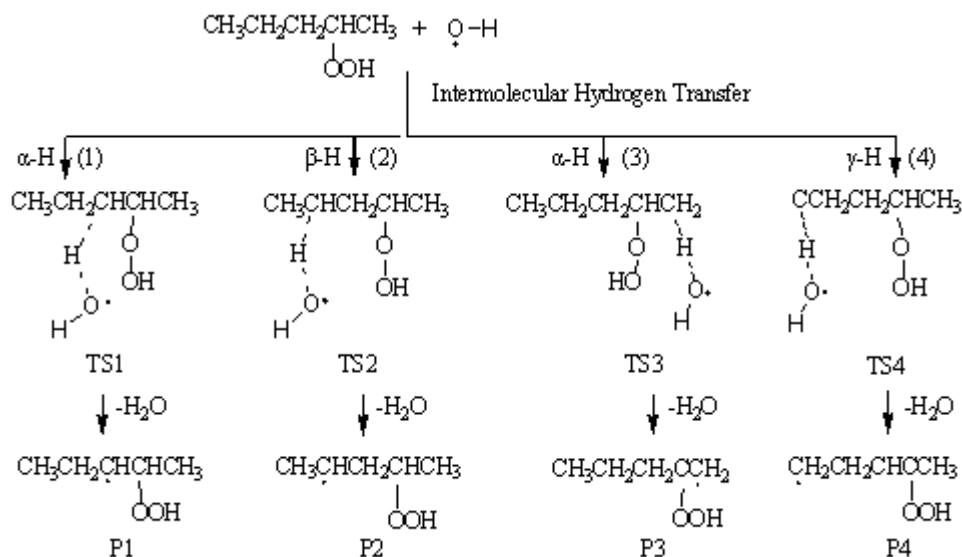


**Fig. 1.** Intermolecular hydrogen-atom transfer from 1-methylbutyl peroxide to hydroxyl radical for hydrogen at different positions.

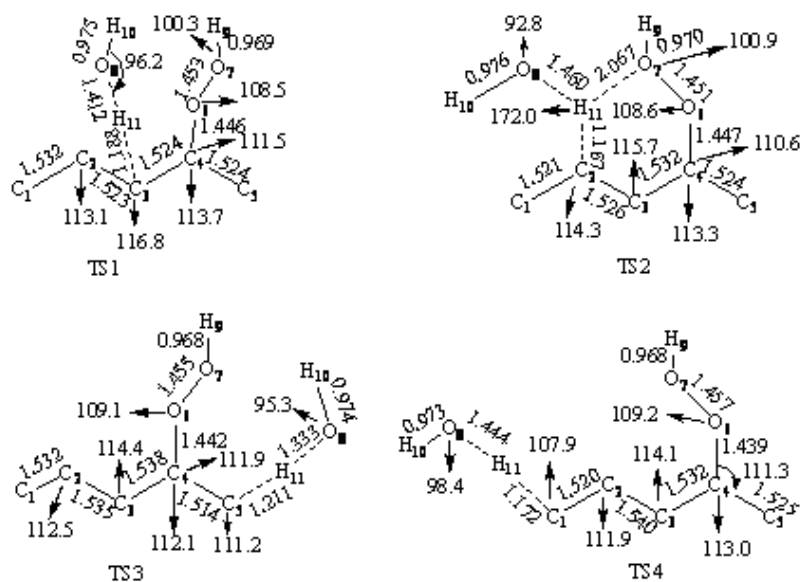


**Fig. 2.** Optimized structures of transition states (bond length in Angström, bond angle in degree).

**Table 1.** Total energies ( $E$ , in Hartree), zero point vibrational energies ( $E_{\text{vib}}$ , in kJ/mol) and relative energies ( $\Delta E$ , in kJ/mol) at the B3LYP level <sup>a</sup>

Species	$E$	$E_{\text{vib}}$	$\Delta E$	$\Delta E^c$	Species	$E$	$E_{\text{vib}}$	$\Delta E^d$
Reactant <sup>b</sup>	-423.997945	468.80	0.00	—	P1	-347.557871	400.87	-60.52
TS1	-423.993055	458.61	2.65	140.41	P2	-347.559594	399.39	-66.52
TS2	-423.994906	461.19	0.37	90.02	P3	-347.551672	399.32	-45.79
TS3	-423.990191	456.34	7.90	152.10	P4	-347.554205	399.76	-52.00
TS4	-423.989281	458.27	12.22	100.76	H <sub>2</sub> O	-76.458531	55.87	—

<sup>a</sup>  $\Delta E$  were corrected with zero-point vibrational energy. Relative energy refers to the corresponding reactant, i.e., the complex of 1-methylbutyl peroxide and hydroxyl radical. <sup>b</sup> Complex of 2-pentyl peroxide and hydroxyl radical. <sup>c</sup> Relative energies of transition states for the corresponding intrahydrogen transfers from Ref. [4]. <sup>d</sup> Energy of water is included.

**Table 2.** Atomic Mulliken charges along the reaction pathways at the B3LYP/6-311++G\*\* level.

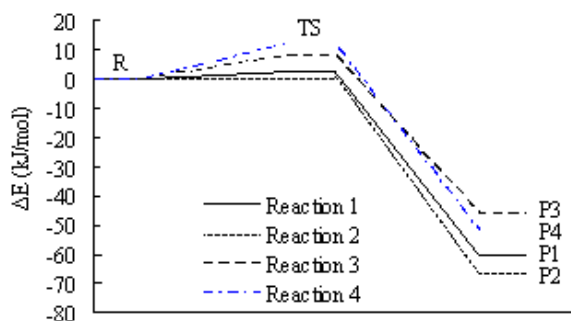
Atom	Reactant	TS1	TS2	TS3	TS4	P1	P2	P3	P4
C <sub>1</sub>	-0.625	-0.604	-0.644	-0.635	-0.644	-0.453	-0.755	-0.620	-0.386
C <sub>2</sub>	0.054	-0.100	-0.100	-0.040	-0.100	-0.442	0.318	-0.046	-0.136
C <sub>3</sub>	-0.336	-0.397	-0.451	-0.297	-0.451	0.331	-0.424	-0.490	-0.313
C <sub>4</sub>	-0.130	-0.183	0.029	-0.114	0.029	-0.326	-0.122	0.152	-0.023
C <sub>5</sub>	-0.585	-0.576	-0.615	-0.634	-0.615	-0.652	-0.592	-0.473	-0.607
O <sub>6</sub>	-0.088	-0.067	-0.090	-0.009	-0.090	-0.044	-0.056	-0.066	-0.059
O <sub>7</sub>	-0.188	-0.192	-0.197	-0.258	-0.197	-0.214	-0.207	-0.198	-0.198
O <sub>8</sub>	-0.248	-0.318	-0.358	-0.367	-0.358	-0.502	-0.502	-0.502	-0.502
H <sub>11</sub> <sup>a</sup>	0.097–0.189	0.361	0.333	0.301	0.239	0.251	0.251	0.251	0.251

<sup>a</sup> Refers to the transferred hydrogen atom.

**Table 3.** Atomic spin densities for the transferred hydrogen atom and its neighbor atoms along the reaction pathways at the B3LYP/6-311++G\*\* level.

Atom <sup>a</sup>	Reactant	TS1	TS2	TS3	TS4	P1	P2	P3	P4
O <sub>8</sub>	1.021	0.685	0.721	0.629	0.712	0.000	0.000	0.000	0.000
H <sub>10</sub>	-0.021	-0.003	0.001	0.002	-0.011	0.000	0.000	0.000	0.000
C	-0.005–0.002	0.344	0.293	0.410	0.300	1.018	1.095	1.117	1.156
H	0.00	-0.020	-0.023	-0.028	-0.016	0.000	0.000	0.000	0.000

<sup>a</sup> H and C atoms refer to the transferred hydrogen atom and its neighbor carbon, respectively.

**Fig. 3.** Energy changes along the reaction pathway at B3LYP/6-311++G\*\* level.

All the spin density primarily locates on the carbon atom in the products. This clearly indicates that it is the hydrogen radical that transfers from the carbon atom to the hydroxyl oxygen atoms with water as a leaving moiety.

## CONCLUSIONS

The reactions of hydrogen atom migration from one of the C–H of 1-methylbutyl peroxide to hydroxyl radical were investigated by the DFT-B3LYP method. Transition states with six-membered rings were formed in the process of  $\beta$ -H transfer when the hydrogen atom migrates from the

methylene group to hydroxyl radical. The six-membered ring facilitates the formation of transition state. The atomic charges and spin distribution on the radical seem to be adequate in helping to understand the trends of the intermolecular hydrogen transfer. The  $\beta$ -H is easier to transfer than the  $\alpha$ - and  $\gamma$ -H. The hydroxyl radical greatly facilitates all three types of hydrogen transfer. This presents a rational explanation of the fact that the combustion of diesel oil is accelerated by the addition of small amounts of water.

**Acknowledgements:** We gratefully thank for the support by the Nature Science Foundation of Jiangsu Higher Education Institutions of China (Grant No. 13KJB530002) and the National Natural Science Foundation of China (Grant No. 11404127). S.-Q. Zhou thanks the Research Support of Huaiyin Institute of Technology (Grant No. HGA1008).

## REFERENCES

1. F. -F. Pischinger, in: E. Sher (ed.). Handbook of Air Pollution from Internal Combustion Engines. London: Academic Press, 1998, p. 261.
2. M. Lapuerta, R. García-Contreras, J. Campos-Fernández, *Energ. Fuel*, **24**, 4497 (2010).

3. Y.-C. Lin, W.-J. Lee, H.-R. Chao, *Environ. Sci. Technol.*, **42**, 3849 (2008).
4. J.-B. Huang, D. Wu, H. Tong, W.-M. Li, *J. Energy Inst.*, **86**, 189 (2013).
5. G. Chen, D. Tao, *Fuel Process. Technol.*, **86**, 499 (2005).
6. Y. Liu, G.-H. Huang, Y.-P. Cai, C. Dong, *Int. J. Green Energy*, **11**, 1013 (2014).
7. P. Manivasagan, P. Sivasankar, J. Venkatesan, K. Sivakumar, S.-K. Kim, *Bioprocess Biosyst. Eng.*, **37**, 783 (2014).
8. Y.-P. Li, T.-J. Wang, W. Liang, C.-Z. Wu, *Energ. Fuel*, **24**, 1987 (2010).
9. A. -M. Al-Sabagh, M. -E. Mostafa, E. -M. -R. Noor, W. -R. Aly, *Egypt. J. Petrol.*, **20**, 17 (2011).
10. G. -R. Yu, J. -J. Zhao, D. -D. Song, *Ind. Eng. Chem. Res.*, **50**, 11690 (2011).
11. M. Lapuerta, O. Armas, R. García-Contreras, *Energ. Fuel*, **23**, 4343 (2009).
12. M.-V.-E. Santana, Q. Zhang, J.-R. Mihelcic, *Environ. Sci. Technol.*, **48**, 3084 (2014).
13. E.-B. Webb, C.-A. Koh, M.-W. Liberatore, *Ind. Eng. Chem. Res.*, DOI: 10.1021/ie5008954.
14. P.-B.-L. Fregolente, L.-V. Fregolente, M.-R.-W. Maciel, *J. Chem. Eng. Data*, **57**, 1817 (2012).
15. K.-Y. Lee, J.-J. Blaker, R. Murakami, J.-Y.-Y. Heng, A. Bismarck, *Langmuir*, **30**, 452 (2014).
16. M. Li, L. -F.Xie, X. -H. Ju, F. -Q. Zhao, *Petrol. Chem.*, **53**, 431 (2013).
17. J.-M. Seminario, P. Politzer, *Modern Density Functional Theory: A Tool for Chemistry*, Elsevier: Amsterdam, 1995.
18. L.-F. Xie, C.-C. Ye, X.-H. Ju, F.-Q. Zhao, *J. Struct. Chem.*, **53**, 659 (2012).
19. M. Wang, J.-J. Geng, Z.-B. Wei, Z.-Y. Wang, *Chinese J. Struct. Chem.*, **32**, 890 (2013).
20. M.-J. Frisch, G.-W. Trucks, H. -B. Schlegel, Gaussian, Inc. Pittsburgh PA, 2003.

## МЕХАНИЗЪМ НА ПРЕНОСА НА ВОДОРОД ОТ 1-МЕТИЛ-БУТИЛОВ ПЕРОКСИД КЪМ ХИДРОКСИЛЕН РАДИКАЛ

С. К. Жоу, Х. В. Куай, И. Х. Гу, В. Зоу, А. Р. Ли

Факултет по инженерна химия, Технологичен институт Хуайин, Хуаян, 223003, КНР

Постъпила на 4 ноември, 2014 г.; приета на 28 декември, 2015 г.

(Резюме)

Използван е DFT-методът за да се изследва механизма на преноса на водород от 1-метил-бутилов пероксид [ $n\text{-C}_3\text{H}_7\text{CH}(\text{CH}_3)\text{OOH}$ ] към хидроксилен радикал. Използван е B3LYP-методът заедно с базисна мрежа 6-311++G\*\*. Геометричната конфигурация на реагентите, продуктите и преходните състояния са оптимизирани на повърхностите на потенциалната енергия. Активиращите енергии на пренос на водорода са в интервала от 0.37 до 7.9 kJ/mol. Резултатите показват, че  $\beta\text{-H}$  е най-лесен за пренос от термодинамична и кинетична гледна точка. Обратно, преносът  $\gamma\text{-H}$  изисква по-големи активиращи енергии спрямо  $\alpha\text{-}$  and  $\beta\text{-H}$ . Тези три типа пренос на водород се извършват по-лесно в присъствие на хидроксилни радикали, отколкото вътрешно-молекулния пренос, което е в добро съгласие с експерименталния факт, че емулсификацията на дизелово гориво във вода води до по-добри горивни качества.

## Two ammonium ionic liquids as efficient catalysts for the one-pot green synthesis of 3,4,5-substituted furan-2(5H)-ones

S. Salahi<sup>1</sup>, M. T. Maghsoodlou<sup>1\*</sup>, N. Hazeri<sup>1</sup>, M. Lashkari<sup>2</sup>, R. Doostmohammadi<sup>1</sup>, A. Kanipour<sup>1</sup>, F. Farhadpour<sup>1</sup>, A. Shojaei<sup>1</sup>

<sup>1</sup>Department of Chemistry, Faculty of Science, University of Sistan & Baluchestan, P. O. Box 98135-674 Zahedan, Iran

<sup>2</sup>Faculty of Science, Velayat University, Iranshahr, Iran

Received September 9, 2014; Accepted September 16, 2015

An efficient and environmentally friendly method for one-pot preparation of 3,4,5-substituted furan-2(5H)-ones is described by condensation of aromatic aldehydes, aromatic amines and dialkyl acetylenedicarboxylates under solvent-free conditions using ammonium ionic liquids as catalysts. This synthetic approach benefits from cleaner reaction profiles, use of easily available, inexpensive, recyclable and environmentally benign catalyst, high yields, and simple experimental and work-up procedures.

**Keywords:** Ammonium ionic liquids ([Et<sub>2</sub>NH<sub>2</sub>][HSO<sub>4</sub>], [Et<sub>3</sub>NH][HSO<sub>4</sub>]), Multi-component reaction, Green chemistry, Furan-2(5H)-ones.

### INTRODUCTION

2(5H)-Furanones are attractive for organic chemists since they are key structural elements in many biologically active natural products [1]. They are abundant in nature and recently have been widely used as plant-growth regulators, antiulcer agents, and fish-growth promoters [2]. Attempts are ongoing to develop new synthetic approaches for the efficient preparation of natural products containing furanone ring units (Figure 1: freelingyne 1, tetrenoline 2, and sarcophine 3) because of their importance in biological activities such as antibacterial, antifungal, antimicrobial, antiviral, anticancer, anti-inflammatory, antipsoriasis, and anti-phospholipase A2 activities [3]. The wide range of application of compounds containing the butenolide ring results in considerable attention toward the synthesis of these compounds.

Recently, a multi-component reaction (MCR) of aromatic amines, aldehydes and dialkyl acetylenedicarboxylate has been used for the synthesis of furan-2(5H)-ones. Multi-component reactions offer an efficient and powerful mode of synthesis of complex structures, which is a convenient route for the synthesis of new drugs and chemical compounds by the combination of various starting materials [4].

Narayana *et al.* applied  $\beta$ -cyclodextrin for the synthesis of 2(5H)-furanone by condensation of anilines, aldehydes and diethyl acetylenedicarboxylate in a one pot three-

component reaction [5]. Other synthetic methods have also been developed by employing nano-ZnO [6], Al(HSO<sub>4</sub>)<sub>3</sub> [7], KOH [8] and SnCl<sub>2</sub>·2H<sub>2</sub>O [9].

Ionic liquids (ILs) are considerably popular among chemists since they have some specific characteristics such as very low vapor pressure, non-explosiveness, thermal stability in a wide temperature range and environmental safety, which make them a green alternative to conventional organic solvents [10-13].

ILs are categorized in a wide range such as acidic ILs, basic ILs, metal-containing ILs, guanidinium ILs, chiral ILs, and ILs containing OH groups [14]. Because of their usefulness, preparation and application of various kinds of ionic liquids in chemical processes have been quickly developed. Of the many different kinds of ILs available, the Brønsted acidic ILs offer the greatest potential for the development of environmentally friendly acid catalysts for organic synthesis [15,16]. Combination of a Brønsted acid and a Brønsted base produces protic ionic liquids [17]. Protic ionic liquid such as [Et<sub>3</sub>NH][HSO<sub>4</sub>] has been used by Li as a catalyst and green solvent for the cracking reactions of dialkoxypropanes [18].

In continuation of our research [19-22], herein we present the ionic liquids ([Et<sub>2</sub>NH<sub>2</sub>][HSO<sub>4</sub>] and [Et<sub>3</sub>NH][HSO<sub>4</sub>]) as catalysts in a simple and efficient method for the synthesis of 4,5-substituted furan-2(5H)-ones by one-pot condensation of aromatic aldehydes, aromatic amines and dialkyl acetylenedicarboxylates under solvent-free conditions.

\* To whom all correspondence should be sent:

E-mail: mt\_maghsoodlou@chem.usb.ac.ir ,  
mt\_maghsoodlou@yahoo.com



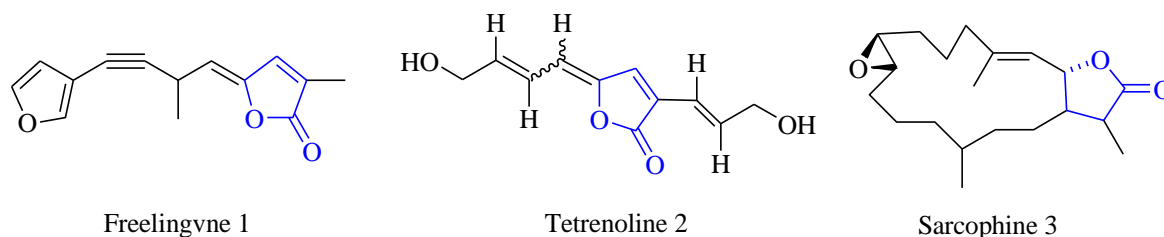


**Fig. 1.** Natural products containing a furanone ring fragment.

## EXPERIMENTAL

### General

Melting points and IR spectra of all compounds were measured on an Electrothermal 9100 apparatus and a JASCO FTIR 460 Plus spectrometer, respectively. The  $^1\text{H}$  and  $^{13}\text{C}$  NMR spectra were obtained on a Bruker DRX-400 Avance instrument with  $\text{CDCl}_3$  as a solvent. All reagents and solvents were purchased from Fluka and Merck and were used without further purification.

#### Preparation of diethylamine hydrogen sulfate [Et<sub>2</sub>NH<sub>2</sub>][HSO<sub>4</sub>]

In an ice bath, 0.5 mol sulfuric acid was added dropwise to the solution of diethylamine (0.5 mol diethylamine in 150 mL chloroform) under vigorous stirring. After completion of the reaction, the chloroform was removed on a rotary evaporator. Finally, after cooling the ionic liquid a white solid was obtained. This white crystalline powder was dried in high vacuum at 50°C overnight (>99% yield) [23].

#### Preparation of triethylamine hydrogen sulfate [Et<sub>3</sub>NH][HSO<sub>4</sub>]

Solution of sulfuric acid 98% (19.6 g, 0.2 mol) in water was dropped into triethylamine (20.2 g, 0.2 mol) under stirring at 60 °C for 1 h. Afterwards, the reaction mixture was stirred for another 1 h at 70 °C to ensure completion of the reaction. Finally, in order to remove the traces of water, the residue was heated at 80°C in high vacuum until the weight of the residue remained constant [24].

#### General procedure for the synthesis of 3,4,5-substituted furan-2(5H)-one derivatives

The mixture of aldehyde (1.0 mmol), amine (1.0 mmol), dialkylacetylenedicarboxylate (1.0 mmol) and 40 mol % of the ionic liquids [Et<sub>2</sub>NH<sub>2</sub>][HSO<sub>4</sub>] and [Et<sub>3</sub>NH][HSO<sub>4</sub>] was stirred for 10-15 minutes at 70-80°C. After completion of the reaction monitored by thin-layer chromatography (TLC), the reaction mixture was filtrated and washed with water/ethanol (3×3 mL) to purify the product and

separate the catalyst. The analytical and spectral data for the unknown products (**4p** and **4q**) are represented below:

#### *t*-Butyl-2,5-dihydro-5-oxo-2-(4-bromophenyl)-4-(phenylamino)furan-3-carboxylate (**4p**)

White powder; m.p. 169-172 °C; IR (KBr):  $\nu$  3208, 1716, 1677, 1596, 1499  $\text{cm}^{-1}$ ;  $^1\text{H}$  NMR ( $\text{CDCl}_3$ , 400 MHz):  $\delta$ = 1.39 (s, 9H, 3×Me), 5.65 (s, 1H, H<sub>benzylic</sub>), 7.09-7.14 (m, 3H, H<sub>Ar</sub>), 7.27-7.31 (m, 2H, H<sub>Ar</sub>), 7.38-7.41 (m, 2H, H<sub>Ar</sub>), 7.34-7.45 (m, 2H, H<sub>Ar</sub>), 9.32 (brs, 1H, NH);  $^{13}\text{C}$  NMR ( $\text{CDCl}_3$ , 100 MHz):  $\delta$ =28.0 (3×Me), 61.0 (C<sub>benzylic</sub>), 83.5 (OCMe<sub>3</sub>), 114.0, 122.3, 122.4, 125.9, 129.0, 129.3, 131.6, 134.5, 136.0 and 156.9 (C<sub>Ar</sub> and C=C), 162.7 and 164.8 (C=O).

#### *t*-Butyl-2,5-dihydro-5-oxo-2-phenyl-4-(3-nitrophenylamino)furan-3-carboxylate (**4q**)

White powder; m.p. 165-168 °C; IR (KBr):  $\nu$  3142, 1715, 1681, 1531, 1456  $\text{cm}^{-1}$ ;  $^1\text{H}$  NMR ( $\text{CDCl}_3$ , 400 MHz):  $\delta$ = 1.37 (s, 9H, 3×Me), 5.76 (s, 1H, H<sub>benzylic</sub>), 7.24-7.32 (m, 5H, H<sub>Ar</sub>), 7.64 (t, 1H,  $J$ =8.0 Hz, H<sub>Ar</sub>), 7.93 (ddd,  $J$ =8.0, 2.0, 0.8 Hz, 1H, H<sub>Ar</sub>), 8.09 (ddd,  $J$ =8.4, 2.4, 0.8 Hz, 1H, H<sub>Ar</sub>), 8.32 (t, 1H,  $J$ =2.4 Hz, H<sub>Ar</sub>), 9.40 (brs, 1H, NH);  $^{13}\text{C}$  NMR ( $\text{CDCl}_3$ , 100 MHz):  $\delta$ =  $^{13}\text{C}$  NMR ( $\text{CDCl}_3$ , 100 MHz):  $\delta$ =27.9 (3×Me), 61.3 (C<sub>benzylic</sub>), 83.8 (OCMe<sub>3</sub>), 115.1, 115.9, 119.9, 127.3, 127.5, 128.8, 128.9, 129.8, 134.4, 137.6, 148.3 and 156.9 (C<sub>Ar</sub> and C=C), 163.1 and 164.9 (C=O).

## RESULTS AND DISCUSSION

To examine the effect of catalyst loading and temperature on the three-component condensation reaction of 4,5-substituted furan-2(5H)-ones, the reaction of aromatic aldehydes, aromatic amines and dialkyl acetylenedicarboxylates was selected as a model in the presence of the ionic liquids, diethylamine hydrogen sulfate [Et<sub>2</sub>NH<sub>2</sub>][HSO<sub>4</sub>] and triethylammonium hydrogensulfate ([Et<sub>3</sub>NH][HSO<sub>4</sub>]) as catalysts (Table 1). Different amounts of diethylamine hydrogensulfate and triethylammonium hydrogensulfate were applied as catalysts (15, 20, 30, 40, 50 and 55 mol %) at various temperatures (45, 50, 60, 70, 80, 90 and 100

°C) (Table 1). As the Table shows, the addition of 40 mol % of acidic ionic liquid catalyst at 80 and 70 °C results in a corresponding product within 15 min with 85 % yield. Afterwards, the three-component condensation reaction of aromatic aldehydes, aromatic amines and dialkyl acetylenedicarboxylates was investigated under optimized conditions for preparation of 4,5-substituted furan-2(5*H*)-one derivatives (Table 2).

To better understanding the effect of the substituent, diverse substituted aldehydes were used

to synthesize the desired products in high to excellent yields using the ammonium ionic liquids ([Et<sub>2</sub>NH<sub>2</sub>][HSO<sub>4</sub>], [Et<sub>3</sub>NH][HSO<sub>4</sub>]) as catalysts (Table 2).

The proposed speculative mechanism for the formation **4** is shown in Scheme 2. The mechanism can proceed through Michael addition, iminium-enamine tautomerization and  $\gamma$ -lactonization [25,26].

**Table 1.** Optimization of reaction conditions in the presence of different amounts of ionic liquids, A: diethylamine sulfate [Et<sub>2</sub>NH<sub>2</sub>][HSO<sub>4</sub>] B: triethylamine sulfate [Et<sub>3</sub>NH][HSO<sub>4</sub>] as catalysts at different temperatures <sup>a</sup>

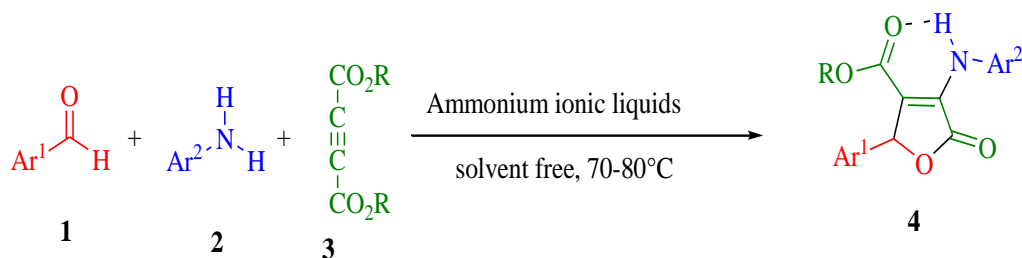
Entry	Catalyst/mol %		Temperature/ °C		Time/min		Isolated Yield/ %	
	A	B	A	B	A	B	A	B
1	15	15	80	70	15	15	36	49
2	15	15	80	70	20	20	57	55
3	20	20	80	70	15	15	65	67
4	30	30	80	70	15	15	83	81
<b>5</b>	<b>40</b>	<b>40</b>	<b>80</b>	<b>70</b>	<b>15</b>	<b>15</b>	<b>85</b>	<b>85</b>
6	50	50	80	70	15	15	87	83
7	55	55	80	70	15	15	88	83
8	30	40	45	45	20	20	56	46
9	30	40	50	50	20	20	57	50
10	30	40	60	60	15	15	61	73
11	30	40	70	70	15	15	74	81
12	30	40	80	80	15	15	83	77
13	30	40	90	90	15	15	66	72
14	30	40	100	100	15	15	70	70
15	30	40	80	70	5	5	66	61
16	30	40	80	70	10	10	78	79
17	30	40	80	70	15	15	83	81
18	30	40	80	70	20	20	80	77

<sup>a</sup> Reaction conditions: benzaldehyde (1.0 mmol), aniline (1.0 mmol), diethyl acetylenedicarboxylate (1.0 mmol)

**Table 2.** Synthesis of furan-2(5*H*)-one derivatives in the presence of ammonium ionic liquids, A: diethylammonium hydrogensulfate [Et<sub>2</sub>NH<sub>2</sub>][HSO<sub>4</sub>] B: triethylammonium hydrogensulfate [Et<sub>3</sub>NH][HSO<sub>4</sub>] as catalysts.

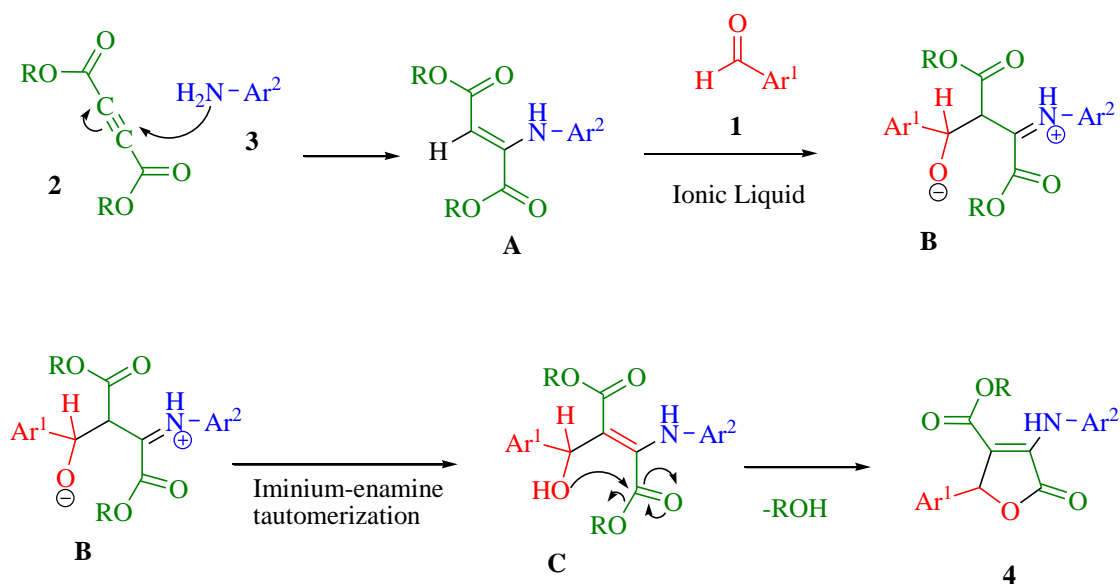
Entry	Ar <sup>1</sup>	Ar <sup>2</sup>	R	Products	Isolated Yield/ %		Ref.
					A	B	
1	Ph	Ph	CH <sub>3</sub>	<b>4a</b>	88	85	7
2	4-Me- C <sub>6</sub> H <sub>4</sub>	Ph	CH <sub>3</sub>	<b>4b</b>	80	76	7
3	3-NO <sub>2</sub> - C <sub>6</sub> H <sub>4</sub>	Ph	CH <sub>3</sub>	<b>4c</b>	81	78	7
4	4-NO <sub>2</sub> -C <sub>6</sub> H <sub>4</sub>	Ph	CH <sub>3</sub>	<b>4d</b>	89	85	19
5	4-OMe- C <sub>6</sub> H <sub>4</sub>	Ph	CH <sub>3</sub>	<b>4e</b>	88	87	19
6	Ph	4-F-C <sub>6</sub> H <sub>4</sub>	CH <sub>3</sub>	<b>4f</b>	71	67	19
7	Ph	4-Cl-C <sub>6</sub> H <sub>4</sub>	CH <sub>3</sub>	<b>4g</b>	72	69	19
8	Ph	3-NO <sub>2</sub> -C <sub>6</sub> H <sub>4</sub>	CH <sub>3</sub>	<b>4h</b>	79	78	19
9	Ph	Ph	CH <sub>3</sub> CH <sub>2</sub>	<b>4i</b>	89	85	5
10	Ph	4-Me-C <sub>6</sub> H <sub>4</sub>	CH <sub>3</sub> CH <sub>2</sub>	<b>4j</b>	90	87	5
11	4-Me-C <sub>6</sub> H <sub>4</sub>	Ph	CH <sub>3</sub> CH <sub>2</sub>	<b>4k</b>	85	82	5
12	4-Cl-C <sub>6</sub> H <sub>4</sub>	Ph	CH <sub>3</sub> CH <sub>2</sub>	<b>4m</b>	91	89	5
13	4-OMe-C <sub>6</sub> H <sub>4</sub>	Ph	CH <sub>3</sub> CH <sub>2</sub>	<b>4n</b>	90	85	5
14	1- naphthyl	Ph	CH <sub>3</sub> CH <sub>2</sub>	<b>4o</b>	64	63	5
15	4-Br-C <sub>6</sub> H <sub>4</sub>	Ph	<i>t</i> -Bu	<b>4p</b>	86	81	<i>a</i>
	Ph-C <sub>6</sub> H <sub>4</sub>	3-NO <sub>2</sub> -C <sub>6</sub> H <sub>4</sub>	<i>t</i> -Bu	<b>4q</b>	80	76	<i>a</i>

<sup>a</sup> New compounds synthesized in this work.



Ammonium ionic liquids: [Et<sub>2</sub>NH<sub>2</sub>][HSO<sub>4</sub>], [Et<sub>3</sub>NH][HSO<sub>4</sub>]

**Scheme 1.** Synthesis of 3,4,5-substituted furan-2(5*H*)-one derivative.



**Scheme 2.** Proposed mechanism for the formation of furan-2(5*H*)-one derivatives.

## CONCLUSION

In summary, a simple method for the preparation of furan-2(5*H*)-one derivatives in solvent-free conditions *via* one-pot three-component reaction from commonly available starting materials was developed. The products can be easily collected by filtration.

**Acknowledgements:** We gratefully acknowledge financial support from the Research Council of the University of Sistan and Baluchestan.

## REFERENCES

1. Y. S. Rao, *Chem. Rev.*, **76**, 625 (1976).
2. (a) V. V. Nemchenko, N. P. Ivanova, *Khim. Sel'sk. Khoz.*, **1**, 91 (1991); (b) H. Aihara, M. Muramatsu, I. Arai, *Jpn Kokai Tokyo Koho*, 225315 (1988); (c) L. N. Tsen, V. S. Suleimanyan, *Rybn. Khoz.*, **5**, 37 (1982).
3. (a) R. A. Massy-Westropp, G. D. Reynolds, T. M. Spotswood, *Tetrahedron Lett.*, **7**, 1939 (1966); (b) A. Khalid, E. Sayed, Y. Khaled, D. Orabi, C. Dunbar, M. T. Hamann, A. A. Mitchell, A. S. Yogesh, S. M. Jaber, El-Feraly, S. Farouk *Tetrahedron*, **58**, 3699 (2002); (c) S. Ma, Z. Shi, *J. Org. Chem.*, **63**, 6387 (1998); (d) A. Alaa, Y. El-Tombary, A. S. F. B. Abdel-Ghany, A. Shams, S. El-Dine, S. G. S. Farid, *Med. Chem. Res.*, **20**, 865 (2011).
4. (a) J. Zhu, H. Bienaymé, *Multicomponent Reactions*, Wiley-VCH, Weinheim, 2005; (b) A. Aminkhani, G. Marandi, *Lett. Org. Chem.*, **9**, 7 (2012); (c) J.-N. Sangshetti, N.-D. Kokare, D.-B. Shinde, *Chin. J. Chem.*, **26**, 1506 (2008); (d) S. Song, Z. Shan, Y. A. Jin, *Lett. Org., Chem.*, **7**, 64 (2010).
5. S. N. Murthy, B. Madhav, A. V. Kumar, K. R. Rao, Y. V. D. Nageswar, *Tetrahedron*, **65**, (2009).
6. S. U. Tekale, S. S. Kauthale, V. P. Pagore, V. B. Jadhav, R. P. Pawar, *J. Iran Chem. Soc.*, **10**, 1271 (2013).
7. M. R. Mohammad Shafiee, S. S. Mansoor, M. Ghashang, A. Fazlinia, *C. R. Chimie*, **17**, 131 (2014).
8. S. Ramesh, R. Nagarajan, *Synthesis*, **20**, 3307 (2011).
9. L. Nagarapu, U. N. Kumar, P. Upendra, R. Bantu, *Synth. Commun.*, **42**, 2139 (2012).
10. (a) R. D. Rogers, K. R. Seddon, *Science*, **302**, 792 (2003); (b) R. Sheldon, *Green Chem.*, **7**, 267 (2005); (c) P. Wasserscheid, W. Keim, *Angew. Chem. Int. Ed.*, **39**, 3773 (2000).
11. (a) J. S. Wilkes, J. A. Levisky, R. A. Wilson, C. L. Hussey, *Inorg. Chem.*, **21**, 1263 (1982); (b) J. S. Wilkes, M. J. Zaworotko, *J. Chem. Soc., Chem. Commun.*, 965 (1992).
12. M. A. Zolfigol, A. Khazaei, A. R. Moosavi-Zare, A. Zare, V. Khakyzadeh, *Appl. Catal. A: General*, **400**, 70 (2011).
13. A. R. Moosavi-Zare, M. A. Zolfigol, V. Khakyzadeh, C. Böttcher, M. H. Beyzavi, A. Zare, A. Hasaninejad, R. Luque, *J. Mater. Chem. A*, **2**, 770 (2014).
14. C.B. Yue, D. Fang, L. Liu, T.F. Yi, *J. Mol. Liq.*, **163**, 99 (2011).
15. A. Zare, A. R. Moosavi-Zare, M. Merajoddin, M. A. Zolfigol, T. Hekmat-Zadeh, A. Hasaninejad, A. Khazaei, M. Mokhlesi, V. Khakyzadeh, F. Derakhshan-Panah, M. H. Beyzavi, E. Rostami, A. Arghoon, R. Roohandeh, *J. Mol. Liq.*, **167**, 69 (2012).
16. A. Zare, F. Abi, A. R. Moosavi-Zare, M. H. Beyzavi, M. A. Zolfigol, *J. Mol. Liq.*, **178**, 113 (2013).
17. T. L. Greaves, C. J. Drummond, *Chem. Rev.*, **108**, 206 (2008).
18. C. Wang, L. Guo, H. Li, Y. Wang, J. Weng, L. Wu, *Green Chem.*, **8**, 603 (2006).
19. R. Doostmohammadi, M. T. Maghsoodlou, N. Hazeri, S. M. Habibi-Khorassani, *Res. Chem. Intermed.*, **39**, 4061 (2013).
20. R. Doostmohammadi, M.T. Maghsoodlou, N. Hazeri, S.M. Habibi-Khorassani, *Chin. Chem. Lett.*, **24**, 901 (2013).
21. N. Hazeri, M. T. Maghsoodlou, N. Mahmoudabadi, R. Doostmohammadi, S. Salahi, *Current Organocatal.*, **1**, 45 (2014).
22. R. Doostmohammadi, N. Hazeri, *Lett. Org. Chem.*, **10**, 199 (2013).
23. J. Weng, C. Wang, H. Li, Y. Wang, *Green Chem.*, **8**, 96 (2006).
24. Z. Zhou, X. Deng, *J. Mol. Catal. A: Chem.*, **367**, 99 (2013).
25. J. Safaei-Ghomi, F. Salimi, A. Ramazani, F. Zeinali Nasrabadi, Y. Ahmadi, *Turk. J. Chem.*, **36**, 485 (2012).
26. M. B. Teimouri, T. Abbasi, *Tetrahedron*, **66**, 3795 (2010).

## ДВЕ АМОНИЕВИ ЙОННИ ТЕЧНОСТИ КАТО ЕФЕКТИВНИ КАТАЛИЗАТОРИ ЗА ЕДНОСТАДИЙНА ЗЕЛЕНА СИНТЕЗА НА 3,4,5-ЗАМЕСТЕНИ ФУРАН-2(5*H*)-ОНИ

С. Салахи<sup>1</sup>, М.Т. Максудлу<sup>1</sup>, Н. Хазери<sup>1</sup>, М. Лашкари<sup>2</sup>, Р. Дустмохамади<sup>1</sup>, А. Канипур<sup>1</sup>, Ф. Фархадпур<sup>1</sup>, А. Шоджаеи<sup>1</sup>

<sup>1</sup>Департамент по химия, Научен факултет, Университет в Систан и Балучестан, Захедан, Иран

<sup>2</sup>Научен факултет, Велаят, Иранишахр, Иран

Постъпила на 9 септември, 2014 г.; приета на 16 септември, 2015 г.

(Резюме)

Описана е едностадийна и екологично съвместима кондензация на ароматни алдехиди, ароматни амини и диалкил-ацетилен-дикарбоксилати за синтезата на 3,4,5-заместени фуран-2(5*H*)-они без разтворител с амониеви йонни течности като катализатори. Този подход има предимствата на чисти реакционни профили, използването на лесно достъпни, евтини, рециклируеми и екологично съвместими катализатори и проста процедура.

## Convenient approach for the one-pot, three-component synthesis of 1-(benzothiazolylamino)methyl-2-naphthol using fumaric acid as a green catalyst

M. T. Maghsoodlou<sup>1\*</sup>, M. Karima<sup>1</sup>, M. Lashkari<sup>2</sup>, B. Adrom<sup>1</sup>, N. Hazeri<sup>1</sup>

<sup>1</sup>Department of Chemistry, Faculty of Science, University of Sistan and Baluchestan, P. O. Box 98135-674 Zahedan, Iran

<sup>2</sup>Faculty of Science, Velayat University, Iranshahr, Iran

Received August 24, 2014; Accepted September 15, 2015

One-pot, efficient three-component condensation of aldehydes, 2-naphthol, and 2-aminobenzothiazole in the presence of fumaric acid as an effective catalyst for the synthesis of 1-(benzothiazolylamino)methyl-2-naphthol derivatives under thermal and solvent-free conditions is described. The present approach of this methodology offers several advantages such as mild conditions, high yields, clean reaction profiles, operational simplicity, and environmentally benign and simple work-up procedures.

**Keywords:** Green protocol, 1-(Benzothiazolylamino)methyl-2-naphthol, Multi-component reaction, Fumaric acid, Solvent-free conditions.

### INTRODUCTION

Multicomponent condensation reactions have a wide range of applicability in the field of synthetic organic chemistry. They constitute an especially attractive synthetic strategy because they provide easy and rapid access to large libraries of organic compounds with diverse substitution patterns. Being one-pot reactions, they are easier to carry out than multistep syntheses, and the products are formed in a single step. Diversity can be achieved simply by varying the components [1]. In the past few years, combinatorial methods using multicomponent reactions have been closely examined as fast and convenient solutions for the synthesis of diverse classes of compounds [2]. Recently, this strategy became important in drug discovery in the context of synthesis of biologically active compounds. This method increases the efficiency of the reactions and decreases the number of laboratory operations along with solvents and chemicals used. It also reduces reaction time and increases the yield of products in comparison with normal multistep methods [3].

2-Aminobenzothiazoles are unique scaffolds that are widely used in medicinal and biological chemistry [4]. Their diverse functions range from electron transfer facilitation in the firefly luciferin cycle [5], through antitumor [6], and antidiabetic activity [7] to Alzheimer's disease tracer (8) and anticancer agent in pharmaceutical chemistry [9].

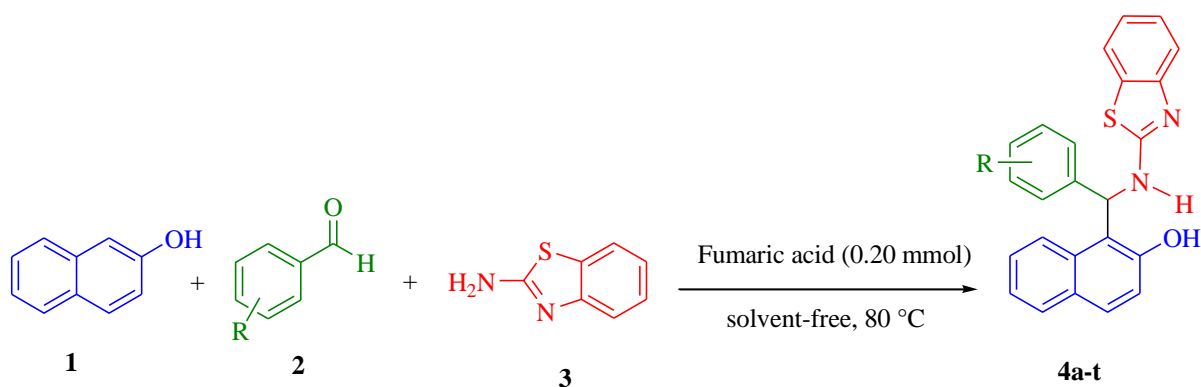
Also, benzothiazoles are commercially important as reactive dyes [10], hair dyes [11], agrochemical fungicides, insecticides, acaricides, herbicides, plant desiccants and defoliants [12].

Fumaric acid (C<sub>4</sub>H<sub>4</sub>O<sub>4</sub>) is an organic acid widely found in nature, and is a component of organic biosynthesis in humans. Chemically, it is an unsaturated dicarboxylic acid. It exists as white or nearly white crystals, odorless, with a very tart taste. Fumaric acid is generally nontoxic and nonirritant. Fumaric acid has been used in food and beverage products since the 1940s. Food research shows that fumaric acid can improve quality and reduce the costs of many food and beverage products. It is non-hygroscopic (absorbs no moisture). In the cosmetic industry, it is used as a bath salt cleaning agent for dentures. It is also used in animal feeds. Fumaric acid is used in oral pharmaceutical formulations and clinically in the treatment of psoriasis.

Because of the above-mentioned properties of 2-aminobenzothiazole and fumaric acid and as a part of our ongoing program on multi-component reactions [13,14], herein we present an eco-friendly, simple and efficient method for the synthesis of 1-(benzothiazolylamino)methyl-2-naphthol compounds *via* a one-pot three-component reaction using 2-naphthol, 2-aminobenzothiazole and aromatic aldehydes in the presence of fumaric acid under solvent-free conditions (Scheme 1).

\* To whom all correspondence should be sent:

E-mail: mt\_maghsoodlou@chem.usb.ac.ir ,  
mt\_maghsoodlou@yahoo.com



**Scheme 1.** Fumaric acid catalyzed synthesis of 1-(benzothiazolylamino)methyl-2-naphthols **4a-t**.

## EXPERIMENTAL

### General

Melting points and IR spectra were measured on an Electrothermal 9100 apparatus and a JASCO FT/IR-460 plus spectrometer, respectively. The  $^1\text{H}$  and  $^{13}\text{C}$  NMR spectra were obtained on a Bruker DRX-400 Avance instrument with DMSO as a solvent. All reagents and solvents were purchased from Fluka and Merck and were used without further purification.

### Typical procedure for the synthesis of 1-amidoalkyl-2-naphthols (**4a-t**)

Fumaric acid (0.20 mmol, 0.023 g) was added into a mixture of benzaldehyde (1.0 mmol), 2-naphthol (1.0 mmol) and 2-aminobenzothiazole (1.0 mmol), then the reaction mixture was stirred at 80 °C for the appropriate time (Table 1). After completion of the reaction (monitored by TLC), the reaction mixture was washed with  $\text{H}_2\text{O}$  ( $3 \times 10$  mL). As the catalyst is soluble in water, it was removed from the reaction mixture. Then, the residue was recrystallized from EtOH.

### 1-((Benzo[d]thiazol-2-ylamino)(2,5-dimethoxyphenyl)methyl)naphthalen-2-ol (**4s**)

Yield: 90 %; m.p. 209-211 °C; IR (KBr,  $\text{cm}^{-1}$ ): 3368 (N-H), 3060 (O-H), 1628 (C=N),  $^1\text{H}$  NMR (400 MHz, DMSO- $d_6$ ):  $\delta$  = 3.50 and 3.64 (2s, 6H, 2OCH<sub>3</sub>), 6.76 (d, 1H,  $J=8.4$  Hz,  $H_{\text{Ar}}$ ), 6.84 (d, 1H,  $J=8.8$  Hz,  $H_{\text{Ar}}$ ), 6.98 (d, 1H,  $J=7.2$  Hz,  $H_{\text{Ar}}$ ), 7.15-7.45(m, 7H,  $H_{\text{Ar}}$ , 1 $H_{\text{benzylic}}$ ), 7.63 (d, 1H,  $J=7.6$  Hz,  $H_{\text{Ar}}$ ), 7.71 (d, 1H,  $J=8.8$  Hz,  $H_{\text{Ar}}$ ), 7.77 (d, 1H,  $J=8$  Hz,  $H_{\text{Ar}}$ ), 8.26 (d, 1H,  $J=8.4$  Hz,  $H_{\text{Ar}}$ ), 8.61 (brs, 1H, NH), 9.92 (s, 1H, OH).  $^{13}\text{C}$  NMR (100 MHz, DMSO- $d_6$ ):  $\delta$  = 50.56, 55.69, 56.44, 111.64, 112.41, 116.22, 118.46, 118.72, 119.06, 121.22, 121.26, 122.66, 123.89, 125.82, 126.39, 128.70, 128.80, 129.51, 131.07, 131.70, 133.06, 151.37, 152.74, 153.24, 153.81, 166.14.

### 1-((Benzo[d]thiazol-2-ylamino)(2-hydroxy-3-methoxyphenyl)methyl)naphthalen-2-ol (**4t**)

Yield: (92%); m.p. 200-202 °C ; IR (KBr,  $\text{cm}^{-1}$ ): 3366 (N-H), 3141 (O-H), 1632 (C=N);  $^1\text{H}$  NMR (400 MHz, DMSO- $d_6$ ):  $\delta$  = 3.74 (s, 3H, OCH<sub>3</sub>), 6.67 (t, 1H,  $J=7.6$  Hz,  $H_{\text{Ar}}$ ), 6.82 (d, 1H,  $J=7.6$  Hz,  $H_{\text{Ar}}$ ), 6.96 (t, 1H,  $J=7.6$  Hz,  $H_{\text{Ar}}$ ), 7.01 (d, 1H,  $J=7.2$  Hz,  $H_{\text{Ar}}$ ), 7.14-7.40 (m, 6H,  $H_{\text{Ar}}$ , 1 $H_{\text{benzylic}}$ ), 7.61 (d, 1H,  $J=7.2$  Hz,  $H_{\text{Ar}}$ ), 7.71 (d, 1H,  $J=8$  Hz,  $H_{\text{Ar}}$ ), 7.76 (d, 1H,  $J=8$  Hz,  $H_{\text{Ar}}$ ), 8.18 (d, 1H,  $J=8.4$  Hz,  $H_{\text{Ar}}$ ), 8.64 and 8.79 (brs, 2H, NH and OH), 9.95 (brs, 1H, OH).  $^{13}\text{C}$  NMR (100 MHz, DMSO- $d_6$ ):  $\delta$  = 50.90, 56.12, 56.27, 110.81, 118.29, 118.53, 118.86, 119.16, 121.13, 121.24, 122.66, 123.43, 125.81, 126.42, 128.82, 129.30, 130.96, 132.17, 133.22, 144.29, 147.79, 151.68, 152.69, 153.66, 166.27.

## RESULTS AND DISCUSSION

Our initial aim was to develop an efficient one-pot procedure for the synthesis of 1-(benzothiazolylamino)methyl-2-naphthol derivatives through the reaction of 2-naphthol, 2-aminobenzothiazole and aldehydes in the presence of fumaric acid. To find out the optimum amount of fumaric acid, the reaction was carried out by varying the quantity of catalyst. The maximum yield was obtained when 0.20 mmol of catalyst was used (Table 1). Further increase in the amount of fumaric acid did not have any significant effect on the product yield. The results are summarized in Table 1. As shown in Table 1, the shortest time and best yield were achieved at 80 °C.

In order to evaluate the generality of the process, several examples illustrating the present method for the synthesis of 1-(benzothiazolylamino)methyl-2-naphthols (**4**) were studied (Table 2). The reactions of 2-naphthol with various aromatic aldehydes and 2-aminobenzothiazole were carried out in the presence of 0.20 mmol fumaric acid at 80°C. In all reactions, good to excellent yields were obtained at

short reaction times (4–15 min). Using these optimized reaction conditions, the generality of the reaction was examined using several types of aldehydes. As shown in Table 2, the direct three-component reaction worked well with a variety of aryl aldehydes including those bearing electron-withdrawing and electron-donating groups, and the desired compounds were obtained in good yields. However, the yield of product was lower in

comparison with aryl aldehydes containing electron-withdrawing substituents (Table 2).

The products were identified by IR, <sup>1</sup>H NMR and <sup>13</sup>C NMR spectroscopy. The <sup>1</sup>H NMR spectrum of **4s** exhibited a multiplet at  $\delta = 7.15\text{--}7.45$  for the 7 aromatic hydrogens and benzylic hydrogen and two singlets at  $\delta = 8.61$  and  $\delta = 9.92$  for the NH and OH groups, respectively.

**Table 1.** Optimization of catalyst for the synthesis of 1-(benzothiazolylamino)methyl-2-naphthols.<sup>a</sup>

Entry	Catalyst (mmol)	Temperature (°C)	Time (min)	Isolated Yield (%)
1	Fumaric acid (0.10)	80	15	78
2	Fumaric acid (0.15)	80	14	84
<b>3</b>	<b>Fumaric acid (0.20)</b>	<b>80</b>	<b>12</b>	<b>93</b>
4	Fumaric acid (0.30)	80	9	87
5	Fumaric acid (0.20)	50	60	10
6	Fumaric acid (0.20)	60	20	35
7	Fumaric acid (0.20)	100	10	52

<sup>a</sup> Reaction conditions: 2-naphthol (1.0 mmol), 2-aminobenzothiazole (1.0 mmol) and benzaldehyde (1.0 mmol) in the presence of catalyst at different temperatures.

**Table 2.** Synthesis of 1-(benzothiazolylamino)methyl-2-naphthol derivatives

Entry	R	Time (min)	Yield (%) <sup>a</sup>	Product	M.p. (lit. m.p.) (°C)[Ref.]
1	4-NO <sub>2</sub>	15	52	<b>4a</b>	188–190 (189–191)[15]
2	4-Cl	4	89	<b>4b</b>	208–210(209–210)[16]
3	3-NO <sub>2</sub>	5	50	<b>4c</b>	190–192( 191-194)[17]
4	2,4-Cl <sub>2</sub>	5	82	<b>4d</b>	204–206(206–207)[15]
5	3-MeO	5	89	<b>4e</b>	185–187(184–186)[17]
6	4-Me	10	92	<b>4f</b>	183–185(182–183)[16]
7	2-Cl	4	88	<b>4g</b>	187–189(189–190)[15]
8	2,4-(MeO) <sub>2</sub>	9	89	<b>4h</b>	162-164(161-163)[17]
9	4-OMe	7	92	<b>4i</b>	173-175(175-176)[16]
10	2-NO <sub>2</sub>	15	58	<b>4j</b>	212–214(215–216)[15]
11	2,6-Cl <sub>2</sub>	7	86	<b>4k</b>	194–196(193–195)[20]
12	3-Br	4	90	<b>4l</b>	200–202(202–204)[17]
13	4- Br	4	90	<b>4m</b>	200–202(200–202)[20]
14	4-F	11	82	<b>4n</b>	175–177(176–178)[17]
15	5-Br,2-HO	7	90	<b>4o</b>	181-183(183–185)[20]
16	Thienyl	8	90	<b>4p</b>	190–192(191–193)[20]
17	2,3-(MeO) <sub>2</sub>	10	93	<b>4q</b>	200–202(201–203)[20]
18	H	8	89	<b>4r</b>	202-204(202–203)[15]
19	2,5-(MeO) <sub>2</sub>	10	90	<b>4s</b>	209-211 <sup>b</sup>
20	5- MeO,2-HO	6	92	<b>4t</b>	200-202 <sup>b</sup>

<sup>b</sup> New compounds synthesized in this work. All known products reported previously in the literature were characterized by comparison of m.p., IR and NMR spectra with those of authentic samples.

## CONCLUSION

In summary, an efficient method for the synthesis of 1-(benzothiazolylamino)methyl-2-naphthol derivatives is described. The reactions were carried out under solvent-free conditions with short reaction times and gave the corresponding products in good yields. The present methodology offers several advantages such as good yields, simple procedure, shorter reaction times, clean reaction conditions. Moreover, the products were purified without chromatography.

**Acknowledgements:** We gratefully acknowledge financial support from the Research Council of the University of Sistan and Baluchestan.

## REFERENCES

1. (a) J. Zhu, H. Bienayme, (eds.) Multicomponent Reactions; Wiley-VCH: Weinheim, 2005, p. 1; (b) C. O. Kappe, *Curr. Opin. Chem. Biol.*, **6**, 314 (2002); (c) A. Dömling, I. Ugi, *Angew. Chem., Int. Ed.*, **39**, 3168 (2000); (d) K. Kumaravel, G. Vasuki, *Curr. Org. Chem.*, **13**, 1820 (2009); (e) I. Ugi, A. Dömling, W. Hörl, *Endeavour*, **18**, 115 (1994); (f) B. Ganem, *Acc. Chem. Res.*, **42**, 463 (2009); (g) I. Ugi, *Pure Appl. Chem.*, **73**, 187 (2001); (h) J. Zhu, H. Bienayme, (eds.) Multicomponent Reactions, Wiley-VCH: Weinheim, 2005.
2. (a) L. F. Tietze, *Chem. Rev.*, **96**, 115 (1996); (b) Dömling, A. *Chem. Rev.*, **106**, 17 (2006); (c) D. J. Ramon, M. Yus, *Angew. Chem., Int. Ed.*, **44**, 1602 (2005).
3. (a) M. Zhang, H.-F. Jiang, H.-L. Liu, Q.-H. Zhu, *Org. Lett.*, **9**, 4111 (2007); (b) J.-P. Zhu, H. Bienayme, (eds.) Multicomponent Reactions, Wiley-VCH: Weinheim, 2005, p. 1499; (c) R. M. Armstrong, A. P. Combs, P. A. Tempest, S. D. Brown, T. A. Keating, *Acc. Chem. Res.*, **29**, 123 (1996).
4. A.R. Katritzky, D.O. Tymoshenko, D. Monteux, V. Vvedensky, G. Nikonov, C.B. Cooper, M. Deshpande, *J. Org. Chem.*, **65**, 8059 (2000).
5. E. H. White, F. McCapra, G.F. Field, *J. Am. Chem. Soc.*, **85**, 337 (1963).
6. C. G. Mortimer, G. Wells, J. P. Crochard, E. L. Stone, T. D. Bradshaw, M. F. G. Stevens, A.D. Westwell, *J. Med. Chem.*, **49**, 179 (2006).
7. M. C. V. Zandt, M. L. Jones, D. E. Gunn, L. S. Geraci, J. H. Jones, D. R. Sawicki, J. Sredy, J. L. Jacot, A. T. DiCioccio, T. Petrova, A. Mitschler, A. D. Podjarny, *J. Med. Chem.*, **48**, 3141 (2005).
8. C. Rodrigues-Rodrigues, N. S. Groot, A. Rimola, A. Alvarez-Larena, V. Lloveras, J. Vidal-Gancedo, S. Ventura, J. Vendrell, M. Sodupe, P. Gonzalez-Duarte, *J. Am. Chem. Soc.*, **131**, 1436 (2009).
9. S.T. Huang, I.J. Hsei, C. Chen, *Bioorg. Med. Chem.*, **14**, 6106 (2006).
10. C.K. Desai, K.R. Desai, *Orient. J. Chem.*, **16**, 311 (2000).
11. H. Moller, D. Oberkobusch, H. Hoeffkes, *Chem. Abstr.*, **134**(12), 168045c (2001).
12. U. Heinemann, H. Gayer, P. Gerdes, B. Krueger, F. Maurer, M. Vaupel, A. Mauler-Machnik, U. Wachendorff-Neumann, G. Haenssler, K. Kuck, C. Erdelen, P. Loesel, *Chem. Abstr.*, **135**(4), 46178y (2001).
13. A. Aminkhani, R. Kabiri, S. M. Habibi-Khorassani, R. Heydari, M. T. Maghsoodlou, G. Marandi, M. Lashkari, M. Rostamizadeh, *J. Sulfur Chem.*, **30**, 500 (2009).
14. M. T. Maghsoodlou, R. Heydari, S. M. Habibi Khorassani, M. K. Rofouei, M. Nassiri, E. Mosaddegh, A. Hassankhani, *J. Sulfur Chem.*, **27**, 341 (2006).
15. Y. Yi, G. Hongyunv, *Chin. J. Org. Chem.*, **31**, 96 (2011).
16. A. Shaabani, A. Rahmati, E. Farhangi, *Tetrahedron Lett.*, **48**, 7291 (2007).
17. A. Kumar, M.-S. Rao, V.-K. Rao, *Aust. J. Chem.*, **63**, 1538 (2010).
18. B. Adrom, N. Hazeri, M. T. Maghsoodlou, M. Mollamohammadi, *Res. Chem. Intermed.*, in press DOI 10.1007/s11164-014-1564-2.
19. S. Javanshir, A. Ohanian, M.M. Heravi, M.R. Naimi-Jamal, F. F. Bamoharram, *J. Saudi Chem. Soc.*, **18**, 502 (2014).
20. A. Hosseinian, H. R. Shaterian, *Phosphorus, Sulfur, and Silicon*, **187**, 1056 (2012).

## УДОБЕН ПОДХОД ЗА ЕДНОСТАДИЙНА ТРИ-КОМПОНЕНТНА СИНТЕЗА НА 1-(БЕНЗОТИАЗОЛАМИНО) МЕТИЛ-2-НАФТОЛ С ФУМАРОВА КИСЕЛИНА КАТО ЗЕЛЕН КАТАЛИЗАТОР

М.Т. Максудлу<sup>1</sup>, М. Карима<sup>1</sup>, М. Лашкари<sup>2</sup>, Б. Адром<sup>1</sup>, Н. Хазери<sup>1</sup>

<sup>1</sup> Департамент по химия, Научен факултет, Университет в Систан и Балучестан, Захедан, Иран

<sup>2</sup> Научен факултет, Велаят, Иранияхр, Иран

Постъпила на 24 август, 2014 г.; приета на 16 септември, 2015 г.

(Резюме)

Описана е едностадийна три-компонентна кондензация на алдехиди, 2-нафтол и 2-аминобензотиазол за синтезата на 1-(бензотиазоламино) метил-2-нафтолови производни с фумарова киселина като ефективен катализатор при висока температура и в отсъствието на разтворител. Този подход предлага няколко предимства: меки условия, високи добиви, чист реакционен профил, оперативна простота, екологично съвместима и проста процедура.



## BTTPC-catalyzed one-pot synthesis of 1,4-dihydropyridine derivatives *via* Hantzsch condensation under solvent-free conditions

M. Alikarami<sup>1\*</sup>, M. Ghasemian<sup>2</sup>

<sup>1</sup>Department of Chemistry, Ilam Branch, Islamic Azad University, Ilam, Iran.

<sup>2</sup>Department of Chemistry, Borujerd Branch, Islamic Azad University, Borujerd, Iran.

Received September 17, 2014, Accepted November 16, 2015

Benzyltriphenylphosphonium chloride (BTTPC) catalyzed efficient Hantzsch reaction *via* three-component coupling reactions of aldehydes, ethyl acetoacetate and ammonium acetate under solvent-free conditions is described for the preparation of 1,4-dihydropyridine derivatives. The process presented here is operationally simple, environmentally benign, inexpensive and gives good to excellent yields.

**Keywords:** Hantzsch reaction, BTTPC, Solvent free, Three-component coupling.

### INTRODUCTION

Five- and six-member heterocyclic compounds are important constituents that often exist in biologically active natural products and synthetic compounds of medicinal interest [1-4]. Among these compounds, 1,4-dihydropyridine (1,4-DHP) heterocyclic rings are a common feature of various bioactive compounds such as vasodilator, bronchodilator, anti-atherosclerotic, anti-cancer and anti-diabetic agents [5–8]. Furthermore, 1,4-DHPs have several other medicinal applications which include neuroprotecting [9] and cerebral anti-ischemic properties for the treatment of Alzheimer's disease [10,11]. Classical method used for the synthesis of these compounds is one-pot condensation of aldehyde with ethyl acetoacetate and ammonia in acetic acid or in refluxing alcohol [12]. This method suffers from several disadvantages such as long reaction time, harsh refluxing conditions, excessive use of volatile organic solvents and low yields. In recent years, due to the importance of 1,4-DHPs, the attention to the synthesis of 1,4-DHPs increased. Different approaches for the synthesis of 1,4-dihydropyridine derivatives using various catalysts, such as cellulose-sulfuric acid [13] triphenylphosphine [14] iron (III) trifluoroacetate [15], ionic liquid [tbmim]Cl<sub>2</sub>/AlCl<sub>3</sub> [16], nickel nanoparticles [17], aluminium phosphate [18], titanium dioxide nanoparticles [19], diphenylammonium triflate [20], visible light [21], melamine trisulfonic acid [22], Cu(OTf)<sub>2</sub> [23], Fe<sub>2</sub>(SO<sub>4</sub>)<sub>3</sub>.xH<sub>2</sub>O [24], Fe<sub>3</sub>O<sub>4</sub>@SiO<sub>2</sub> nanoparticles [25], *p*-TSA [26] and hydrotalcites or hydrotalcite-like materials [27]

have been reported.

Unfortunately, many of these reported methods suffer from major or minor limitations such as the use of expensive reagents, low yields, long reaction times, tedious work-up procedures or the use of hazardous and volatile organic solvents. Thus, the search for new reagents and methods is still of growing importance.

Herein, we report a simple, efficient and cost-effective one-pot method for the synthesis of DHPs from ethyl acetoacetate, ammonium acetate and an aldehyde, using the BTTPC catalyst (Scheme 1).

### RESULTS AND DISCUSSION

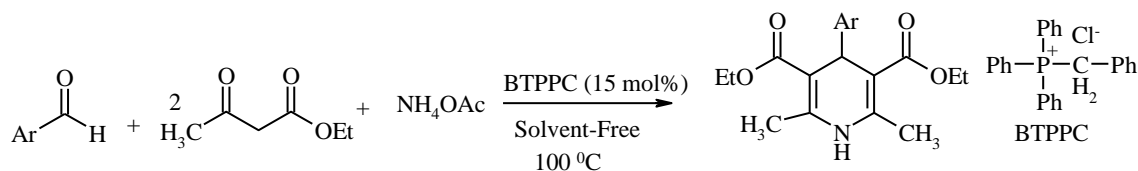
Initially, benzaldehyde was used to react with ethyl acetoacetate and ammonium acetate in the presence of 15 mol% BTTPC in various solvents like EtOH, THF, CHCl<sub>3</sub>, CH<sub>3</sub>CN and DMF at reflux temperature in order to optimize the reaction conditions (Table 1, entries 1–5). The reaction was studied under solvent-free conditions too.

It was found that the best results were obtained with 15 mol% BTTPC under solvent-free conditions (Table 1, entry 6). The reaction was completed within 30 min and the expected product was obtained in a 90% yield.

Next, we studied the effect of temperature on the model reaction. The reaction was studied at various temperatures like room temperature, 60, 100 and 130 °C. The yield of the product increased up to 100°C. After 100°C, the increase in the temperature did not lead to an increase in the yield.

Therefore, our optimized conditions were: 15 mol% of BTTPC, solvent-free at 100 °C, Table 2.

\* To whom all correspondence should be sent:  
E-mail: alikarami58@yahoo.com



**Scheme 1.** Synthesis of 1,4-dihydropyridine derivatives using BTPPC under solvent-free conditions.

**Table 1.** Synthesis of 2,6-dimethyl-4-(phenyl)-1,4-dihydropyridine-3,5-diethylcarboxylate from benzaldehyde, ethyl acetoacetate and ammonium acetate catalyzed by BTPPC under various conditions <sup>a</sup>.

Entry	Solvent	Amount of Catalyst (mol %)	Time (h)	Yield (%) <sup>b</sup>
1	EtOH	15	5	48
2	THF	15	5	43
3	CHCl <sub>3</sub>	15	5	45
4	CH <sub>3</sub> CN	15	5	55
5	DMF	15	5	38
6	None	15	0.5	90

<sup>a</sup> Reaction conditions: benzaldehyde (1 mmol), ethyl acetoacetate (2 mmol) and ammonium acetate (1.5 mmol), the amount of solvent used for entries 1–5 was 5 mL.

<sup>b</sup> Isolated yields.

**Table 2.** Optimisation of temperature using BTPPC (15 mol%) as catalyst <sup>a</sup>.

Entry	Temperature (°C)	Time (h)	Yield (%) <sup>b</sup>
1	r.t	5	-
2	60	1	78
3	100	0.5	90
4	130	0.5	90

<sup>a</sup> Reaction conditions: benzaldehyde (1 mmol), ethyl acetoacetate (2 mmol) and ammonium acetate (1.5 mmol), under solvent-free conditions.

<sup>b</sup> Isolated yields.

**Table 3.** Synthesis of 1,4-dihydropyridine derivatives using aldehyde, ethyl acetoacetate and ammonium acetate in the presence of BTPPC (15 mol%) under solvent-free conditions <sup>a</sup>.

Entry	Ar-H	Product	Yield (%)	Time (min)	M.p. [Lit. m.p. °C]
1			90	30	158 [158-160] <sup>28</sup>
2			75	40	138-140 [140-142] <sup>29</sup>

Table 3 continues on the next page

Table 3 – continuation

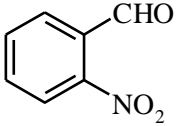
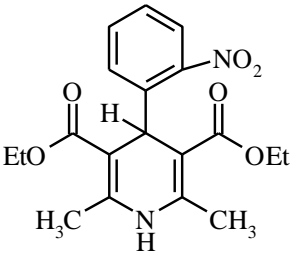
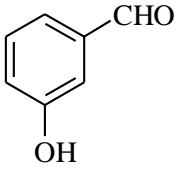
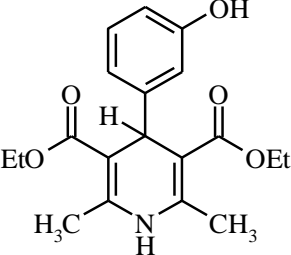
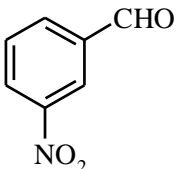
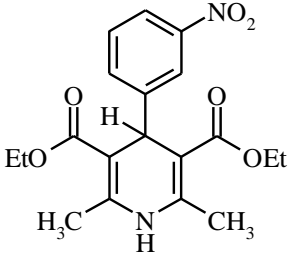
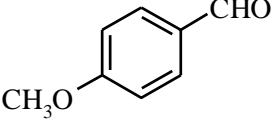
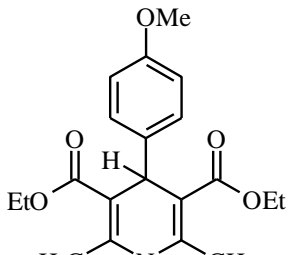
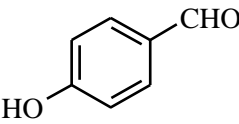
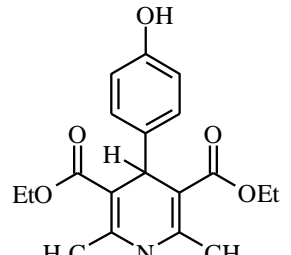
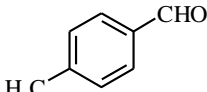
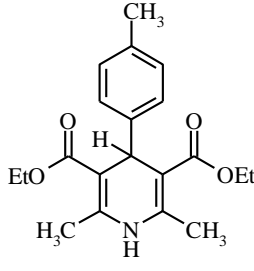
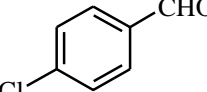
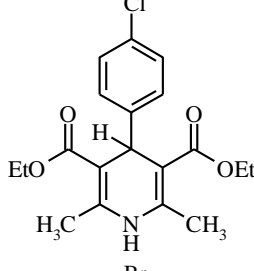
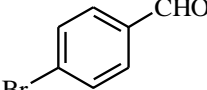
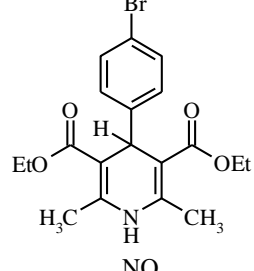
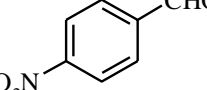
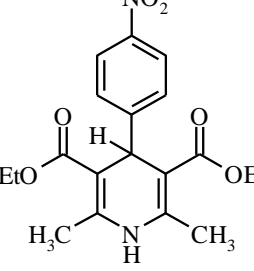
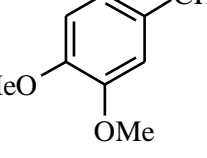
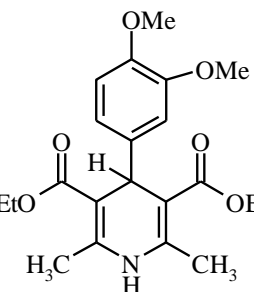
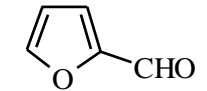
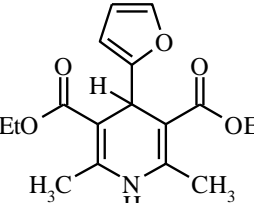
3			75	45	117-119 [118] <sup>21</sup>
4			79	35	179-181 [180-182] <sup>30</sup>
5			80	40	159-161 [161-163] <sup>31</sup>
6			87	30	160-162 [158-160] <sup>30</sup>
7			80	38	230-232 [229-232] <sup>29</sup>

Table 3 continues on the next page

Table 3 – continuation

8			84	35	139-140 [137-139] <sup>32</sup>
9			84	35	143-145 [144-145] <sup>23</sup>
10			82	35	164-166 [160-162] <sup>30</sup>
11			82	35	130-132 [130-131] <sup>31</sup>
12			85	35	160-162 [156-158] <sup>33</sup>
13			87	30	161-163 (160-162) <sup>29</sup>

<sup>a</sup> Reaction conditions: aldehyde (1 mmol), ethyl acetoacetate (2 mmol) and ammonium acetate (1.5 mmol), under solvent-free conditions at 100 °C.

<sup>b</sup> Isolated yields.

A series of 1,4-dihydropyridines were synthesized by using diverse aldehydes, ethyl acetoacetate and ammonium acetate in the presence of BTPPC (15 mol%) as a catalyst under solvent-free conditions (Table 3).

As shown in Table 3, the reaction proceeds equally well irrespective of the nature of the carbonyl compounds (aromatic, heteroaromatic) to afford the corresponding products in excellent yields (75–90%). The catalytic system works well. It is noteworthy to mention that the effect of the nature of the substituents on the aromatic ring showed no obvious effect on the conversion, because they were obtained in high yields in relatively short reaction times.

The mechanism of this reaction in the presence of BTPPC is similar to that of Hantzsch reaction mechanism. BTPPC may increase the electrophilic character of the carbonyl carbon of the aldehydes by forming intermolecular bonds between the phosphonium cations and the carbonyl oxygen of the aldehydes.

## CONCLUSIONS

In conclusion, BTPPC was found to be an efficient catalyst in the one-pot reaction of aldehydes, ethyl acetoacetate and ammonium acetate to afford 1,4-dihydropyridines.

The low cost, availability, low toxicity and stability of the catalyst under normal temperatures and pressures, good to excellent yields of products and short reaction times make this methodology a valid contribution to the existing processes in the field of 4-substituted-1,4-dihydropyridines derivatives synthesis.

## EXPERIMENTAL

### Chemicals and Apparatus

All chemicals were obtained from Merck and Fluka Companies. The melting points were measured using an Electrothermal IA 9100 digital melting point apparatus. The IR spectra were recorded on a Bruker (4000–400  $\text{cm}^{-1}$ ) spectrometer.  $^1\text{H}$  NMR spectra were recorded on a 400 MHz spectrometer using TMS as internal standard.

### General Procedure

A mixture of aldehyde (1 mmol), ethyl acetoacetate (2 mmol), and ammonium acetate (1.5 mmol) was stirred at 100 °C in the presence of BTPPC (15 mol%) for the appropriate time. After completing the reaction, as indicated by TLC, the reaction mixture was dissolved in ethanol and

poured into water. The resulting precipitate was filtered and purified by recrystallization from ethanol to afford the desired compound in pure form. All products were identified by comparison of their physical and spectroscopic data with those reported for authentic samples.

Diethyl 1,4-dihydro-2,6-dimethyl-4-phenylpyridine-3,5-dicarboxylate (**Entry 1, Table 3**): IR (KBr):  $\gamma_{\text{max}}$  3342, 1689, 1651, 1491, 1218, 1127, 704 $\text{cm}^{-1}$ .  $^1\text{H}$ NMR (400 MHz, DMSO- $d_6$ ,  $\delta$ /ppm): 1.12 (t,  $J= 7.2$  Hz, 6H), 2.25 (s, 6H), 3.98 (m, 4H), 4.85 (s, 1H), 7.21-7.07 (m, 5H), 8.80 (s, 1H).  $^{13}\text{C}$ NMR (100 MHz, DMSO- $d_6$ ,  $\delta$ /ppm): 14.2, 19.5, 39.6, 59.7, 104.1, 126.1, 127.8, 128.0, 143.9, 143.7, 167.6.

1,4-Dihydro-2,6-dimethyl-4-(4-methoxyphenyl)pyridine-3,5-dicarboxylate (**Entry 6, Table 3**): IR (KBr):  $\gamma_{\text{max}}$  3342, 2983, 1694, 1491 $\text{cm}^{-1}$ .  $^1\text{H}$ NMR (400 MHz,  $\text{CDCl}_3$ ,  $\delta$ /ppm): 1.24 (t,  $J= 7.2$  Hz, 6H), 2.33 (s, 6H), 3.76 (s, 3H), 4.01 (m, 4H), 4.94 (s, 1H), 5.70 (s, 1H), 6.76 (d,  $J= 8.8$  Hz, 2H), 7.21 (d,  $J= 8.8$  Hz, 2H).  $^{13}\text{C}$ NMR (100 MHz,  $\text{CDCl}_3$ ,  $\delta$ /ppm): 14.2, 19.5, 38.7, 55.1, 59.7, 104.3, 113.1, 128.9, 140.3, 143.5, 157.8, 167.7.

Diethyl 1,4-dihydro-2,6-dimethyl-4-(4-nitrophenyl)pyridine-3,5-dicarboxylate (**Entry 11, Table 3**): IR (KBr):  $\gamma_{\text{max}}$  3326, 1694, 1646, 1523, 1346, 1218, 1116, 704 $\text{cm}^{-1}$ .  $^1\text{H}$ NMR (400 MHz,  $\text{CDCl}_3$ ,  $\delta$ /ppm): 1.23 (t,  $J= 7.2$  Hz, 6H), 2.37 (s, 6H), 4.11 (m, 4H), 5.10 (s, 1H), 5.79 (s, 1H), 7.46 (d,  $J= 8.4$  Hz, 2H), 8.10 (d,  $J= 8.4$  Hz, 2H).  $^{13}\text{C}$ NMR (100 MHz,  $\text{CDCl}_3$ ,  $\delta$ /ppm): 14.2, 19.6, 40.1, 60.0, 103.2, 123.3, 128.9, 144.6, 146.3, 155.1, 167.0.

Diethyl 1,4-dihydro-2,6-dimethyl-4-(3,4-dimethoxyphenyl)pyridine-3,5-dicarboxylate (**Entry 12, Table 3**):  $^1\text{H}$ NMR (400 MHz, DMSO- $d_6$ ,  $\delta$ /ppm): 1.15 (t,  $J= 7.2$  Hz, 6H), 2.25 (s, 6H), 3.67 (s, 6H), 4.10-3.90 (m, 4H), 4.79 (s, 1H), 6.63 (dd,  $J= 8.4$  Hz, 2.0 Hz, 1H), 6.73 (d,  $J= 2$  Hz, 1H), 6.79 (d,  $J= 8.4$  Hz, 1H), 8.77 (s, 1H).  $^{13}\text{C}$ NMR (100 MHz, DMSO- $d_6$ ,  $\delta$ /ppm): 14.7, 18.6, 38.7, 55.7, 55.8, 59.4, 102.4, 111.9, 112.1, 119.6, 141.4, 145.5, 147.5, 148.3, 167.5.

**Acknowledgement:** Financial support of this work from the Research Council of Islamic Azad University of Ilam is gratefully acknowledged.

## REFERENCES

1. A. Mobinikhaledi, N. Foroughifar, S. M. Shariatzade, M. Fallah, *Heterocycl. Commun*, **12**, 427 (2006).
2. G. D. Henry, *Tetrahedron*, **60**, 6043 (2004).
3. J. P. Michael, *Nat. Prod. Rep.*, **22**, 627 (2005).
4. N. I. Abdel-sayed, *Bulg. Chem. Commun.* **42**, 20 (2010).

5. A. Sausins, G. Duburs, *Heterocycles*, **27**, 269 (1988).
6. M. F. Gordeev, D.V. Patel, E. M. Gordon, *J. Org. Chem.*, **61**, 924 (1996).
7. R. A. Coburn, M. Wierzba, M. J. Suto, A. J. Solo, A. M. Triggler, D. J. Triggler, *J. Med. Chem.*, **31**, 2103 (1988).
8. T. Godfraind, R. Miller, M. Wibo, *Pharmacol. Rev.*, **38**, 321 (1986).
9. V. Klusa, *Drugs Fut.*, **20**, 135 (1995).
10. R. G. Bretzel, C. C. Bollen, E. Maeser, K. F. Federlin, *Drugs Fut.*, **17**, 465 (1992).
11. G. Tenti, E. Parada, R. León, J. Egea, S. Martínez-Revelles, A. M. Briones, V. Sridharan, M. G. López, M. T. Ramos, J. C. Menéndez, *J. Med. Chem.*, **57**, 4313 (2014).
12. A. Hantzsch, *Ber. Dtsch. Chem. Ges.*, **21**, 942 (1888).
13. J. Safari, S. H. Banitaba, S. D. Khalili, *J. Mol. Catal. A: Chem.*, **335**, 46 (2011).
14. A. Debache, W. Ghalem, R. Boulcina, A. Belfaitah, S. Rhouati, B. Carboni, *Tetrahedron Lett.*, **50**, 5248 (2009).
15. H. Adibi, H.A. Samimi, M. Beygzadeh, *Catal. Commun.*, **8**, 2119 (2007).
16. B.P. Reddy, K. Rajesh, V. Vijayakumar, *Arab. J. Chem.*, **8**, 138 (2015).
17. L. Saikia, D. Dutta, D. K. Dutta, *Catal. Commun.*, **19**, 1 (2012).
18. K. Purandhar, V. Jyothi, P.P. Reddy, M. A. Chari, K. Muktantid., *J. Heterocycl. Chem.*, **49**, 232 (2012).
19. M. Tajbakhsh, E. Alaee, H. Alinezhad, M. Khanian, F. Jahani, S. Khaksar, P. Rezaee, *Chin. J. Catal.*, **33**, 1517 (2012).
20. J. Li, P. He, Ch. Yu, *Tetrahedron*, **68**, 4138 (2012).
21. S. Ghosh, F. Saikh, J. Das, A. K. Pramanik, *Tetrahedron Lett.*, **54**, 58 (2013).
22. S. Sheik Mansoor, K. Aswin, K. Logaiya, S.P.N. Sudhan, *Journal of King Saud University – Science*, **25**, 191 (2013).
23. A. S. Paraskar, A. Sudalai, *Indian J. Chem.*, **46B**, 331 (2007).
24. K. Islama, D. K. Dasa, A. T. Khana, *Tetrahedron Lett.*, **55**, 5613-5617, (2014).
25. B. Dam, S. Nandi, A. K. Pal, *Tetrahedron Lett.*, **55**, 5236 (2014).
26. M. Nasr-Esfahani, M. Montazerzohori, R. Raeatikia, *Maejo Int. J. Sci. Technol.*, **8**, 32-40 (2014).
27. Ch. A. Antonyraj, S. Kannan, *Applied Catalysis A: General*, **338**, 121 (2008).
28. A. Debache, L. Chouguiat, R. Boulcina, B. Carboni, *The Open Organic Chemistry Journal*, **6**, 12 (2012).
29. L. Ming, G. Wei-Si, W. Li-Rong, L. Ya-Feng, Y. Hua-Zheng, *J. Mol. Catal. A: Chem.*, **258**, 133 (2006).
30. Y. L. N. Murthy, A. Rajack, M. T. Ramji, J. J. Babu, Ch. Praveen, K. A. Praveen, *Bioorg. Med. Chem. Lett.*, **22**, 6016 (2012).
31. S. Sajjadifar, H. Saeidian, S. Zare, H. Veisi, S. Rezayati, *Iranian Chem. Commun.*, **1**, 7 (2013).
32. S. M. Vahdat, F. Chekin, M. Hatami, M. Khavarpour, S. Bagheri, Z. Roshan-Kouhi, *Chinese Journal of Catalysis*, **34**, 758 (2013).
33. T. Shahani, H. K. Fun, B. P. Reddy, V. Vijayakumar, S. Sarveswari, *Acta Crystallographica Section E: Struct. Rep. Online*, **66**, 1355 (2010).

## ВТРРС-КАТАЛИЗИРАНА ЕДНОСТАДИЙНА СИНТЕЗА НА 1,4-ДИХИДРОПИРИДИНОВИ ПРОИЗВОДНИ ЧРЕЗ КОНДЕНЗАЦИЯ НА HANTZSCH БЕЗ РАЗТВОРИТЕЛ

М. Аликарами<sup>1</sup>, М. Гасемян<sup>2</sup>

<sup>1</sup> Департамент по химия, Клон Илам, Ислямски университет „Азад“, Илам, Иран

<sup>2</sup> Департамент по химия, Клон Боруджерд, Ислямски университет „Азад“, Боруджерд, Иран

Постъпила на 17 септември, 2014 г.; приета на 16 ноември, 2015 г.

(Резюме)

Бензил-трифенил-фосфониев хлорид (ВТРРС) катализира ефективна реакция на Hantzsch чрез три-компонентна синтеза на 1,4-дихлоропиридинови производни от алдехиди, етилацетат и амониев ацетат в условия без разтворител. Процесът е прост за изпълнение, екологично съвместим, евтин и с добри до отлични добиви.

## Chromium(VI) removal from water by using polyaniline biocomposites with *Madhuca longifolia* and *Szygium cumini* leaves

F. Kanwal, R. Rehman\*, S. Rasul, K. Liaqat

*Institute of Chemistry, University of the Punjab, Lahore-54590, Pakistan*

Received December 12, 2014; Revised February 26, 2016

Biocomposites of polyaniline with *Madhuca longifolia* (PANI/ML) and *Szygium cumini* (PANI/SC) were synthesized, characterized and used for batch-wise adsorption of Cr(VI) from water. Optimum conditions for PANI/ML: 20 min contact time, adsorbent dose 0.3 g in 50 mL solution of Cr(VI), 50° C temperature and pH 2; and for PANI/SC: 80 min contact time, adsorbent dose 0.1 g in 50 mL solution of Cr(VI), 10° C temperature and pH 5. Langmuir isotherm shows that chemisorptive monolayer removal of Cr(VI) has occurred on the composite binding sites. 13.334 mg/g is the maximum adsorption capacity of PANI/ML, in case of PANI/SC it is 4 mg/g.  $\Delta G^\circ$  negative value confirms the feasibility and spontaneity of the adsorption process. Freundlich isotherm tells about heterogeneously distributed sites and physio-sorptive metal ion removal. For PANI/ML and PANI/SC the constant  $K_F$  values are 0.019 and 0.005, respectively. Results revealed that PANI/ML is a better ecofriendly biocomposite for Cr(VI) removal from water as compared to PANI/SC.

**Keyword:** Cr(VI), Polyaniline composites, ecofriendly, leaves, water.

### INTRODUCTION

In Pakistan uncontrolled industrialization has become the main cause of environmental degradation. Industrial effluents which contain hazardous substances and heavy metals are disposed either into water bodies or onto open land directly or indirectly. Through different routes these hazardous substances enter and disturb the lifecycle and also cause diseases, e.g, cancer [1]. One of these toxic substances is chromium which is present in aqueous systems in trivalent and hexavalent form. Different industries, for example metal finishing, pigments, glass, inks, dyes, certain glues and ceramics use chromium [2]. Heavy metals are not biodegradable and bring high level toxicity to the environment [3].

The French chemist Vauquelin discovered chromium in 1798 [4]. Cr(VI) is more poisonous than Cr(III) [5]. Cr (VI) compounds are responsible for many clinical problems. Its retention and inhalation can cause asthma, nasal septum perforation, pneumonitis, bronchitis, liver and larynx inflammation, and bronchogenic carcinoma [6-8]. For Cr(VI) removal, adsorption on activated carbon is a very efficient process but it is very expensive [9]. In the last decades, metal ion adsorption by conducting polymers as PANI and polythiophene has been reported [10]. Among conducting polymers polyaniline (PANI) is very efficient. Abundant amine and imine groups in it

can chelate metal ions [8]. In this research work, polyaniline composites with plant leaves of *Szygium cumini* (Jamun) PANI/SC, and *Madhuca longifolia* (Mahva) PANI/ML were prepared and used for Cr(VI) adsorption in batch mode.

### EXPERIMENTAL WORK

Instruments used were: Digital balance, Chiller apparatus Caoran CAN-7000-B, FT-IR spectrophotometer, atomic absorption spectrophotometer (Perkin Elmer Analyst 100). Chemicals used were: aniline monomer, anhydrous ferric chloride, HCl (AnalaR), DMF (PRS Panreac), acetone (BDH). Aniline was purified by distillation before use. The middle fraction of the distillate was collected, kept under nitrogen atmosphere and stored in a refrigerator. Aniline polymerization was carried out as already reported [7].

#### *Synthesis of PANI composites with Szygium cumini, Madhuca longifolia leaves*

The composites were prepared in a similar way as already reported [11] and characterized by UV/Visible spectroscopy and FT-IR.

#### *Preparation of stock solution and standards for adsorption studies of Cr (VI):*

For a stock solution of 1000 ppm, 2.82 g of potassium dichromate was dissolved in 1000 ml of water and further standards were prepared by dilution.

\* To whom all correspondence should be sent:  
E-mail: grinorganic@yahoo.com

### ADSORPTION STUDIES

The adsorption studies of Cr(VI) were carried out in batch mode separately for both composites as described earlier [7]. The percent removal of Cr(VI) ions was calculated by:

$$\text{Adsorption \% age} = [(C_{in} - C_{fin}) / C_{in}] \times 100$$

where  $C_{in}$  is the initial concentration of Cr(VI),  $C_{fin}$  is Cr(VI) concentration after adsorption.

### RESULTS AND DISCUSSION

#### UV/VISIBLE spectroscopic analysis

PANI and its composites were analyzed after dissolution in dimethyl formamide and their spectra were taken. The  $\lambda_{max}$  of PANI and its composites are given in Table 1. Absorption at  $\lambda_{max1}$  330 nm is due to a  $\pi - \pi^*$  transition of aniline in the benzenoid ring [11]. Absorption at 645 nm is due to an excitonic transition of benzenoid to quinonoid ring. Presence of two peaks in the UV/Vis spectra shows that two non equivalent rings, benzenoid and quinonoid, are present in the polymer chain.

#### FT-IR Characterization

FT-IR was used to characterize PANI and its composites (PANI/ML, PANI/SC) and relevant peaks are given in Table 2 [12]. By comparing the FT-IR spectra of PANI and its composites (PANI/ML, PANI/SC) it was observed that the

band (due to amino group (N-H) [13] stretching frequency) for PANI at  $3431 \text{ cm}^{-1}$  is shifted to  $3425 \text{ cm}^{-1}$  in case of PANI/ML and PANI/SC. The absorption band at  $1571 \text{ cm}^{-1}$  is due to benzenoid to quinonoid rings nitrogen bond, because of benzenoid to quinonoid transition. In case of PANI/ML it is shifted to  $1584 \text{ cm}^{-1}$  and in case of PANI/SC - to  $1575 \text{ cm}^{-1}$ . Peaks due to secondary amine stretching [14] are shifted from  $1293 \text{ cm}^{-1}$  (PANI) to  $1288 \text{ cm}^{-1}$  (PANI/ML) and  $1266 \text{ cm}^{-1}$  (PANI/SC). Bands in the range of  $1571\text{-}1116 \text{ cm}^{-1}$  are due to the conductive nature of PANI.

#### CONDUCTIVITY MEASUREMENTS

The conductivity of PANI and its composites was measured by the Four Probe Method using Keithley 4200-SCS. The conductivity of polymers depends upon their size, type of monomer, doping level, shape, and interaction between filler molecules. Temperature dependent conductivity measurements were carried out with the samples at room temperature. Results in Table 3 show that PANI/ML is less conductive than PANI/SC. Its lower conductivity is due to the poorer connectivity between grinded leaves and polymer due to which its compactness and packing density decrease, because of the presence of chains of polymer not supported by leave particles, so conductivity also decreases [11].

**Table 1.**  $\lambda_{max}$  of PANI and its composites

Sample	$\lambda_{max1}$ (nm)	Absorbance	$\lambda_{max2}$ (nm)	Absorbance
PANI	330	0.376	645	.285
PANI/SC	330	0.373	635	.227
PANI/ML	325	0.327	645	.169

**Table 2.** FT-IR analysis of PANI and its composites

Vibrational Assignment	Reference absorption band ( $\text{cm}^{-1}$ )	PANI ( $\text{cm}^{-1}$ )	PANI/ML ( $\text{cm}^{-1}$ )	PANI/SC ( $\text{cm}^{-1}$ )
N-H Stretching	3426	3431	3425	3425
N=Q=N	1577	1571	1583	1575
N=B=N	1489	1493	1499	1499
-C=N Stretching	1295	1293	1288	1266
Aromatic C-N-C	1121	1116	1132	1132

**Table 3.** Conductivity, resistivity and thickness of PANI and its composites.

Sr. No.	Samples	Thickness (cm)	Resistivity ( $\Omega$ )	Conductivity (S/cm)
1.	PANI	0.014	60.3613	$16.5669 \times 10^{-3}$
2.	PANI/ML	0.0172	$1.6495 \times 10^3$	$606.2393 \times 10^{-6}$
3.	PANI/SC	0.0188	76.42753	$1.3084 \times 10^{-2}$



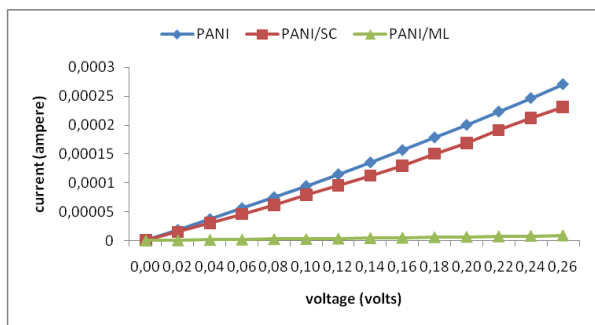


Fig.1. I-V Plots by PANI and its composites.

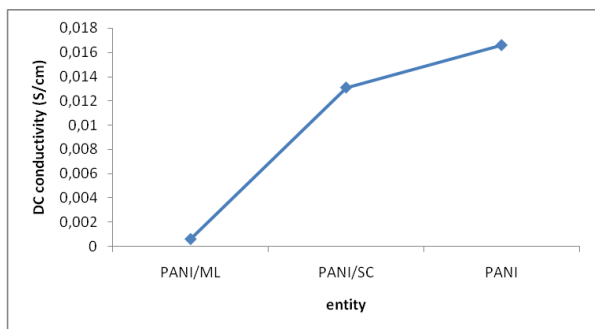


Fig.2. Comparison of conductivity of PANI and its composites.

## BATCH ADSORPTION EXPERIMENTS

### ADSORBENT DOSE

The effect of various adsorbent doses was studied for the percent removal of Cr(VI) metal. The results are given in Fig.3. The maximum percent removal of Cr (VI) was observed with 0.1 g of PANI/SC (89.52% removal) and 0.3 g of PANI/ML (91.03% removal). The results revealed that preventing the PANI/ML particles from aggregation and exposing Cr(VI) towards available active sites for adsorption showed greater efficiency in its removal. In case of PANI/ML adsorption firstly increases and then decreases because of adsorbent particles coagulation, due to which the number of sites available for adsorption decreases [12].

### CONTACT TIME

Adsorption phenomenon is time dependent. The effect of different time intervals on the percent removal of Cr (VI) by PANI/ML and PANI/SC was observed. Results are shown in Fig.4. The maximum percent removal value was 82 % for PANI/SC composite for 80 min, and 88.236 % for PANI/ML composite for 20 min. The reduced time interval for maximum removal of Cr(VI) using PANI/ML composite showed that it has more adsorption sites which are available for adsorption of metal ions. After the maximum removal of Cr (VI), the adsorption decreased with increase in

contact time because all available sites were occupied [13]. PANI/ML was more appropriate for removal of Cr (VI) than PANI/SC.

### METAL SOLUTION pH

The results of the pH study are shown in Fig.5. Solution pH is responsible for the type and ionic state of functional groups present on the sorbing material and the ionic state of chromium. Cr(VI) is converted to Cr(III) in acidic medium, which is further converted to  $\text{Cr(OH)}_2^{2+}$  and  $\text{Cr(OH)}_2^+$ , that can interact with  $-\text{NH}$ ,  $\text{N}=\text{Q}=\text{N}$  and  $\text{N}=\text{B}=\text{N}$  functional groups of PANI composites [14-18]. The Cr(VI) adsorption mechanism on the composites may be an exchange between the  $\text{Cl}^-$  and  $\text{Cr}_2\text{O}_7^-$  anions [19,21]. The maximum percent removal value was 88.666 % for PANI/SC composite at pH 5 and 91.03 % for PANI/ML composite at pH 2. PANI/ML was more appropriate for removal of Cr(VI) than PANI/SC.

### TEMPERATURE

The adsorption of Cr (VI) was studied at various temperatures ranging from 10 to 100° C on PANI/ML and PANI/SC (Fig.6). The maximum percent removal of Cr(VI) was observed at 10 °C using PANI/SC and at 50 °C using PANI/ML composite. The percent removal values were 85.655 and 87.161% for PANI/SC and PANI/ML composites, respectively. The results showed that PANI/ML was more appropriate for removal of Cr(VI) than PANI/SC.

### ADSORPTION ISOTHERMS

The Langmuir and Freundlich isotherms for PANI/ML and PANI/SC are shown in Tables 4 and 5, respectively.

Table 4. Langmuir isothermal parameters

Adsorbent	Slope	Intercept	R <sup>2</sup>	q <sub>m</sub> (mg/g)	b (L/mg)	ΔG° (KJ/mol)	R <sub>L</sub>
PANI/ML	13.27	0.075	0.912	13.334	0.005	-13.129	0.7
PANI/SC	13.99	0.250	0.979	4.0	0.017	-10.096	0.5

Table 5. Freundlich isothermal parameters

Adsorbent	Slope	Intercept	R <sup>2</sup>	K <sub>F</sub>	n
PANI/ML	1.730	1.710	0.853	0.019	0.578
PANI/SC	1.749	2.272	0.862	0.005	0.571

Langmuir isotherm indicated that monolayer chemisorptive removal of Cr(VI) ions has occurred on the homogeneously distributed composites' binding sites [22-24]. It is predominant over the Freundlich model. This means that chemisorption is predominant over physisorption, as indicated by the greater R<sup>2</sup> value of Langmuir than Freundlich. Maximum adsorption capacity (q<sub>m</sub>) values for

PANI/ML and PANI/SC are 13.34 and 4 mg/g, respectively.

The negative sign of  $\Delta G^\circ$  showed that the adsorption process is feasible and spontaneous. Results revealed that PANI/ML shows better adsorption than PANI/SC, where 'n' and 'K<sub>F</sub>' are Freundlich isotherm constants. 'K<sub>F</sub>' value was 0.019 and 0.005 for PANI/ML and PANI/SC, respectively. For Cr(VI) ions the value of 'n' was 0.578 for PANI/SC and 0.571 for PANI/JL. Separation factor R<sub>L</sub> value is between 0 and 1, indicating the favorability of this process [23]. At higher values of 'n' the affinity and heterogeneity of adsorbent sites will be greater.

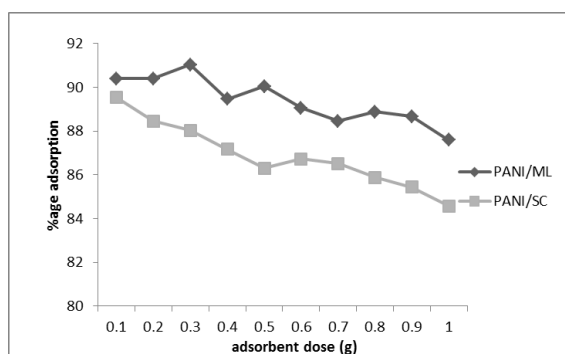


**Fig. 3.** Comparative graph of PANI/ML and PANI/SC showing the effect of adsorbent dose on the % adsorption of Cr(VI).

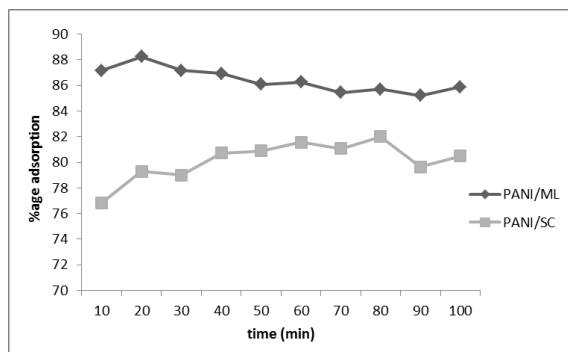


**Fig. 4.** Comparative graph of PANI/ML and PANI/SC showing the effect of contact time on the % adsorption of Cr(VI).

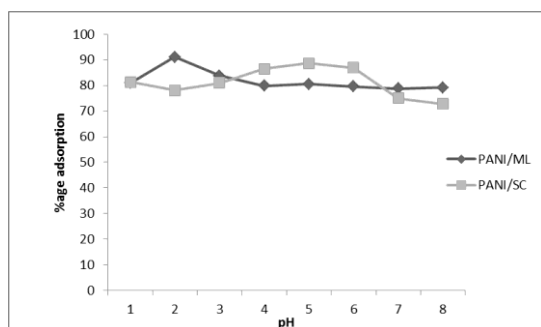


**Fig. 5.** Comparative graph of PANI/ML and PANI/SC showing effect of pH on the % adsorption of Cr(VI).

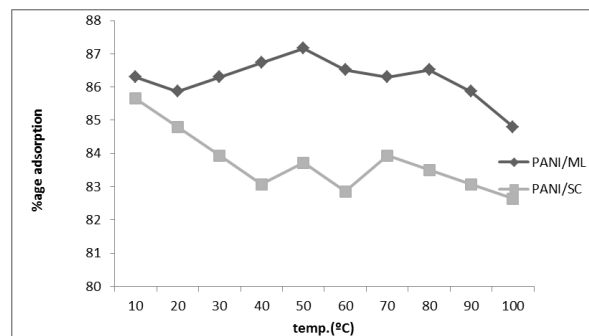


**Fig. 6.** Comparative graph of PANI/ML and PANI/SC showing the effect of temperature on the % adsorption of Cr(VI).

## CONCLUSIONS

Polyaniline composites PANI/ML and PANI/SC were synthesized, characterized and used as adsorbents for Cr(VI) removal from water. It was observed that PANI composite formation enhanced the adsorption capacity due to morphology modification and prevention of polyaniline particles aggregation. The batch experiments showed that Langmuir adsorption isothermal model is better fitted during adsorption of Cr(VI), which suggested that chemisorption occurred during removal of Cr(VI). The negative value of  $\Delta G^\circ$  confirmed the spontaneity and feasibility of the adsorption process. The observed trend of adsorption is

$$\text{PANI/ML} > \text{PANI/SC}.$$

Results revealed that polyaniline composites with *Syzygium cumini* (PANI/SC), and *Madhuca longifolia* (PANI/ML) are good adsorbents for removal of Cr(VI).

## REFERENCES

1. S.A. Khan, Riaz-ur-Rehman, M. Ali Khan, *Waste Manag.*, **15**, 271 (1995).
2. C. Namasivayam, R.T. Yamuna, *Chemosphere*, **30**, 561 (1995).
3. R.K. Gupta, R.A. Singh, S.S. Dubey, *Sep. Purif. Tech.*, **38**, 225 (2004)
4. A.K. Shanker, C.Cervantes, H. Loza-Tavera, S. Avudainayagam, *Env. Int.*, **31**, 739 (2005).
5. M.R. Samani, S.M. Borghei, A.Olad, M.J. Chaichi, *J. Hazard. Mat.*, **184**, 248 (2010).
6. J. Kotas, Z. Stasicka, *Env. Poll.*, **107**, 263 (2000).
7. F.Kanwal, R.Rehman, J. Anwar , M. Saeed, *J. Chem. Soc. Pak.*, **34**,1134 (2012).
8. Q. Li, L. Sun, Y. Zhang, Y. Qian, J. Zhai, *Desalination*, **266**, 188 (2011).
9. E. Malkoc, Y. Nuhoglu, M. Dundar, *J. Hazard. Mat.,B*, **138**, 142 (2006).
10. A.G Yavuz, E. Dincturk-Atalay, A.Uygun, F. Gode, E. Aslan, *Desalination*, **279**, 325, (2011).

11. F.Kanwal, A. Batool, S. Rasool, S. Naseem, R. Rehman, *Asian J. Chem.*, **26**, 7519 (2014).
12. K.Y. Xu, X. Zheng, C.L. Li and W.L. She, *Phys. Rev.*, **71**, 066604 (2005).
13. J.B. Pendry, A.J. Holden, W.J. Stewart, I. Youngs, *Phys. Rev. Lett.*, **76**, 4773 (1996).
14. L. Ai, J. Jiang, R. Zhang, *Syn Mat*, **160**, 762 (2010).
15. A.Olad, A. Rashidzadeh, *Iranian J. Chem. Eng.*, **5**, 45 (2008).
16. O.V.Dalgov, D.A.Kirzh, E.G.Maksimov, *Rev. Mod. Phys.*, **53**, 81, (1981).
17. P.A.Kumar, S.Chakraborty, M.Ray, *J. Chem. Eng.*, **141**, 130 (2008).
18. J.Anwar, U.Shafique, W.Zaman, M.Salman, Z.Hussain, M.Saleem, N.Shahid, S.Mahboob, S.Ghafoor, M.Akram, R.Rehman, N. Jamil, *Green Chem. Lett. Revs.*, **3**, 239 (2010).
19. Y.Zhang, Q.Li, L.Sun, R.Tang, J.Zhai, *J. Hazard. Mat.*, **175**, 404 (2010).
20. F.Kanwal, R. Rehman, J. Anwar, T. Mahmud, *EJEAFChe*, **10**, 2972, (2011).
21. R.Rehman, J. Anwar, T. Mahmud, *J. Chem. Soc. Pak.*, **34**, 460 (2012).
22. Li. X, M. Zhong, *J. Sep. Sci.*, **31**, 2839, (2008).
23. F. Kanwal, R.Rehman, J. Anwar and T. Mahmud, *J. Chil. Chem. Soc.*, **57**, 1058 (2012).
24. J. Anwar, U. Shafique, M. Salman, W. Zaman, S. Anwar, *J. Hazard. Mat.*, **171**, 797 (2009).

## ОТСТРАНЯВАНЕ НА ХРОМ (VI) ОТ ВОДИ С ИЗПОЛЗВАНЕТО НА ПОЛИАНИЛИНОВИ БИОКОМПОЗИТИ С ЛИСТА ОТ *Madhuca longifolia* И *Szygium cumini*

Ф. Канвал, Р. Рехман\*, С. Расул, К. Лиакат

*Институт по химия, Университет на Пунджаб, Лахор-54590, Пакистан*

Постъпила на 12 декември, 2014 г.; коригирана на 26 февруари, 2016 г.

(Резюме)

Синтезирани са биоконпозити от полианилин с листа от *Madhuca longifolia* (PANI/ML) и *Szygium cumini* (PANI/SC). Те са охарактеризирани и използвани за периодична адсорбция на Cr(VI) от вода. Оптималните условия за PANI/ML са: контактно време 20 мин., доза адсорбент 0.3 г в 50 mL разтвор на Cr(VI), 50° С и рН 2. За PANI/SC: контактно време 80 мин., доза адсорбент 0.1 г в 50 mL разтвор на Cr(VI), 10° С и рН 5. С помощта на изотермата на Лангмюир е показано, че отстраняването на хрома става чрез мономолекулярна хемисорбция върху активните центрове на адсорбента. Максималният адсорбционен капацитет на PANI/ML е 13.334 mg/g, докато за PANI/SC той е 4 mg/g. Отрицателната стойност на  $\Delta G^\circ$  потвърждава надеждността и спонтанността на адсорбционния процес. Изотермата на Freundlich свидетелства за хетерогенно разположени активни центрове и физичното отстраняване на металните йони. Стойностите на  $K_F$  за PANI/ML и PANI/SC са съответно 0.019 и 0.005. Резултатите показват, че PANI/ML е екологично по-добър биоконпозит за отстраняването на Cr(VI) от води спрямо биоконпозита PANI/SC.

## Effect of ultraviolet radiation on the free radicals formation in hypothyroid rat's liver

M. L. Valcheva-Traykova<sup>1\*</sup>, G. S. Bocheva<sup>2</sup>

<sup>1</sup>Department of Medical Physics and Biophysics, Faculty of Medicine, Sofia Medical University, 2 Zdrave Street, 1431 Sofia, Bulgaria

<sup>2</sup>Department of Pharmacology and Toxicology, Faculty of Medicine, Sofia Medical University, 2 Zdrave Street, 1431 Sofia, Bulgaria

Submitted February 27, 2015; Accepted September 3, 2015

Prolonged exposure to sunlight or solar simulated UV irradiation (SSUV) leads to oxidative stress in tissues. The literature data concerning the effect of this factor on hypothyroidism are controversial. The aim of this study was to investigate the influence of hypothyroidism and UV radiation on free radicals formation in rat's liver. After one week of adaptation, hypothyroid model was developed in 4 weeks, by continuous administration of 0.01% 6-n-propyl-2-thiouracil in the drinking water of male Wistar-Albino rats. Hypothyroidism was confirmed by the significant reduction of blood free thyroxin (approximately 0.44 ng/l, while 18 ng/l in the controls). The model was also proved by the loss of both appetite and body weight gain of the hypothyroid rats. During the 6-th week of the experiment, half of the PTU treated rats were irradiated with SSUV lamp for 60 min, divided into 4 portions with respective 15 min breaks. After decapitation, the accumulation of free radicals in rats' livers was measured spectrophotometrically using MTT-assay. Data were presented as percentage of the corresponding data for controls.

Alone, SSUV irradiation increased, while hypothyroidism decreased the free radicals accumulation in the rat liver. This was in agreement with the literature data about the individual effects of these factors on the oxidative stress. When the SSUV irradiation was applied on the hypothyroid rats, the relative increase of the free radicals in the liver was much higher than that in the livers of SSUV irradiated normothyroid animals.

**Key words:** hypothyroidism, UV radiation, free radicals, liver

### INTRODUCTION

Prolonged exposure to sun or solar simulated UV (SSUV) irradiation leads to accumulation of free radicals in the skin [1], immune suppression and synthesis of excessive proinflammatory cytokines, all resulting in oxidative stress in different tissues [2,3]. The sunburn and UV-radiation are major factors for set-up and development of UV-initiated diseases [4-7]. Clinical, biochemical and histological observations showed that both humans and animals develop hypothyroidism during long lasting spaceflight [8]. This has been associated with effects of sub-apoptotic doses of UVC [9], which compromised thyrocytes proliferation and the expression of genes involved in thyroid hormones production.

Thyroid hormones are involved in setting of the basal metabolic rates in the liver [10] and in decreasing of the oxidative stress-induced toxicity both in animals and humans [11,12]. But literature data about oxidative stress levels in hypothyroidism are controversial. Thyroid dysfunction was associated with enhanced oxidative stress [13] due to reduced antioxidant defense [14,15] and

increased free radicals production [16,17], although the interrelation is complicated. The oxidative stress in subclinical hypothyroidism has been associated with secondary hypercholesterolemia to thyroid dysfunction, but not to the hypothyroidism *per se* [18]. Other experimental data proved that the decreased metabolic rates due to hypothyroidism can diminish the tissue damages, opposing the deleterious effects of both increased free radicals and incapacitated antioxidant defense [19-21].

As thyroid hormones are involved in the control over the oxidative stress in a very complex manner, and the pre-exposition to solar (or solar simulated) UV radiation tends to initiate oxidative stress in tissues, the question arises about the effect of the prolonged exposition to sun or SSUV radiation on individuals with hypothyroidism.

In the present work, the effect of systemic pre-exposition to SSUV radiation on the free radicals production in the liver of hypothyroid rat model was estimated. The aim of the study was to monitor the individual and mutual effects of SSUV and hypothyroidism on the free radicals accumulation in the liver, and to compare this parameter with the corresponding level for the control animals. The accumulation of free radicals in a tissue is among the major factors for developing of the oxidative stress, later resulting in tissue damage. The free radicals accumulation was monitored by using

---

\* To whom all correspondence should be sent:  
E-mail: m\_traykova@mail.bg

spectrophotometric method, with MTT as a marker molecule. The activity of xanthine oxidase was estimated using uric acid as a marker.

## MATERIALS AND METHODS

*Animal model:* 30 male Wistar albino rats of body weight  $135 \pm 5$  g were separated in 4 groups named C (control), UV (normothyroid rats exposed to SSUV), PTU (hypothyroid rats) and PTU+UV (hypothyroid rats exposed to SSUV), housed in transparent standard containers. All animals were treated in agreement with the General regulations for treatment of experimental animals, established by the Ethic Committee at the Medical University of Sofia, in agreement with the "Guide to the care and use of Experimental Animal Care" (Canadian Council on Animal Care Guidelines, 1984).

After one week of adaptation, the groups PTU and PTU+UV were provided with 0.01% (w/w) aqueous solution of 6-n-propyl-2-thiouracil (Sigma-Aldrich), *ad libitum* for 5 weeks. The water and food consumptions were measured everyday, at the same hour, and data were used to calculate the average daily food and water consumption of one animal of a group. The body weight of the rats was measured two times per week, and the weekly body weight gain of an animal in a group was estimated. The average daily dose of 6-n-propyl-2-thiouracil consumed by the model animals was  $16 \pm 3$  mg/kg<sub>BW</sub>. At the end of the fourth week of the experiment, FT<sub>4</sub> was measured for each group. During the 5-th week, the normothyroid UV group and the hypothyroid PTU+UV group were exposed to ultraviolet radiation, by using UV lamp (type "Helios" 125W, IBORA, Bulgaria). The lamp combined UV (180 – 400 nm) and IR sources adjusted to mimic sunlight. The SSUV source was positioned at a distance of one meter from the animals' cage. The two groups were irradiated for 15 min four times per day, with periods of 15 min pause between sessions.

*Preparation of the supernatanta:* After the 7-th day of SSUV-exposure all animals were decapitated under anesthesia (Urethane, 2 mg/100 g BW). Livers were extracted and homogenized in sonified ice-cold PBS (50 mM, pH 7.45) solution of 0.04% BHT (for preventing the autooxidation with oxygen in the air). The homogenates were prepared using "Mechanik Prezsizna" type 302 homogenizer, at a speed of 2500 rpm and 20 vertical movements of the vessel. After centrifugation at 4°C and 2500 rpm for 10 min in a centrifuge (JERNETZKI K24), the supernatanta was collected and stored in ice-cold bath.

The amount of proteins in the supernatanta was determined as described by Stoscheck [22].

*Xanthine oxidase activity assessment:* The activity of xanthine oxidase was determined by measuring the relative change of the absorbance at 293 nm due to transformation of xanthine to uric acid, in a quartz cuvette, as previously described [23]. Briefly, one milliliter of the cuvette contained 0.02 ml xanthine solution, 0.02 ml supernatanta, and 0.96 ml PBS, against reference cuvette containing PBS. The blank measurement was performed by estimation of the relative change of the absorbance at 293 nm in a sample in PBS alone, with reference cuvette containing PBS. The amount of uric acid formed in the cuvette for one minute was calculated after subtracting the relative change of the absorbance at 293 nm measured in the blank sample. The activity of xanthine oxidase was calculated in mU/mg proteins, one unit of the enzyme being the amount needed to convert 1  $\mu$ mole of xanthine to uric acid for one minute at 25°C. To assess the effect of the treatment on the xanthine oxidase activity, the latter was presented as a percentage of this for the control group.

*Measurement of the free radicals accumulation:* The accumulation of free radicals in the liver supernatanta was evaluated using a marker molecule named MTT (Nitroblue tetrazolium bromide; Sigma-Aldrich) [23,24]. In presence of free radicals MTT transforms to formazan [25], with characteristic absorbance at 578 nm [25,26]. Recently, MTT has been successfully used in evaluations of free radicals accumulation in presence of pharmaceuticals [24,27], plant extracts [28,29] and animal tissues [30], proving to be very efficient and cheap. One ml of the cuvette contained 0.02 ml liver supernatanta, 0.02 ml xanthine, 0.1 ml MTT and PBS. The relative change of the absorbance at 576 nm was monitored for 5 min. The amount of MTT formazan formed for one minute in the presence of supernatanta, containing 1 mg proteins was calculated, and then data were presented as percentage of these for the control animals.

*Statistical analysis.* All parameters were presented as percentages of the corresponding parameter for the control animals. The activity of the xanthine oxidase and the formation of MTT-formazan were treated as two factors, each of them having four levels ("control", "hypothyroid", "SSUV- irradiated", and "hypothyroid and SSUV- irradiated").

The statistical significance of the mean values and standard deviations for each factor were

analyzed using Bartlett test, followed by ANOVA and Bonferoni post-test.

## RESULTS

The hypothyroidism was achieved at the end of the 4-th week, as proved by both low free thyroxin ( $0.44 \pm 0.31$  ng/l compared with  $18.41 \pm 0.28$  ng/l for the controls), loss of appetite, as well as by the loss of weight gain ( $p < 0.01$ , Figure 1).

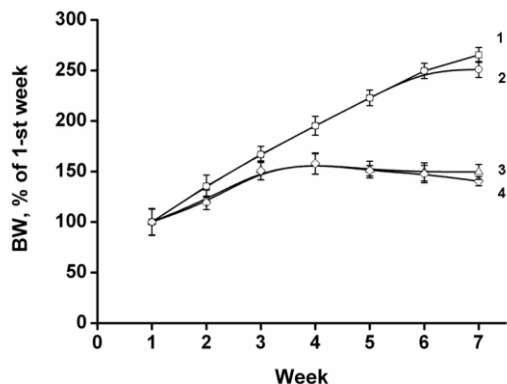


**Fig. 1.** Effect of 6-n-propyl-2-thiouracil on the body weight gain (BW, % of the 1-st week) of the experimental animals: 1 (□)- body weight of the control norm thyroid animals (group C); 2 (○)- body weight of the normothyroid rats exposed to SSUV-radiation (group UV); 3 (Δ)- body weight of the hypothyroid animals (group PTU); 4 (◇)- body weight of the hypothyroid animals exposed to SSUV-radiation for one week (group PTU+UV).

In agreement with literature [31-33], the loss of the body weight gain was associated with the decreased appetite of the animals, due to drastically decreased thyroid hormones levels.

Our data, presented in Figure 1, suggested that the hypothyroidism was the main factor for the loss of body weight gain ( $p < 0.001$ ). The SSUV exposure resulted in a slight but statistically significant ( $p < 0.05$ ) additional body weight loss for the normothyroid group.

When applied alone, SSUV treatment increased, while 6-n-propyl-2-thiouracil decreased the activity of xanthine oxidase, compared with the control group (Figure 2).

The activity of xanthine oxidase in the livers of the hypothyroid rats (group PTU) was ( $47 \pm 4$ )% of this in the livers of the control animals. This decrease could be related with the decreased overall metabolic rates of the animals due to 6-n-propyl-2-thiouracil-induced hypothyroidism [18, 20, 21].

After one week of SSUV irradiation, the xanthine oxidase activity in the liver relatively increased to ( $115 \pm 1$ )% and ( $170 \pm 2$ )% for normothyroid and hypothyroid rats, respectively, compared to this in the livers of the corresponding

untreated groups. In accordance with previously published data, this increased activity can be explained with adaptation-related oxidative stress [2,3].

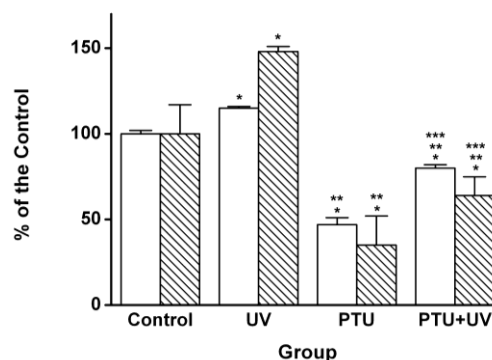


**Fig. 2.** Effects of SSUV-radiation and hypothyroidism alone and in combination on the activity of xanthine oxidase (□) and on the production of MTT- formazan (▨) in the liver homogenate of the model animals: Control – control group, PTU- hypothyroid rats, UV- normothyroid rats exposed to SSUV-radiation for 1 week, PTU+UV- hypothyroid rats irradiated for 1 week with SSUV. Data are presented as percentages of the corresponding parameters for the control group (\* -  $p < 0.05$ , \*\* -  $p < 0.01$ , \*\*\* -  $p < 0.001$ ).

However, we found, that even after SSUV exposure, the activity of xanthine oxidase in the livers of the group PTU+UV was still significantly lower than this of the control group. Statistical analysis suggested that in the hypothyroid-induced suppressed metabolism, the effect of the SSUV induced adaptive oxidative stress ( $p < 0.001$ ) due to the domination of xanthine oxidase activity in the rat liver.

The formation of MTT-formazan in the liver was enhanced due to SSUV irradiation to ( $148 \pm 3$ )%. In the hypothyroid state, the MTT-formazan decreased to ( $35 \pm 17$ )% in comparison with control animals. The SSUV exposure resulted in relatively more MTT-formazan in livers of normothyroid ( $148 \pm 3$ )% and hypothyroid ( $182 \pm 11$ )% rats, compared with the corresponding SSUV- untreated groups. The statistically significant ( $p < 0.001$ ) collective effect of SSUV and hypothyroidism on the MTT-formazan in the rat livers ( $64 \pm 11$ )%, compared to this of the control group ( $100 \pm 17$ )% indicated the prevailing impact of the SSUV.

## DISCUSSION

As the MTT-formazan was formed by interaction of MTT with free radicals [23-30], its appearance in presence of our model systems indicated free radicals formation. In our investigation, the formation of free radicals in the

liver supernatanta was prompted by addition of xanthine to the system. The increased content of xanthine provided enough substrate for xanthine oxidase to produce uric acid and reactive oxygen species [34,35].

Our study proved that, if applied alone, the 6-n-propyl-2-thiouracil-induced hypothyroidism decreased, while the SSUV-radiation increased the xanthine oxidase activity and free radicals liver accumulation. The former effect was associated with the decreased metabolic rates in the hypothyroid rats, while the latter was associated with adaptive UV-radiation induced oxidative stress.

The effects of the SSUV radiation on both xanthine oxidase activity and free radicals accumulation were stronger within the hypothyroid than within the normothyroid rats.

### CONCLUSIONS

1. SSUV irradiation and hypothyroidism alone result in opposite effects on the oxidative stress in rat's liver: the former increases, while the latter decreases the free radicals accumulation in the liver tissue.
2. The SSUV treatment of hypothyroid rats resulted in less free radicals in their livers than these accumulated in the livers of normothyroid animals.
3. The relative increase of the oxidative stress in the hypothyroid rat's liver is higher than this in the normothyroid animal.

**Acknowledgement:** This work is financially supported by Grant № 73/2013 of the Scientific Board at the Medical University of Sofia, Bulgaria

### REFERENCES:

1. F. A. Wagener, C. E. Carels, D. M. Lundvig, *Int. J. Mol. Sci.*, **14**, 9126 (2013).
2. H. Wei, X. Zhang, Y. Wang, M. *Cancer Lett.*, **185**, 21 (2002).
3. G. M. Halliday, D. L. Damian, S. Rana, S. N. Byrne, *J. Dermatol. Sci.*, **66**, 176 (2012).
4. R. K. Singh, M., Gutman, R. Reich, M., *Cancer Res.*, **55**, 3669 (1995).
5. A. Monnereau, S. L. Glaser, C. W. Schupp, K. Ekström Smedby, S. de Sanjosé, E. Kane, M. Melbye, L. Forétova, M. Maynadié, A. Staines, N. Becker, A. Nieters, P. Brennan, P. Boffetta, P. Cocco, I. Glimelius, J. Clavel, H. Hjalgrim, E. T. Chang, *Blood*, **122**, 3492 (2013).
6. P. Boffetta, O. van der Hel, A. Krickler, A. Nieters, S. de Sanjosé, M. Maynadié, P. L. Cocco, A. Staines, N. Becker, R. Font, A' Mannetje, C. Goumas, P. Brennan, *Int. J. Epidemiol.*, **37**, 1080 (2008).

7. T. Bald, T. Quast, J. Landsberg, M. Rogava, N. Glodde, D. Lopez-Ramos, J. Kohlmeyer, S. Riesenberger, D.-van den Boorn-Konijnenberg, C. Hömig-Hölzel, R. Reuten, B. Schadow, H. Weighardt, D. Wenzel, I. Helfrich, D. Schadendorf, W. Bloch, M. E. Bianchi, C. Lugassy, R. L. Barnhill, M. Koch, B. K. Fleischmann, I. Förster, W. Kastenmüller, W. Kolanus, M. Hölzel, E. Gaffal, T. Tüting, *Nature*, **507**, 109 (2014).
8. P. Dayanandan, *J. Biosci.*, **36**, 911 (2011).
9. E. Baldini, M. D'Armiento, S. Sorrenti, M. Del Sordo, R. Mocini, S. Morrone, L. Gnessi, F. Curcio, S. Ulisse, *Astrobiology*, **13**, 536 (2013).
10. A. Guerro, R. Pamplona, M. Postero-Olin, J. Barja, M. Lopez-Torrez, *Free Rad. Biol. Med.*, **26**, 73 (1999).
11. R. Gredilla, G. Barja, M. López-Torres, *Free Rad. Res.*, **35**, 417 (2001).
12. N. Petrovic, G. Cvijic, J. Djordjevic, V. Davidovic, *Ann. N.-Y. Acad. Sci.*, **1040**, 431 (2005).
13. U. Resch, G. Hersel, F. Tatzber, H. Sinzinger, *Clin. Chem. Lab. Med.*, **40**, 1132 (2002).
14. A. N. Torun, S. Kulaksizoglu, M. Kulaksizoglu, B. Q. Pamuk, E. Isbilen, N. B. Tutunku, *Clin. Endocrinol. (Oxf)*, **70**, 469 (2009).
15. P. Pasupathi, R. Latha *Thyroid Sci.*, **3**, CLS1-6 (2008).
16. S. Mukherjee, L. Samanta, A. Roy, S. Bhanja, G. B. Chainy, *Biomed Res. Int.*, Article ID 590897 (2014).
17. S. Yilmaz, S. Ozan S, F. Benzer, H. Canatan, *Cell Biochem. Funct.*, **21**, 325 (2003).
18. A. Santi, M. M. Duarte, C. C. Menezes, V. L. Loro, *Int. J. Endocrinol.*, Article ID 856359 (2012).
19. P. Venditti, M. Balestrieri, S. Di Meo, T. De Leo, *J. Endocrinol.*, **155**, 151 (1997).
20. M. J. Coria, A. I. Pastrán, M. S. Gimenez, *Acta Biomed.*, **80**, 135 (2009).
21. M. Messarah, A. Boumendjel, A. Chouabia, F. Klíbet, C. Abdennour, M. S. Boulakoud, A. E. Feki, *Exp. Toxicol. Pathol.*, **62**, 301 (2010).
22. C. M. Stoscheck, *Methods Enzymol.*, **182**, 50 (1990).
23. B. Memedi, M. Traykova, N. Boyadjieva, *Trakia J. Sci.*, **10**, 321 (2012).
24. I. Kostova, M. Traykova, V. K. Rastogi, *Med. Chem.*, **4**, 371 (2008).
25. M.V. Berridge, P. M. Herst, A.S. Tan, *Biotechnol. Annu. Rev.*, **11**, 127 (2005).
26. R. H. Burdon, V. Gill, C. Rice-Evans, *Free Radic. Res. Commun.*, **18**, 369 (1993).
27. I. Kostova, M. Traykova, *Med. Chem.*, **2**, 463 (2006).
28. I. A. Muraina, M. M. Suleiman, J. N. Eloff, *Phytomedicine*, **16**, 665 (2009).
29. Y. Liu, M. G. Nair, *J. Nat. Prod.*, **73**, 1193 (2010).
30. M. Traykova, L. Astasidi, T. Traykov, N. Boyadjieva, *Trakia J. Sci.*, **10**, 336 (2012).
31. V. Welch-White, N. Dawkins, T. Graham, R. Pace, *Lipids Health Dis.*, **12**, 100 (2013).
32. S. Walrand, K. R. Short, L. A. Heemstra, C. M. Novak, J. A. Levine, J. M. Coenen-Schimke, K. S. Nair, *FASEB J.*, **28**, 1499 (2014).
33. R. Mullur, Y. Y. Liu, G. A. Brent, *Physiol. Rev.*, **94**, 355 (2014).

34. Y. Y. Sautin, R. J. Johnson, *Nucleosides Nucleotides Nucleic Acid*, **27**, 608 (2008).

35. G. Deliconstantinos, V. Villiotou, J. C. Stavrides, *Biochem. Pharmacol.*, **51**, 1727 (1996).

## ЕФЕКТ НА УЛТРАВИОЛЕТОВОТО ОБЛЮЧВАНЕ ВЪРХУ ОБРАЗУВАНЕТО НА СВОБОДНИ РАДИКАЛИ В ЧЕРЕН ДРОБ НА ПЛЪХОВЕ С ХИПОТИРЕОИДИЗЪМ

М. Л. Вълчева-Трайкова<sup>1</sup>, Г. С. Бочева<sup>2</sup>

<sup>1</sup>*Катедра по медицинска физика и биофизика, Медицински факултет, Медицински Университет – София, ул. Здраве 2, 1431 София, България*

<sup>2</sup>*Катедра по фармакология и токсикология, Медицински факултет, Медицински Университет – София, ул. Здраве 2, 1431 София, България*

Получена на 27 февруари 2015 г., приета на 3 септември 2015 г.

(Резюме)

Продължителното облъчване на здрави тъкани със симулирана слънчева ултравиолетова радиация (ССУВР) води до окислителен стрес в тях. Литературните данни за ефекта на този фактор при хипотиреоидизъм са противоречиви. Цел на това изследване бе да се проучи влиянието на хипотиреоидизма и УВ радиацията върху образуването на свободни радикали в черен дроб на плъх. След едноседмична адаптация на мъжки бели плъхове от линията Вистар, хипотиреоидизмът у тях беше постигнат чрез хронично администриране на 0.01% б-п-пропил-2-тиоурацил (пропицил) в питейната им вода за 4 седмици. Хипотиреоидизмът бе потвърден от значителното намаление на тироксина в кръвта на моделните животни (около 0.44 нг/л, при 18 нг/л за нормотиреоидните плъхове). Хипотиреоидизмът бе потвърден и от загубата на апетит, и от забавеното относително нарастване на телесното тегло на моделните животни.

През шестата седмица на опита, половината от третираните с пропицил плъхове бяха облъчвани с лампа, симулираща слънчева УВ радиация в продължение на 60 минути, групирани в 4 равни интервала, с междинни прекъсвания от по 15 минути.

След декапитиране на опитните животни, натрупването на свободни радикали в черния дроб бе изследвано спектрофотометрично, с прилагането на МТТ-методика. Резултатите за моделната група бяха представени като процент от съответните данни за контролната група.

Приложени поотделно, ССУВР увеличаваше, докато хипотиреоидизмът намаляваше натрупването на свободни радикали в черен дроб на плъх. Този резултат бе в съгласие с литературните данни за индивидуалните ефекти на тези фактори върху окислителния стрес. След прилагане на ССУВР върху хипотиреоидни плъхове, натрупването на свободни радикали в черния им дроб беше много по-голямо от това в черния дроб на третирани по същия начин нормотиреоидни животни.



## H<sub>3</sub>PW<sub>12</sub>O<sub>40</sub> (PW<sub>12</sub>) encapsulated on cotton-like mesoporous (CLM) silica as an efficient, reusable nano photocatalyst for the decolorization of Rhodamine B

R. Fazaeli\*

Department of Chemistry, Shahreza Branch, Islamic Azad University, 86145-311, Iran.

Received January 26, 2015; Revised February 3, 2016

Cotton-like mesoporous silica (CLM) was prepared by sol-gel technology. PW<sub>12</sub>-containing cotton-like mesoporous silica system (PW<sub>12</sub>@CLM) was studied with regard to its performance towards photodecolorization of Rhodamine B (RhB) dye solutions. The surface properties of the functionalized catalyst were analyzed by a series of characterization techniques like FTIR, XRD, N<sub>2</sub> adsorption–desorption, UV-vis and TEM. The photoefficiency of PW<sub>12</sub>@CLM towards photodecolorization of RhB was investigated in a photocatalytic reactor using UV lamp as a light source.

**Keywords:** Supported photocatalyst; Encapsulation method; cotton-like mesoporous (CLM) silica; Rhodamine B.

### INTRODUCTION

Azo dye containing waste water released into water bodies without decolorization is toxic to the ecosystem and also has significant influence on human health. Therefore, such pollutants have to be treated prior to discharging into the environment. They can be efficiently eliminated by photocatalytic decolorization, as an advanced oxidation process [1,2]. Rhodamine B (RhB) is a highly water soluble, basic red dye of the xanthenes class. It is widely used as a colorant in textiles and food stuffs, and is also a well-known fluorescent water tracer. RhB is highly soluble in water and organic solvents, and its color is fluorescent bluish-red. This compound is now banned from use in foods and cosmetics because it has been found to be potentially toxic and carcinogenic. So the photodecolorization of RhB is important with regard to the purification of dye effluents [3,4]. Many catalysts such as PbMoO<sub>4</sub> [5], MgFe<sub>2</sub>O<sub>4</sub>/TiO<sub>2</sub> [6], TiO<sub>2</sub> bilayer films [7], TiO<sub>2</sub>/AC [8] and GdVO<sub>4</sub>/g-C<sub>3</sub>N<sub>4</sub> [9] have been developed for degradation of RhB.

The photo-oxidation efficiency of POMs is comparable to that of the semiconductor TiO<sub>2</sub> [10-12]. Incorporation of H<sub>3</sub>PW<sub>12</sub>O<sub>40</sub> (PW<sub>12</sub>) into a silica matrix to prepare insoluble POMs with mesoporous structure has been used in photocatalytic reactions [13-15].

It is well known that the size, morphology, and structure of mesoporous materials significantly influence their physical and chemical properties and, therefore, their applications [16]. Recently,

much effort has been devoted to developing novel approaches for tailoring the structure of mesoporous materials to have specific morphologies, which is an important goal of material scientists. Studies have shown that combinations of various micelle interactions have led to the development of helical rods [17], helical fibers [18], shells [19], hollow or solid spheres [20,21], and faceted rhombododecahedra [22]. Based on this idea, a series of mesoporous materials with special morphologies, including solid spheres, hollow spheres and leaf shapes have been synthesized using different dual-template combinations [23-26].

The focus of the present work is to synthesize PW<sub>12</sub>@CLM and apply it in the photodecolorization of RhB (C.I.No: 45170, formula weight=479.02, structure shown in Fig. 1), using UV irradiation. The effect of different parameters like initial dye concentration, catalyst loading, pH of the medium, temperature of the dye solution on the photodecolorization of RhB were studied in detail.

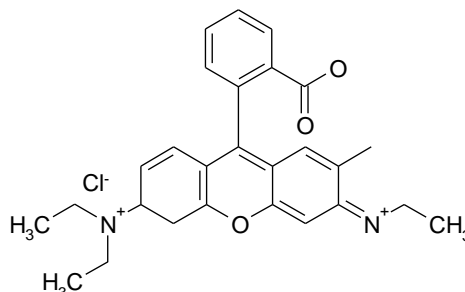


Fig. 1. Structure of Rhodamine B (RhB).

\* To whom all correspondence should be sent:  
E-mail: fazaeli@iaush.ac.ir

### Preparation of CLM

LSM was synthesized using dodecylamine (DDA, 1.17 g) and F127 (0.5 g) as templates. The templates were dissolved in a mixture of ethanol (12 mL) and water (23 mL) under stirring for 30 min. TEOS (5 mL) was then added and the mixture was stirred for 24 h at ambient temperature. The solid product was recovered by filtration, then dried for 4 h at 110 °C and calcined for 4 h at 350 °C [27].

### Preparation of $PW_{12}@CLM$

The supported  $PW_{12}$  catalyst was prepared under hydrothermal conditions. In a typical process, a 50 mg portion of  $PW_{12}$  was dissolved in deionized water and impregnated dropwise into 100 mg support (CLM) in 25 ml distilled water. The mixture was added to a Teflon container and kept under static conditions at 493 K for 8 h. The resulting solid was dried at 110 °C for 4 h and calcined at 350 °C for 4 h. According to elemental analysis, the loading was 27 wt% (Fig.2).

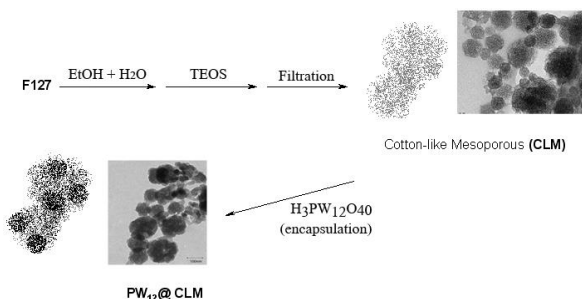


Fig. 2. Preparation of CLM and  $PW_{12}@CLM$

## RESULTS AND DISCUSSION

### Physico-chemical characterization

The surface properties of  $PW_{12}@CLM$  were analyzed by a series of characterization techniques like FTIR, XRD, N<sub>2</sub> adsorption–desorption, UV-vis and TEM.

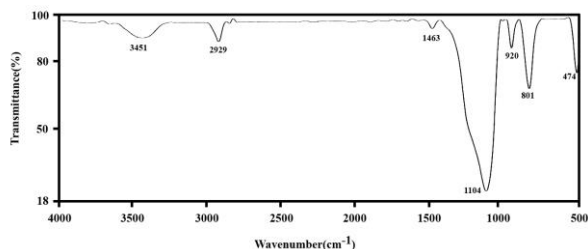


Fig. 3. FT-IR spectrum of  $PW_{12}@CLM$ .

FT-IR spectroscopy proved to be a powerful technique for studying the surface interaction between HPA and organic and inorganic supports.

Fig. 3 presents the FT-IR spectrum in the skeletal region of 4000–400 cm<sup>-1</sup> for the  $PW_{12}@CLM$  materials. In the spectrum of the parent CLM silica, a main band at 1090 cm<sup>-1</sup> with a shoulder at 1201 cm<sup>-1</sup> is observed that is due to asymmetric Si–O–Si stretching modes. Also, the corresponding symmetric stretching bands are observed at 812 and 961 cm<sup>-1</sup> [21]. The FT-IR spectrum of  $PW_{12}@CLM$  indicates that most of the characteristic bands of the parent Keggin structure, which could be found in the  $PW_{12}$  fingerprint region (1250–500 cm<sup>-1</sup>), are not shown or appeared in the same assignable position of the bands corresponding to the ordered mesoporous silica host materials [28].

Fig.4 shows the XRD patterns of the parent CLM and  $PW_{12}@CLM$  in the low angle region ( $2\theta = 0.6-8^\circ$ ). The main diffraction peak for CLM and  $PW_{12}@CLM$  is observed at  $2\theta=3.93$  and  $2\theta=4.02$ , respectively. For  $PW_{12}@CLM$  systems, on low-angle X-ray diffraction, a slight shift of the primary peak to higher  $2\theta$  values, with a corresponding decrease in the peak intensity was also noted. The shift of the primary peak to higher scattering angles can be taken as an indication of a slight decrease in the sphere diameters, possibly due to a contraction of their frameworks with increasing  $PW_{12}$  loading during the calcination procedure. For  $PW_{12}@CLM$ , the intensities of the reflections decrease, indicating that the adopted synthesis procedure leads to less ordered materials than traditional CLM [29]. However, the arrangement of the CLM framework was still well retained after incorporation of  $PW_{12}$ , as can be seen from the TEM and N<sub>2</sub> adsorption data.

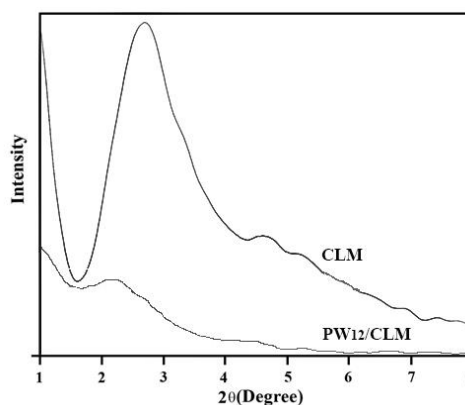
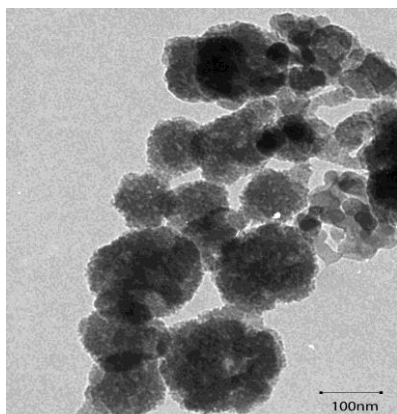


Fig.4. XRD patterns of CLM and  $PW_{12}@CLM$ .

The TEM image of the  $PW_{12}@CLM$  sample is shown in Fig. 5. The synthesized cotton-like mesoporous material clearly displayed a cotton shape and worm-like porous structure [27]. The same morphology was obtained for  $PW_{12}@CLM$ . TEM analyses indicate that the wrinkled porous structure of the CLM is robust enough to survive

the  $PW_{12}$  incorporation process and so offers an excellent matrix to support highly dispersed  $PW_{12}$  species. The places with darker contrast could be assigned to the presence of  $PW_{12}$  particles with different dispersion. The small dark spots in the image could be ascribed to  $PW_{12}$  particles, probably located in the  $PW_{12}$ @CLM cavities. The larger dark areas over the cavities most likely correspond to  $PW_{12}$  agglomerates on the external surface.



**Fig. 5.** TEM image of  $PW_{12}$ @CLM.

Structural properties of CLM and  $PW_{12}$ @CLM are listed in Table 1. CLM showed BET surface area of  $1255 \text{ m}^2/\text{g}$  and pore volume of  $1.21 \text{ cm}^3/\text{g}$ . After  $PW_{12}$  modification, the nitrogen adsorption isotherm (Fig. 6) became an even line and the adsorbed volume decreased distinctly, suggesting the occupation of the pore by  $PW_{12}$ . BET surface area and pore volume of  $PW_{12}$ @CLM samples decreased which confirms that  $PW_{12}$  has occupied the channels in CLM.

Two main absorptions are present in the DRUV-vis spectrum of pure  $PW_{12}$ : the first one is centered at 255 nm, and is attributed to the oxygen-tungsten charge-transfer absorption band for Keggin anions [30]. The second broad absorption in the  $PW_{12}$  is centered at 360 nm with a shoulder at 345 nm. For  $PW_{12}$ @CLM (Fig. 7), these bands are clearly observed, and since pure nano- $\text{SiO}_2$  shows no UV absorption peak, therefore, these results indicated that a primary Keggin structure has been introduced into the nanostructure framework.

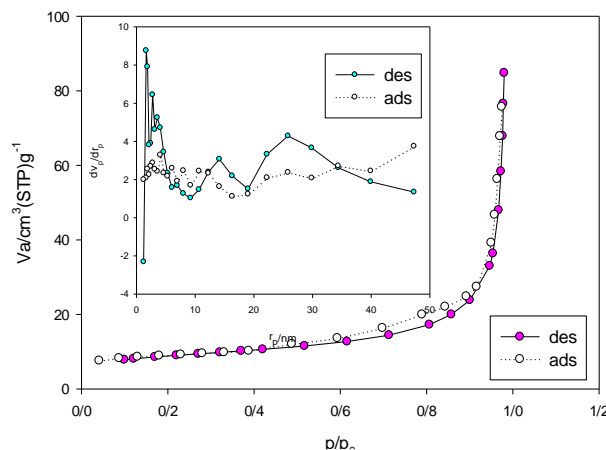


**Fig. 6.**  $\text{N}_2$ -adsorption-desorption isotherms of  $PW_{12}$ @CLM.

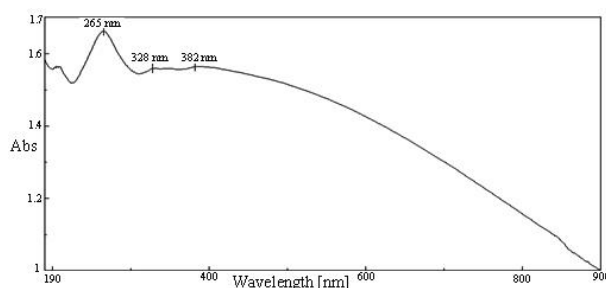


**Fig. 7.** DRUV-vis spectrum of  $PW_{12}$ @CLM.

#### Photocatalytic activity

After characterizing  $PW_{12}$ @CLM, the obtained material was used for the photocatalytic decolorization of a 40 ppm RhB dye solution containing  $1 \text{ g L}^{-1}$  photocatalyst under UV irradiation at varied conditions. A negligible decrease in the concentration of dye was observed under irradiation in the absence of photocatalyst or in the presence of photocatalyst without a light source. It is evident from the following results that the photolysis of the RhB solution in the presence of photocatalyst leads to the disappearance of the compound. In the absence of catalyst, direct photolysis of RhB was very slow and no appreciable photodecolorization, about 7 %, was observed during 60 min of UV irradiation, while in the presence of catalyst, the percentage of dye degraded after 60 min ranged from 7% to 92%.

**Table 1.** Texture parameters of CLM and  $PW_{12}$ @CLM samples.

Material	Surface area ( $\text{m}^2/\text{g}$ )	Texture parameters ( $\text{N}_2$ adsorption)	
		Pore volume ( $\text{cm}^3/\text{g}$ ) <sup>a,b</sup>	Pore diameter (nm)
CLM	1255	1.21	3.3
$PW_{12}$ @CLM	380	0.96	1.8

<sup>a</sup>Total pore volume measured at  $p/p_0 = 0.99$ .

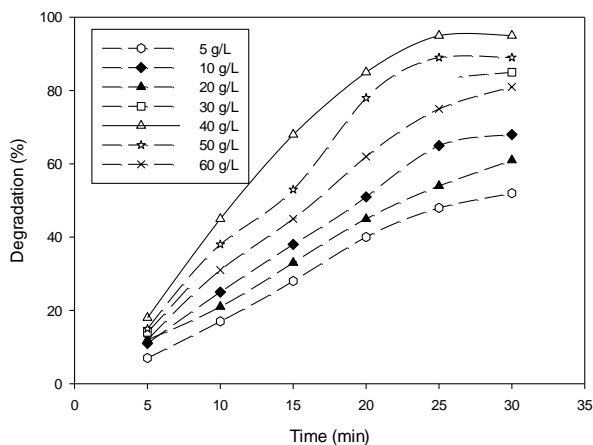
<sup>b</sup>Pore volume and pore size (by BJH method) determined from  $\text{N}_2$  adsorption at 77K.

### Effect of photocatalyst dosage

The effect of the amount of  $PW_{12}@CLM$  on the photodecolorization of RhB *versus* time is shown in Fig. 8a. It was observed that the decolorization percentage increased with increasing the amount of photocatalyst, reached the highest value ( $0.40 \text{ g L}^{-1}$  of the photocatalyst) and then decreased. The reason for this decrease is thought to be the fact that when the concentration of the catalyst rises, the solid particles increasingly block the penetration of the photons.

So, the overall number of photons that can reach the catalyst particles and the production of OH radicals decrease with the loading of the catalyst. Another reason may be the decolorization of solid particles while using large amounts of catalyst [31].

a)



b)

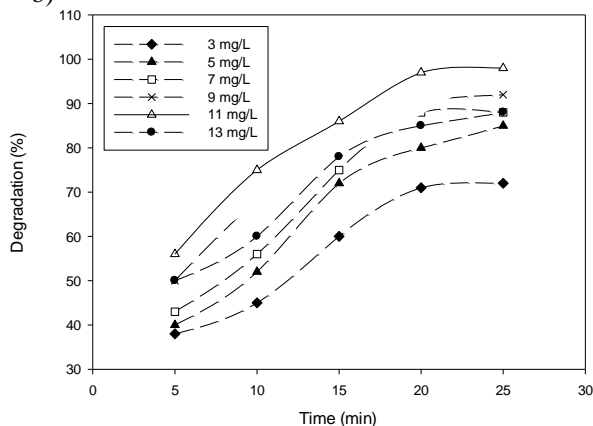


**Fig. 8.** (a) Effect of  $PW_{12}@CLM$  dosage on decolorization efficiency; initial RhB concentration,  $11 \text{ mg L}^{-1}$ ; initial pH, 9; (b) Effect of initial dye concentration on RhB decolorization efficiency;  $0.40 \text{ g L}^{-1}$  of the catalyst; initial solution pH= 9.

### Effect of the initial dye concentration

After optimizing the photocatalyst dosage, the effect of initial dye concentration ranging from 3 to  $13 \text{ mg L}^{-1}$  on the photodecolorization of RhB was investigated. The obtained results are shown in Fig.

8b. It can be seen that the rate of photodecolorization increases with increasing dye concentration up to  $11 \text{ mg L}^{-1}$ . This may be due to the fact that as the dye concentration was increased, more dye molecules were available for consecutive decolorization. The rate of photodecolorization was found to decrease with further increase in dye concentration, i.e., above  $11 \text{ mg L}^{-1}$ . The reason for this decrease is attributed to the shielding effect of the dye at high concentration that retards the penetration of light to the dye molecules deposited over the catalyst surface.

### Influence of pH

The effect of pH in the range of 1-11 on RhB dye decolorization efficiency *versus* time is presented in Fig. 9. The pH value of the original solution of RhB is 9. Dilute hydrochloric acid solution or potassium hydroxide solution was used to tune the pH value when necessary. The initial concentration of RhB solution and dosage of the photocatalyst were kept at  $11 \text{ mg L}^{-1}$  and  $0.40 \text{ g L}^{-1}$ , respectively. Cationic dyes, such as RhB, undergo efficient degradation in the presence of  $PW_{12}@CLM$  under UV-Vis irradiation in alkaline media. These observations suggest that the charge characteristics of the dye substrates greatly influence their degradation. The effect of pH on the degradation of dyes in the presence of  $\text{SiO}_2$  has been explained on the basis of point of zero charge ( $\text{pH}_{\text{pzc}}$ ) of  $\text{SiO}_2$  particles. The  $\text{pH}_{\text{pzc}}$  of  $\text{SiO}_2$  particles is 5.5 [32]. Thus,  $\text{SiO}_2$  is positively charged in acidic solution ( $\text{pH} < 5.5$ ) and negatively charged in alkaline solution. According to this explanation and because of electrostatic interactions, cationic dyes (Rh.B) should be degraded at alkaline solution (Fig. 9). In alkaline solutions, the interaction between catalyst surface ( $\text{Si-O}^-$ ) and dye [specifically the nitrogen group, such as RhB, (Fig. 1)] favors the adsorption of the dye on the surface and accordingly, the photocatalytic activity increases [33].

### Reusability of the catalyst

In our experiments, the stability and reusability of the photocatalyst were examined by repetitive use of the catalyst. After the dye was degraded in the first cycle, the photocatalyst was removed by filtration, washed several times with deionized water and dried at 90 and  $350 \text{ }^\circ\text{C}$  for 2 h. This recovered catalyst was used again with the same concentration of RhB solution. The decomposition of RhB in the second cycle was almost as fast as in the first run. The fourth run of the decolorization of RhB showed no significant loss of photoactivity of

the catalyst, which indicated the considerable stability of the photocatalyst under the present conditions.

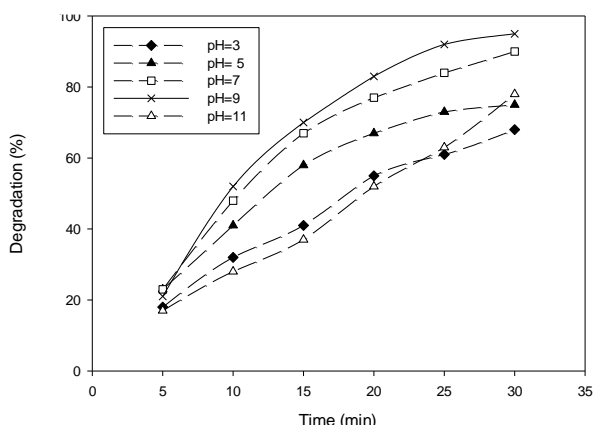


**Fig. 9.** Influence of solution pH on the RhB dye decolorization;  $0.40 \text{ g L}^{-1}$  of the catalyst; initial RhB concentration,  $11 \text{ mgL}^{-1}$ .

Comparison of  $PW_{12}@CLM$  with recently reported catalysts [5-9] for degradation of RhB shows that the photocatalytic activity of  $PW_{12}@CLM$  seems to be comparable with that of other known catalysts.

## CONCLUSIONS

The results of this research demonstrated that  $PW_{12}@CLM$  is an efficient catalyst for the photodegradation of RhB. The results of the UV-Vis spectral changes indicate that the photocatalytic process can be used for complete decolorization and mineralization of RhB in the presence of  $PW_{12}@CLM$  in a photochemical reactor.

**Acknowledgements:** We gratefully thank Shahreza Branch, Islamic Azad University, for financial support.

## REFERENCES

- C.G. Feng, X.X. Zhuo, X. Liu, *J. Rare Earths*, **25**, 717 (2009).
- K. Bubacz, J. Choina, D. Dolat, A.W. Morawski, *Polish J. Env. Stud.*, **19**, 685 (2010).
- N. Barka, S. Qourzal, A. Assabbane, A. Nounah, Y. Ait-ichou, *J. Photochem. Photobiol. A.*, **195**, 346 (2008).
- L. You-ji, C. Wei, *Catal. Sci. Technol.*, **1**, 802 (2011).
- D.B. Hernández-Uresti, J.A. Aguilar-Garib, A.M. la Cruz, *J. Microwave Power EE*, **46** (3), 163 (2012).
- L. Zhang, Y. He, Y. Wu, T. Wu, *Mater. Sci. Eng. B.*, **176**, 1497 (2011).
- J. Zhuang, W. Dai, Q. Tian, Z. Li, L. Xie, J. Wang, P. Liu, *Langmuir*, **26**(12), 9686 (2010).
- Y. Li, S. Sun, M. Ma, Y. Ouyang, W. Yan, *Chem. Eng. J.*, **142**, 147 (2008).
- Y. He, J. Cai, T. Li, Y. Wu, H. Lin, L. Zhao, M. Luo, *Chem. Eng. J.*, **215-216**, 721 (2013).
- A. Pearson, S. K. Bhargava, V. Bansal, *Langmuir*, **27**, 9245 (2011).
- C. Yang, L. Tian, L. Ye, T. Peng, K. Deng, L. Zan, *J. Appl. Polymer Sci.*, **120**, 2048 (2011).
- Z. Jiang, J. Han, X. Liu, *Adv. Mater. Res.*, **152-153**, 202 (2011).
- Y.H. Guo, C.W. Hu, X.L. Wang, Y.L. Wang, E.B. Wang, Y.C. Zou, H. Ding, S.H. Feng, *Chem. Mater.*, **13**, 4058 (2001).
- Y. Guo, Y. Wang, C. Hu, Y. Wang, E. Wang, Y. Zhou, S. Feng, *Chem. Mater.* **12**, 3501 (2000).
- G. Marci, E. García-López, M. Bellardita, F. Parisi, C. Colbeau-Justin, S. Sorgues, L. F. Liotta, L. Palmisano, *Phys. Chem. Chem. Phys.*, **15**, 13329 (2013).
- H.L. Xu, W.Z. Wang, *Angew. Chem. Int. Ed.* **46**, 1489 (2007).
- S. Yang, L.Z. Zhao, C.Z. Yu, X.F. Zhou, J.W. Tang, P. Yuan, D.Y. Chen, D.Y. Zhao, *J. Am. Chem. Soc.* **128**, 10460 (2006).
- G.L. Lin, Y.H. Tasi, H.P. Lin, C.Y. Tang, C.Y. Lin, *Langmuir*, **23**, 4115 (2007).
- Y.Q. Yeh, B.C. Chen, H.P. Lin, C.Y. Tang, *Langmuir*, **22**, 6 (2006).
- Y.F. Zhu, J.L. Shi, H.R. Chen, W.H. Shen, X.P. Dong, *Micropor. Mesopor. Mat.*, **85**, 75 (2005).
- W.Q. Wang, J.G. Wang, P.C. Sun, D.T. Ding, T.H. Chen, *J. Colloid Interf. Sci.* **331**, 156 (2009).
- B.C. Chen, M.C. Chao, H.P. Lin, C.Y. Mou, *Micropor Mesopor Mat.*, **81**, 241 (2005).
- J.G. Wang, F. Li, H.J. Zhou, P.C. Sun, D.T. Ding, T.H. Chen, *Chem. Mater.*, **21**, 612 (2009).
- H. Blas, M. Save, P. Pasetto, C. Boissiere, C. Sanchez, B. Charleux, *Langmuir*, **24**, 13132 (2008).
- Z. Feng, Y.S. Li, D.C. Niu, L. Li, W.R. Zhao, H.R. Chen, L. Lei, J.H. Gao, M.L. Ruan, J.L. Shi, *Chem. Commun.*, 2629 (2008).
- F. Cavani, N. Ballarini, A. Cericola, *Catal. Today*, **127**, 113 (2007).
- L. Du, H. Song, S. Liao, *Appl. Sur. Sci.* **255**, 936 (2009).
- R. Fazaeli, H. Aliyan, S. Parishani Froushani, Z. Mohagheghian, *Turk. J. Chem.*, **38**, 372 (2014).
- R. Fazaeli, H. Aliyan, E. Naderi, *Phosphorus, Sulfur*, **188**, 745 (2013).
- J. Juan-Alcaniz, E. V. Ramos-Fernandez, U. Lafont, J. Gascon, F. Kapteijn, *J. Catal.*, **269** 229 (2010).
- H. Aliyan, R. Fazaeli, R. Jalilian, *Appl. Sur. Sci.*, **276**, 147 (2013).
- M. Guedes, J.A.F. Ferreira, A.C. Ferro, *J. Colloid Inter. Sci.* **337**, 439 (2009).
- H. Aliyan, R. Fazaeli, R. Jalilian, *Appl. Sur. Sci.*, **276**, 147 (2013).

**H<sub>3</sub>PW<sub>12</sub>O<sub>40</sub> (PW<sub>12</sub>) КАПСУЛИРАН В ПАМУКО-ПОДОБЕН МЕЗОПОРЪОЗЕН СИЛИЦИЕВ ДИОКСИД (CLM) КАТО ЕФЕКТИВЕН И МНОГОКРАТНО УПОТРЕБЯВАН НАНО-ФОТОКАТАЛИЗАТОР ЗА ОБЕЗЦВЕТЯВАНЕТО НА RHODAMINE B**

**Р. Фазаели**

*Департамент по химия, Клон Шахреза, Ислямски университет „Азад“, 86145-311, Иран*

Постъпила на 26 януари, 2015 г.; коригирана на 3 февруари, 2016 г.

(Резюме)

Приготвен е памуко-подобен мезопоръозен силииев диоксид (CLM) по зол-гел технология. Изследвана е PW<sub>12</sub>-съдържаща система с памуко-подобен мезопоръозен силииев диоксид (PW<sub>12</sub>@CLM) по отношение на фото-химичното обезцветяване на Rhodamine B (RhB) в багрилни разтвори. Повърхностните свойства на този катализатор са анализирани с различни техники, като FTIR, XRD, N<sub>2</sub> адсорбция/десорбция, UV-Vis и TEM. Ефективността спрямо PW<sub>12</sub>@CLM фото-обезцветяването на RhB е изследвана във фото-каталитичен реактор с UV-лампа като светлинен източник.

## A novel eco-friendly method for the synthesis of 2,3-dihydroquinazolin-4(1H)-ones in aqueous media under ultrasonication using $ZrOCl_2$ -MCM-41 as a highly efficient nanocatalyst/nanoreactor

Ali Mohammad Amani<sup>\*1,2,3</sup>, Younes Ghasemi<sup>1,2</sup>, Amir Savardashtaki<sup>4</sup>, Kamiar Zomorodian<sup>5</sup>, Esmaeil Mirzaei<sup>1</sup>, Bijan Zare<sup>4</sup>, Hamid Sepehrian<sup>6</sup>

<sup>1</sup>Department of Medical Nanotechnology, School of Advanced Medical Sciences and Technologies, Shiraz University of Medical Sciences, Shiraz, Iran

<sup>2</sup>Pharmaceutical Sciences Research Center, Shiraz University of Medical Sciences, Shiraz, Iran

<sup>3</sup>Department of Chemistry Shiraz University of Technology Shiraz, Iran

<sup>4</sup>Department of Medical Biotechnology, School of Advanced Medical Sciences and Technologies, Shiraz University of Medical Sciences, Shiraz, Iran

<sup>5</sup>Basic Sciences in Infectious Diseases Research Center, Shiraz University of Medical Sciences. Postal code 71348-45794, Shiraz, Iran.

<sup>6</sup>Nuclear Science and Technology Research Institute, Tehran, Iran

Received August 26, 2015, Revised September 25, 2015

Simple, convenient, and green synthetic protocols are developed for the one-pot synthesis of 2,3-disubstituted quinazolin-4(1H)-ones through one-pot condensation of arylaldehydes, isatoic anhydride and ammonium acetate in the presence of  $ZrOCl_2$ -MCM-41 as a highly efficient novel nanocatalyst/nanoreactor under sonication. The main advantages of this protocol include short reaction times, practical simplicity, high yields, recyclable catalysts, safety, and cheapness of benign solvents.

**Keywords:**  $ZrOCl_2$ -MCM-41, Nanocatalyst, Ultrasound irradiation, 2,3-Dihydroquinazolinone, Heterocycles, Multicomponent reactions, Solvent-free conditions

### INTRODUCTION

Quinazolin-4-ones are pharmacologically the most important classes of heterocyclic compounds and occur widely in natural products such as rutaecarpine (Figure 1) [1]. These compounds possess versatile types of biological activities; some of these are well known for their anticancer [2,3], antitubercular [4], antibacterial [5], antifungal [6], anti-HIV [7], antihelminthic [8], anti-inflammatory [9] and antihypertensive activities [10].

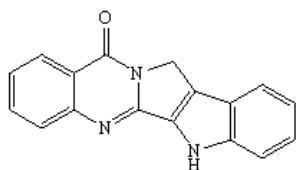


**Fig. 1.** Structure of rutaecarpine

Multicomponent reactions (MCRs) leading to interesting heterocyclic scaffolds are particularly useful for the creation of diverse chemical libraries of drug-like molecules for biological screening [11]. Some reported synthetic routes include the

reaction of isatoic anhydride and aldehydes with ammonium acetate or primary amine in the presence of various reagents or catalysts [12-28].

Recently, we have reported the preparation of 2,3-disubstituted quinazolin-4(3H)-ones via multicomponent reactions [29]. Now, a three-component one-step synthesis of 2,3-dihydroquinazolin-4(1H)-ones has been designed. For this, the use of  $ZrOCl_2$  incorporated in MCM-41, which is relatively non-toxic and inexpensive, was at the centre of our study. In the course of our work on the application of zirconium containing MCM-41 in different organic reactions, we have found it as an effective promoter for the preparation of 2,3-dihydroquinazolin-4(1H)-ones.

Zirconia is a special transition metal oxide that is widely used in catalytic processes as a catalyst, a support, and a promoter [30]. However, its relatively low surface area (usually below  $50 \text{ m}^2 \text{ g}^{-1}$ ) limits the number of active sites [31]. Ordered mesoporous silicas with a tunable pore structure and tailored composition have received considerable interest with broad application ranging from adsorption [32], gas separation [33], and catalysis [34] to biological uses [35]. Some properties of these materials are: mechanically stable structure, high surface area, and large, ordered pores with narrow size distribution of an

\* To whom all correspondence should be sent:  
E-mail: amani\_a@sums.ac.ir, amani@sutech.ac.ir;  
amani@chemist.com

inorganic backbone. Therefore, it would be reasonable to consider these materials as numerous combined nanosized vessels of the same properties. One of the best-known nanosized inorganic backbones is MCM-41, which is a structurally well ordered mesoporous material with a narrow pore size distribution between 1.5 and 10 nm, depending on the surfactant cation and a very high surface area of up to 1500 m<sup>2</sup> g<sup>-1</sup> [36]. While several types of solid sulfonic acids, based on ordered mesoporous silicas, have been created in recent years [34], there have been only a few reports of their applications as catalysts in chemical transformations. Herein, we report the preparation of ZrOCl<sub>2</sub>-MCM-41 as a new modified Lewis acid.

The application of ultrasonic irradiation in reactions using heterogeneous catalysts is a promising technique. Compared with traditional methods, the procedure is more convenient and can be carried out in a shorter reaction time and milder conditions under ultrasound irradiation to give a higher yield of products. Sonication accelerates the reaction by providing driving energy by cavitation and formation and collapse of bubbles (production of high pressure and high temperature) and ensures a better contact, increasing the reaction rate and selectivity [37]. Our efforts for development of new green synthetic methods for various heterocyclic compounds prompted us to investigate the utility of ZrOCl<sub>2</sub>-MCM-41 as a heterogeneous nanocatalyst under sonication to afford substituted quinazolinones.

Therefore, we present a versatile procedure for the selective production of mono and di-substituted 2,3-dihydroquinazolin-4(1H)-ones in the presence of ZrOCl<sub>2</sub>-MCM-41 employing three-component reactions of isatoic anhydride with aldehydes and primary amines (or ammonium salts) (Scheme 1).

## EXPERIMENTAL

### Reagents

All the chemicals used were of analytical grade (E. Merck or Fluka).

### Apparatus

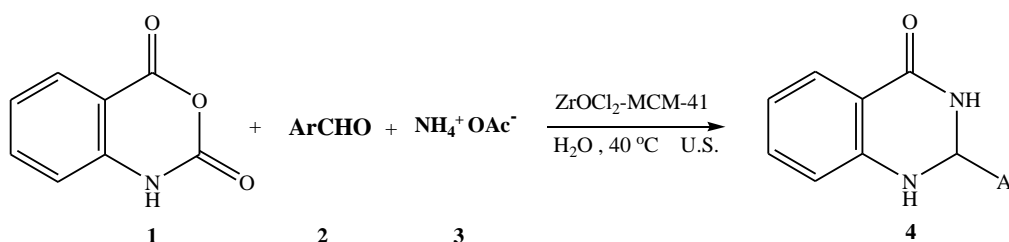
**Nanocatalyst:** A Philips X'pert powder diffractometer system with Cu-K $\alpha$  ( $\lambda=1.541\text{\AA}$ )

radiation was used for the X-ray studies. Nitrogen sorption studies were made with a Quantachrome NOVA instrument and scanning electron micrographs were recorded using a Philips microscope XL30. FT-IR spectra were obtained using a Bruker FT-IR spectrophotometer model Vector-22. Thermogravimetric analysis was performed on a Rheometric Scientific model STA-1500.

**Products:** Melting points were measured on a Buchi B-540 apparatus. IR spectra were obtained on an ABB Bomem Model FTLA200-100 spectrophotometer. <sup>1</sup>H and <sup>13</sup>C NMR spectra were recorded on a Bruker Avance DRX-300 spectrometer at 300 and 75 MHz, using TMS as an internal standard. Mass spectra were obtained on a Shimadzu QP 1100 EX with an ionization potential of 70 eV.

### Preparation of Mesoporous Zirconium Silicate

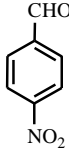
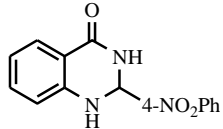
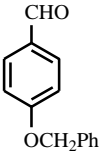
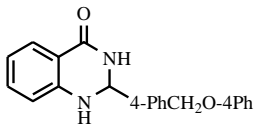
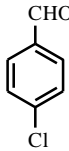
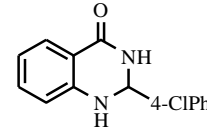
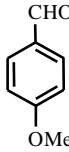
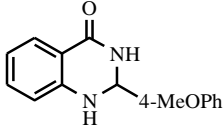
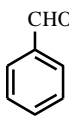
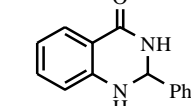
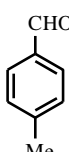
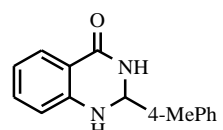
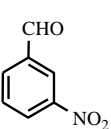
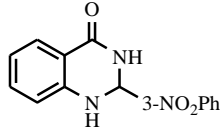
Five different samples of mesoporous zirconium silicate were prepared by mixing sodium silicate as a silicon source, zirconium oxychloride as a zirconium source, and cetyltrimethylammonium bromide (CTMABr) as a surfactant under non-thermal conditions. In a typical procedure, 0.6 g of CTMABr was added in 23 g of demineralized water, the mixture was stirred at 3270 H for 15 min (140 rpm), after that 3 g of sodium silicate was added to the mixture and it was further stirred for 30 min. The pH value was adjusted at 9 by adding sulfuric acid (2M). Then a solution of ZrOCl<sub>2</sub>.8H<sub>2</sub>O (0.45 g in 50 mL demineralized water) was dropwise added. The stirring was continued for 4 h. A bulky white precipitate was formed. It was filtered, washed five times with demineralized water, and dried in an air oven at 50°C for 48 h. A small portion of this material was calcined at 600 °C for 6 h. The material was digested in 0.1M HNO<sub>3</sub> for 24 h and then washed with demineralized water. The samples prepared had Si/Zr molar ratios: 10; 20; 40; and 80. They were marked as: Zr<sub>x</sub>MCM-41 where x indicated the Si/Zr molar ratio and MCM-41 indicated a hexagonal ordered mesoporous silicate.



**Scheme 1.** Synthesis of new substituted 2,3-dihydroquinazolinones.



**Table 1.** Synthesis of 2-aryl substituted 2,3-dihydroquinazolin-4(1H)-ones in the presence of ZrOCl<sub>2</sub>-MCM-41.

Entry	Ar	Product	Time (min)	Yield (%) <sup>a</sup>	M.P. (°C)	
					Found	Reported [Ref]
1		 <b>(4a)</b>	8	87	300-302	310-312[29]
2		 <b>(4b)</b>	5	79	238-240	238-240[29]
3		 <b>(4c)</b>	10	75	207-208	207-208[29]
4		 <b>(4d)</b>	15	75	183-184	183-184[29]
5		 <b>(4e)</b>	20	86	225-226	225-226[29]
6		 <b>(4f)</b>	25	70	228-230	229-231[29]
7		 <b>(4g)</b>	8	87	180-182	180-182[29]

<sup>a</sup>Isolated yields

*General Procedure for the Synthesis of 2, 3-Dihydroquinazolin-4(1H)-ones*

A mixture of 0.163 g isatoic anhydride (1 mmol), aromatic aldehyde (1 mmol), and ammonium acetate (1.2 mmol) was added to 5 mg of ZrOCl<sub>2</sub>-MCM-41 (Zr/Si molar ratio 0.27) and water (5 mL) and the temperature was then raised to 40 °C and maintained under ultrasonic irradiation (25 kHz) for the appropriate time (Table 1). When the reaction was complete (TLC; n-hexane-EtOAc, 2:1) the water was evaporated, CHCl<sub>3</sub>:methanol (10 mL, 3:1) was added. The mixture was stirred for at least 10 min and the solid catalyst was separated by

filtration. The mixture was evaporated in vacuum; the residues were purified by recrystallization from EtOH.

*General Procedure for the Synthesis of 2, 3-Dihydroquinazolin-4(1H)-ones*

A mixture of 0.163 g isatoic anhydride (1 mmol), aromatic aldehyde (1 mmol), and ammonium acetate (1.2 mmol) was added to 5 mg of ZrOCl<sub>2</sub>-MCM-41 (Zr/Si molar ratio 0.27) and water (5 mL) and the temperature was then raised to 40 °C and maintained under ultrasonic irradiation (25 kHz) for the appropriate time (Table 1). When

the reaction was complete (TLC; n-hexane–EtOAc, 2:1) the water was evaporated and CHCl<sub>3</sub>:methanol (10 mL, 3:1) was added. The mixture was stirred for at least 10 min and the solid catalyst was separated by filtration. The mixture was evaporated in vacuum; the residues were purified by recrystallization from EtOH.

#### Compound 4a

IR (KBr):  $\bar{\nu}$  = 3360, 3345, 3065, 1679, 1608 cm<sup>-1</sup>; <sup>1</sup>H-NMR (300 MHz, DMSO-d<sub>6</sub>),  $\delta$ : 7.56(t, *J*=6/0 Hz, 1H, 1CH), 7.86(m, 3H, 2CH, 1NH), 8.16(d, *J*=6/0 Hz, 1H, CH), 8.39(m, 5H, CH), 12.8(s, 1H, NH) ppm; <sup>13</sup>C-NMR (75 MHz, DMSO-d<sub>6</sub>),  $\delta$ : 65.5, 121.2, 123.6, 125.9, 127.7, 129.3, 134.8, 138.6, 148.3, 149.0, 150.8, 162.1 ppm; MS, *m/z* (regulatory intensity): 50(45), 76(50), 92(29), 119(97.5), 192(24), 221(43), 267(100), 269(2.5)[M<sup>+</sup>].

#### Compound 4d

IR (KBr):  $\bar{\nu}$  = 3291, 3178, 3060, 2931, 2829, 1663 cm<sup>-1</sup>; <sup>1</sup>H-NMR (300 MHz, DMSO-d<sub>6</sub>),  $\delta$ : 3.84-3.9(s, 3H, CH<sub>3</sub>), 4.34(s, 1H, NH), 5.72(s, 1H, NH), 5.86(s, 1H, CH), 6.65-6.8(d, *J*=8.0 Hz, 1H, CH, Ph), 6.88-7.00(m, 3H, CH, Ph), 7.31-7.36(d, *J*=7.8Hz, 1H, CH, Ph), 7.51-7.53(d, *J*= 8.6 Hz, 2H, CH, Ph), 7.93-7.96(d, *J*=7.7Hz, 1H, CH, Ph) ppm.

#### Compound 4g

IR (KBr):  $\bar{\nu}$  = 3350, 3245, 3050, 2910, 1608 cm<sup>-1</sup>; <sup>1</sup>H-NMR (300 MHz, DMSO-d<sub>6</sub>),  $\delta$ : 5.93(s, 1H, CH), 6.66(t, *J*= 6.0Hz, 1H, CH), 6.77(d, *J*=6.0Hz, 1H, CH), 7.26(d, t, *J*<sub>1</sub>=1.2Hz, *J*<sub>2</sub>=9.0Hz, 1H, CH), 7.33(s, 1H, NH), 7.59(d, *J*=9.0Hz, CH), 7.83(m, 1H, CH), 7.92(d, 1H, *J*=9.0Hz, CH), 8.19(d, *J*=6.0Hz, 1H), 8.34(s, 1H, CH), 8.54(s, 1H, NH) ppm; <sup>13</sup>C-NMR (75 MHz, DMSO-d<sub>6</sub>),  $\delta$ : 65.1, 114.6, 114.9, 117.5, 121.6, 122.7, 123.3, 125.9, 127.4, 131.3, 133.4, 133.6, 134.7, 144.3, 147.3, 147.7, 163.3 ppm; MS, *m/z* (regulatory intensity): 50(15), 92(35), 119(29), 120(40), 147(100), 221(15), 269(6.7) [M<sup>+</sup>].

## RESULTS AND DISCUSSION

In continuation of our search for application of functionalized ordered mesoporous silicas [38], our attempt was focused on the application of novel nanoreactors for ultrasound assisted synthesis of substituted quinazolinones. These Lewis acidic nanoporous zirconium silicates were prepared with various mole ratios of Si/Zr. Infrared spectra of these nanocatalysts were measured by a standard KBr disc technique. The FT-IR spectrum of the Zr10MCM-41 nanocatalyst shown in Fig. 2 is closely similar to that of mesoporous molecular

sieves which also show a series of bands that are characteristic of the SiO<sub>4</sub> tetrahedron and its modification by introduction of metal ions [39]. The spectrum shows five main absorption bands in the regions 3000–3700, 1055–1090, 960–970, 790–850, 440–465 cm<sup>-1</sup>. The band in the region 1055–1090 cm<sup>-1</sup> is due to the internal asymmetric stretching mode of SiO<sub>4</sub> (TO<sub>4</sub>) skeleton, the strongest band in the spectra of silicates [40]. The peak in the region 960–970 cm<sup>-1</sup> is generally considered as a proof for the incorporation of a heteroatom into the framework [41]. Camblor *et al.* have proposed that the band at 960 cm<sup>-1</sup> is due to the Si-O stretching vibrations of the Si-OH groups present.

The SEM image of the mesoporous Zr10MCM-41 was taken using gold coating during 2 minutes for high magnification and is shown in Fig. 3. The SEM image of the mesoporous Zr10MCM-41 exhibits uniform spherical crystallites ~0.4–0.8 mm in size.

XRD analysis was performed from 1.5° (2 $\theta$ ) to 10.0° (2 $\theta$ ) at a scan rate of 0.02° (2 $\theta$ )/sec. The XRD patterns after calcination of the synthesized zirconium silicate samples are presented in Fig. 4. There is a strong diffraction at 2 $\theta$  smaller than 3° along with the presence of small peaks, which confirms the formation of mesoporous materials [42].

The thermogravimetric analysis of these nanocatalysts was performed from ambient temperature to 900°C at a heating rate of 10°C/min. The thermograms of the nanocatalysts are presented in Fig. 5. The thermograms of the uncalcined samples show a gradual weight loss up to 900°C. The TGA curve of the samples shows five steps of weight loss (35-130, 130-300, 300-380, 380-480, and 480-600 °C). The weight loss is ~4.0% in the first step and is due to desorption of the physisorbed water in the pores of the uncalcined samples. The weight losses in the second (~20.0%) and third (~7.0%) steps are mainly associated with oxidative decomposition of templates; in the fourth step, the weight loss (~7.0%) is due to removal of coke formed in the previous steps by the decomposition of templates. In the final step, the weight loss (~2.0%) is mainly due to the loss of water formed by condensation of the silanol groups.

In the present communication, we report a simple and ecofriendly synthesis of 2-aryl substituted 2,3-dihydroquinazolin-4(1H)-ones by treatment of isatoic anhydride, aromatic aldehyde, and ammonium acetate in the presence of ZrOCl<sub>2</sub>-MCM-41 as catalyst under ultrasound irradiation (Scheme 1).

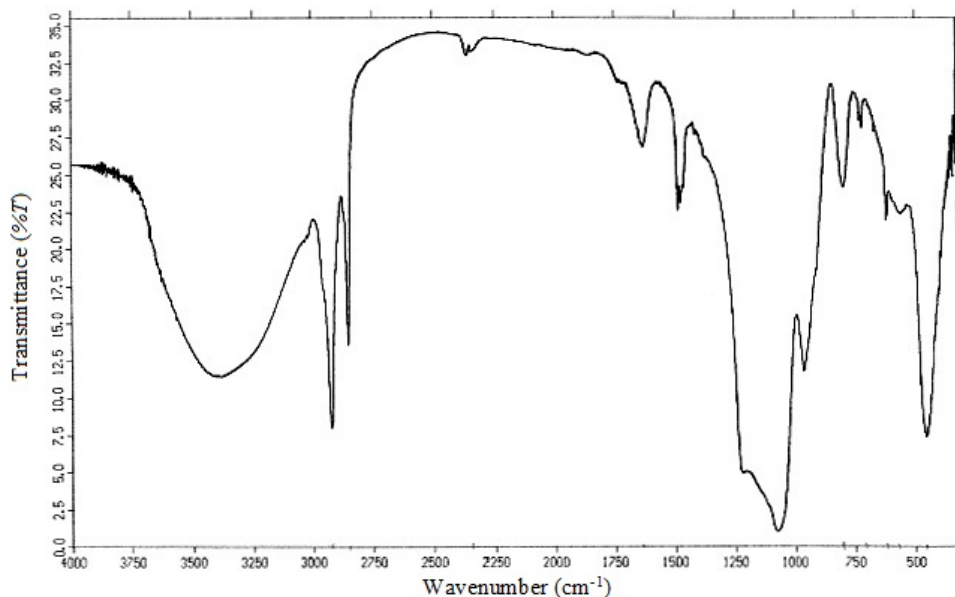


Fig. 2. FT-IR spectrum of the synthesized  $ZrOCl_2$ -MCM-41.

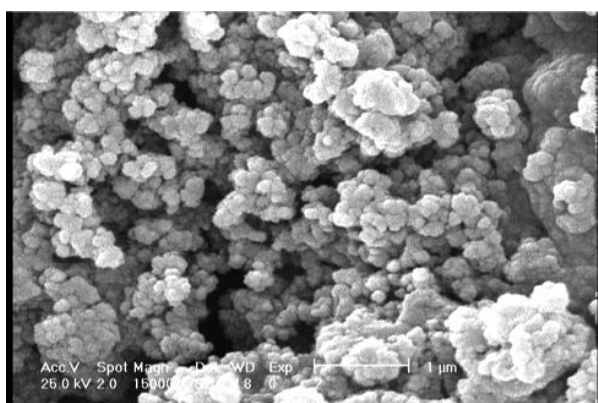


Fig. 3. SEM image of  $ZrOCl_2$ -MCM-41.

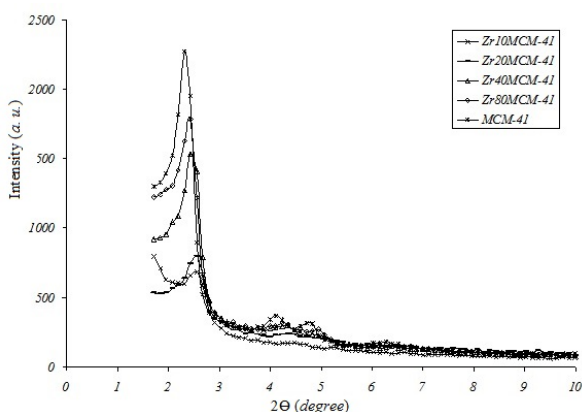


Fig. 4. XRD patterns of the synthesized  $ZrOCl_2$ -MCM-41 and MCM-41

The results showed that the reaction without ultrasound irradiation needs very long time and gives relatively low yields. Thus, it seemed that ultrasound irradiation played the main role in

enhancement of the reaction rate and the combination of ultrasound and  $ZrOCl_2$ -MCM-41 was found to be ideal for the faster synthesis in high yield.

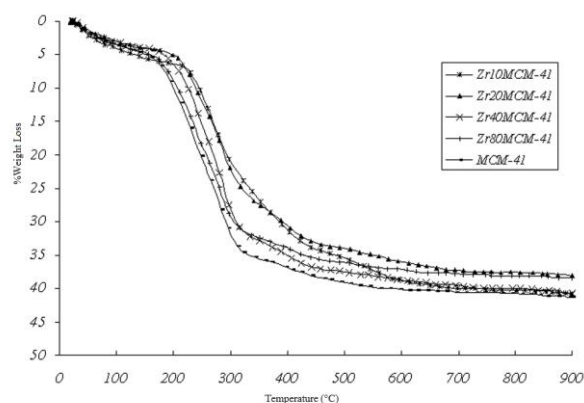


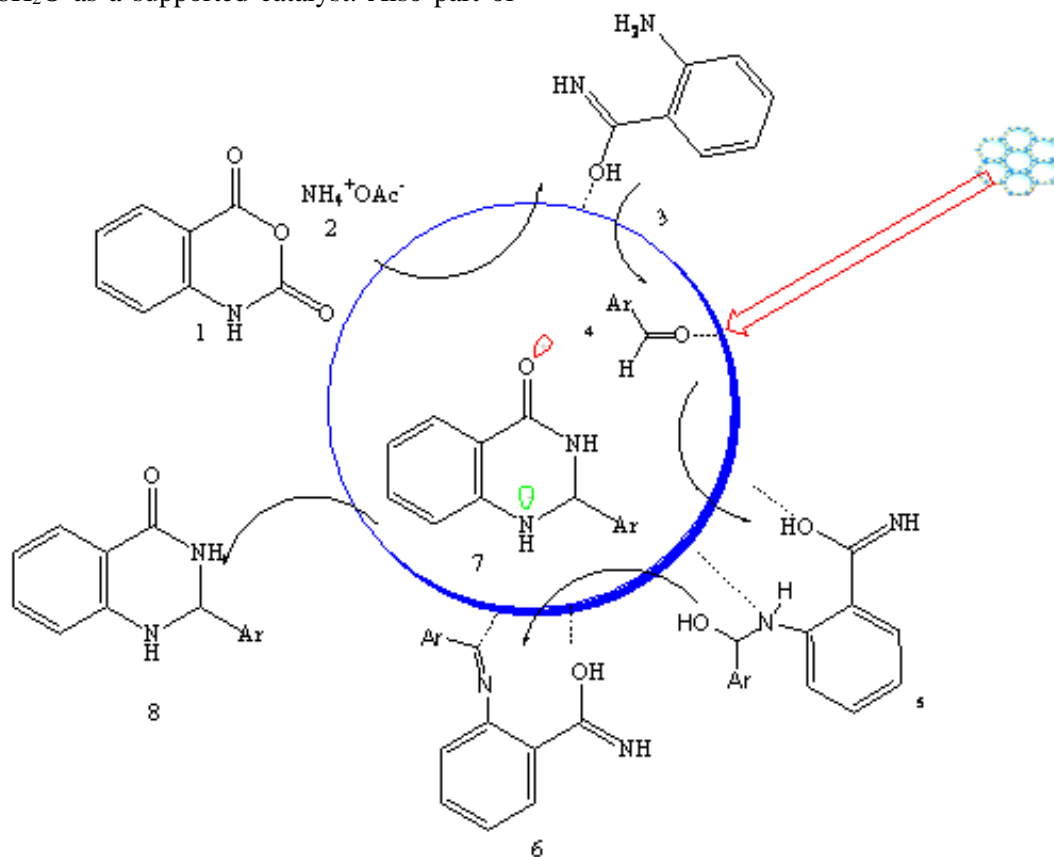
Fig. 5. TGA curve of the synthesized  $ZrOCl_2$ -MCM-41 and MCM-41.

A variety of aldehydes including heterocyclic and aromatic aldehydes, possessing both electron-donating and electron-withdrawing groups, were employed for the formation of 2,3-dihydroquinazolin-4(1H)-ones. In all cases, the yields were excellent (Scheme 1, Table 1). Among the various benzaldehydes tested, the reaction worked well with electron-donating groups (Me, MeO) (entries 6 and 4, Table 1), as well as electron-withdrawing groups ( $NO_2$ , Cl) (entries 1 and 3, Table 1) giving various 2,3-dihydroquinazolin-4(1H)-ones in 75–87% yields.

We have found that  $ZrOCl_2$ -MCM-41 is an effective eco-friendly and efficient promoter for the synthesis of 2,3-dihydroquinazolin-4(1H)-ones. A plausible mechanistic pathway to 2-aryl-substituted

2,3-dihydroquinazolin-4(1H)-ones is illustrated in Scheme 2. In the initial step, the reaction of isatoic anhydride (1), and ammonium acetate (2) within the  $ZrOCl_2$ -MCM-41 tunnels, together with decarboxylation, gives 2-aminobenzamide (5). The intermediate (3) is formed through nucleophilic attack of the amino group in 2-aminobenzamide at the activated carbonyl group in the aldehyde by  $ZrOCl_2 \cdot 8H_2O$  as a supported catalyst. Also part of

the amide in the imine intermediate (5) is converted into its tautomer in the presence of the catalyst. Then the Schiff base intermediate (6) is produced by intermediate (5) dehydration. The intramolecular nucleophilic addition reaction between the amide group nitrogen and the activated Schiff base carbon gives intermediate (7), which is followed by a 1,5-proton transfer giving the products.



**Scheme 2.** Proposed reaction mechanism

## CONCLUSION

In conclusion, a simple green method for the synthesis of a novel class of the quinazolinone family is developed.  $ZrOCl_2$ -MCM-41 is an efficient nanoreactor for the synthesis of 2,3-dihydroquinazolinones. The method offers several advantages, such as avoiding toxic solvents or catalysts, simple work-up procedure without using any chromatographic method, and improved yields. Starting materials are inexpensive and commercially available. We believe that many biologically active derivatives could be synthesized by this multi-component reaction with high atomic economy.

## REFERENCES

1. a) Z.Z. Ma, Y. Hano, T. Nomura, Y. J. Chen, *Heterocycles.*, **46**, 541(1997); (b) A.L. Chen, K.K. Chen, *J. Am. Pharm. Assoc.*, **22**, 716 (1933).
2. J.B. Jiang, D.P. Hesson, B.A. Dusak, D.L. Dexter, G.J. Kang, E. Hamel, *J. Med. Chem.*, **33**, 1721(1990).
3. Y. Xia, Z.N. Yang, M.J. Hour, S.C. Kuo, P. Xia, K.F. Bastow, Y. Nakanishi, P. Nampoothiri, T. Hackl, E. Hamel, K.H. Lee, *Bioorg. Med. Chem. Lett.*, **11**, 1193 (2001).
4. P.B. Trivedi, N.K. Undavia, A.M. Dave, K.N. Bhatt, N.C. Desai, *Indian J. Chem.*, **32B**, 497 (1993).
5. N.A. Gangwal, U.R. Kothawade, A.D. Galande, D.S. Pharande, A.S. Dhake, *Indian J. Het. Chem.*, **10**, 291 (2001).
6. J. Bartroli, E. Turmo, M. Alguero, E. Boncompte, M.L. Vericat, L. Conte, J. Ramis, M. Merlos, J.G. Rafanell, J. Forn, *J. Med. Chem.*, **41**, 1869 (1998).
7. V. Alagarsamy, R. Revathi, S. Meena, K.V. Ramaseshu, S. Rajasekaran, E. De-Clerco, *Indian J. Pharm. Science.*, **4**, 459 (2004).

8. D. P. Gupta, S. Ahmad, K. Ashok, K. Shanker, *Indian J. Chem.*, **27B**, 1060 (1988).
9. Q. Chao, L. Deng, H. Shih, L.M. Leoni, D. Genini, D.A. Carson, H. B. Cottam., *J. Med. Chem.*, **42**, 3860 (1999).
10. W.B. Wright, A.S. Tomcufcik, P.S. Chan, J.W. Marsico, J.B. Press, *J. Med. Chem.*, **30**, 2277 (1987).
11. (a) A. Domling, *Curr. Opin. Chem. Biol.*, **6**, 306 (2002) (b) L. Weber, *Drug Discovery Today*, **7**, 143 (2002).
12. (a) P. Salehi, M. Dabiri, M.A. Zolfigol, M. Baghbanzadeh, *Synlett.*, **1155**(2005); (b) M. Dabiri, P. Salehi, S. Otokesh, M. Baghbanzadeh, G. Kozehgary, A.A. Mohammadi, *Tetrahedron Lett.*, **46**, 6123 (2005).
13. M. Narasimhulu, Y.R. Lee, *Tetrahedron*, **67**, 9627 (2011).
14. J.X. Chen, D.Z. Wu, F. He, M.C. Liu, H.Y. Wu, J.C. Ding, W.K. Su, *Tetrahedron Lett.*, **49**, 3814 (2008).
15. A. Ghorbani-Choghamarani, T. Taghipour, *Lett. Org. Chem.*, **8**,470 (2011).
16. K. Niknam, N. Jafarpour, E. Niknam, *Chin. Chem. Lett.*, **22**, 69 (2011).
17. K. Niknam, M.R. Mohammadizadeh, S. Mirzaee, *Chin. J. Chem.*, **29**, 1417 (2011).
18. M. Dabiri, P. Salehi, M. Baghbanzadeh, M.A. Zolfigol, M. Agheb, S. Heydari, *Catal. Commun.*, **9**, 785 (2008).
19. M. Wang, T.T. Zhang, Y. Liang, J.J. Gao, *Chin. Chem. Lett.*, **22**, 1423 (2011).
20. Z.H. Zhang, H.Y. Lü, S.H. Yang, J.W. Gao, *J. Comb. Chem.* **12**, 643(2010).
21. H.R. Shaterian, A.R. Oveisi, M. Honarmand, *Synth. Commun.*, **40**, 1231 (2010).
22. P. Salehi, M. Dabiri, M. Baghbanzadeh, M. Bahramnejad, *Synth. Commun.*, **36**, 2287 (2006).
23. M.Z. Kassae, S. Rostamizadeh, N. Shadjou, E. Motamedi, M. Esmaeizadeh, *J Heterocyclic Chem.*, **47**, 1421 (2010).
24. M. Baghbanzadeh, P. Salehi, M. Dabiri, G. Kozehgary, *Synthesis*, **344** (2006).
25. (a) J. Chen, W. Su, H. Wu, M. Liu, C. Jin, *Green Chem.*, **9**, 972 (2007); (b) N.B. Darvatkar, S.V. Bhilare, A.R. Deorukhkar, D.G. Raut, M.M. Salunkhe, *Green Chem. Lett. Rev.*, **3**, 301 (2010).
26. M.P. Surpur, P.R. Singh, S.B. Patil, S.D. Samant, *Synth. Commun.*, **37**, 1965 (2007)..
27. J. Safari, S. Gandomi-Ravandi, *J. Mol. Catal A: Chem.*, **371**, 135 (2013).
28. B.H. Chen, J.T. Li, G.F. Chen, *Ultrasonics Sonochem.*, **23**, 59 (2015).
29. a) S. Rostamizadeh, A. M. Amani, R. Aryan, H. R. Ghaieni, N. Shadjou, *Synth. Commun.*, **38**, 3567 (2008) b) S. Rostamizadeh, A.M. Amani, G.H. Mahdavinia, H. Sepehrian, S. Ebrahimi, *Synthesis*, **8**, 1356 (2010).
30. H. Teterycz, R. Klimkiewicz, M. Laniecki, *Appl. Catal. A.*, **249**, 313(2003).
31. T. Yamaguchi, *Catal. Today*, **20**,199 (1994).
32. H. Yoshitake, *New J. Chem.*, **29**, 1107 (2005).
33. P.J.E. Harlick, A. Sayari, *Ind. Eng. Chem. Res.*, **46**, 446 (2007).
34. B. Karimi, D. Zareyee, *Org. Lett.*, **10**, 3989 (2008).
35. M. Hartmann, *Chem. Mater.*, **17**, 4577 (2005).
36. W. Zhang, T.R. Pauly, T. Pinnavaia, *J. Chem. Mater.*, **9**, 2491 (1997).
37. a)R. Cella, H.A. Stefani, *Tetrahedron*, **65**, 2619 (2009); b)T.J. Mason. Practical Sonochemistry, A user's guide to applications in chemistry and chemical engineering, Ellis Horwood Limited, New York; 1991: c) M. Mečiarová, Š. Toma, P. Babiak, *Chem. Pap.*, **55**, 302 (2001).
38. a) S. Rostamizadeh, A.M. Amani, G.H. Mahdavinia, G. Amiri, H. Sepehrian *Ultrasonics Sonochem.*, **17**, 306 (2010) b) H. Sepehrian, R. Yavari, S. Waqif-Husain, M. Ghannadi-Maragheh, *Sep. Sci. Tech.*, **43**, 3269 (2008).
39. X. Chen, L. Huan, , G. Ding, Q. Li, *Catal. Lett.*, **44**, 123 (1997).
40. C.Y. Chen, S.L. Burkett, H.X. Lin, M.E. Davis, *Microporous Mater.*, **2**, 27 (1993).
41. M.A. Camblor, A. Corma, J. Perez-Pariente, *J. Chem. Soc. Chem. Commun.* **13**, 557 (1993).
42. C.T. Kresge, M.E. Leonowics, W.J. Roth, J.C. Vartuli, J.S. Beck, *Nature*, **359**, 710 (1992).

НОВ ЕКОЛОГИЧНО СЪВМЕСТИМ МЕТОД ЗА СИНТЕЗА НА 2,3-ДИХИДРОХИНАЗОЛИН-4(1H)-ОНИ ВЪВ ВОДНА СРЕДА ПРИ УЛТРАЗВУКОВО ВЪЗДЕЙСТВИЕ, ИЗПОЛЗВАЙКИ  $ZrOCl_2$ -МСМ-41 КАТО ВИСОКОЕФЕКТИВЕН НАНОКАТАЛИЗАТОР/НАНОРЕАКТОР

А.М. Амани<sup>1,2,3\*</sup>, Ю. Гасеми<sup>1,2</sup>, А. Савардацаки<sup>4</sup>, К. Зомородиан<sup>5</sup>, Е. Мирзаеи<sup>1</sup>, Б. Заре<sup>4</sup>, Х. Сефериан<sup>6</sup>

<sup>1</sup>Департамент по медицински нанотехнологии, Училище за нови медицински науки и технологии, Университет за медицински науки в Шираз, Иран

<sup>2</sup>Изследователски фармацевтичен център, Университет за медицински науки в Шираз, Иран

<sup>3</sup>Департамент по химия, Технологичен университет, Шираз, Иран

<sup>4</sup>Департамент по медицинска биотехнология, Училище по модерна медицина и технология, Университет за медицински науки в Шираз, Иран

<sup>5</sup>Изследователски център по инфекциозни болести, Университет за медицински науки в Шираз, Иран

<sup>6</sup>Изследователски институт по ядрени науки и технологии, Техеран, Иран

Постъпила на 26 август, 2015 г.; коригирана на 25 септември, 2015 г.

(Резюме)

Прости, удобни и „зелени“ рецептури са разработени за едностадийната синтеза на 2,3-дихидрохиназолин-4(1H)-они чрез кондензация на арилалдехиди, изатинов анхидрид и амониев ацетат в присъствие на  $ZrOCl_2$ -МСМ-41 като високоефективен нанокатализатор/нанореактор при ултразвуково действие. Главните предимства на метода са кратките времена, високите добиви, рециклирания катализатор, безопасността и ниската цена на разтворителя.

## Spectroscopic studies of charge-transfer complexes of 2,3-dichloro-5,6-dicyano-p-benzo-quinone with p-nitroaniline

N. Singh, A. Ahmad\*

Department of Chemistry, Faculty of Science, Aligarh Muslim University, Aligarh -202002, India

Received August 2, 2015, Accepted October 5, 2015

The charge-transfer complexes of the donor p-nitroaniline (PNA) with the acceptor 2, 3-dichloro-5,6-dicyano-p-benzoquinone (DDQ) were studied spectrophotometrically in various solvents such as  $\text{CH}_2\text{Cl}_2$ ,  $\text{CHCl}_3$ , and  $\text{CCl}_4$  at different temperatures. Two charge-transfer bands were observed in each case. The results indicate that the formation of the CT-complex in a less polar solvent is comparatively high. The stoichiometry of the CT-complex was found to be 1:1. The physical parameters of the CT-complex were evaluated by the Benesi–Hildebrand equation. The data are discussed in terms of the formation constant ( $K_{CT}$ ), molar extinction coefficient ( $\epsilon_{CT}$ ), standard free energy ( $\Delta G^\circ$ ), oscillator strength ( $f$ ), transition dipole moment ( $\mu_{EN}$ ), resonance energy ( $R_N$ ) and ionization potential ( $I_D$ ). The results indicate that the formation constant ( $K_{CT}$ ) for the complex is dependent upon the nature of electron acceptor, donor and polarity of solvents used. The formation of the complex was confirmed by UV-visible, FT-IR, and  $^1\text{H-NMR}$  techniques. The possible structure of the CT-complex between DDQ and PNA was proposed.

**Keywords:** Charge-transfer complex; 2, 3-dichloro-5, 6-dicyano-p-benzo-quinone (DDQ); p-nitro aniline (PNA); UV-Visible, FT-IR,  $^1\text{H-NMR}$ .

### INTRODUCTION

Various aromatic molecules can behave as electron donors and form molecular complexes with electron acceptor molecules such as halogens, nitro compounds and quinines [1-2]. Extensive works have been carried out to elucidate the nature of intermolecular interactions in these molecular complexes. Mulliken has developed the theory of the intermolecular CT interactions, which has been successfully applied to the interpretation of the absorption bands characteristic of molecular complexes in various systems [3]. DDQ is a strong electron acceptor having electron affinity of 1.9 e.v. [4].

In the present paper, spectrophotometric studies were carried out for CT complexes of DDQ with p-nitroaniline, special attention being paid to the appearance of two CT bands. Orgel first reported two bands in the case of methylbenzene complexes of chloranil and 1, 2, 5-trinitrobenzene [5]. Orgel related the two ionization potentials of the donor molecules to the frequencies of the CT bands.

This paper presents studies of the charge-transfer interaction between DDQ and p-nitroaniline in both liquid and solid states. The aim of the work is to determine the reaction stoichiometry, the nature of bonding between DDQ and PNA, and also some physical parameters. In

addition, the nature and structure of the reaction product (CT-complex) in both solution and solid states can be estimated using spectroscopic techniques like FT-IR,  $^1\text{H NMR}$  and UV-Vis electronic absorption to obtain the stoichiometry, molecular structure and nature of interaction for the CT-complexes [6-9].

### EXPERIMENTAL

#### Materials

Analytical grade (AR) chemicals were used throughout. 2,3-Dichloro-5,6-dicyano-p-benzoquinone (DDQ) and p-nitro aniline (PNA) were obtained from Sigma Aldrich, (CDH). Dichloromethane (Merck), chloroform (Merck) and carbon tetrachloride (Merck) were used without further purification.

#### Preparation of standard solutions

Solutions of the donor of different concentrations, 0.01M, 0.02M, 0.03M, 0.04M, and 0.05M, were prepared in different volumetric flasks by dissolving accurately weighed amounts of p-nitro aniline in different solvents such as carbon tetrachloride, chloroform and dichloromethane.

A standard solution of the acceptor, DDQ (0.01M) was prepared by dissolving accurately weighed amounts of the acceptor in the above solvents in different volumetric flasks.

\* To whom all correspondence should be sent:

E-mail: afaqahmad212@gmail.com;  
neetisingh72@gmail.com

### Synthesis of solid CT- complex

Analar R grade samples of DDQ and p-nitroaniline were employed for the synthesis of the title compound. Equimolar solutions of the two reactants were separately prepared in methanol and mixed together. The resulting solution was stirred well for about thirty min.

The precipitated adduct was filtered off at the pump and repeatedly recrystallised from methanol to enhance the degree of purity of the synthesized compound.

### Analyses

The electronic absorption spectra of the donor P-nitroaniline, acceptor DDQ and the resulting complex in dichloromethane, chloroform and carbon tetrachloride were recorded at different temperatures, i.e. 20°C, 25°C and 30°C in the visible range 200 nm–600 nm using a UV- visible spectrophotometer Perkin-Elmer-  $\lambda$ -850 with a 1 cm quartz cell path length. The FT-IR spectra of the reactants and the resulting CT-complex were recorded with the help of the FT-IR spectrometer INTERSPEC– 2020 (spectra lab U.K.) in KBr pellets. The <sup>1</sup>H NMR spectrum of the CT-complex was measured in acetone using Bruker Advance II 400 NMR spectrometer.

## RESULTS AND DISCUSSION

### Observation of CT- bands

3-ml volumes of the donor and the acceptor were scanned separately by spectrophotometric titration [10] at their wavelengths of maximum absorption: 280 nm for DDQ, 400 nm for PNA, 320 nm for the blank solvent (dichloromethane) and 440 nm and 560 nm for the CT-complex of 0.01M PNA and 0.01M DDQ in dichloromethane, as shown in Fig 1. The reaction mixture of the donor (10 ml) and the acceptor (10 ml) in the different solvents, viz., carbon tetrachloride, chloroform and dichloromethane, formed a yellow colored charge transfer complex. The complex for each of the reaction mixtures was let to standing overnight at different temperatures i.e. 20°C, 25°C and 30°C to form a stable complex before analysis at the maximum absorbance 440 nm and 560 nm for dichloromethane, 430 nm and 550 nm for chloroform and 420 nm and 540 nm for carbon tetrachloride.

The concentration of the donor in the reaction mixture was kept higher than that of the acceptor,  $[D_0] \gg [A_0]$  [11, 12] and changed over a wide range of concentrations from 0.01M to 0.5M while the concentration of the  $\pi$ -acceptor (DDQ) was kept

fixed [11] at 0.01M in each solvent; these produced solutions with donor: acceptor molar ratios varying from 1:1 to 50:1, these concentration ratios were used to obtain a straight line diagram for determination of the formation constants of the CT-complex.

The spectra of the solutions of 0.01M PNA, and 0.01M DDQ in different solvents were recorded with solvents used as a reference, the longest wavelength peak was considered as the CT-peak [13]. The changes of the absorption intensity to higher values for all complexes in this study when adding the donor were detected and investigated, as shown in Table 5. These measurements were based on the CT-absorption bands exhibited in the spectra of the above mentioned systems given in Figs. 2- 4. In all systems studied the absorption spectra are of similar nature except for the position of the absorption maxima ( $\lambda_{CT}$ ) of the complexes. The CT-complex absorption spectra were analyzed by fitting to the Gaussian function

$$y = y_0 + [A/ w\sqrt{(\pi/2)}] \exp [-^2 (x - x_c)^2/w^2]$$

where  $x$  and  $y$  denote wavelength and absorbance, respectively. The results of the Gaussian analysis for all systems under study are shown in Table 1. The wavelengths of these new absorption maxima ( $\lambda_{CT} = x_c$ ) and the corresponding transition energies ( $h\nu$ ) are summarized in Tables 2-4.

### Determination of the ionization potentials of the donor

The ionization potentials of the donor ( $I_D$ ) in the charge transfer complexes were calculated using the empirical equation derived by Aloisi and Piganatro [14]

$$I_D \text{ (eV)} = 5.76 + 1.53 \times 10^{-4} \nu_{CT} \quad (1)$$

where  $\nu_{CT}$  is the wave number in  $\text{cm}^{-1}$  of the complex determined in different solvents, viz., carbon tetrachloride, chloroform and dichloromethane. The data are summarized in Tables 2-4.

### Determination of oscillator strength, ( $f$ ), and transition dipole moment, ( $\mu EN$ )

From the CT-absorption spectra, one can determine the oscillator strength. The oscillator strength  $f$  is estimated using the formula

$$f = 4.32 \times 10^{-9} \int \epsilon_{CT} dv \quad (2)$$

where  $\int \epsilon_{CT} dv$  is the area under the curve of the extinction coefficient of the absorption band in question vs. frequency. To a first approximation

$$f = 4.32 \times 10^{-9} \epsilon_{CT} \Delta\nu_{1/2} \quad (3)$$

where  $\epsilon_{CT}$  is the maximum extinction coefficient of



the band and  $\Delta v_{1/2}$  is the half-width, i.e., the width of the band at half the maximum extinction. The observed oscillator strengths of the CT-bands are summarized in Tables 2-4.

The extinction coefficient is related to the transition dipole by

$$\mu_{EN} = 0.0952 [\epsilon_{CT} \Delta v_{1/2} / \Delta v]^{1/2} \quad (4)$$

where  $\Delta v \approx v$  at  $\epsilon_{CT}$  and  $\mu_{EN}$  is defined as  $-e \int \psi_{ex} \sum_i r_i \psi_{yg} dt$ .  $\mu_{EN}$  for the complexes of PNA with DDQ is given in Tables 2-4.

### Determination of resonance energy ( $R_N$ )

Briegleb and Czekalla [15] theoretically derived the relation

$$\epsilon_{CT} = 7.7 \times 10^{-4} / [h\nu_{CT} / [R_N] - 3.5], \quad (5)$$

where  $\epsilon_{CT}$  is the molar extinction coefficient of the complex at the maximum of the CT absorption,  $\nu_{CT}$  is the frequency of the CT-peak and  $R_N$  is the resonance energy of the complex in the ground state, which is obviously a contributing factor to the stability constant of the complex (a ground state property). The values of  $R_N$  for the complexes under study are given in Tables 2-4.

**Table 1.** Gaussian curve analysis for the CTC in the spectra of DDQ with PNA in different polar solvents.

Complex	Solvent	Temperature	A	W	Xc	Y <sub>0</sub>
DDQ + PNA	CH <sub>2</sub> Cl <sub>2</sub>	20°C	34.75 ± 6.66	95.74±15.05	419.37	0.8232±0.0235
DDQ + PNA	CHCl <sub>3</sub>	20°C	28.28 ± 4.52	67.84±9.66	421.56	0.9350±0.0197
DDQ + PNA	CCl <sub>4</sub>	20°C	32.42 ± 4.69	49.17±6.18	423.69	1.042±0.0290

**Table 2.** CT-complex absorption maxima ( $\lambda_{CT}$ ), transition energies ( $h\nu_{CT}$ ), of the DDQ+PNA complexes, experimentally determined values of ionization potentials ( $I_D$ ), oscillator strength ( $f$ ), dipole moments ( $\mu_{EN}$ ), and resonance energies ( $R_N$ ) of the complexes in dichloromethane.

Complex	Solvent	Temp.	$\lambda_{CT}$ (nm)	$f \times 10^{-5}$	$\mu_{EN}$ (Debye)	$R_N$ (ev)	$h\nu_{CT}$ (ev)	$I_D$ (ev)	$\Delta G$
DDQ + PNA	CH <sub>2</sub> Cl <sub>2</sub>	20°C	419.37nm	3.63×10 <sup>-5</sup>	0.892	0.00671	2.96	9.40	13.408
DDQ + PNA	CH <sub>2</sub> Cl <sub>2</sub>	20°C	549.17nm	3.48×10 <sup>-5</sup>	0.757	0.00370	2.26	8.54	14.721
DDQ + PNA	CH <sub>2</sub> Cl <sub>2</sub>	25°C	423.39nm	2.36×10 <sup>-5</sup>	0.912	0.00694	2.93	9.37	13.465
DDQ + PNA	CH <sub>2</sub> Cl <sub>2</sub>	25°C	558.46nm	1.73×10 <sup>-5</sup>	0.775	0.00381	2.22	8.49	14.778
DDQ + PNA	CH <sub>2</sub> Cl <sub>2</sub>	30°C	428.15nm	2.64×10 <sup>-5</sup>	0.934	0.00720	2.90	9.32	13.636
DDQ + PNA	CH <sub>2</sub> Cl <sub>2</sub>	30°C	530.30nm	6.58×10 <sup>-5</sup>	0.798	0.00425	2.34	8.63	14.492

**Table 3.** CT-complex absorption maxima ( $\lambda_{CT}$ ), transition energies ( $h\nu_{CT}$ ), of the DDQ+PNA complexes, experimentally determined values of ionization potentials ( $I_D$ ), oscillator strength ( $f$ ), dipole moments ( $\mu_{EN}$ ), and resonance energies ( $R_N$ ) of the complexes in chloroform.

Complex	Solvent	Temp.	$\lambda_{CT}$ (nm)	$f \times 10^{-5}$	$\mu_{EN}$ (Debye)	$R_N$ (ev)	$h\nu_{CT}$ (ev)	$I_D$ (ev)	$\Delta G$
DDQ + PNA	CHCl <sub>3</sub>	20 <sup>o</sup> C	421.56nm	$2.65 \times 10^{-5}$	0.905	0.00690	2.95	9.38	13.808
DDQ + PNA	CHCl <sub>3</sub>	20 <sup>o</sup> C	563.95nm	$2.42 \times 10^{-5}$	0.801	0.00403	2.20	8.47	14.549
DDQ + PNA	CHCl <sub>3</sub>	25 <sup>o</sup> C	425.36nm	$1.93 \times 10^{-5}$	0.914	0.00695	2.92	9.35	14.549
DDQ + PNA	CHCl <sub>3</sub>	25 <sup>o</sup> C	575.23nm	$6.75 \times 10^{-5}$	0.736	0.00334	2.16	8.40	15.120
DDQ + PNA	CHCl <sub>3</sub>	30 <sup>o</sup> C	425.23nm	$2.13 \times 10^{-5}$	0.930	0.00718	2.92	9.35	14.778
DDQ + PNA	CHCl <sub>3</sub>	30 <sup>o</sup> C	579.73nm	$7.57 \times 10^{-5}$	0.752	0.00345	2.14	8.39	15.006

**Table 4.** CT-complex absorption maxima ( $\lambda_{CT}$ ), transition energies ( $h\nu_{CT}$ ), of the DDQ+PNA complexes, experimentally determined values of ionization potentials ( $I_D$ ), oscillator strength ( $f$ ), dipole moments ( $\mu_{EN}$ ), and resonance energies ( $R_N$ ) of the complexes in carbon tetrachloride

Complex	Solvent	Temp.	$\lambda_{CT}$ (nm)	$f \times 10^{-5}$	$\mu_{EN}$ (Debye)	$R_N$ (ev)	$h\nu_{CT}$ (ev)	$I_D$ (ev)	$\Delta G$
DDQ + PNA	CCl <sub>4</sub>	20 <sup>o</sup> C	423.69nm	$2.07 \times 10^{-5}$	0.939	0.00735	2.93	9.37	15.120
DDQ + PNA	CCl <sub>4</sub>	20 <sup>o</sup> C	572.066nm	$6.26 \times 10^{-5}$	0.775	0.00372	2.17	8.43	14.835
DDQ + PNA	CCl <sub>4</sub>	25 <sup>o</sup> C	421.65nm	$1.87 \times 10^{-5}$	0.949	0.00753	2.94	9.38	15.291
DDQ + PNA	CCl <sub>4</sub>	25 <sup>o</sup> C	512.78nm	$1.54 \times 10^{-5}$	0.798	0.00440	2.42	8.74	14.435
DDQ + PNA	CCl <sub>4</sub>	30 <sup>o</sup> C	418.89nm	$2.27 \times 10^{-5}$	0.972	0.00795	2.96	9.40	15.291
DDQ + PNA	CCl <sub>4</sub>	30 <sup>o</sup> C	513.89nm	$1.22 \times 10^{-5}$	0.829	0.00474	2.42	8.72	14.093

**Table 5.** Absorption maxima  $\lambda_{CT}$ , association constants (K), molar absorptivities ( $\epsilon$ ), of the CT-complex of DDQ and PNA in dichloromethane, chloroform and carbon tetrachloride at 20°C, 25°C and 30°C.

Systems	Solvent	$\lambda_{CT}$ (nm)		$K_{20}$ (l mol <sup>-1</sup> )		$K_{25}$ (l mol <sup>-1</sup> )		$K_{30}$ (l mol <sup>-1</sup> )		$\epsilon_{20}$ (l mol <sup>-1</sup> cm <sup>-1</sup> )		$\epsilon_{25}$ (l mol <sup>-1</sup> cm <sup>-1</sup> )		$\epsilon_{30}$ (l mol <sup>-1</sup> cm <sup>-1</sup> )	
DDQ + PNA	CH <sub>2</sub> Cl <sub>2</sub>	44 0	56 0	22 8	383	234	39 3	24 7	35 1	176	127	184	133	193	141
DDQ + PNA	CHCl <sub>3</sub>	43 0	55 0	26 9	362	356	455	39 3	43 4	181	142	185	120	191	125
DDQ + PNA	CCl <sub>4</sub>	42 0	54 0	45 3	399	482	340	48 8	30 1	195	133	199	141	209	152

**Table 6.** Characteristic infrared frequencies\*(cm<sup>-1</sup>) and tentative assignments for DDQ, PNA and their complex.

DDQ	PNA	Complex	Assignments
3325 w	3480 s	3481s	v (N-H)
3218br	3356s, br	3416br	v (O-H),
-	3320s,br	3369br	v(C-H), aromatic
	-	3222sh	v ( <sup>1</sup> NH)
2250vw		-	v <sub>s</sub> (C-H), CH <sub>3</sub> + CH <sub>3</sub>
2231ms	3108 w	3231w	v(C-H), aromatic v ( <sup>1</sup> NH)
-	1923w	2928ms	
	1747w	2209ms	v (C?N):DDQ
1673 vs	1635ms	1633vs	v(C=O)+v(C=C)+
-	-	1606s	v (C-N): v <sub>as</sub> (NO <sub>2</sub> )
1552 vs	1591vs	1589ms	v(C=C), aromatic
	-	-	$\delta$ def (N-H), +NH <sub>2</sub> ring breathing bands
-	1474s	1498vs	$\delta$ (C-H) deformation
1451ms	1442s	1435vs	
	1398vs	1327vs	v(C=C)
1358w	1302w	1255m, sh	v <sub>as</sub> (C-N)
-		1240vs	
1267s	-	-	v(C-O)
1172 vs	1183w	1112ms	
1072w -	1110br	1110ms	v <sub>s</sub> (C-N)
1010vw	-	-	
-	998s	-	$\delta$ (C-H) in plane bending
893vs	842sharp	987mw	$\delta$ rock, +NH <sub>2</sub>
800vs		850m	v(C-Cl); DDQ, complex
	754vs	760w	C-H out of plane
720s	698vs	629mw	bending
-	534ms	563ms	
615 ms	490ms	495br	C-H wagging
428s	418sharp	420ms	CNC deformation

S, strong, w, weak, m, medium, sh, shoulder, v, very, vs, very strong, br, broad; v, stretching, vs, symmetrical stretching; v<sub>as</sub>, asymmetrical stretching

*Determination of standard free energy changes ( $\Delta G^\circ$ ) and energy ( $E_{CT}$ ) of the  $\pi$ - $\pi^*$  interaction between donor and acceptor*

The standard free energy changes of complexation ( $\Delta G^\circ$ ) were calculated from the association constants by the following equation derived by Martin, Swarbrick and Cammarata [16].

$$\Delta G^\circ = -2.303 RT \log K_{CT} \quad (6)$$

where  $\Delta G^\circ$  is the free energy change of the CT-complexes ( $KJ \text{ mol}^{-1}$ ),  $R$  is the gas constant ( $8.314 \text{ Jmol}^{-1}K$ ),  $T$  is the temperature and  $K_{CT}$  is the association constant of the complex ( $l \text{ mol}^{-1}$ ) in different solvents at different temperatures  $20^\circ\text{C}$ ,  $25^\circ\text{C}$  and  $30^\circ\text{C}$ , shown in Tables 2-4.

The energy ( $E_{CT}$ ) of the  $\pi$ - $\pi^*$  interaction between donor (PNA), and acceptor (DDQ), is calculated using the following equation derived by G. Briegleb and Z. Angew [17]:

$$E_{CT} = 1243.667 / \lambda_{CT} \quad (7)$$

where  $\lambda_{CT}$  is the wavelength of the CT band.

The calculated values of  $E_{CT}$  are given in Tables 2-4.

*Spectrophotometric study of the formation constants of the charge transfer complexes in different polar solvents*

The stoichiometries and the formation constants of the charge transfer complex of p-nitroaniline with DDQ were determined in different polar solvents, viz., carbon tetrachloride, chloroform and dichloromethane at different temperatures  $20^\circ\text{C}$ ,  $25^\circ\text{C}$  and  $30^\circ\text{C}$  using the Benesi-Hildebrand equation [18, 19]. The spectrophotometric data were employed to calculate the values of the formation constants,  $K_{CT}$  of the complexes. The changes in the absorbance upon addition of PNA to a solution of DDQ of fixed concentration follow the Benesi-Hildebrand equation [18, 19] in the form:

$$[A]_0 / A = (1 / K_{CT}\epsilon_{CT}) \times 1 / [D]_0 + 1/\epsilon_{CT} \quad (8)$$

where  $[D]_0$  and  $[A]_0$  are the concentrations of the PNA donor, and DDQ acceptor, respectively,  $A$  is the absorbance of the donor-acceptor mixture at  $\lambda_{CT}$ , against the solvents as reference,  $K_{CT}$  is the formation constant and  $\epsilon_{CT}$  is the molar extinction coefficient, different from that of the complex in eq.(8) [18,19], which is valid under the condition  $[D]_0 \gg [A]_0$  [11, 12] for 1:1 donor-acceptor complexes. The concentration of the donor PNA was changed over a wide range from 0.01M to 0.5M while the concentration of the  $\pi$  acceptor DDQ was kept fixed at 0.01M in each reaction

mixture. These produced solutions with donor: acceptor molar ratio varying from 1:1 to 50:1. The experimental data are given in Table 3.

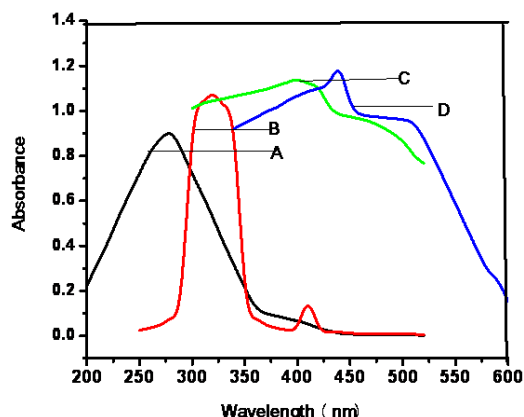


**Fig. 1.** Absorption spectra of (A) 0.01M DDQ (B) Blank solvent (dichloromethane) (C) 0.01 M p-nitro aniline (D) CT-complex of 0.01 M PNA and 0.01 M DDQ in dichloromethane.

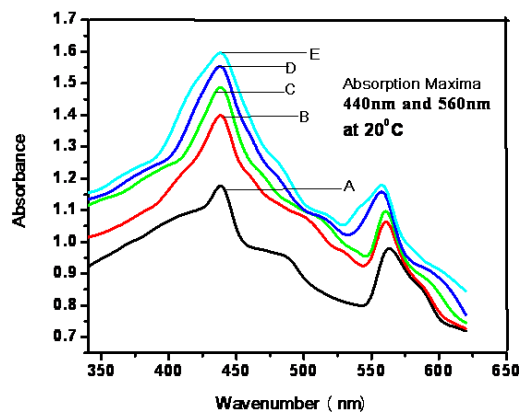


**Fig. 2.** Absorption spectra of DDQ ( $1 \times 10^{-2}M$ ) in dichloromethane at  $20^\circ\text{C}$  with addition of p-nitroaniline concentrations ranging from 0.01M to 0.05M with increasing concentrations from bottom to top.

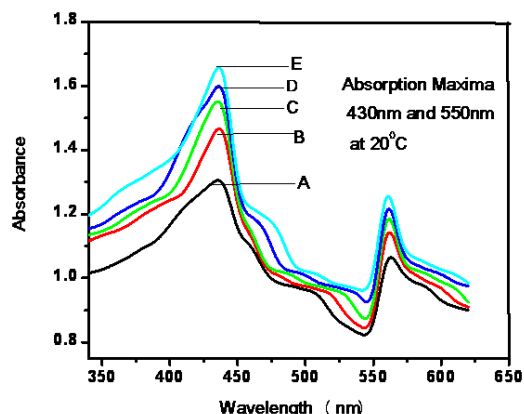


**Fig. 3.** Absorption spectra of DDQ ( $1 \times 10^{-2}M$ ) in chloroform at  $20^\circ\text{C}$  with addition of p-nitroaniline concentrations ranging from 0.01M to 0.05M with increasing concentrations from bottom to top.

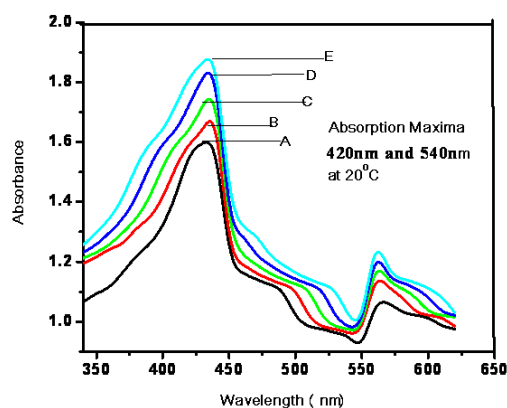


Fig. 4. Absorption spectra of DDQ ( $1 \times 10^{-2}$ M) in carbon tetrachloride at  $20^{\circ}\text{C}$  with addition of p-nitroaniline concentrations ranging from 0.01M to 0.05M with increasing concentrations from bottom to top.

The Benesi – Hildebrand [18, 19] method is an approximation that has been used many times and gives decent results. The intensity in the visible region of the absorption bands, measured against the solvent as reference, increases with the increase in the polarity and addition of PNA. The typical absorbance data for the charge transfer complexes of PNA with DDQ in different polar solvents at different temperatures  $20^{\circ}\text{C}$ ,  $25^{\circ}\text{C}$  and  $30^{\circ}\text{C}$  are reported in Table 5. In all systems very good linear plots according to eq. (8) [18, 19] were obtained, as shown in Figs 5-7.

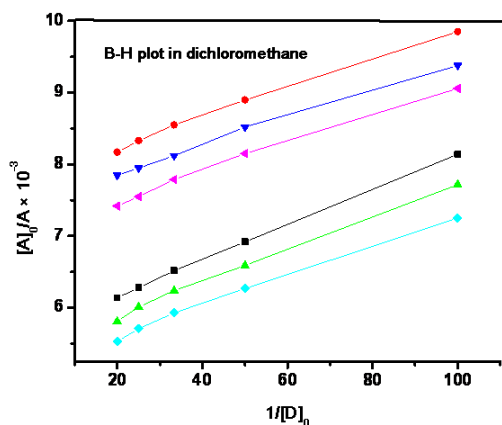


Fig. 5. Relation between  $[A]_0/A$  and  $1/[D]_0$  of DDQ+PNA in  $\text{CH}_2\text{Cl}_2$ .

Formation constants for the complexes in different polar solvents at different temperatures  $20^{\circ}\text{C}$ ,  $25^{\circ}\text{C}$  and  $30^{\circ}\text{C}$  determined from the BH plots are summarized in Table 5. The correlation coefficients of all plots were above 0.99. Plots of  $[A]_0/A$  against  $1/[D]_0$  were found to be linear in all systems in Figs. 5-7 showing 1:1 charge transfer complexes, i.e. the straight lines are obtained with the slopes  $1/K_{CT}\epsilon_{CT}$ . These results are an evidence of 1:1 CT-complexes. From the slope  $1/K_{CT}\epsilon_{CT}$  and

the intercept,  $1/\epsilon_{CT}$ ,  $K_{CT}$  and  $\epsilon_{CT}$  of the CT-complex were calculated in different polar solvents

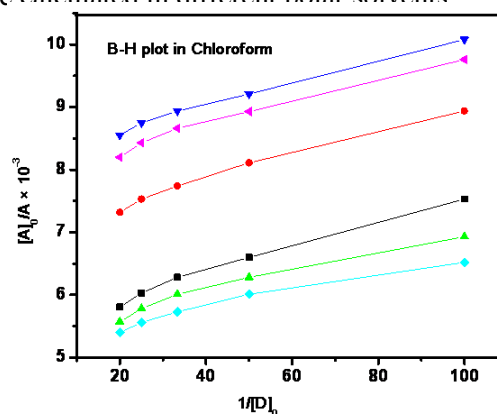


Fig. 6. Relation between  $[A]_0/A$  and  $1/[D]_0$  of DDQ+PNA in  $\text{CHCl}_3$ .

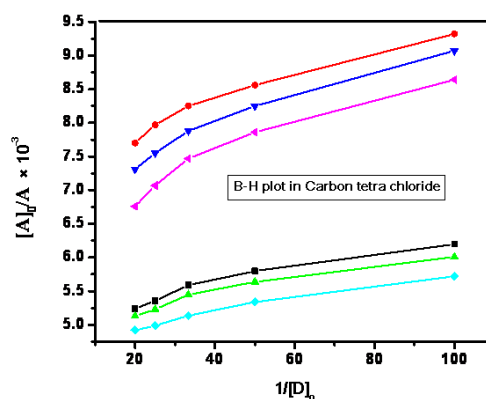


Fig. 7. Relation between  $[A]_0/A$  and  $1/[D]_0$  of DDQ+PNA in  $\text{CCl}_4$ .

#### Appearance of two CT-bands

The two absorption peaks of the CT-complex in each system and their  $\lambda_{\text{max}}$  are given in Table 5.

Well defined absorption peaks of the two CT bands were observed for the DDQ complexes with PNA. Multi-CT absorption bands have been found in the CT complexes containing strong electron acceptors such as chlorine, bromanil and TCNE [20].

The origin of the multi-CT bands observed in the case of DDQ/PNA complex can be explained by the existence of two closely located occupied orbitals of the donors [21].

#### Effect of temperature on the formation constant

Temperature affects the values of  $K_{CT}$ , generally  $K_{CT}$  for DDQ complexes increases with the increase in temperature. But in some cases, such as the complexes of DDQ with PNA at  $25^{\circ}\text{C}$ , and  $\lambda_{\text{max}}$  540 nm in  $\text{CCl}_4$ , at  $30^{\circ}\text{C}$ , and  $\lambda_{\text{max}}$  560 nm in  $\text{CH}_2\text{Cl}_2$ , at  $30^{\circ}\text{C}$ , and  $\lambda_{\text{max}}$  550 nm in  $\text{CHCl}_3$ , and at  $30^{\circ}\text{C}$ , and  $\lambda_{\text{max}}$  540 nm in  $\text{CCl}_4$ , its value decreases with the increase in temperature, as shown in Table 5. There may be a decrease in the

stability of the complex with the increase in temperature in these systems. This trend is similar to that reported in many systems, such as TCNB-benzene complexes and DDQ and acetanilide, biphenyl and naphthalene systems [21].

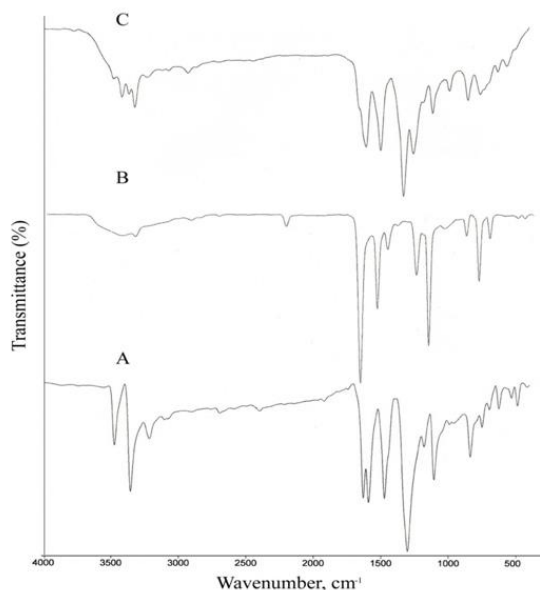


**Fig. 8.** FT-IR spectrum of (A) complex of DDQ and PNA, (B) acceptor DDQ and (C) donor (PNA).

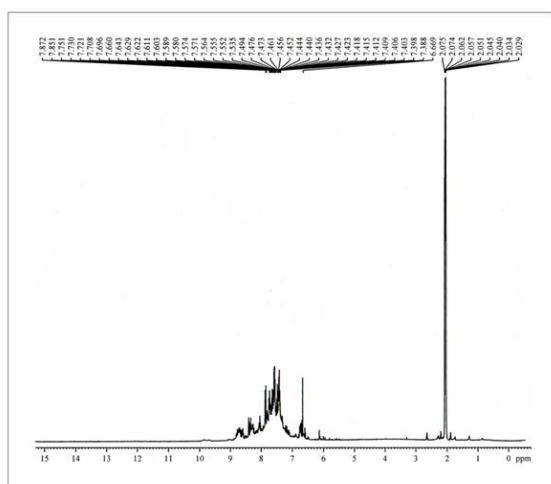


**Fig. 9.** <sup>1</sup>H NMR spectrum of the CT-complex

*Effect of solvents on the formation of CT-complexes*

The spectroscopic properties were markedly affected by varying solvent polarity. In the present investigation, the  $K_{CT}$  values increased significantly from dichloromethane to carbon tetrachloride with decreasing solvent polarity. The values of the association constant  $K_{CT}$  and the values of molar extinction coefficient are shown in Table 5. Moreover, the experimental results of the CT interaction between DDQ with PNA in different polar solvents reveal that the values of the

association constant  $K_{CT}$ , in dichloromethane at  $\lambda_{CT}$  440 nm and 560 nm are 228 ( $1 \text{ mol}^{-1}$ ), 383 ( $1 \text{ mol}^{-1}$ ) at 20°C, 234 ( $1 \text{ mol}^{-1}$ ), 393 ( $1 \text{ mol}^{-1}$ ) at 25°C and 247 ( $1 \text{ mol}^{-1}$ ) and 351 ( $1 \text{ mol}^{-1}$ ) at 30°C. In chloroform the values of the association constant  $K_{CT}$ , at  $\lambda_{CT}$  430 nm and 550 nm are 269 ( $1 \text{ mol}^{-1}$ ), 362 ( $1 \text{ mol}^{-1}$ ) at 20°C, 356 ( $1 \text{ mol}^{-1}$ ), 455 ( $1 \text{ mol}^{-1}$ ) at 25°C and 393 ( $1 \text{ mol}^{-1}$ ), 434 ( $1 \text{ mol}^{-1}$ ) at 30°C. In carbon tetrachloride the values of the association constant  $K_{CT}$ , at  $\lambda_{CT}$  420 nm and 540 nm are 453 ( $1 \text{ mol}^{-1}$ ), 399 ( $1 \text{ mol}^{-1}$ ), at 20°C 482 ( $1 \text{ mol}^{-1}$ ), 340 ( $1 \text{ mol}^{-1}$ ), at 25°C, 488 ( $1 \text{ mol}^{-1}$ ), 301 ( $1 \text{ mol}^{-1}$ ), at 30°C. The values of the molar extinction coefficients  $\epsilon_{20}$ ,  $\epsilon_{25}$ , and  $\epsilon_{30}$  in dichloromethane are 176 ( $1 \text{ mol}^{-1}\text{cm}^{-1}$ ), 127 ( $1 \text{ mol}^{-1}\text{cm}^{-1}$ ) and 184 ( $1 \text{ mol}^{-1}\text{cm}^{-1}$ ), 133 ( $1 \text{ mol}^{-1}\text{cm}^{-1}$ ) and 193 ( $1 \text{ mol}^{-1}\text{cm}^{-1}$ ), 141 ( $1 \text{ mol}^{-1}\text{cm}^{-1}$ ), respectively. The values of the molar extinction coefficients  $\epsilon_{20}$ ,  $\epsilon_{25}$ , and  $\epsilon_{30}$  in chloroform are 181 ( $1 \text{ mol}^{-1}\text{cm}^{-1}$ ), 142 ( $1 \text{ mol}^{-1}\text{cm}^{-1}$ ), 185 ( $1 \text{ mol}^{-1}\text{cm}^{-1}$ ), 120 ( $1 \text{ mol}^{-1}\text{cm}^{-1}$ ), and 191 ( $1 \text{ mol}^{-1}\text{cm}^{-1}$ ), 125 ( $1 \text{ mol}^{-1}\text{cm}^{-1}$ ), respectively, as shown in Table 5. The values of the molar extinction coefficients  $\epsilon_{20}$ ,  $\epsilon_{25}$ , and  $\epsilon_{30}$  in carbon tetrachloride are 195 ( $1 \text{ mol}^{-1}\text{cm}^{-1}$ ), 133 ( $1 \text{ mol}^{-1}\text{cm}^{-1}$ ), 199 ( $1 \text{ mol}^{-1}\text{cm}^{-1}$ ), 141 ( $1 \text{ mol}^{-1}\text{cm}^{-1}$ ), 209 ( $1 \text{ mol}^{-1}\text{cm}^{-1}$ ), 152 ( $1 \text{ mol}^{-1}\text{cm}^{-1}$ ), respectively, as represented in Table 5. The increase in the  $K_{CT}$  values with decreasing solvents polarity may also be due to the fact that the CT-complex should be stabilized in less polar solvents [22].

The influence of solvent polarity on the spectroscopic and thermodynamic properties of molecular electron-donor-acceptor (EDA) complexes is discussed. The data given in Table 5 show that DDQ interacts more strongly with PNA in carbon tetrachloride than in the other two solvents.

The experimentally determined values of oscillator strength, ( $f$ ) in dichloromethane at 20°C are  $3.63 \times 10^{-5}$  and  $3.48 \times 10^{-5}$ ; at 25°C are  $2.36 \times 10^{-5}$ , and  $1.73 \times 10^{-5}$ ; and at 30°C are  $2.64 \times 10^{-5}$  and  $6.58 \times 10^{-5}$ , as given in Table 2. The values of the oscillator strength, ( $f$ ) in chloroform at 20°C are  $2.65 \times 10^{-5}$  and  $2.42 \times 10^{-5}$ ; at 25°C are  $1.93 \times 10^{-5}$  and  $6.75 \times 10^{-5}$ ; and at 30°C are  $2.13 \times 10^{-5}$  and  $7.57 \times 10^{-5}$ , respectively, as shown in Table 3. In carbon tetrachloride the values of the oscillator strength, ( $f$ ) at 20°C are  $2.07 \times 10^{-5}$  and  $6.26 \times 10^{-5}$ ; at 25°C are  $1.87 \times 10^{-5}$  and  $1.54 \times 10^{-5}$ ; and at 30°C are  $2.27 \times 10^{-5}$  and  $1.22 \times 10^{-5}$ , respectively (Table 4).

The values of the transition dipole moment, ( $\mu_{EN}$ ) in dichloromethane are 0.892 Debyes and 0.757 Debyes at 20°C; 0.912 Debyes and 0.775 Debyes at 25°C; and 0.934 Debyes and 0.798 Debyes at 30°C (see Table 2). In chloroform the

values of the transition dipole moment, ( $\mu_{EN}$ ) are 0.905 Debyes and 0.801 Debyes at 20°C; 0.914 Debyes and (0.736 Debyes at 25°C; and 0.930 Debyes and 0.752 Debyes at 30°C (Table 3). In carbon tetrachloride the values of the transition dipole moment, ( $\mu_{EN}$ ) are 0.939 Debyes and 0.775 Debyes at 20°C; 0.949 Debyes and 0.798 Debyes at 25°C; and 0.972 Debyes and 0.829 Debyes at 30°C (Table 4), which indicate that the complex should be more stable in the less polar solvent CCl<sub>4</sub> than in the other two solvents.

The free energy change of the complexation also reveals that the CT-complex formation between the donor (PNA) and the acceptor (DDQ) is exothermic in nature. The values of  $\Delta G^\circ$  in dichloromethane: -13.408 KJmol<sup>-1</sup> and -14.721 KJmol<sup>-1</sup> at 20°C; -13.405 KJmol<sup>-1</sup> and -14.778 KJmol<sup>-1</sup> at 25°C; and -13.636 KJmol<sup>-1</sup> and -14.492 KJmol<sup>-1</sup> at 30°C are shown in Table 2. In chloroform the values of  $\Delta G^\circ$  at 20°C are -13.808 KJmol<sup>-1</sup> and -14.549 KJmol<sup>-1</sup>; at 25°C are -14.549 KJmol<sup>-1</sup> and -15.120 KJmol<sup>-1</sup>; and at 30°C -14.778 KJmol<sup>-1</sup> and -15.006 KJmol<sup>-1</sup> (Table 3). In carbon tetrachloride the values are -15.120 KJmol<sup>-1</sup> and -14.835 KJmol<sup>-1</sup> at 20°C; -15.291 KJmol<sup>-1</sup> and -14.435 KJmol<sup>-1</sup> at 25°C; and -15.291 KJmol<sup>-1</sup> and -14.093 KJmol<sup>-1</sup> at 30°C (Table 4). The values of  $\Delta G^\circ$  generally become more negative as the association constants of the molecular complex increase.

The calculated values of  $I_D$  of the DDQ/PNA system in dichloromethane at 20°C are 9.40(*ev*), 8.54(*ev*); 9.37(*ev*) and 8.49 (*ev*) at 25°C and 9.32(*ev*) and 8.63(*ev*) at 30°C (Table 2). In chloroform the values of  $I_D$  at 20°C are 9.38 (*ev*) and 8.47 (*ev*); at 25°C are 9.35 (*ev*) and 8.40 (*ev*); and at 30°C are 9.35 (*ev*) and 8.39 (*ev*) (Table 3). The calculated values of  $I_D$  in carbon tetrachloride at 20°C are 9.37 (*ev*) and 8.43 (*ev*); at 25°C are 9.38 (*ev*) and 8.74 (*ev*); and at 30°C are 9.40 (*ev*) and 8.72 (*ev*) (Table 4). The approximate constancy of the  $I_D$  values indicates that the ionization potential has a negligibly small effect on the  $K_{CT}$  value.

#### FT-IR spectra of CT-complex and reactants

FT-IR spectra of p-nitroaniline (donor), DDQ (acceptor) and their CT-complex are shown in Fig 8. while the assignments of their characteristic FT-IR spectral bands are reported in Table 6. The formation of the charge transfer complex during the reaction of DDQ with PNA is strongly evidenced by the presence of the main characteristic infrared bands of the donor and acceptor in the spectrum of the product. There are changes in their intensities compared with those of the free donor and acceptor. This shift was attributed to the charge transfer from

donor to acceptor upon complexation.

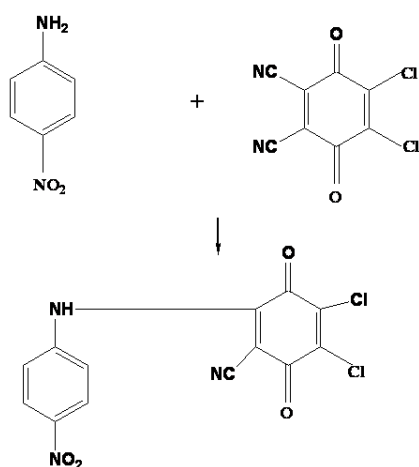
The FT-IR spectrum of the DDQ/PNA complex indicated that the band that results from the  $\nu$  (C $\equiv$ N) vibration of the free DDQ acceptor changed in frequency and decreased in intensity in the complexes upon CT complexation. Free DDQ shows two  $\nu$  (C $\equiv$ N) vibrations at 2250 and 2231 cm<sup>-1</sup>, while in its complex  $\nu$  (C $\equiv$ N) occurs at a lower wave number value, 2209 cm<sup>-1</sup>. It is clear that  $\nu$  (C $\equiv$ N) of DDQ is decreased upon complexation [23]. The characteristic band of  $\nu$  (N-H) of PNA is observed at 3480 cm<sup>-1</sup> (strong) and 3356 cm<sup>-1</sup> (strong). In the CT-complex a new band is observed at 3481 cm<sup>-1</sup>(strong). The band at 3076 cm<sup>-1</sup>(weak) is due to the aromatic C-H stretching vibration. The -NH<sub>2</sub> deformation mode is observed by the absorption at 1633 cm<sup>-1</sup> (very strong) in the CT-complex, whereas in free PNA this is observed at 1635 cm<sup>-1</sup> (medium strong). This band overlaps with the aromatic C=C stretching vibrations. The -NO<sub>2</sub> group is observed at 1606 cm<sup>-1</sup>(strong) in the CT complex, whereas in free PNA this is observed at 1591 cm<sup>-1</sup> (very strong). The group of bands assigned to  $\nu$  (C-Cl) vibrations, which appeared at 893 cm<sup>-1</sup> and 800 cm<sup>-1</sup> in the free DDQ, exhibited a shift to lower wave numbers at 862 cm<sup>-1</sup> and 780 cm<sup>-1</sup> and a decrease in intensity of the characteristic peaks [23]. These observations clearly confirm that the (C $\equiv$ N) group in the DDQ acceptor participates in the complexation process. Because DDQ lacks acidic centers, the molecular complex can be assumed to form through  $\pi$ - $\pi^*$  and/or n- $\pi^*$  charge migration from the HOMO of the donor to the LUMO of the acceptor. The  $\pi$ - $\pi^*$  CT complex is formed *via* the benzene ring (electron-rich group) of the PNA and DDQ reagents (electron- acceptor).

The cyano group (C $\equiv$ N) is an electron-withdrawing group that exists in DDQ in a conjugated bonding system. The 2 CN groups in DDQ withdraw electrons from the aromatic ring, and such a process will make the aromatic ring an electron-accepting region. The  $\pi^*$ -CN electron density appears to increase and more easily accept a proton from the donor because of the electron-withdrawing process and the conjugated electron system. So, the interaction mode between PNA and the DDQ acceptor also occurs through migration of an H<sup>+</sup> ion to one of the cyano groups in the DDQ acceptor to form a positive ion (-C $\equiv$ N<sup>+</sup>H) that associates with the -NH<sub>2</sub> group in PNA.

#### <sup>1</sup>H- NMR spectrum of the CT- complex

The <sup>1</sup>H-NMR spectrum of the 2, 3-dichloro-5, 6-dicyano-*p*-benzoquinone and *p*-nitro aniline product in acetone is shown in Figure 9. *P*-nitro

aniline ring system was specified in the region  $\delta = 8.40\text{--}6.66$  ppm. The  $\text{NH}_2$  group of p-nitroaniline occurring at  $\delta = 6.71$  in the free donor was shifted to  $\delta = 6.66$ . This indicates that one of the CN groups of DDQ has been eliminated by the amino group of the p-nitroaniline donor eliminating HCN [24] (Scheme 1). The doublet peaks at  $\delta = 8.40$  ppm and the triplet peaks at  $\delta = 7.62$  ppm assigned to the rest of protons of p-nitroaniline are in the same kind in DDQ moiety in the CT-complex. The intensities and chemical shifts of the aromatic signals were significantly affected by the elimination and the accompanying changes in the structured configuration. Mechanism and structure of the CT-complex of acceptor and donor is given in Scheme 1.



**Scheme 1.** Mechanism of the interaction between p-nitroaniline and DDQ

## CONCLUSION

The UV-Vis spectrophotometric method for the study of the CT-complex of DDQ with PNA ascertains the formation of a 1:1 (A:D) complex in all three solvents, viz., carbon tetrachloride, chloroform and dichloromethane. In all systems the stoichiometry is unaltered by changing the solvent. The association constants,  $K_{CT}$  and molar extinction coefficients,  $\epsilon_{CT}$ , of all systems were evaluated by the Benesi-Hildebrand method. The spectroscopic and thermodynamic parameters of the CT-complexes were found to be dependent on the polarity of the solvents. The values of oscillator strengths, ( $f$ ) transition dipole moments, ( $\mu_{EN}$ ) resonance energies, ( $R_N$ ) and standard free energies, ( $\Delta G^\circ$ ) were estimated for the PNA/DDQ systems in different polar solvents. The results show that the investigated CT-complex is stable, exothermic and spontaneous. From the trends in the CT absorption bands, the ionization potentials of the donor molecules were estimated. The FT-IR and  $^1\text{H}$  NMR

spectra revealed that the charge transfer complex is present as an ion pair and there are few free ions in solution.

**Acknowledgements:** Authors thank Dr. Sakir Ali, Chairman of Chemistry Department, Aligarh Muslim University, India, for providing the facilities of instruments of FT-IR spectrometer, UV-Visible spectrophotometer. Financial assistance from the UGC, New Delhi extended through the Women-PDF fellowship is also gratefully acknowledged. The authors also thank the learned referee for making valuable comments.

## REFERENCES

1. L. J. Andrews, *Chem. Rev.*, **54**, 713 (1954).
2. S. P. Mc Glynn, *Chem. Rev.*, **58**, 1113 (1958).
3. R. S. Mulliken, *J. Am. Chem. Soc.*, **74**, 811 (1952).
4. R. Foster, *Organic Charge-Transfer Complexes*, New York, 1969, p.387.
5. L. E. Orgel, *J. Chem. Phys.*, **23**, 1352 (1955).
6. A.S. Amin, A.M. El-Beshbeshy, *Microchim. Acta*, **63**, 137 (2001).
7. S.M. Andrade, S.M.B. Costa, R. Pansu, *J. Colloids Interface Sci.*, **226**, 260 (2000).
8. A. Eychmuller, A.L. Rogach, *Pure Appl. Chem.*, **72**, 179 (2000).
9. M. Hayashi, T.S. Yang, J. Yu, A. Mebel, S.H. Lin, *J. Phys. Chem. A*, **101**, 4156 (1997).
10. D.A. Skoog, *Principle of analytical Chemistry*, 3<sup>rd</sup> ed. Sannder College Publishing, New York, 1985, (Chapter7).
11. M. Hasani, R. Alireza, *Spectrochim. Acta Part A*, **65**, 1093 (2006).
12. S. Bhattacharya, K. Gosh, S.C. Momas, *Spectrochim. Acta Part A*, **65**, 659 (2006).
13. R. K. Gupta, R.A. Sig, *J. App. Sci.*, **5** (1), 28 (2005).
14. G. Aloisi, S. Pignataro, *J. Chem. Soc. Faraday Trans.*, **69**, 534 (1972).
15. G. Briegleb, J. Czekalla, *Z. Physikchem. (Frankfurt)*, **24**, 237 (1960).
16. A.N. Martin, J. Swarbrick, A. Cammarata, *Physical Pharmacy*, 3<sup>rd</sup>ed, Lee & Febiger, Philadelphia, PA, 1969, p. 344.
17. G. Briegleb, *Z. Angew. Chem.* **76**, 326 (1964).
18. H.A. Benesi, J. H. Hildebrand, *J. Am. Chem. Soc.*, **71**, 2703 (1949).
19. P. Douglas, G. Waechter, A. Mills, *Photochem. Photobiol.*, **52**, 473 (1990).
20. G. Briegleb, *Electronen-Donator-Acceptor-Complex*, Springer-Verlag, Berlin, 1961.
21. M.S. Subhani, N.K. Bhatti, M. Mohammad, A.Y. Khan, *Turk J Chem.*, **24**, 223 (2000).
22. M. E. El - Zaria, *Spectrochim. Acta A*, **69**, 216 (2008).
23. H. H. Eldaroti, S. A. Gadir, M. S. Refat, A.M. A. Adam, *J. Pharm. Anal.*, **4**, 81 (2014).
24. M. S Refat, N. M. El-Metwally, *Chin. Sci. Bull.*, **56**, 19 (1993).



## СПЕКТРОСКОПСКИ ИЗСЛЕДВАНИЯ НА КОМПЛЕКСИ С ПРЕНОС НА ЗАРЯДА ОТ 2,3-ДИХЛОРО-5,6-ДИЦИАНО-р-БЕНЗОХИНОН С р-НИТРОАНИЛИН

Н. Сингх, А. Ахмад \*

Департамент по химия, Научен факултет, Мюсюлмански университет, Алигар - 202002, Индия

Постъпила на 2 август, 2015 г.; приета на 5 октомври, 2015 г.

(Резюме)

Комплекси с пренос на заряда (СТ-комплекси) с донор р-нироанилин (PNA) и акцептор 2,3-дихлоро-2,6-дициано-р-бензохинон (DDQ) са изследвани спектро-фотометрично в различни разтворители, като  $\text{CH}_2\text{Cl}_2$ ,  $\text{CHCl}_3$  и  $\text{CCl}_4$  при различни температури. Във всички случаи са наблюдавани по две линии на пренос на заряда. Резултатите показват, че образуването на СТ-комплекс в по-малко полярен разтворител сравнително високо. Стехиометрията на СТ-комплекса е 1:1. Физичните параметри на СТ-комплекса са оценени по уравнението на Benesi-Hildebrand. Данните са обсъдени в смисъла на константите на образуване ( $K_{CT}$ ), коефициента на моларна екстинкция ( $\epsilon_{CT}$ ), стандартния термодинамичен потенциал ( $\Delta G^\circ$ ), силата на осцилатора ( $f$ ), преодния диполен момент ( $\mu_{EN}$ ), рзонансната енергия ( $R_N$ ) и йонизационния потенциал ( $I_D$ ). Резултатите показват, че константата на образуване на комплекса ( $K_{CT}$ ) е зависима от природата на акцептора на електрони, на донора и от полярността на използвания разтворител. Образуването на комплекса се потвърждава чрез UV-Vis – спектроскопия, FTIR и  $^1\text{H}$ -ЯМР. Предложена е структура на СТ-комплекса между DDQ и PNA.

## Synthetic flavone derivatives. An antibacterial evaluation and structure-activity relationship study

M. Shoaib<sup>1</sup>, S. W. A. Shah<sup>1\*</sup>, N. Ali<sup>2</sup>, I. Shah<sup>1</sup>, M. N. Umar<sup>3</sup>, Shafiullah<sup>1</sup>, M. N. Tahir<sup>4</sup>, M. Ghias<sup>1</sup>.

<sup>1</sup>Department of Pharmacy, University of Malakand, Chakdara 18550, Dir Lower, Khyber Pakhtunkhwa, Pakistan

<sup>2</sup>Department of Pharmacology, Institute of Basic Medical Sciences, Khyber Medical University, Peshawar 25000, Khyber Pakhtunkhwa, Pakistan

<sup>3</sup>Department of Chemistry, University of Malakand, Chakdara 18550, Dir Lower, Khyber Pakhtunkhwa, Pakistan

<sup>4</sup>Department of Physics, University of Sargodha 40100, Punjab, Pakistan

Received September 4, 2015, Accepted December 16, 2015

Biologically active flavone derivatives with antibacterial potentials were synthesized *via* Claisen-Schmidt condensation of ketones with different aldehydes with good yields. The structures were established by different spectroscopic techniques like <sup>1</sup>H NMR, <sup>13</sup>C NMR, IR and elemental analysis. The findings showed that some of the substituted flavones possess higher antibacterial potentials than simple flavones as regards their minimum inhibitory concentration (MIC) and are potential candidates for the treatment of a wide range of infectious diseases.

**Keywords:** Flavone derivatives, antibacterial, MIC, infectious diseases.

### INTRODUCTION

Infectious diseases are among the main causes of mortality and morbidity worldwide. Advancement in the innovation of antimicrobial agents has safeguarded the way for human wellbeing. However, effectiveness of antibiotics in future is to some extent in doubtful condition due to the development of resistance to these agents in an unavoidable manner [1]. The emergence of hitherto unidentified microbes that cause infections poses a colossal health concern regarding the combat towards infectious diseases [2]. The need for new, effective and affordable drugs to treat microbial diseases in the developing world is one of the major issues facing global health today and consequently, this has created a new dimension in the search for new drugs [3]. Structural modification of anti-infective agents has confirmed to be an effective way of enhancing the lifespan of these agents [4]. Natural products have been reported to be a potential source of anti-infective agents and the prime examples are penicillin and tetracycline. Generally, polyphenolic compounds like flavonoids (natural compounds) have been reported for a wide range of pharmacological actions [5]. At present, this class of natural products is the area of interest in medical research and is known to possess pharmacological actions including antiallergic [6], anti-inflammatory [7], antiviral [8], antithrombotic [9], antimutagenic [10], antioxidant [11],

antidiabetic [12], anticancer [13], hepatoprotective [14] and antimicrobial [15-18] effects.

Most of the scientific reports are on natural flavonoids and acquire a special place in natural and heterocyclic chemistry because of their structural ornamentation in many pharmacologically active compounds. In view of the above facts regarding the significance of flavonoids in nature, it was considered worthwhile to synthesize flavonoid derivatives and to attempt to portray the structure-activity relationships (SAR).

### EXPERIMENTAL

#### *Materials and Methods*

Substituted ketones and benzaldehyde were purchased from Sigma Aldrich Chemical Company. TLC plates were Merck 60 F254, Darmstadt Germany. Solvents and chemicals like ethanol, n-hexane, ethyl acetate, DMSO of extra pure analytical grade were purchased from Merck. Mueller-Hinton agar and nutrient broth were purchased from Oxoid, UK. Ciprofloxacin and ampicillin were gifted by local pharmaceutical industries.

<sup>1</sup>H-NMR and <sup>13</sup>C NMR spectra were recorded in deuterated chloroform (CDCl<sub>3</sub>) on a Bruker SF spectrometer operating at 300 and 75 MHz frequencies, respectively. Chemical shift values are expressed in  $\delta$  (ppm) downfield relative to TMS which was used as an internal standard. Infrared spectra were recorded on Thermoscientific, USA (Nicolet 6700) infrared spectrometer by the KBr disk method. All melting points are uncorrected and

\* To whom all correspondence should be sent:  
E-mail: pharmacistsyed@gmail.com

were taken in open capillary tubes using an Electrothermal 9100 apparatus (Barnstead, UK). Reaction extents and final products purities were checked on TLC plates (Merck 60 F254) and spots were visualized under UV lamp (180-365 nm) by staining with iodine vapor.

### Synthesis and characterization

#### General procedure for the synthesis of flavone derivatives

To an ethanolic solution of substituted 2-hydroxy acetophenone (15 mM), sodium hydroxide (10 ml, 40% ethanolic) was dropwise added at room temperature. Then the corresponding benzaldehyde derivatives (15 mM) were dropwise added to this mixture and stirred for 24-48 h at room temperature ( $25 \pm 2^\circ\text{C}$ ). The reaction was monitored by TLC and upon completion, the contents were poured into crushed ice and neutralized with 1N HCl solution resulting in yellow precipitates of the corresponding chalcones. The latter were filtered and washed with water to remove the impurities.

In the next step, the respective chalcones were separately cyclized to flavone derivatives in 15 ml DMSO in the presence of iodine (375 mg) at  $140^\circ\text{C}$  for 1 h. Upon completion of the reaction, the mixtures were cooled to room temperature and poured into water followed by extraction with ethyl acetate (25 ml $\times$ 3), treated with sodium thiosulfate solution (20%), brine solution and dried over sodium sulfate. The final products (a mixture of flavone and chalcone) were subjected to column chromatography using n-hexane: ethyl acetate (9:1) to purify the flavone derivatives (Scheme 1) [19, 20].

#### 2-Phenyl-4H-chromen-4-one (F1)

The compound was obtained by stirring equimolar amounts of 2'-hydroxyacetophenone and benzaldehyde in ethanol, and adding sodium hydroxide solution with continuous stirring to get the desired chalcone. In the next step, the chalcone was cyclized to flavone by refluxing in DMSO in the presence of catalytic iodine as described above.

$^1\text{H NMR}$  (300 MHz, chloroform-*d*)  $\delta$  8.22 (dd,  $J = 8.0, 1.7$  Hz, 1H), 7.75 – 7.53 (m, 5H), 7.50 – 7.37

(m, 4H), 6.85 (s, 1H).  $^{13}\text{C NMR}$  (75 MHz,  $\text{CDCl}_3$ )  $\delta$  178.48, 163.42, 156.26, 133.79, 131.77, 131.61, 129.04, 126.66, 125.71, 125.24, 123.95, 118.09, 107.58 IR (KBr),  $\nu$ ,  $\text{cm}^{-1}$ , 1635.4, 1463.3, 1372.4, 766.0. Found, %: C 81.07; H 4.54.  $\text{C}_{15}\text{H}_{10}\text{O}_2$ . Calculated, %: C 81.19; H 4.60 [20-22].

#### 2-(4-(Dimethylamino)phenyl)-4H-chromen-4-one (F2)

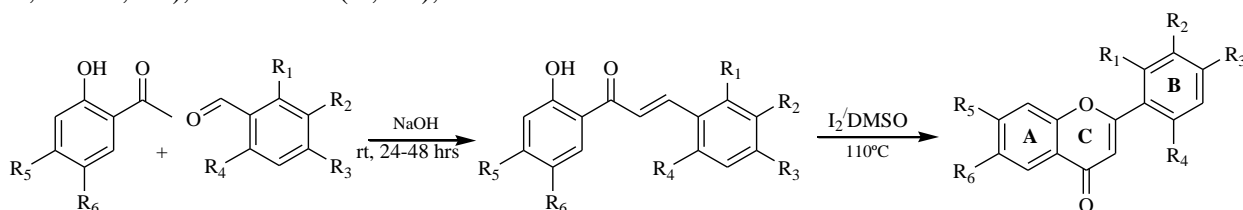
The compound was obtained by stirring equimolar amounts of 2'-hydroxyacetophenone and 4-(dimethylamino) benzaldehyde in ethanol, and adding sodium hydroxide solution under continuous stirring to get the desired chalcone. In the next step, the chalcone was cyclized to flavone by refluxing in DMSO in the presence of catalytic iodine.

$^1\text{H NMR}$  (300 MHz, chloroform-*d*)  $\delta$  8.24 (dd,  $J = 7.9, 1.7$  Hz, 1H), 7.89 – 7.81 (m, 2H), 7.68 (ddd,  $J = 8.7, 7.1, 1.7$  Hz, 1H), 7.55 (dd,  $J = 8.4, 1.3$  Hz, 1H), 7.40 (ddd,  $J = 8.1, 7.1, 1.1$  Hz, 1H), 6.80 – 6.76 (m, 2H), 6.73 (s, 1H), 3.10 (s, 6H).  $^{13}\text{C NMR}$  (75 MHz, chloroform-*d*)  $\delta$  ppm= 178.20, 163.7, 156.50, 152.60, 133.22, 127.75, 125.58, 124.81, 124.03, 117.84, 111.66, 104.39, 40.10. IR (KBr)  $\nu$ ,  $\text{cm}^{-1}$ , 2919.4 (CH) 1730.3(C=O), 1197.8 and 1363.2 (C-N), 1558.1(C=C), 3311.5 (=C-H) 1127.2 (C-O). Found, %: C 76.96; H 5.70; N 5.28.  $\text{C}_{17}\text{H}_{15}\text{NO}_2$ . Calculated, %: C 76.59; H 5.60; N 5.60 [20].

#### 2-(*p*-Tolyl)-4H-chromen-4-one (F3)

The compound was obtained by stirring equimolar amounts of 2'-hydroxyacetophenone and 4-methylbenzaldehyde (*p*-tolylaldehyde) in ethanol, and adding sodium hydroxide solution under continuous stirring to get the desired chalcone. In the next step, the chalcone was cyclized to flavone by refluxing in DMSO in the presence of catalytic iodine.

$^1\text{H NMR}$  (300 MHz, chloroform-*d*)  $\delta$  8.23 (dd,  $J = 7.9, 1.7$  Hz, 1H), 7.85 (d,  $J = 8.3$  Hz, 2H), 7.71 (td,  $J = 8.4, 7.2, 1.2$  Hz, 1H), 7.53 (d,  $J = 8.5$  Hz, 1H), 7.39 (td,  $J = 7.9, 0.8$  Hz, 1H), 7.27 (d, 2H), 6.92 (s, 1H), 2.39 (s, 3H).  $^{13}\text{C NMR}$  (75 MHz,  $\text{CDCl}_3$ )  $\delta$  178.1, 162.7, 156.2, 142.5, 134.1, 129.6, 128.4, 126.5, 125.6, 125.2, 123.5, 118.2, 106.5, 104.1, 21.5. IR (KBr)  $\nu$ ,  $\text{cm}^{-1}$ , 1640, 1465, 817 [21, 22].



Scheme 1. Synthesis of flavone derivatives.

*2-(4-Chlorophenyl)-4H-chromen-4-one (F4)*

The compound was obtained by stirring equimolar amounts of 2'-hydroxyacetophenone and 4-chlorobenzaldehyde in ethanol, and adding sodium hydroxide solution under continuous stirring to get the desired chalcone. In the next step, the chalcone was cyclized to flavone by refluxing in DMSO in the presence of catalytic iodine.

<sup>1</sup>H NMR (300 MHz, chloroform-*d*) δ 8.24 (dd, *J* = 8.0, 1.6 Hz, 1H), 7.83 (d, 2H), 7.72 (td, *J* = 8.7, 7.1, 1.7 Hz, 1H), 7.53 (d, *J* = 8.4 Hz, 1H), 7.47 (d, 2H), 7.40 (t, *J* = 7.6 Hz, 1H), 6.75 (s, 1H). <sup>13</sup>C NMR (75 MHz, CDCl<sub>3</sub>) δ 178.2, 162.1, 156.1, 137.8, 133.9, 130.2, 129.3, 127.5, 125.7, 125.3, 123.9, 118.0, 107.6. IR (KBr) *v*, cm<sup>-1</sup>, 1662, 1374, 1092, 827, 754 [21, 22].

*2-(2,4-Dichlorophenyl)-4H-chromen-4-one derivative (F5)*

The compound was obtained by stirring equimolar amounts of 2'-hydroxyacetophenone and 2,4-dichlorobenzaldehyde in ethanol and adding sodium hydroxide solution under continuous stirring to get the desired chalcone. In the next step, the chalcone was cyclized to flavone by refluxing in DMSO in the presence of catalytic iodine.

<sup>1</sup>H NMR (300 MHz, chloroform-*d*, ppm) δ 8.27 (dd, *J* = 8.0, 1.7 Hz, 1H, H-3'), 7.74 (ddd, *J* = 8.7, 7.1, 1.7 Hz, 1H, 5'-H), 7.64 – 7.56 (m, 2H, 5-H, 6'-H), 7.55 – 7.40 (m, 3H, 6-H, 7-H, 8-H), 6.68 (s, 1H, H-3). <sup>13</sup>C NMR (75 MHz, CDCl<sub>3</sub>, ppm) δ 177.98 (C-4), 161.51 (C-2), 156.54 (C-8a), 137.43 (C-2'), 134.06 (C-4'), 133.81 (C-6'), 131.42 (C-5'), 130.77 (C-3'), 130.40 (C-1'), 127.58 (C-7), 125.82 (C-6), 125.50 (C-5), 123.81 (C-4a), 118.18 (C-8), 113.16 (C-3). IR (KBr) *V*<sub>max</sub> cm<sup>-1</sup>: 3066.5, 2920.6, 1734.1, 1645.4, 1221.1, 748.2. Anal. Calcd. for C<sub>15</sub>H<sub>8</sub>Cl<sub>2</sub>O<sub>2</sub>: C, 61.88; H, 2.77. Found: C, 60.99; H, 2.28 [20].

*2-(2,3-Dichlorophenyl)-4H-chromen-4-one (F6)*

The compound was obtained by stirring equimolar amounts of 2'-hydroxyacetophenone and 2,3-dichlorobenzaldehyde in ethanol and then sodium hydroxide solution was added under continuous stirring to get the desired chalcone. In the next step, the chalcone was cyclized to flavone by refluxing in DMSO in the presence of catalytic iodine.

<sup>1</sup>H NMR (300 MHz, chloroform-*d*) δ 8.32 – 8.17 (m, 1H, H4'), 7.86 – 7.61 (m, 2H, H5', 6'), 7.56 – 7.21 (m, 4H, H-5,6,7,8), 6.67 (s, 1H, H3). <sup>13</sup>C NMR (75 MHz, CDCl<sub>3</sub>) δ 178.39(C4), 162.62(C2), 156.58(C8a), 134.60(C7), 134.26(C3'), 134.08(C1'), 132.62(C5), 129.80(C4'), 128.93(C5'), 127.65(C2'), 125.85(C6'),

125.61(C4a), 123.69(C6), 118.23(C8), 112.98(C3). IR (KBr) *V*<sub>max</sub> cm<sup>-1</sup>: 3048.9, 2918.5, 1714.7, 1659.3, 1191.3, 747.8. Anal. Calcd. for C<sub>15</sub>H<sub>8</sub>Cl<sub>2</sub>O<sub>2</sub>: C, 61.88; H, 2.77. Found: C, 62.02; H, 2.46 [20].

*2-(3,4-Dichlorophenyl)-4H-chromen-4-one (F7)*

The compound was obtained by stirring equimolar amounts of 2'-hydroxyacetophenone and 3,4-dichlorobenzaldehyde in ethanol and adding sodium hydroxide solution with continuous stirring to get the desired chalcone. In the next step, the chalcone was cyclized to flavone by refluxing in DMSO in the presence of catalytic iodine.

<sup>1</sup>H NMR (300 MHz, chloroform-*d*) δ 8.24 (dd, *J* = 8.0, 1.7 Hz, 1H), 8.04 (d, *J* = 2.1 Hz, 1H), 7.74 (tq, *J* = 7.0, 2.2 Hz, 2H), 7.65 – 7.56 (m, 2H), 7.46 (ddd, *J* = 8.2, 7.1, 1.1 Hz, 1H), 6.80 (s, 1H). <sup>13</sup>C NMR (75 MHz, CDCl<sub>3</sub>) δ 178.03, 160.82, 156.08, 135.96, 134.09, 133.70, 131.69, 131.11, 128.06, 125.78, 125.55, 125.25, 123.87, 118.06, 108.19. IR (KBr) *v*, cm<sup>-1</sup>, 1659.3, 1413.7, 1378.8, 750.04, 747.8. Found, %: C 61.92; H 2.53. C<sub>15</sub>H<sub>8</sub>Cl<sub>2</sub>O<sub>2</sub>. Calculated, %: C 61.88; H 2.77 [20].

*2-(2,6-Dichlorophenyl)-4H-chromen-4-one (F8)*

The compound was obtained by stirring equimolar amounts of 2'-hydroxyacetophenone and 2,6-dichlorobenzaldehyde in ethanol and adding sodium hydroxide solution under continuous stirring to get the desired chalcone. In the next step, the chalcone was cyclized to flavone by refluxing in DMSO in the presence of catalytic iodine.

<sup>1</sup>H NMR (300 MHz, chloroform-*d*) δ 8.30 (dd, *J* = 8.0, 1.7 Hz, 1H), 7.83 – 7.68 (m, 1H), 7.58 – 7.36 (m, 5H), 6.47 (s, 1H). <sup>13</sup>C NMR (75 MHz, CDCl<sub>3</sub>) δ 178.06, 162.03, 156.96,, 133.65, 133.39, 128.48, 126.58, 125.75, 125.50, 124.89, 123.43, 120.38, 117.58. IR (KBr) *v*, cm<sup>-1</sup>, 2918.5, 1714.7, 1659.3, 1191.3, 747.8. Found, %: C 61.94; H 2.49. C<sub>15</sub>H<sub>8</sub>Cl<sub>2</sub>O<sub>2</sub>. Calculated, %: C 61.88; H 2.77.

*2-(4-(Trifluoromethyl)phenyl)-4H-chromen-4-one (F9)*

The compound was obtained by stirring equimolar amounts of 2'-hydroxyacetophenone and 4-(trifluoromethyl) benzaldehyde in ethanol and adding sodium hydroxide solution under continuous stirring to get the desired chalcone. In the next step, the chalcone was cyclized to flavone by refluxing in DMSO in the presence of catalytic iodine.

<sup>1</sup>H NMR (300 MHz, chloroform-*d*) δ 8.25 (dd, *J* = 8.0, 1.7 Hz, 1H), 8.06 (d, *J* = 8.2 Hz, 2H), 7.85 – 7.69 (m, 3H), 7.61 (dd, *J* = 8.4, 1.1 Hz, 1H), 7.47 (m, 1H), 6.88 (s, 1H). <sup>13</sup>C NMR (75 MHz, CDCl<sub>3</sub>) δ 178.14, 161.57, 156.17, 135.16, 134.10, 133.77, 132.90, 126.62, 126.02, 125.77, 125.54, 123.91, 118.11, 108.71. IR (KBr) *v*, cm<sup>-1</sup>, 3073.3 (=C-H),

1641.8 (C=O), 1316.8 (C-F), 1165.3 (C-O), 849.8 (C-F). ESI:  $m/z$  ( $C_{16}H_9F_3O_2$ )  $H^+$ : calculated, 291.0627, found: 291.0629 [23, 24].

*2-(4-(Trifluoromethyl)phenyl)-7-methoxy-4H-chromen-4-one (F10)*

The compound was obtained by stirring equimolar amounts of 2'-hydroxy-4'-methoxyacetophenone and 4-(trifluoromethyl) benzaldehyde in ethanol and adding sodium hydroxide solution under continuous stirring to get the desired chalcone. In the next step, the chalcone was cyclized to flavone by refluxing in DMSO in the presence of catalytic iodine.

$^1H$  NMR (300 MHz, chloroform-*d*)  $\delta$  8.16 (d,  $J = 8.7$  Hz, 1H), 8.10 – 8.00 (m, 2H), 7.80 (d,  $J = 8.3$  Hz, 2H), 7.09 – 6.97 (m, 2H), 6.83 (s, 1H), 3.97 (s, 3H).  $^{13}C$  NMR (75 MHz,  $CDCl_3$ )  $\delta$  177.56, 164.45, 161.23, 157.98, 135.27, 132.77, 127.18, 126.51, 126.08, 125.98, 125.93, 117.82, 114.76, 108.76, 55.91. IR (KBr)  $\nu$ ,  $cm^{-1}$ , 3130.4 (=C-H), 2815.3 (C-H), 1650.4 (C=O), 1381.4 (C-F), 1111.7 (C-O), 836.4 (C-F). HRMS ( $ES^+$ )  $m/z$   $C_{34}H_{22}F_6O_6Na$  requires 663.1213; Found 663.1234 [25].

*6-Bromo-2-(4-(trifluoromethyl)phenyl)-4H-chromen-4-one (F11)*

The compound was obtained by stirring equimolar amounts of 2'-hydroxy-5'-bromoacetophenone and 4-(trifluoromethyl) benzaldehyde in ethanol and adding sodium hydroxide solution under continuous stirring to get the desired chalcone. In the next step, the chalcone was cyclized to flavone by refluxing in DMSO in the presence of catalytic iodine.

$^1H$  NMR (300 MHz, chloroform-*d*)  $\delta$  8.38 (d,  $J = 2.5$  Hz, 1H), 8.06 (d,  $J = 8.1$  Hz, 2H), 7.88 – 7.78 (m, 3H), 7.58 – 7.45 (m, 1H), 6.90 (s, 1H).  $^{13}C$  NMR (75 MHz,  $CDCl_3$ )  $\delta$  176.88, 161.93, 154.95, 137.13, 134.13, 128.47, 126.72, 126.18, 126.13, 125.21, 124.32, 120.13, 119.07, 108.73. IR (KBr)  $\nu$ ,  $cm^{-1}$ , 3090.4 (=C-H), 1633.7 (C=O), 1316.3 (C-F), 1173.2, 828.4 (C-F), 632.1 (C-Br). HRMS ( $ES^+$ )  $m/z$   $C_{32}H_{16}Br_2F_6O_4Na$  requires 760.9212; found 760.9164 [25].

*Antibacterial Activity*

Antibacterial screening of the flavone derivatives mentioned above was performed against Gram-positive and Gram-negative bacterial strains using the agar well diffusion method. Briefly, about 20 ml of sterile Mueller-Hinton Agar was poured in sterile petri plates and allowed to solidify. The

sterile cotton swab was dipped into the bacterial culture ( $10^6$  to  $10^8$  CFU/ml) and the agar plates were evenly inoculated by swabbing followed by the wells formation using a sterile cork-borer (6 mm diameter). Each prelabeled well was filled with 100  $\mu$ l of various concentrations of flavone derivatives and allowed to diffuse by refrigerating for 30 min. The plates were then incubated at 37°C for 24 h. Triplicate plates were prepared for each treatment and the average zone of inhibition excluding well was recorded. DMSO was used as a negative control. The antibacterial potential in the form of zone of inhibition in millimeters (mm) was compared with the standard antibiotics ampicillin and ciprofloxacin [26-28].

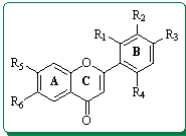
*Minimum inhibitory concentration (MIC)*

Compounds inhibiting growth of one or more of the above microorganisms were again tested for their minimum inhibitory concentration values (MIC). The MIC values were determined by the broth dilution technique. Briefly, a stock solution of each compound was prepared in dimethylsulfoxide (DMSO) and serially diluted to achieve the desired concentration range. To each of the preidentified sterile test tubes containing a specific concentration of the test compound, a standard volume of nutrient broth medium was added. The inoculum consisting of an overnight broth culture of microorganisms was added to each tube. The tubes were incubated at 37°C for 24 h and examined for turbidity. A control tube containing no antimicrobial agent was also included and ciprofloxacin was used as a standard. The lowest concentration required to stop the growth of bacteria was regarded as MIC [29].

RESULTS AND DISCUSSION

The general structure and physical parameters of the flavone derivatives are given in Scheme 1 and Table 1 while the spectroscopic parameters are given in the experimental section of this study. Results of the antibacterial activity of synthetic flavones in respect to their zone of inhibition are given in Table 2. It is reported that substitution in the ring A and ring B may increase or decrease the antibacterial response. Results from the study reveal that addition of halogen (Br) at ring A and trifluoromethyl at ring B enhances the antibacterial response against Gram positive and Gram negative bacteria.

**Table 1.** Physical parameters of the flavone derivatives



Flavone	R <sub>1</sub>	R <sub>2</sub>	R <sub>3</sub>	R <sub>4</sub>	R <sub>5</sub>	R <sub>6</sub>	Yield	Appearance	R <sub>f</sub>	M.P (°C)
F1	H	H	H	H	H	H	68.7%	Creamy white solid	0.58	96-98
F2	H	H	N(CH <sub>3</sub> ) <sub>2</sub>	H	H	H	73.6%	Brick red solid	0.67	107-109
F3	H	H	CH <sub>3</sub>	H	H	H	77.8%	Off white solid	0.64	154-158
F4	H	H	Cl	H	H	H	84.2%	White crystals	0.69	178-181
F5	Cl	H	Cl	H	H	H	87.0%	White solid	0.57	190-193
F6	Cl	Cl	H	H	H	H	81.0%	White solid	0.64	188-191
F7	H	Cl	Cl	H	H	H	79.3%	White solid	0.61	195-197
F8	Cl	H	H	Cl	H	H	81.6%	White solid	0.63	182-185
F9	H	H	CF <sub>3</sub>	H	H	H	85.3%	Monoclinic crystals	0.63	134-137
F10	H	H	CF <sub>3</sub>	H	OCH <sub>3</sub>	H	83.4%	Triclinic crystals	0.57	167-170
F11	H	H	CF <sub>3</sub>	H	H	Br	85.7%	Monoclinic crystals	0.71	171-173

**Table 2.** Antibacterial activity (Zone of inhibition) of compounds F1–F11.

Flavones	Concentration (µg/ml)	Zone of inhibition (mm)		
		Gram-positive bacteria		Gram-negative bacteria
		<i>B. subtilis</i>	<i>S. aureus</i>	<i>P. aeruginosa</i>
<b>F1</b>	25	19.4±1.67	25.2±1.06	23.1±0.91
	50	23.6±2.13	29.8±0.81	25.4±1.33
	100	21.1±1.28	28.3±1.27	29.2±1.72
<b>F2</b>	25	13.5±0.97	16.2±0.84	15.3±1.41
	50	15.3±1.71	16.8±1.27	16.1±2.08
	100	19.6±2.25	18.1±1.15	21.4±1.14
<b>F3</b>	25	18.0±1.67	20.3±1.31	21.1±1.47
	50	19.2±2.08	18.6±1.01	19.4±1.07
	100	21.4±1.27	19.1±2.17	23.8±1.31
<b>F4</b>	25	12.2±0.87	10.1±1.15	13.3±1.54
	50	15.8±1.19	13.5±1.52	18.1±1.73
	100	16.3±1.65	15.8±1.37	17.4±0.87
<b>F5</b>	25	10.6±1.07	6.0±1.48	7.1±2.13
	50	13.4±1.12	8.1±0.85	8.3±1.04
	100	14.7±1.89	8.4±1.14	8.8±1.26
<b>F6</b>	25	10.3±1.38	8.1±0.91	9.3±1.66
	50	13.5±1.25	10.3±1.12	11.0±0.83
	100	13.1±1.87	10.8±1.54	11.3±1.24
<b>F7</b>	25	13.2±1.09	12.3±1.76	13.1±0.88
	50	13.0±1.18	15.5±2.08	18.0±1.34
	100	17.1±1.05	17.3±1.43	16.2±1.02
<b>F8</b>	25	9.7±1.31	5.4±3.04	5.2±1.07
	50	12.5±1.14	7.1±2.14	6.3±1.51
	100	14.8±1.07	7.7±1.87	6.4±1.25
<b>F9</b>	25	20.6±1.62	28.3±2.11	25.1±1.04
	50	23.2±0.74	31.1±1.33	26.4±0.79
	100	23.1±0.93	33.5±2.05	29.3±0.94
<b>F10</b>	25	15.3±1.61	22.4±0.87	19.2±1.17
	50	17.0±0.91	15.2±1.13	17.2±0.86
	100	18.4±1.18	23.8±1.25	21.8±1.21
<b>F11</b>	25	23.6±1.37	33.1±1.38	27.4±1.02
	50	25.3±0.74	35.0±1.15	29.2±1.14
	100	25.7±1.31	34.6±1.07	29.5±0.87
Ciprofloxacin		31±1.02	35±0.93	32±1.05
Ampicillin		29±0.87	38±1.15	33±0.96

All values are taken as mean±SEM (n=3)

The replacement of the methoxy group at ring A decreases the response in comparison to other trifluoromethyl groups at ring B in the flavone derivatives. The standard antibiotics ciprofloxacin and ampicillin showed a significant response on both Gram positive and Gram negative bacteria.

On the other hand, the simple flavone and the methyl containing flavones at ring B also showed significant response in comparison to other flavone derivatives. It is also worth mentioning that a resistance was observed by *S. aureus* and *P. aeruginosa* in some of the halogenated flavones that showed the ineffectiveness of these compounds. The order of response with respect to the zone of inhibition is **F11, F9, F10, F1, F3, F2, F4, F7, F6, F5, F8**.

Table 2 illustrates the minimum inhibitory concentrations MIC ( $\mu\text{g/ml}$ ) of the synthetic flavone derivatives against Gram positive and Gram negative bacteria. It is observed that flavone substituted at both rings (F11) possesses an inhibitory potential at low concentration against all tested bacteria which is reported to be 12.5, 6.25 and 6.25 ( $\mu\text{g/ml}$ ), respectively, that is almost equal to the response of the standard ciprofloxacin. This attested that the introduction of halogen and trifluoromethyl moiety enhances the potential in comparison with simple flavones and other derivatives. The MICs in  $\mu\text{g/ml}$  of the tested flavones derivatives are given in Table 3.

The plants have an unlimited capability to produce aromatic substances. Generally, these aromatic compounds are phenols or oxygen-substituted molecules that naturally serve as a defensive tool against attacks by insects, herbivores and microorganisms [30]. An in-depth literature survey reported the significance of natural and synthetic flavonoid derivatives as regards antibacterial activity [31–35]. In the present study, the antibacterial activities of synthetic flavone derivatives were compared with respect to zone of inhibition and minimum inhibitory concentration (MIC) values. From the results it is evident that there is a significant co-relationship between the presence of functional groups and the antibacterial response of the compounds. The present study illustrates an effort to predict the SAR of flavone derivatives with good activity against Gram-positive and Gram-negative bacteria.

Based upon the findings of this study, it can be concluded that the presence of a halogen group at ring A and a trifluoromethyl group at ring B produces flavones (**F9, F10 and F11**) with potent activity.

Apart from simple flavone (**F1**), addition of methyl and dimethylamino groups at ring B (**F3 and F2**) also showed promising results against all bacteria. On the other hand, halogenated substituted flavones at ring B (**F4–F8**) showed almost minimum activity.

**Table 3.** Antibacterial activity (minimum inhibitory concentration) of compounds F1–F11.

Flavone	MIC ( $\mu\text{g/ml}$ )		
	Gram-positive bacteria		Gram-negative bacteria
	<i>B.subtilis</i>	<i>S.aureus</i>	<i>P.aeruginosa</i>
<b>F1</b>	25	37.5	25
<b>F2</b>	75	75	62.5
<b>F3</b>	62.5	50	50
<b>F4</b>	87.5	87.5	100
<b>F5</b>	100	100	100
<b>F6</b>	125	125	100
<b>F7</b>	75	87.5	87.5
<b>F8</b>	>125	>125	>125
<b>F9</b>	12.5	25	25
<b>F10</b>	50	50	37.5
<b>F11</b>	12.5	6.25	6.25
<b>Ciprofloxacin</b>	6.25	6.25	6.25

Several antibacterial mechanisms of action have been assigned to flavonoids.

Among those, the possible mechanisms of action are inhibition of nucleic acid synthesis by inhibition of the enzymes topoisomerase and DNA gyrase; causing pores in the membrane or reduction in fluidity; damage of the cytoplasmic membrane, inhibition of the cellular metabolism, resulting from the inhibition of the enzyme NADH-cytochrome C reductase; inhibition of cell membrane synthesis; inhibition of cell wall synthesis caused by D-alanine/D-alanine ligase inhibition and aggregation of bacterial cells [36-39].

## CONCLUSIONS

Researchers are constantly designing and synthesizing new anti-infective molecules

worldover. The dilemma of resistance to these agents is on the rise and there is a dire necessity for the discovery of new agents with antibiotic activity against the resistant bacterial strains. The present study is an effort to assess flavone derivatives as potential drug candidates for antibacterial activity. The SAR study of flavone derivatives with antibacterial potentials revealed a correlation between the presence of additional functional groups at different positions of the flavone ring A and B structure and the antibacterial activity. Of the compounds included in this study, **F9**, **F10** and **F11** were found to be the most active compounds. Thus, these three compounds can act as future potential candidates to develop newer synthetic antibacterial agents. These new molecules can either be used alone or in combination with other antibiotics to combat infections and would reduce the effective dose to be administered.

**Acknowledgements:** We are thankful to the Department of Pharmacy, University of Malakand Khyber Pakhtunkhwa Pakistan for Provision of laboratory facilities.

#### REFERENCES:

1. B. Ocelik, M. Kartal, & I. Orhan. *Pharmaceutical Biology*, **49**, 396 (2011).
2. M. W. Iwu, A. R. Duncan, C. O. Okunji. New antimicrobials of plant origin. In: Perspectives on new crops and new uses J. Jannick (ed). ASHS Press; 1999, p. 457.
3. P.M. Shah. *Clin. Microbiol. Infect.* **11**, 36 (2005).
4. K. Poole. *J. Pharm. Pharmacol.* **53**, 283 (2001).
5. B. Havsteen. *Biochem. Pharmacol.* **32**, 1141 (1983).
6. M. Kawai, T. Hirano, S. Higa, J. Arimitsu, M. Maruta, Y. Kuwahara, T. Ohkawara, K. Hagihara, T. Yamadori, Y. Shima, A. Ogata, I. Kawase, & T. Tanaka. *Allergol. Int.* **56**, 113 (2007).
7. A.G. Lafuente, E. Guillamon, A. Villares, M.A. Rostagno, & J.A. Martinez. *Inflamm. Res.*, **58**, 537 (2009).
8. J. Johari, A. Kianmehr, M. R. Mustafa, S. Abubakar, & K. Zandi. *Int. J. Mol. Sci.* **13**, 16785 (2012).
9. M.R. Peluso. *Exp. Biol. Med.* , **231**, 1287 (2006).
10. K.Y. Park, G.O. Jung, K.T. Lee, M.Y. Choi, G.T. Kim, H.J. Jung, & H.J. Park. *J. Ethnopharmacol.*, **90**, 73 (2004).
11. C. Kanaswami, L.T. Lee, P.P. Lee, J.J. Hwang, F.C. Ke, Y.T. Huang, & M.T. Lee. *In Vivo*, **19**, 895 (2005).
12. M. Jung, M. Park, H.C. Lee, Y.H. Kang, E.S. Kang, & S.K. Kim. *Curr. Med. Chem.*, **13**, 1203 (2006).
13. P. Batra, & A. K. Sharma. *Biotech.* **3**, 439 (2013).
14. H. Oh, D.H. Kim, J.H. Cho, & Y.C. Kim. *J. Ethnopharmacol.*, **95**, 421 (2004).
15. C. Proestos, I.S. Boziaris, J.E. Nychas, & M. Komaitis. *Food Chem.*, **95**, 664 (2006).
16. D.I. Batovska, & I.T. Todorova, *Curr. Clin. Pharmacol.*, **05**, 01 (2010).
17. G. Casano, A. Dumetre, C. Pannecouque, S. Hutter, N. Azas, & M. Robin. *Bioorg. Med. Chem.*, **18**, 6012 (2010).
18. H. L. Liu, W.B. Jiang, & M.X. Xie. *Anticancer Drug Discov.*, **5**, 152 (2010).
19. V.H.E Susanti, S. Matsjeh, T.D. Wahyuningsih, Mustofa & T. Redjeki. *Indo. J Chem*, **12**, 146 (2012).
20. M. Shoaib, S. W. A. Shah, N. Ali, I. Shah, M. N. Umar, Shafiullah, M. Ayaz, M. N. Tahir, S. Akthar. *Journal of Chemistry*, **2015**, 1 (2015).
21. K. Donghee, H. Kyungrok & H. Sungwoo. (2012). *Org. Biomol. Chem.*, **10**, 7305 (2012).
22. Z. Jie, Z. Yufen & F. Hua. *Angew. Chem. Int. Ed.*, **50**, 3769 (2011).
23. L. Klier, T. Bresser, T. A. Nigst, K. Karaghiosoff, P. Knochel, *J. Am. Chem. Soc.*, **134**, 13584, (2012).
24. D. Zhao, B. Beiring, F. Glorius, *Angew. Chem. Int. Ed.*, **52**, 8454, (2013).
25. S.B.A. Ghani, P.J. Mugisha, J.C. Wilcox, E.A.M. Gado, E.O. Medu, A.J. Lamb, & R.C.D. Brown, *Synth. Commun.*, **43**, 1549 (2013).
26. P. O. Olutiola, O. Famurewa, H.G. Sonntag, An Introduction to General Microbiology—A Practical Approach, 2nd edition, Bolabay publication, Nigeria, 1991, p. 112.
27. J. G. Colle, J. P. Duguid, A. G. Fraser, B. P. Marmion, Laboratory strategies in diagnosis. in Practical Medical Microbiology, T.J. Mackie, J.E. MacCartney (eds), Churchill Livingstone, London 1989, p. 601.
28. F. Mujeeb, P. Bajpai, & N Pathak. *Biomed. Res. Int.*, **2014**, 1 (2014).
29. A. Husain, M. Rashid, R. Mishra & D. Kumar. *Acta Pol. Pharm.*, **70**, 443 (2013).
30. T. Arif, J.D. Bhosalea, N. Kumara, T.K. Mandala, R.S. Bendreb, G.S. Lavekara, & R. Dabura. *J. Asian Nat. Prod. Res.*, **11**, 621 (2009).
31. J.C. Chukwujekwu, F.R.V. Heerden FR & J.V. Staden. *Phytother. Res.*, **25**, 46 (2011).
32. J.M. Favela-Hernandez, A. Garcia, E. Garza-Gonzalez, V.M. Rivas-Galindo, & J.M. Camacho-Corona. *Phytother. Res.*, **26**(12), 1957 (1960).
33. A.P. Mukne, V. Viswanathan, & A.G. Phadatare. *Pharmacogn. Rev*, **5**, 13 (2011).
34. M. Tomczyk, A. Wiater, M. Pleszczynska. *Phytother. Res.*, **25**, 343 (2011).
35. A. Baldisserotto, S. Vertuani, A. Bino, D. De Lucia, I. Lampronti, R. Milani, R. Gambari, S. Manfredini. *Bioorg. Med. Chem.*, **23**, 264 (2015).
36. T.P. Cushnie, A.J. Lamb. *Int. J. Antimicrob. Agents*, **27**, 181 (2006).
37. T.P. Cushnie, A.J. Lamb. *Int. J. Antimicrob. Agents*, **38**, 99 (2011).
38. N.C. Gordon & D.W. Wareham, *Int. J. Antimicrob. Agents*, **36**, 129 (2010).
39. D. Wu, Y. Kong, C. Han, J. Chen, L Hu, H. Jiang, & X. Shen, *Int. J. Antimicrob. Agents*, **32**, 421 (2008).



## СИНТЕТИЧНИ ФЛАВОНОВИ ПРОИЗВОДНИ. АНТИБАКТЕРИАЛНИ СВОЙСТВА И ВРЪЗКА МЕЖДУ АКТИВНОСТ И СТРУКТУРА

М. Шоахиб<sup>1</sup>, С.У.А. Шах<sup>1\*</sup>, Н. Али<sup>2</sup>, И. Шах<sup>1</sup>, М.Н. Умар<sup>3</sup>, Шафиула<sup>1</sup>, М.Н. Тахр<sup>4</sup>, М. Гиас<sup>1</sup>

<sup>1</sup>Департамент по фармация, Университет в Малаканд, Чакдара 18550 Дир Лоуер, Кхибер Пактункуа, Пакистан

<sup>2</sup>Департамент по фармакология, Институт по базови медицински науки, Кхибер Медицински Университет, Пешавар 25000, Кхибер Пактункуа, Пакистан

<sup>3</sup>Департамент по химия, Университет в Малаканд, Чакдара 18550 Дир Лоуер, Кхибер Пактункуа, Пакистан<sup>4</sup>  
Департамент по физика, Университет Саргодха 40100 Пунджаб, Пистан

Постъпила на 4 септември 2015 г.; приета на 16 декември 2015 г.

(Резюме)

Синтезирани са с висок добив биологично активни флавонови производни с антибактериален потенциал от кетони с различни алдехиди чрез кондензация на Claisen-Schmidt. Структурите им са установени чрез различни спектроскопски методи: <sup>1</sup>H ЯМР, <sup>13</sup>C ЯМР, ИЧ и елементарен анализ. Резултатите показват, че някои от заместените флавонови производни проявяват по-висока антибактериална активност от простите флавонови производни по отношение на тяхната минимална концентрация на инхибиране (МИС) и са потенциални кандидати за лечението на широк спектър от инфекциозни заболявания.

## Interaction studies of DNA binding with a new Cu(II) complex by spectrophotometric, spectrofluorometric, voltammetric and circular dichroism techniques

M. Bordbar<sup>1,\*</sup>, F. Khodaie<sup>2</sup>, M. Tabatabaee<sup>2</sup>, A. Yeganeh-Faal<sup>3</sup>, Z. Mehri lighvan<sup>4</sup>, S. Mohammad-Ganji<sup>5</sup>

<sup>1</sup>Department of Chemistry, Faculty of Science, University of Qom, Qom 37185-359, Iran.

<sup>2</sup> Department of Chemistry, Yazd Branch, Islamic Azad University, Yazd, Iran.

<sup>3</sup>Department of Chemistry, Faculty of Science, Payame Noor University, Tehran, Iran.

<sup>4</sup>Young Researchers and Elites Club, Department of Chemistry, Isfahan University of Technology, Isfahan, 84156/8311

<sup>5</sup>National Institute for Genetic Engineering & Biotechnology (NIGEB), P. O. Box: 14965-161 Tehran, Iran.

Received September 14, 2015, Accepted March 28, 2016

The binding ability of the water-soluble copper(II) complex with pyridine-2,6-dicarboxylate (pydc<sup>2-</sup>) and 2-aminopyrimidine (amp) with the formula [Cu(pydc)(amp)].2H<sub>2</sub>O.H<sub>2</sub>O (**1**) to calf thymus DNA (CT-DNA) was investigated. The binding ability of **1** was studied by measuring the effects on the electronic absorption spectra, thermal denaturation studies, fluorescence quenching studies using methylene blue (MB) as a fluorescent probe and circular dichroism (CD) spectra. All results suggest that the interaction mode between (**1**) and DNA takes place by intercalation with a binding constant of  $(9.51 \pm 0.2) \times 10^4 \text{ M}^{-1}$ .

**Keywords:** Intercalative Interaction, CT-DNA, Methylene Blue, Mixed Nitrogen Donor Ligands, Cu (II) Complex.

### INTRODUCTION

Cis-platine is one of the widely utilized antitumor drugs [1]. In order to decrease the toxicity of this kind of platinum complexes, many kinds of amine-substituted compounds are employed in the research of antitumor agents [2-4]. Some natural products have been used as amine-substituted ligands in this research [5], such as D-glucosamine [6], chitosan [7] and their derivatives. These are non-toxic towards the human body and the amino group in the chain has special activity. However, one disadvantage of normal chitosan is its low solubility in water. Recently there has been considerable interest in the binding of small water-soluble molecules to DNA [8]. Investigations of the interaction between small molecules and DNA are basic works in the design of new types of pharmaceutical molecules. A small molecule which can interact with DNA can be assigned to several categories: metal ions and metal complexes, such as metal bipyridyl complex [9] and metal phenanthroline complex [10]; heavy metals which cause damage of DNA, such as chromium [11], antibiotics, organic dyes and organic pesticides [12], protein molecules and nanoparticle markers [13]. Studies of the interaction between transition

metal complexes and DNA have been pursued in recent years [14]. Metal complexes are known to bind to DNA *via* both covalent and non-covalent interactions. In covalent binding, the labile ligands of the complexes are replaced by a nitrogen base of DNA such as guanine N7. On the other hand, non-covalent DNA interactions include intercalative, electrostatic and groove (surface) binding of cationic metal complexes both outside the DNA helix, and along major or minor grooves. Among these interactions, intercalation is one of the most important DNA binding modes, as it invariably leads to cellular degradation and is an enthalpically driven process resulting from the insertion of a planar aromatic ring system between ds-DNA base pairs with concomitant unwinding and lengthening of the DNA helix [15]. Copper is a cofactor essential for the tumor angiogenesis processes [16]. Among the metal complexes, copper (II) complexes containing heterocyclic bases have been developed as a result of their diverse applications following the discovery of the “chemical nuclease” activity of the [Cu(phen)<sub>2</sub>]<sup>2+</sup> complex [17]. Furthermore, copper complexes have shown strong interactions with DNA *via* surface associations or intercalation [18]. The factors that may affect their association with DNA include their size, the type of ligands, the presence and the position of small lipophilic groups. On the other hand, copper complexes having strong association with DNA are also capable of inducing a hydrolytic cleavage [19], as

\* To whom all correspondence should be sent:  
E-mail: m.bordbare@gmail.com

several copper-based synthetic nucleases have been reported [20]. Their importance is due to their capacity to cleave DNA *via* oxidative mechanisms resulting from copper's ability to adopt different oxidation states.

In this work, the Cu (II) complex of 2-aminopyrimidine (amp) and pyridine-2,6-dicarboxylate (pydc) (**1**) was synthesized [21]. Interactions of this complex with calf thymus DNA (CT-DNA) were studied by UV-Vis, fluorescence using MB as a fluorescence probe [22], depressing emission quenching of this complex by  $K_4[Fe(CN)_6]$  in presence of DNA [23], circular dichroism spectroscopic methods and cyclic voltammetry (CV) measurements in order to gain a better understanding of the binding mechanism of this complex [24].

## EXPERIMENTAL

### Reagents

The reagents and chemicals were purchased from commercial sources and used as received without further purification. Calf thymus DNA (CT-DNA) was obtained from Sigma. The stock solution of CT-DNA gave a ratio of UV absorbance at 260 and 280 nm ( $A_{260}/A_{280}$ ) of 1.89 to check DNA purity and making sure that the DNA was sufficiently free from protein contamination [25]. The DNA concentration was determined by UV absorbance ( $\epsilon = 6600 M^{-1} cm^{-1}$  at 260 nm) [26]. The stock solutions were stored at 4° C and used within 4 days. All experiments involving interaction of the complex with DNA were carried out in doubly distilled water buffer containing 5mM Tris-HCl [Tris(hydroxymethyl)-aminomethane] and 50 mM NaCl, adjusted to pH 7.3 with hydrochloric acid.

### Electronic Absorption Spectra

The UV-Vis spectra were recorded on a Varian Cary-100 UV-Vis spectrophotometer. Absorption titration experiments were conducted by fixing constant concentration of the complex at 783  $\mu M$  while varying the concentrations of CT-DNA or by fixing constant concentration of the (amino) and (pydc) ligands at 70  $\mu M$  while varying the concentration of Cu(II) metal cation ( $[Cu(II)]/[L]=0-5$ ). All experiments were conducted in a buffer containing 5 mM Tris-HCl (pH 7.3) and 50 mM NaCl. CT-DNA being an absorbing species in the absorption range of the complex, the titrations were carried out by adding the same amounts of CT-DNA solution to both reference and measuring cell to eliminate the absorbance of DNA itself.

### Fluorescence Spectra

The fluorescence spectra were recorded on a Varian Cary Eclipse spectrofluorometer. The complex at a fixed concentration (19.6  $\mu M$ ) was titrated by increasing amounts of CT-DNA. Excitation wavelength of the complex was 296 nm, scan speed = 100 nm/min, slit width 5/5 nm. All experiments were conducted in a buffer containing 5 mM Tris-HCl (pH 7.3) and 50 mM NaCl. The binding mode of the complex with CT-DNA was studied by using methylene blue (MB) as a fluorescence probe. Also, depressing the emission quenching of this complex by  $K_4[Fe(CN)_6]$  in the presence of DNA was studied.

### Circular Dichroism Measurements

Circular dichroism measurements were carried out on a Jasco-810 spectropolarimeter at room temperature. A rectangular quartz cell of 1 cm path length was used to obtain spectra from 320 to 220 nm with a scanning speed of 100 nm/min and a response time of 4 s. Each spectrum was accumulated at least three times and results were expressed as molar ellipticity (H). The optical chamber of the CD spectrometer was deoxygenated with dry nitrogen before use and kept in a nitrogen atmosphere during the experiments. Scans were accumulated and automatically averaged. CD spectrum was generated which represented the average of three scans from which the buffer background had been subtracted. In the CD spectrum the concentrations of CT-DNA and complex were 100 and 50  $\mu M$ , respectively.

### Thermal Denaturation Experiments

Thermal denaturation experiments were carried out on a Varian Cary-500 UV-Vis double beam spectrophotometer. The absorbance of 75  $\mu M$  DNA at 260 nm was monitored in the absence and presence of 37.5  $\mu M$  complex with temperature ranging from 55 to 100 °C.

### Cyclic Voltammetry Experiments

Cyclic voltammetry experiments were performed at room temperature with a conventional three-electrode electrochemical cell, using a Metrohm Autolab potentiostat/galvanostat. The three-electrode system used in this research consisted of a gold electrode as a working electrode, an Ag/AgCl reference electrode and a Pt foil auxiliary electrode. The solution was prepared by dissolving the complex in aqueous buffer containing 5 mM Tris-HCl (pH 7.3) and 50 mM NaCl.

### Viscometry Measurements

The viscosity was determined using a digital Brookfield circulating bath Ultra DV III viscometer maintained at  $25.0 \pm 0.1$  °C in a circulating water-bath. Data were analyzed as  $(\eta/\eta_0)^{1/3}$  versus the ratio of the concentration of (1) and DNA, where  $\eta$  is the viscosity of DNA in presence of the complex and  $\eta_0$  is the viscosity of DNA alone.

### Synthesis of the Complex

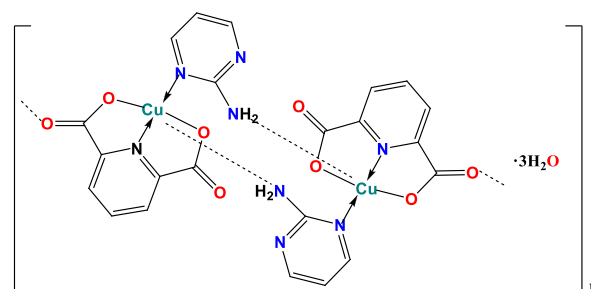
The copper complex was prepared as described by our group [27]. Pyridine-2,6-dicarboxylic acid (0.167 g, 1 mmol) was dissolved in 10 ml of deionized water containing 0.08 g (2 mmol) of NaOH and was stirred for 30 min at room temperature. An aqueous solution of 0.241 g (1 mmol) of  $\text{Cu}(\text{NO}_3)_2 \cdot 3\text{H}_2\text{O}$  and 0.095 g (1 mmol) of 2-aminopyrimidine was added to pyridine-2,6-dicarboxylic acid solution. The reaction mixture was placed in a Parr-Teflon lined stainless steel vessel, sealed and heated at 130°C for 4 h. Blue crystals of the complex were obtained upon slow cooling (yield 91%) [28].

## RESULTS AND DISCUSSION

### Characterization of the Complex

Recently, synthesis and characterization of  $\{[\text{Cu}(\text{pydc})(\text{amp})] \cdot 3\text{H}_2\text{O}\}_n$  by elemental analysis, IR spectroscopy, thermal analysis and X-ray diffraction studies have been reported by our group [28]. As reported in ref. [21], each Cu (II) ion is coordinated by an O,N,O-tridentate  $\text{pydc}^{2-}$  ligand (bound *via* pyridine nitrogen atom and two carboxylate oxygen atoms) and one heterocyclic nitrogen atom of the 2-aminopyrimidine ligand (Scheme 1). The same coordination mode was found for the nickel complex [29]. The six-coordination was completed by two water molecules in the nickel complex, while each metal ion in the copper complex is weakly connected to two neighboring ones, through two carboxylate bridging groups of dipicolinate and the amino-nitrogen of the  $\text{NH}_2$  group of 2-aminopyrimidine (Scheme 1).

The FTIR spectrum of the crystals shows broad strong bands in the region  $3275\text{--}3523\text{ cm}^{-1}$ , which could be related to the existence of  $\text{O}\text{--}\text{H}\cdots\text{O}$  hydrogen bonding between the water molecules. It must have been coupled by other indicative peaks such as N–H and O–H stretching frequencies and the stretching frequencies due to the aromatic rings which originally fall within this region.



**Scheme 1.** Structure of the Cu (II) mixed ligand complex

### Absorption Spectra

Electronic absorption spectroscopy is universally employed to examine the binding mode of DNA with metal complexes [30]. The absorption spectra of (1) in the absence and presence of CT-DNA are given in Fig.1. In the absence of DNA, the absorption spectrum of (1) has a strong  $\pi\text{--}\pi^*$  transition band at 268 nm. Increasing DNA concentration, the absorption band of the complex at 268 nm shows hypochromism of 85.5% and bathochromism of about 8 nm; at 220 nm it shows 51% hypochromism and bathochromism about 9 nm. These phenomena indicate that the complex probably interacts with CT-DNA by intercalation mode, involving strong  $\pi\text{--}\pi$ -stacking interactions between the aromatic rings of the complex and DNA base pairs.

The apparent binding constant,  $K_b$ , for the interaction between the complex and CT-DNA can be determined by analysis of the spectrophotometric titration data at room temperature using Eq. (1) [31].

$$[\text{DNA}]/(\epsilon_a - \epsilon_f) = [\text{DNA}](\epsilon_b - \epsilon_f) + 1/K_b(\epsilon_b - \epsilon_f)(1)$$

where  $[\text{DNA}]$ ,  $\epsilon_a$ ,  $\epsilon_f$  and  $\epsilon_b$  correspond to the total concentration of CT-DNA base-pair,  $A_{\text{obsd}}/[\text{Com}]$ , the extinction coefficient for the free complex and the extinction coefficient for the complex in the fully bound form, respectively. In the plot of  $[\text{DNA}]/(\epsilon_a - \epsilon_f)$  versus  $[\text{DNA}]$ ,  $K_b$  is given by the ratio of the slope to the intercept.

Until now, the binding constant reported in most papers has been calculated at a single wavelength since different parts of a compound do not have similar interaction with DNA. In this case, the absorption spectrum at different wavelengths is differently affected by this interaction and is expected to give different binding constants at different wavelengths. The calculated binding constants for DNA-(1) at some of the selected wavelengths are reported in Table 1. It can be inferred that different values for the binding constant are obtained at different wavelengths. It

seems that the comparative binding constant calculated at a single wavelength for the DNA-compound interaction may not be correct. This probably may be true if the binding constant is reckoned as an average of the binding constants at all wavelengths. Herein, we calculated the binding constant  $K_b$  for the DNA-(1) at all wavelengths in MATLAB and the mean result is  $9.51(\pm 0.2)\times 10^4$  L mol<sup>-1</sup>.

**Table 1.**  $K_b$  values at different wavelengths

Wave length (nm)	280	270	260	220	202
$K_b$ (M <sup>-1</sup> )	$5.46 \times 10^4$	$1.00 \times 10^5$	$3.21 \times 10^4$	$9.52 \times 10^5$	$4.34 \times 10^6$

The  $K_b$  value obtained for our copper(II) complex is considerably higher than those for any other known copper(II) complexes including complexes such as [Cu(phen)<sub>2</sub>Cl<sub>2</sub>] ( $K_b$ ,  $2.70 \times 10^3$  M<sup>-1</sup>) [32], [Cu(phen)(L-Thr)(H<sub>2</sub>O)]ClO<sub>4</sub> ( $K_b$ ,  $6.35 \times 10^3$  M<sup>-1</sup>) [33], [Cu(II) Schiff base complexes] ( $K_b$ ,  $3.20 \times 10^3$  and  $9.60 \times 10^3$  M<sup>-1</sup>) [34] [Cu(phen)(L-Gly)(H<sub>2</sub>O)] ( $K_b$ ,  $4.68 \times 10^3$  M<sup>-1</sup>) [35]

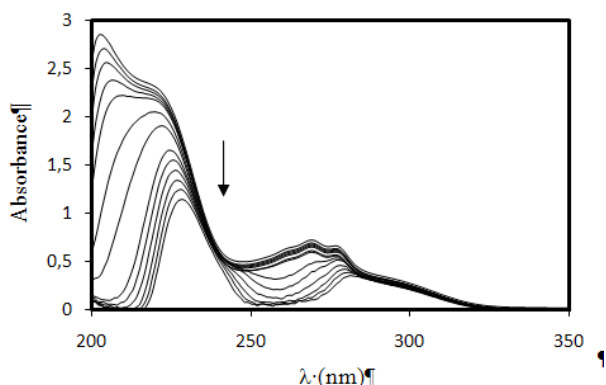


**Fig. 1.** UV-Vis absorption spectra of the complex (70 μM) in the presence of increasing amounts of CT-DNA; [DNA]=(0-950) μM The arrow shows the changes upon increasing the amount of CT-DNA.

### Fluorescence Spectra

The complex showed fluorescence emission in Tris buffer at room temperature, with a maximum at about 363 nm. As shown in Fig. 2, the fluorescence intensity of the complex was steadily quenched with the increasing concentration of CT-DNA.

The interaction mode of the complex binding to DNA can be determined according to the classical Stern-Volmer equation [36]:

$$F_0/F = 1 + K_q [Q] \quad (2)$$

where  $F_0$  and  $F$  represent the emission intensity in the absence and presence of quencher, respectively,  $K_q$  is a linear Stern-Volmer quenching constant and

$[Q]$  is the quencher concentration. The Stern-Volmer quenching plots from the fluorescence titration data are shown in the inset of Fig. 2.

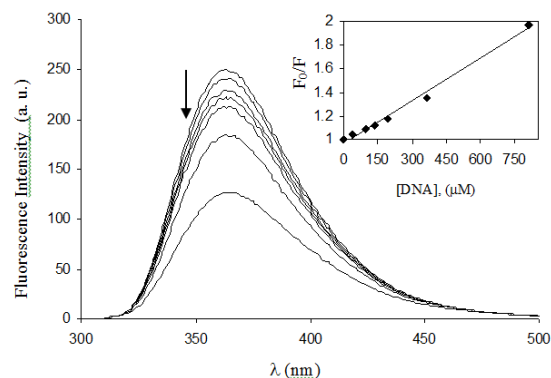


**Fig. 2.** Emission spectra of the complex (a) in Tris-HCl buffer upon addition of CT-DNA. [Complex]= 20 μM, [DNA]= (0-809) μM. Arrow shows the intensity change upon increasing CT-DNA concentration. The inset is a Stern-Volmer quenching plot of (1) with increasing concentrations of CT-DNA.

The fluorescence quenching constant ( $K_q$ ) evaluated using the Stern-Volmer equation is  $1.12 \times 10^3$  M<sup>-1</sup>. When the Stern-Volmer plot is linear, it indicates that only one type of quenching process occurs and the obtained linear relationship could be applied to determine DNA. This phenomenon of the quenching of luminescence of the complex by CT-DNA may be attributed to the photoelectron transfer from the guanine base of DNA to the excited metal-to-ligand charge-transfer (MLCT) state of the complex [37].

### DNA-MB Displacements

Further support for the binding of the complexes to DNA by intercalation mode was given by the competitive binding experiment. MB has long been used as a planar dye molecule for biological straining and diagnosis of diseases including carcinoma [38]. The interaction of methylene blue with DNA has been studied with various methods [39]. Most studies indicated that (at low ionic strength buffer and low concentration of DNA) the major binding mode of MB with DNA was through intercalation. The experiment involves the addition of the present complex CT-DNA pretreated with MB as a fluorescence probe ([DNA]/[MB]=10) and the measurement of emission intensities of DNA-bound MB. Interestingly, the emission intensity of MB is quenched on adding CT-DNA. This emission quenching phenomenon reflects the change in the excited state structure in consequence of the electronic interaction in the MB-DNA complex [40], expected from the strong stacking interaction (intercalation) between the adjacent

DNA base pairs. The emission spectra of the MB–DNA solutions in the presence of increasing amounts of (1) is shown in Fig. 3, which clearly reveals a gradual increase in the fluorescence intensity of the probe molecule (MB) by adding (1). The increase in fluorescence intensity is due to the release of free MB molecules from the DNA–MB complex. Therefore, the formation of metal complex–DNA prevents the binding of MB. The complete metal complex–DNA formation occurs when the probe fluorescence intensity is sufficiently close to the corresponding pure MB fluorescence intensity. Complete recovery of MB fluorescence intensity is indicative of an intercalative mode of binding, but in this experiment, the recovery of MB was 6% in  $[\text{complex}]/[\text{DNA}]=3$  and 37% in  $[\text{complex}]/[\text{DNA}]=92$ , which confirms that the intercalative binding strength of the Cu (II) complex to DNA is weaker than to MB.

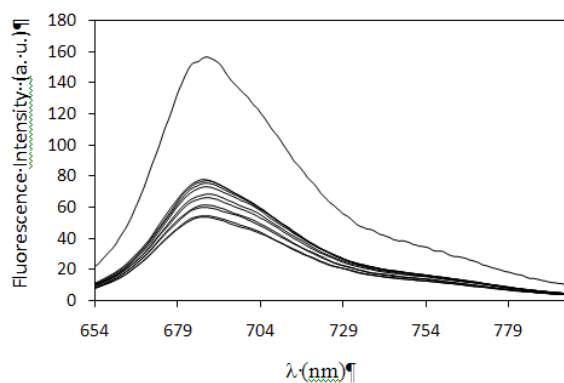


**Fig. 3.** Emission spectra of the competitive reaction between Cu (II) complex and methylene blue with DNA.  $C_{\text{complex}} = 0.0, 144.0, 283.0, 420.0, 550.0, 680.0, 1048.0, 1765.0, 2080.0,$  and  $3129.0 \mu\text{M}$ ,  $C_{\text{MB}} = 5 \mu\text{M}$  and  $C_{\text{DNA}} = 50 \mu\text{M}$  in Tris–HCl buffer (5 mM, pH 7.3) plus 50 mM NaCl.

#### Emission Quenching Titration with $K_4\text{Fe}(\text{CN})_6$

In aqueous solution, iodide and ferrocyanide anions quench the fluorescence of (1) very efficiently, so we used potassium ferrocyanide as the quencher to determine the relative accessibilities of the free and bound (1). The highly negatively charged quencher is repelled away from the negatively charged phosphate backbone of DNA, the bound copper cation should be protected from anionic quenchers, while the emission from free complexes should be readily quenched by an anionic quencher. Fig. 4 shows the linear Stern–Volmer plots with ferrocyanide anion as a quencher for (1), at  $[\text{DNA}]/[\text{Complex}] = 0$  or  $40$ , as expected for a single-component donor–acceptor system.

As illustrated in Fig. 4, the emission of (1) in the presence of DNA is difficult to be quenched. This

may be explained by the fact that the bound cations of the complex are protected from the anionic water-bound quencher by the array of negative charges along the DNA phosphate backbone [41]. The obtained quenching constants were  $3.5$  and  $2.1 \text{ M}^{-1}$  with and without CT-DNA, respectively. The quenching of (1) was in fact enhanced by a factor of  $1.6$  when (1) was bound to the DNA helix.

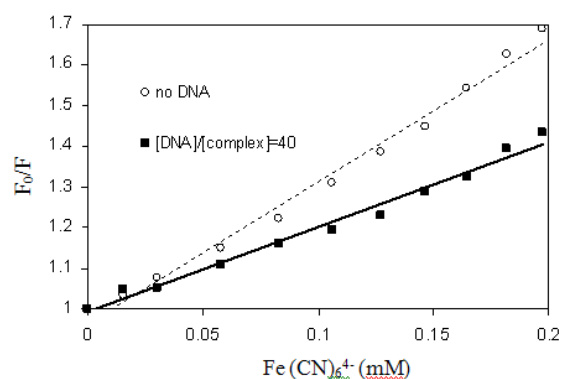


**Fig. 4.** Emission quenching with  $\text{Fe}(\text{CN})_6^{4-}$  for free and DNA-bound (1).

#### CD Spectroscopy

Circular-dichroism (CD) studies were conducted to determine the extent of change in conformation of DNA upon complexation. CD spectral variations of CT-DNA were recorded by addition of the complex to CT-DNA. The CD spectrum of CT-DNA consists of a positive band at  $277 \text{ nm}$  due to base stacking and a negative band at  $248 \text{ nm}$  due to helicity, which is characteristic of DNA in the right-hand B form and is quite sensitive to the mode of DNA interactions with small molecules [24]. Thus simple groove binding and electrostatic interaction of small molecules show less or no perturbation on the base stacking and helicity bands, while intercalation enhances the intensities of both bands, stabilizing the right-hand B conformation of CT-DNA as observed for the classical intercalator methylene blue [42]. Fig. 5 shows the CD spectra of CT-DNA which was added to the complex. In these CD data the intensities of both negative and positive bands decreased significantly similar to that induced by the other Cu (II) complex [43]. This alteration suggests that the DNA binding of the complex induces certain conformational changes, such as the conversion from a more B-like to a more Z-like structure within the DNA molecule [44]. In addition, (1) binds DNA mainly by intercalation mode and indicates an unwinding of the DNA helix upon complex formation and loss of helicity [45].

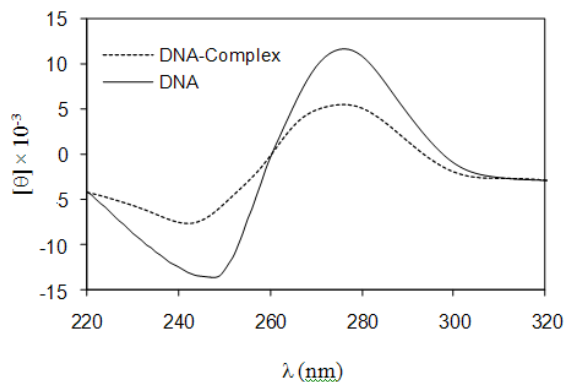


**Fig. 5.** Circular dichroism spectra of DNA (50  $\mu\text{M}$ ) in Tris-HCl (5 mM) in the presence of increasing amounts of copper complex (100  $\mu\text{M}$ ).

#### Thermal Denaturation Studies

Thermal denaturation studies of CT-DNA with the complex provide evidence for the ability of the complex to stabilize the double-stranded DNA [46]. It is well-accepted that when the temperature of the solution increases, the double-stranded DNA gradually dissociates to single strands, generating a hyperchromic effect in the absorption spectra of the DNA bases ( $\lambda_{\text{max}} = 260 \text{ nm}$ ). So the transition temperature of double strands to single strands can be determined by monitoring the absorbance of the DNA bases at 260 nm as a function of temperature [26]. According to the previous reports [47], intercalation normally facilitates base stacking in DNA and increases the melting temperature  $T_m$  of DNA.

The effect of **(1)** on the melting temperature ( $T_m$ ) of CT-DNA in the buffer is shown in Fig. 6. In this experiment, the  $T_m$  of CT-DNA alone was 81.62  $^{\circ}\text{C}$ . After adding the complex,  $\Delta T_m$  increased by 3.95  $^{\circ}\text{C}$  for the mole ratio of  $[\text{Cu}]/[\text{DNA}] = 0.5$ . It has been reported that  $\Delta T_m$  for metallointercalators ( $>10 \text{ }^{\circ}\text{C}$ ) [48] and the organic intercalator EB (13  $^{\circ}\text{C}$ ) [49] were higher than for this complex. These results indicated that the binding strength between the complex and DNA was only moderate [46]. The observed small change in the  $T_m$  of CT-DNA in the presence of **(1)** suggests that the dominating interaction of this complex with DNA is intercalative binding [50, 51].

#### DNA-Binding Study with Cyclic Voltammetry

The application of cyclic voltammetry (CV) to the study of the binding of metal complexes to DNA provides a useful complement to the above methods of investigation [12, 52].

Typical cyclic voltammetric (CV) behavior of 48  $\mu\text{M}$  **(1)** in the absence and presence of CT-DNA

is shown in Fig. 7. The cyclic voltammogram of **(1)** in the absence of DNA (Fig. 7A) featured reduction of 2+ to the 1+ form at a cathodic peak potential,  $E_{\text{PC}}$  of -0.57 V versus SCE.

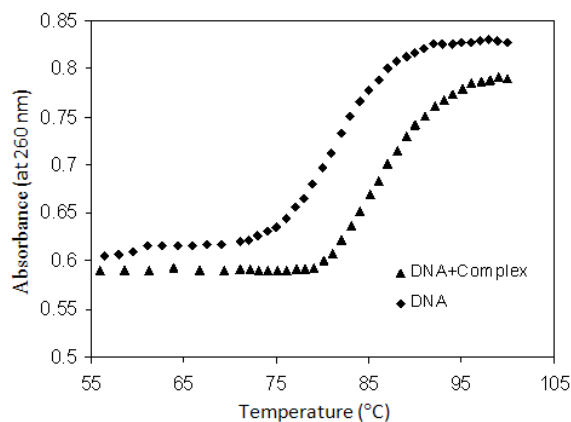


**Fig. 6.** Plots of the changes of absorbance at 260 nm of CT-DNA on heating in the absence and presence of the complex.  $C_{\text{DNA}} = 75 \mu\text{M}$  and  $C_{\text{complex}} = 37.5 \mu\text{M}$  in 50 mM Tris-HCl with 50 mM NaCl.

Reoxidation of 1+ occurred upon scan reversal, at 0.18 V. The separation of the anodic and cathodic peak potentials,  $\Delta E_p = 255 \text{ mV}$ , indicated an irreversible redox process. The formal potential  $E^0$  (or voltammetric  $E_{1/2}$ ), taken as the average of  $E_{\text{PC}}$  and  $E_{\text{PA}}$  is -195 mV, in the absence of DNA. The presence of DNA in the solution at the same concentration of **(1)** causes a decrease in the voltammetric current coupled with a slight shift in the  $E_{\text{PC}}$  (-0.59 V),  $E_{\text{PA}}$  (0.22 V) versus SCE and  $E_{1/2}$  ( $E_{1/2} = -185 \text{ mV}$ ) to a less negative potential (Fig. 7B). The drop of the voltammetric currents in the presence of CT-DNA can be attributed to diffusion of the metal complex bound to the large, slowly diffusing DNA molecule.

#### Viscosity Study

Intercalation and groove binding modes can be distinguished by using hydrodynamic methods such as viscosity, flow dichroism measurements, and NMR [53, 54]. Intercalation of the molecules to the DNA resulted in unwinding and lengthening of the DNA. This DNA elongation causes the viscosity of the solution to increase.

The effect of **(1)** on the viscosity of DNA at  $25.0 \pm 0.1 \text{ }^{\circ}\text{C}$  is shown in Fig. 8. It can be observed that the viscosity of DNA increases with increasing amounts of **(1)**. Such behavior is in accordance with that of other intercalators, which increase the relative specific viscosity for the lengthening of the DNA double helix resulting from intercalation. This result indicates that **(1)** can intercalate between

adjacent DNA base pairs, causing an extension in the helix, and thus increases the viscosity of DNA.

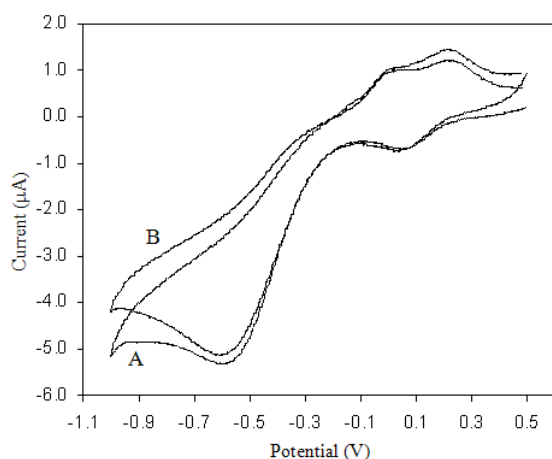


**Fig. 7.** Cyclic voltammograms of (1) in the absence (A) and presence (B) of DNA in 50 mM NaCl, 5 mM Tris, pH 7.3. [Cu]=122 µM, [DNA]/[Cu]=1, Scan rate, 50 mVs<sup>-1</sup>.

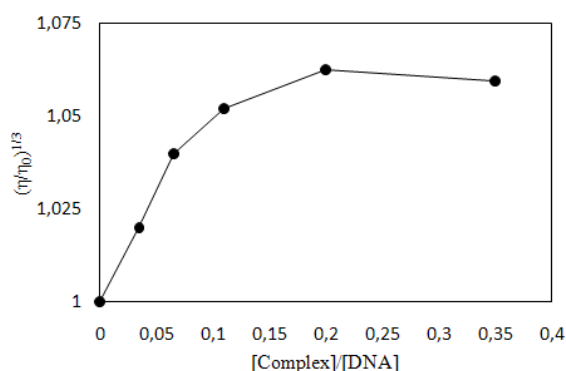


**Fig. 8.** Effect of increasing amount of (1) on the relative viscosity of CT-DNA at 25 ± 0.1 °C, [DNA]= 50 µM, pH 7.3.

## CONCLUSIONS

It is clear that transition metal complexes offer a great potential as structure-selective binding agents for nucleic acids.

In this work the interaction between (1) and calf thymus DNA was investigated using UV, fluorescence and CD spectroscopy, cyclic voltammetry and viscosity measurements. The experimental results indicate that (1) could bind to DNA molecules mainly by intercalative mode, which correlates well with the extended aromatic ring system present in the ligand.

UV-Visible spectroscopy enabled us to find the Cu complex/DNA binding constant. The  $K_b$  of this complex is  $9.51 (\pm 0.2) \times 10^4 \text{ M}^{-1}$ . The existence of hypochromicity, large red shift in the (1) spectra suggests an intercalation binding mode. Increase in DNA viscosity during its interaction with (1) is

consistent with lengthening of DNA due to intercalation. Today many researchers focus their attention on the bioactivity of Cu(II) complexes. So further studies on anticancer activities of the complex are in progress, because non-covalent binding is reversible and is typically preferred over covalent adduct formation, keeping in mind the drug metabolism and toxic side effects.

## REFERENCES

1. E. Wong, C.M. Giandomenico, *Chem. Rev.*, **99**, 2451 (1999).
2. R.N. Bose, K. Allen, M. Wangner, E. Volckova, D.W. Li, R.T. Heath, *Inorganica Chimica Acta*, **300-302**, 937 (2000).
3. I. Haiduc, C. Silvestru, *Coord. Chem. Rev.*, **124**, 55 (1986).
4. D. Kovala-Demertzi, P.N. Yadava, D.M. A., C. M., *J. Inorg. Biochem.*, **78**, 347 (2000).
5. S.A.W. Gruner, E. Locardi, E. Lohof, H. Kessler, *Chem. Rev.*, **102**, 491 (2002).
6. G. Micera, S. Deiana, A. Dessi, P. Decock, B. Dubois, H. Kozłowski, *Inorg. Chim. Acta*, **107**, 45 (1985).
7. X. Fei Liu, Y. Lin Guan, D. Zhi Yang, Z. Li, K. De Yao, *J. Appl. Polym. Sci.*, **79**, 1324 (2001).
8. M. Asadi, E. Safaei, B. Ranjbar, L. Hasani, *J. Mol. Struct.*, **754**, 116 (2005).
9. Z.S. Yang, Y.L. Wang, Y.Z. Zhang, *Electrochem. Commun.*, **6**, 158 (2004).
10. M. Carter, A. Bard, *J. Am. Chem. Soc.*, **109**, 7528 (1987).
11. S. Kawanishi, S. Inoue, S. Sano, *J. Biol. Chem.*, **261**, 5952 (1986).
12. Y.F. Li, C.Z. Huang, X.H. Huang, M. Li, *Anal. Chim. Acta*, **429**, 311 (2001).
13. J. Wang, D. Xu, A.N. Kawde, R. Polsky, *Anal. Chem.*, **73**, 5576 (2001).
14. A. Dimitrakopoulou, C. Dendrinou-Samara, A. Pantazaki, M. Alexiou, E. Nordlander, D. Kessissoglou, *J. Inorg. Biochem.*, **102**, 618 (2008).
15. A.M. Pyle, J.P. Rehmann, R. Meshoyrer, C.V. Kumar, N.J. Turro, J.K. Barton, *J. Am. Chem. Soc.*, **111**, 3051 (1989).
16. X. Zhang, C. Bi, Y. Fan, Q. Cui, D. Chen, Y. Xiao, Q.P. Dou, *Int. J. Mol. Med.*, **22**, 677 (2008).
17. A. Spassky, D.S. Sigman, *Biochemistry*, **24**, 8050 (1985).
18. D.K. Chand, H.-J. Schneider, A. Bencini, A. Bianchi, C. Giorgi, S. Ciattini, B. Valtancoli, *Chem. A Eur. J.*, **6**, 4001 (2000).
19. B.K. Santra, P.A.N. Reddy, G. Neelakanta, S. Mahadevan, M. Nethaji, A.R. Chakravarty, *J. Inorg. Biochem.*, **89**, 191 (2002).
20. M. Lainé, F. Richard, E. Tarnaud, C. Bied-Charretton, C. Verehère-Béaur, *J. Biol. Inorg. Chem.*, **9**, 550 (2004).
21. M. Tabatabaee, *Chem. Cent. J.*, **6:5**, (2012).
22. Z. Hu, C. Tong, *Anal. Chim. Acta*, **587**, 187 (2007).



23. J.Z. Wu, L. Yuan, *J. Inorg. Biochem.*, **98**, 41-45 (2004).
24. V.I. Ivanov, L.E. Minchenkova, A.K. Schyolkina, A.I. Poletayev, *Biopolymers*, **12**, 89 (1973).
25. S. Satyanarayana, J.C. Dabrowiak, J.B. Chaires, *Biochemistry*, **31**, 9319 (1992).
26. C.V. Kumar, E.H. Asuncion, *J. Am. Chem. Soc.*, **115**, 8547 (1993).
27. M. Tabatabaee, *Chem Cent J*, **6**, 5 (2012).
28. R.A. Nyquist, C.L. Putzig, R.O. Kagel, M.A. Leugers, *Infrared Spectra of Inorganic Compounds (3800-45cm<sup>-1</sup>)*, Academic press, 1971.
29. M. Tabatabaee, *Acta Crystallogr.*, **E66**, m647 (2010).
30. J.M. Kelly, M.J. Murphy, D.J. McConnell, C. Ohuigin, *Nucleic Acids Res.*, **13**, 167 (1985).
31. T. Meehan, H. Gamper, J.F. Becker, *J. Biol. Chem.*, **257**, 10479 (1982).
32. T. Gupta, S. Dhar, M. Nethaji, A.R. Chakravarty, *Dalton Trans.*, 1896 (2004).
33. S. Zhang, Y. Zhu, C. Tu, H. Wei, Z. Yang, L. Lin, J. Ding, J. Zhang, Z. Guo, *J. Inorg. Biochem.*, **98**, 2099 (2004).
34. S. Mathur, S. Tabassum, *Cent. Eur. J. Chem.*, **4**, 502 (2006).
35. S. Zhang, J. Zhou, *J. Coord. Chem.*, **61**, 2488 (2008).
36. M.R. Eftink, C.A. Ghiron, *Anal. Biochem.*, **114**, 199 (1981).
37. P.X. Xi, Z.H. Xu, X.H. Liu, F.J. Chen, L. Huang, Z.Z. Zeng, *Chem. Pharm. Bull.*, **56**, 541 (2008).
38. B. Meric, K. Kerman, D. Ozkan, P. Kara, S. Erensoy, U. Akarca, M. Mascini, M. Ozsoz, *Talanta*, **56**, 837 (2002).
39. B.S. Fujimoto, J.B. Clendenning, J.J. Delrow, P.J. Heath, M. Schurr, *J. Phys. Chem.*, **98**, 6633 (1994).
40. E. Long, J. Barton, *Acc. Chem. Res.*, **23**, 271 (1990).
41. J.K. Barton, J.M. Goldberg, C.V. Kumar, N.J. Turro, *J. Am. Chem. Soc.*, **108**, 2081 (1986).
42. B. Nordén, F. Tjerneld, *Biopolymers*, **21**, 1713 (1982).
43. S. Roy, R. Banerjee, M. Sarkar, *J. Inorg. Biochem.*, **100**, 1320 (2006).
44. A.D. Richards, A. Rodger, *Chem. Soc. Rev.*, **36**, 471 (2006).
45. K. Akdi, R.A. Vilaplana, S. Kamah, J.A.R. Navarro, J.M. Salas, F. Gonzalez-Valchez, *J. Inorg. Biochem.*, **90**, 51 (2002).
46. S. Xiao, W. Lin, C. Wang, M. Yang, *Bioorg. Med. Chem. Lett.*, **11**, 437 (2001).
47. G.A. Neyhart, N. Grover, S.R. Smith, W.A. Kalsbeck, T.A. Fairley, M. Cory, H. Holden Thorp, *J. Am. Chem. Soc.*, **115**, 4423 (1993).
48. S. Arounaguirri, B.G. Maiya, *Inorg. Chem.*, **35**, 4267 (1996).
49. M.J. Waring, *J. Mol. Biol.*, **13**, 269 (1965).
50. P.U. Maheswari, M. Palaniandavar, *Inorg. Chim. Acta*, **357**, 901 (2004).
51. R.B. Nair, E.S. Teng, S.L. Kirkland, C.J. Murphy, *Inorg. Chem.*, **37**, 139 (1998).
52. G. Psomas, *J. Inorg. Biochem.*, **102**, 1798 (2008).
53. R. Palchaudhuri, P.J. Hergenrother, *Curr. Opin. Biotechnol.*, **18**, 497 (2007).
54. L. Strekowski, B. Wilson, *Mutat. Res.-Fundam. Mol. Mech. Mutag.*, **623**, 3 (2007).

## ИЗСЛЕДВАНЕ НА ВЗАИМОДЕЙСТВИЕТО НА ДНК С НОВ Cu(II) КОМПЛЕКС ЧРЕЗ СПЕКТРОСКОПСКИ, СПЕКТРОФЛУОМЕТРИЧНИ, ВОЛТАМПЕРОМЕТРИЧНИ МЕТОДИ И С КРЪГОВ ДИХРОИЗЪМ

М. Бордбар<sup>1,\*</sup>, Ф. Ходайе<sup>2</sup>, М. Табатабае<sup>2</sup>, А. И. Фаал<sup>3</sup>, З. Мехрилихван<sup>4</sup>,  
С. Мохамад-Ганджи<sup>5</sup>

<sup>1</sup>Департамент по химия, Научен факултет, Университет в Кум, Кум, Иран

<sup>2</sup>Департамент по химия, Клон Язд, Ислямски университет „Азад“, Язд, Иран

<sup>3</sup>Департамент по химия, Университет Паяме Нур, П.К. 37185-311, Иран

<sup>4</sup>Клуб на младия изследовател, Клон Северен Техеран, Ислямски университет „Азад“, Техеран, Иран

<sup>5</sup>Национален институт за генно инженерство и биотехнология (NIGEB), П.К. 14965-161, Техеран, Иран.

Постъпила на 14 септември, 2015 г.; приета на 28 март, 2016 г.

(Резюме)

Изследвана е свързващата активност на водо-разтворими мед(II) комплекс с пиридин-2,6-диарбоацетат (pydc<sup>2-</sup>) и 2-аминопиримидин (amp) с формула [Cu(pydc)(amp)].2H<sub>2</sub>O.H<sub>2</sub>O (**1**) с DNA (СТ-DNA) от телешки тимус. Свързващата активност на **1** е изследвана чрез ефекта ѝ върху електронните абсорбционни спектри, ефекта на термична денатурация, флуоресцентното закаляване (използвайки метиленово синьо като флуоресцентен маркер) и спектри на кръгов дихроизъм. Всички резултати внушават взаимодействие между (**1**) и ДНК чрез интеркалация с константа на свързване (9.51±0.2)×10<sup>4</sup> M<sup>-1</sup>.

## Structural, magnetic and catalytic properties of Co substituted manganite nano-perovskites

A. Gholizadeh<sup>1\*</sup>, A. Malekzadeh<sup>2</sup>, M. Ghiasi<sup>2</sup>

<sup>1</sup>*School of Physics, Damghan University (DU), Damghan, I.R. Iran*

<sup>2</sup>*School of Chemistry, Damghan University (DU), Damghan, I.R. Iran*

Received August 4, 2015, Revised October 22, 2015

In this work, structural, magnetic and catalytic properties of  $\text{LaMn}_{1-x}\text{Co}_x\text{O}_3$  ( $x = 0.00, 0.25, 0.50, 0.75, 1.00$ ) are investigated. The structural characterization of the samples by X-ray powder diffraction and using the X'Pert package and Fullprof program is evidence for a monoclinic structure (P21/n space group) with  $x = 0.5$  and a rhombohedral structure (R-3c space group) for other samples. These results have been confirmed by FTIR measurements. The magnetic characterizations of the samples have been studied by magnetization measurement versus temperature and field. The structural and magnetic results show the ferromagnetic interactions of  $\text{Co}^{2+}\text{-Mn}^{4+}$  for  $x \leq 0.5$  are being progressively replaced by the less effective  $\text{Co}^{2+}\text{-Co}^{3+}$  and  $\text{Mn}^{4+}\text{-Co}^{3+}$  interactions for  $x > 0.5$ . The catalytic activity of  $\text{LaMn}_{1-x}\text{Co}_x\text{O}_3$  was evaluated for  $\text{C}_2\text{H}_6$  combustion and CO oxidation reactions. Under similar reaction conditions, the catalytic results show that the  $\text{LaMn}_{0.5}\text{Co}_{0.5}\text{O}_3$  nano-perovskite is the best catalyst for  $\text{C}_2\text{H}_6$  combustion and CO oxidation.

**Keywords:** Nano-Perovskite; Manganite-Cobaltite; Structural and Magnetic Phase Transition;  $\text{C}_2\text{H}_6$  combustion; CO oxidation.

### INTRODUCTION

Many efforts have been made to reduce the use of precious metals in catalysts (Pt, Pd and Rh), and use new compounds which are cheaper and have a better catalytic activity. Finding a suitable replacement for expensive catalysts used in various industries, including the automotive industry, to further reduce the environmental pollutants emitted is a major research endeavor in the modern world. A high activity in the reduction-oxidation (redox) reaction, oxygen storage capability and high flexibility in including other metals in the structure, have proposed perovskite compounds  $\text{ABO}_3$  as a good candidate for this replacement. In addition, being inexpensive and having heat and mechanical resistance properties are some other advantages of these compounds. Among perovskite compounds, lanthanum manganites and cobaltites with formulas  $\text{LaMnO}_3$  and  $\text{LaCoO}_3$  are the famous compounds that are used to complete the oxidation reaction of CO and hydrocarbons [1-2].

$\text{LaMn}(\text{Co})\text{O}_3$  with a perovskite structure is an insulator-antiferromagnetic at room temperature due to the absence of ions  $\text{Mn}^{4+}$  ( $\text{Co}^{4+}$ ). With the replacement of the  $\text{La}^{3+}$  ions by bivalent elements (Sr, Ca, ...), the trivalent ions Mn (Co) are converted to a mixture of ions  $\text{Mn}^{3+}$  and  $\text{Mn}^{4+}$  ( $\text{Co}^{3+}$  and  $\text{Co}^{4+}$ ). The measurements reported on

polycrystalline samples of  $\text{La}_{1-y}\text{M}_y\text{Mn}(\text{Co})\text{O}_3$ , showed an insulator-antiferromagnetic behavior for low and high values of  $y$  and metal-ferromagnetic behavior at the concentration  $y \approx 1/3$  [3-4]. In these compounds, the ferromagnetic-paramagnetic transition associated with a metal-insulator transition below the curie temperature ( $100 < T_C$  (K)  $< 350$ ) has been attributed to the double-exchange theory between the ions  $\text{Mn}^{3+}\text{-Mn}^{4+}$  ( $\text{Co}^{3+}\text{-Co}^{4+}$ ) [5]. In manganite-cobaltite  $\text{LaMn}_{1-x}\text{Co}_x\text{O}_3$ , the origin of the metal-ferromagnetic behavior is due to ferromagnetic interaction between the ions of  $\text{Mn}^{3+}\text{-Mn}^{3+}$  and  $\text{Mn}^{4+}\text{-Co}^{2+}$  [6]. Furthermore, all the electronic, magnetic and redox properties of the samples will depend on the nature of the interaction between the Co and Mn ions via oxygen.

Several investigators [5-8] have reported that in  $\text{ABO}_3$  perovskites, the A ions in general are catalytically inactive and the active ions at the B position readily interact with the gas molecules. It should be noted that the substitution at the A-site with a bivalent cation or a tetravalent cation leads to a different behavior of the catalytic activity of manganite-cobaltite compounds. Because the B-O bond length and the bond energy depend on the lattice parameter this alters the B-O<sub>ad</sub> [5]. The Sr substitution for La in  $\text{La}_{1-y}\text{A}_y\text{CoO}_3$  leads to higher oxidation states for Co, so that the higher the amount of Sr, the higher is the concentration of  $\text{Co}^{4+}$  [8]. However, since  $\text{Co}^{4+}$  is unstable, then oxygen release can take place ending in the formation of oxygen vacancies that leads to a

\* To whom all correspondence should be sent:  
E-mail: gholizadeh@du.ac.ir; ah\_gh1359@yahoo.com

decrease of the catalytic activity. By contrast, the insertion of  $Ce^{4+}$  in  $La_{1-y}A_yCoO_3$  leads to a partial reduction of  $Co^{3+}$  to  $Co^{2+}$ , thus affording a large amount of active sites for oxygen adsorption from the gas-phase that leads to an increase in catalytic activity [5].

The changes in the  $AB_{1-x}B'_xO_3$  perovskite catalytic properties of the substituting cation B with B' can be classified in two categories: geometric and electronic structure of cation B' [6]. The effect of B' substitution on geometric and electronic factors is considered in the calculation of the structural and magnetic changes.

In this work, we prepared  $LaMn_{1-x}Co_xO_3$  ( $x = 0.00, 0.25, 0.50, 0.75, 1.00$ ) by the citrate precursor method and tried to explain the structural and magnetic properties and the influence of Co substitution on their catalytic activities for  $C_2H_6$  combustion and CO oxidation reactions by using reasonable experimental data.

## EXPERIMENTAL

The  $LaMn_{1-x}Co_xO_3$  compounds with  $x = 0.00, 0.25, 0.50, 0.75,$  and  $1.00$  were prepared by the citrate precursor method, similar to the recipe reported elsewhere [9]. First, a solution containing appropriate concentrations of metal nitrates  $La(NO_3)_3 \cdot 6H_2O$ ,  $Mn(NO_3)_2 \cdot 4H_2O$ ,  $Co(NO_3)_2 \cdot 6H_2O$  and citric acid, equal to the total number of moles of nitrate ions, was evaporated at  $60^\circ C$ , overnight. The homogeneous sol-like substance was subsequently dried at  $80^\circ C$ , overnight. The resulting spongy and friable materials were completely powdered and kept at  $200^\circ C$ , overnight. The resulting materials were powdered again and calcined at  $600^\circ C$  for 5 h. The samples were subsequently calcined for 5 more hours at  $900^\circ C$ .

The X-ray diffraction (XRD) patterns have been recorded using a Bruker AXS diffractometer D8 ADVANCE with Cu-K $\alpha$  radiation in the range  $2\theta = 20-80^\circ$  at room temperature (RT). The XRD data was analyzed using a commercial X'pert package and the Fullprof program.

XRD profile analysis is a simple and powerful method to evaluate the crystallite size and lattice strain. Two factors determine the breadth of the Bragg peak including the crystallite size-dependent ( $\beta_D$ ) or strain dependent broadening ( $\beta_S$ ) effects, except for the instrument-dependent effect. To do an accurate analysis for size and strain effects, the instrumental broadening must be accounted for. Scherrer's equation is as follows:

$$D = \frac{0.94 \lambda}{\beta_{hkl} \cos \theta}, \quad (1)$$

This shows the broadening of the XRD pattern which is attributed to the crystallite size-induced broadening. Here,  $\beta_{hkl}$  is the full-width at half-maximum of the diffraction peaks. The information on strain ( $\epsilon$ ) and crystallite size ( $D$ ) of the powders have been obtained from  $\beta_{hkl}$  and the planar spacing  $d_{hkl}$  via the Halder-Wagner method [10]:

$$\left(\frac{\beta_{hkl}^*}{d_{hkl}^*}\right)^2 = \left(\frac{1}{D}\right)^2 \left(\frac{\beta_{hkl}^*}{d_{hkl}^*}\right)^2 + \left(\frac{\epsilon}{2}\right)^2, \quad (2)$$

where  $\beta_{hkl}^* = \beta_{hkl} \cos \theta / \lambda$  and  $d_{hkl}^* = 2 \sin \theta / \lambda$ . Finally, the results of the Halder-Wagner method are compared with the Scherrer method.

The FT-IR spectra were recorded in a Perkin-Elmer spectrum RXI-IR spectrometer, operating by ratio, single beam, or interferogram mode, in the range  $400-1500 \text{ cm}^{-1}$ . The samples were finely ground in an agate mortar with KBr as diluent and pelleted for the IR analysis. The morphology of the samples was studied by SEM (Philips XL30) analysis. The particle size of the samples was investigated by TEM (LEO Model 912AB) analysis.

The absorption coefficient is a suitable quantity for studying the band gap energy. Optical absorption spectra of  $LaMn_{1-x}Co_xO_3$  between 200 and 1100 nm wavelengths have been recorded at room temperature using a HP-UV-Vis system (Agilent8453, model). The band gap energies have been calculated in accordance with Ref. [11]. The following relation holds between the optical absorption coefficient,  $\alpha(\lambda)$ , and the optical band gap energy of a direct band transition [25]:

$$(3) \quad (\alpha h\nu)^2 = B(h\nu - E_g)$$

where B is an energy-independent constant and  $\alpha(\lambda) = 2.303 A(\lambda)/t$  is the optical absorption coefficient calculated from the absorption spectra ( $A(\lambda)$  is the mean particle size of the sample (t)). The band gap energy of the samples is estimated by extrapolating the linear part of  $(\alpha h\nu)^2$  vs. a  $h\nu$  plot. The hysteresis loops at 10 K and temperature dependence of magnetization between 10-400 K was carried out in a SQUID magnetometer (Quantum Design, Inc.). The magnetization curve in high fields can usually be fitted by the empirical formula; law of approach to saturation [12]:

$$M(H) = M_s [1 - (a/H) - (b/H^2) - (c/H^3)] + \chi H + EH^{1/2}, \quad (4)$$

where  $M(H)$  and  $M_S$  are the magnetization at the field  $H$  and the saturation magnetization explained by atomic theory, respectively.

Catalytic tests for  $C_2H_6$  combustion and CO oxidation reactions over  $LaMn_{1-x}Co_xO_3$  catalysts were studied in an experimental set-up using a quartz tube, filled with 200 mg of a 60-100 mesh sized catalyst supported on ceramic wool under GHSV of  $12,000\text{ h}^{-1}$ . In a typical experiment, a model exhaust gas obtaining a mixture of 6 vol% CO and 0.2 vol%  $C_2H_6$  as a hydrocarbon (HC) model compound, in Ar and air (a stoichiometric ratio with respect to oxygen) was passed through the catalyst bed with a total gas mixture flow rate of 40 mL/min at STP. Catalytic test studies were carried out by temperature rising in random intervals from  $50^\circ\text{C}$  to the complete oxidation temperature. The product stream was analyzed by a GC on a FI detector.

## RESULTS AND DISCUSSIONS

### *Structural and morphologic properties*

X-ray diffraction patterns of  $LaMn_{1-x}Co_xO_3$  ( $x = 0.00, 0.25, 0.50, 0.75, 1.00$ ), are shown in Fig. 1. The XRD data were analyzed using both the commercial X'Pert High Score package and the Fullprof program. Identification of the structure type using the X'pert package confirms the perovskite structure in all samples without a presence of impurity phases. As shown in the XRD pattern of samples  $x = 0.00, 0.25, 0.75, 1.00$  (Fig. 1), a splitting of the peaks of the perovskite at angles  $\sim 33^\circ, \sim 41^\circ, \sim 58^\circ, \sim 68^\circ$  and  $\sim 78^\circ$  is an indication of a rhombohedral system [13]. Also, for a better comparison, a peak at about  $\sim 33^\circ$  is shown in the inset of Fig. 1. For  $x = 0.00$ , the peak at  $\sim 33^\circ$  is a very intense doublet, while for other samples it is fully split. These results for  $x = 0.00$  suggest a mixture of  $LaMnO_3$  and  $LaMnO_{3+\delta}$  with cubic and rhombohedral structures, respectively. However, the XRD pattern of sample  $x = 0.50$  is different, while more broadening of the peaks mentioned above and a splitting of the peak at the angle  $\sim 47^\circ$  indicate a lower symmetry.

Results of the Rietveld analysis using the Fullprof program indicate that all the diffraction peaks of the sample at  $x = 0.50$  can be quite well indexed in the monoclinic structure (space group  $P2_1/n$ ) and for other samples in the Rhombohedral structure (space group  $R-3c$ ). Also, the results of the Rietveld analysis using the Fullprof program indicate that the best fit with the least difference was carried out (Fig. 1). To perform a Rietveld

refinement we need good initial values for the lattice parameters and the type of space group obtained from a phase analysis of the X'pert package.

The hexagonal cell is no longer primitive and has three times the volume of the rhombohedral cell. When the XRD pattern of a rhombohedral sample is indexed, i.e., with reference to hexagonal axes and the true nature of the lattice determined, we usually want to know the lattice parameters  $a_r$  and  $\alpha$  of the rhombohedral unit cell. But the dimensions of the rhombohedral cell can be determined from the dimensions of the hexagonal cell and this is an easier process than solving the rather complicated plane-spacing equation for the rhombohedral system. The first step is to analyze and index the XRD pattern on the basis of the hexagonal axes using the Fullprof program. Then, the parameters  $a_H$  and  $c$  of the hexagonal cell are calculated in the usual way. Finally, the parameters  $a_r$  and  $\alpha$  of the rhombohedral cell are determined from the refined parameters  $a_H$  and  $c$  of the hexagonal cell using the Fullprof program according to the following equations:

$$a_r = \frac{1}{3}\sqrt{3a_H^2 + c^2}, \quad \sin \frac{\alpha}{2} = \frac{3}{2\sqrt{3+(c/a_H)^2}}, \quad (5)$$

The derived lattice parameters of the samples for rhombohedral and monoclinic structures are given in Table 1. It should be noted that if the  $c/a_H$  ratio of the hexagonal cell takes on the special value of 2.45, then the angle  $\alpha$  of the rhombohedral cell will be equal to  $60^\circ$  and the bond angle  $B-O-B$  is  $180^\circ$ . Consequently, the lattice points will be face-centered cubic ( $t$  is equal to 1). Also, the magnitude of the rotation of  $BO_6$  can be evaluated from either the angle  $\alpha$  of the rhombohedral unit cell written in Table 1 or from the axial ratio  $c/a_H$  of the hexagonal cell. As a result of the rotation (tilting), the  $B-O-B$  bond angle ( $\leq 180^\circ$ ) and  $\alpha$  deviate from the ideal perovskite value. Notice, that for trigonal angles,  $\alpha$ , is less than 60 degrees, the transformation can be achieved by an expansion along the body diagonal [111] of the Rhombohedral or along the  $c$ -axis [001] of the hexagonal; while, for trigonal angles this is greater than 60 degrees, a contraction in the body diagonal [111] of the Rhombohedral or along the  $c$ -axis [001] of the hexagonal. Therefore, the obtained values of the angle  $\alpha$  are higher than  $60^\circ$  this means the  $BO_6$  octahedron is slightly compressed along the (hexagonal  $c$  axis) rhombohedral (111) axis with respect to the cubic structure.

From the X-ray diffraction patterns at about  $33^\circ$  shown in the inset of Fig. 1, two tendencies are

observed for values of  $x \leq 0.50$  and  $x > 0.50$ . For values of  $x \leq 0.50$ , the peaks shift is nearly constant upon increasing the Co-content and means a slight increase of the unit cell volume. But for values of  $x > 0.50$ , an increase of peaks shifts to larger  $2\theta$ , consequently a decrease of the unit cell volume is observed with the degree of substitution. These findings are in accordance with the refined unit cell volume obtained from the Rietveld method using the Fullprof program summarized in Table 1.

There is no apparent linear correlation between the perovskite structure, the substitution degree and that for  $x = 0.50$  when the transformation of the crystal phase occurs. This is due to the substitution of  $Mn^{x+}$  ions in the lattice by  $Co^{x+}$  ions. Therefore, all these findings should be correlated with the ionic radii of each one of the components. The presence of several ionic states ( $Mn^{3+}$ ,  $Mn^{4+}$ ,  $Co^{2+}$  and  $Co^{3+}$ ) makes it difficult to decide just from the XRD data.

**Table 1.** The structure type and unit cell parameters of  $LaMn_{1-x}Co_xO_3$ .

Sample	Structure (space group)	lattice Parameters	V ( $\text{\AA}^3$ )
x = 0.00	Rhombohedral (R-3c)	$a = b = c = 5.45866$ ( $\text{\AA}$ ) $\alpha = \beta = \gamma = 60.4735$ ( $^\circ$ )	116.243
x = 0.25	Rhombohedral (R-3c)	$a = b = c = 5.45903$ ( $\text{\AA}$ ) $\alpha = \beta = \gamma = 60.6003$ ( $^\circ$ )	116.595
x = 0.50	Monoclinic (P 21/n)	$a = 5.36332$ ( $\text{\AA}$ ) $b = 5.46978$ ( $\text{\AA}$ ) $c = 7.74353$ ( $\text{\AA}$ ) $\beta = 88.6507$ ( $^\circ$ )	227.103
x = 0.75	Rhombohedral (R-3c)	$a = b = c = 5.39213$ ( $\text{\AA}$ ) $\alpha = \beta = \gamma = 60.7529$ ( $^\circ$ )	112.741
x = 1.00	Rhombohedral (R-3c)	$a = b = c = 5.37493$ ( $\text{\AA}$ ) $\alpha = \beta = \gamma = 60.7199$ ( $^\circ$ )	111.584

**Table 2.** the values of crystallite size and strain of  $LaMn_{1-x}Co_xO_3$  obtained from Scherrer and H-W methods.

Sample	$D_{m-Sch}$ (nm)	$D_{H-W}$ (nm)	$\epsilon_{H-W} * 10^3$ (no unit)
x = 0.00	28.89	32.36	2.42
x = 0.25	28.45	29.58	2.12
x = 0.50	19.5	23.47	5.48
x = 0.75	14.48	27.55	10.56
x = 1.00	40.91	28.73	5.68

**Table 3.** Magnetic results of  $LaMn_{1-x}Co_xO_3$ .

Sample	$M_S(10\text{ K})$ (emu/g)	$H_C(10\text{ K})$ (Oe)	$M_r(10\text{ K})$ (emu/g)	$T_C$ (K)
x = 0.00	8.96	90	1.50	130
x = 0.25	7.34	2730	3.48	184
x = 0.50	4.21	4310	2.32	230
x = 0.75	1.29	5040	0.30	179
x = 1.00	0.54	4310	0.23	169

**Table 4.** Catalytic performance (%), the C<sub>2</sub>H<sub>6</sub> combustion and CO oxidation temperatures (°C) for LaMn<sub>1-x</sub>Co<sub>x</sub>O<sub>3</sub>.

Sample	Temperature of CO conversion (°C)			Temperature of C <sub>2</sub> H <sub>6</sub> conversion (°C)		
	10%	50%	90%	10%	50%	90%
x = 0.00	255	295	350	260	358	483
x = 0.25	175	195	298	237	376	404
x = 0.50	127	160	190	177	283	393
x = 0.75	160	179	213	180	374	430
x = 1.00	220	330	380	178	576	702

Several considerations can be forwarded, however, at this stage: first of all, it can be expected that for  $x \leq 0.50$ , when substituting Mn<sup>3+</sup> by cobalt ions, this ion enters as Co<sup>2+</sup>, leading to the formation of an equivalent amount of Mn<sup>4+</sup> to preserve the electro-neutrality of the lattice. In such a case, the mean ionic radius of the B cation must show an increase, with an accompanying increase of the lattice volume (Table 1). It is known that the mean ionic radius of Mn<sup>4+</sup>-Co<sup>2+</sup> is larger than that of Mn<sup>3+</sup>-Co<sup>3+</sup> [14]. Therefore, the increase in lattice volume has been attributed to the assumption of substituting Co<sup>2+</sup> by Mn<sup>3+</sup> due to the larger mean ionic radius of Mn<sup>4+</sup>-Co<sup>2+</sup> compared to Mn<sup>3+</sup>-Co<sup>3+</sup>. For  $x > 0.50$ , a large reduction of the lattice volume (Table 1) correlates well with the presence of Co ions as Co<sup>3+</sup> in a low spin (LS) state, for which the ionic radius is lower than the corresponding high spin (HS) state (Co<sup>3+</sup>: HS, 0.61 and LS, 0.545 Å). In such a case, the mean ionic radius of the B-site decreases, with an accompanying decrease of the lattice volume (Table 1). Again, this hypothesis is confirmed by the magnetic and catalytic data presented further in this work. For this, a correlation with the magnetic data is necessary, as will be discussed later in this work.

The influence of substitution on the crystal structure can be described by a tolerance factor ( $t = r_{A-O} / (\sqrt{2} r_{B-O})$ ) introduced by Goldschmidt to estimate the deviation from the ideal structure. As a result, for  $x \leq 0.50$ , as  $\langle r_{B-O} \rangle$  increases,  $t$  decrease, at first the rhombohedral structure for  $x = 0.0$  is further distorted to the rhombohedral structure for  $x = 0.25$  and then for  $x = 0.50$  the structure transforms to monoclinic in which the bending of the B-O-B bond increases and the bond angle deviates from 180°. For  $x > 0.50$  inversely, as  $\langle r_{B-O} \rangle$  decreases,  $t$  increase, the lattice structure transforms from a monoclinic to a rhombohedral structure.

The results for the crystallite sizes obtained from the mean value of 15 strongest peaks shown in Fig. 1 for both structures by using the Scherrer method are summarized in Table 2.

The Halder-Wagner method was used to study the individual contributions of crystallite size and lattice micro-strain on isotropic line broadening of 15 strongest peaks of the LaMn<sub>1-x</sub>Co<sub>x</sub>O<sub>3</sub> compounds.

In this method, the plot of  $\left(\frac{\beta_{hkl}^*}{d_{hkl}^*}\right)^2$  (axis y) versus  $\left(\frac{\beta_{hkl}^*}{d_{hkl}^*}\right)$  (axis-x) is a straight line (see Fig. 2).

The crystallite size is determined from the slope inverse of the linearly fitted data and the root of the y-intercept gives the strain, respectively. The results of crystallite size and micro-strain of LaMn<sub>1-x</sub>Co<sub>x</sub>O<sub>3</sub> ( $x = 0.00, 0.25, 0.50, 0.75, 1.00$ ) estimated by the Scherrer and H-W methods are summarized in Table 2. The values for  $x = 0.50, 0.75$  are less than for the other samples.

The H-W method supposes that the “crystallite size” profile contributes to the line broadening by a Lorentzian function and the “strain” profile by a Gaussian function. This method shows that line broadening is essentially isotropic. However, the advantage of the H-W method over the Scherrer method is that less weight is given to the data from reflections at high angles where the precision is usually lower [10].

However, the mean crystallite size obtained from the Scherrer formula and the H-W analysis (see Table 2) show a greater variation because of the difference in averaging of the particle size distribution and the results of the H-W method are more accurate, with all the data points touching the fitting line. It is noted that the crystallite size obtained from this method is a minimum at about  $x = 0.50$ .

Fig. 3 shows the FTIR spectrum of LaMn<sub>1-x</sub>Co<sub>x</sub>O<sub>3</sub> ( $x = 0.00, 0.25, 0.50, 0.75, 1.00$ ). The presence of metal oxygen bonds i.e. symmetrical lengthening of the O-B-O and asymmetrical lengthening of the B-O bond of the octahedron BO<sub>6</sub> structures could be revealed from the peaks at 410 and 600 cm<sup>-1</sup>, respectively. The widening of the 600 cm<sup>-1</sup> band and/or the appearance of a shoulder indicates a structure with a lower symmetry [6].

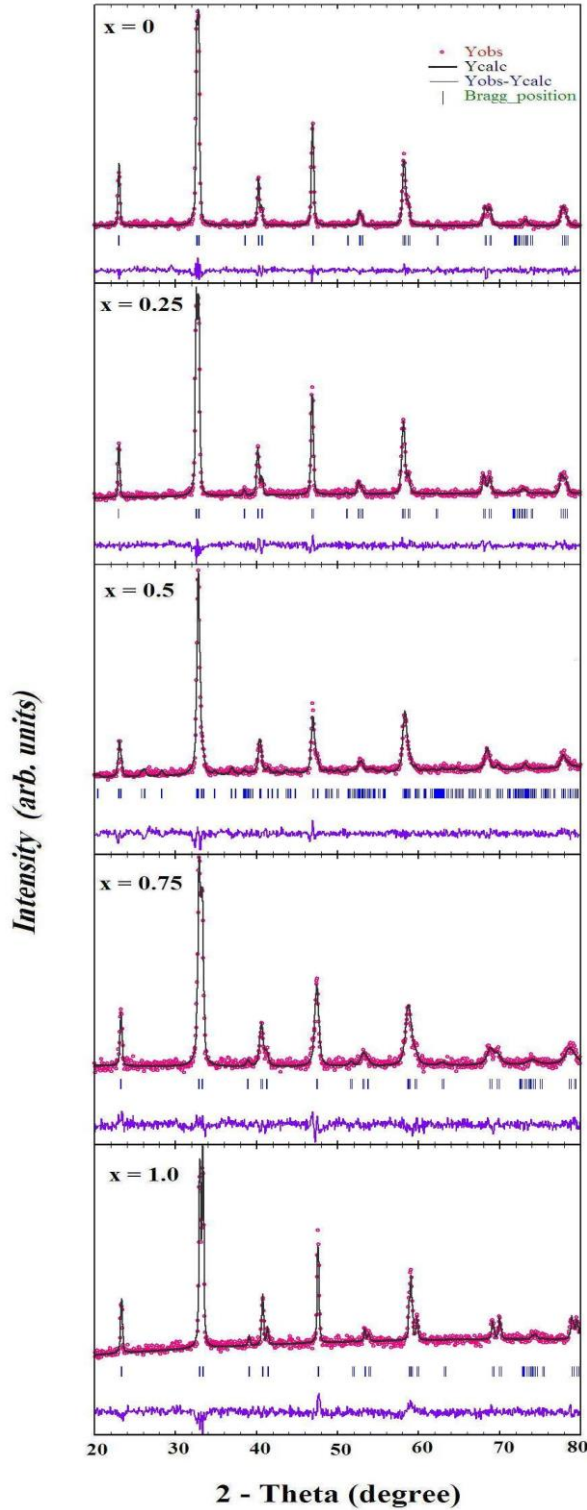


**Fig. 1.** Rietveld analysis of the X-ray diffraction patterns for  $\text{LaMn}_{1-x}\text{Co}_x\text{O}_3$  ( $x = 0.00, 0.25, 0.50, 0.75, 1.00$ ). The circle signs represent the raw data. The solid line represents the calculated profile. Vertical bars indicate the position of Bragg peaks for samples with the rhombohedral structure (Space Group  $R\bar{3}c$ ) and for the sample  $x = 0.5$  with the monoclinic structure (Space Group  $P2_1/n$ ). The lowest curve is the difference between the observed and the calculated patterns. The X-ray diffraction patterns for all samples at about  $33^\circ$  are shown in the inset of  $x = 0.75$ .

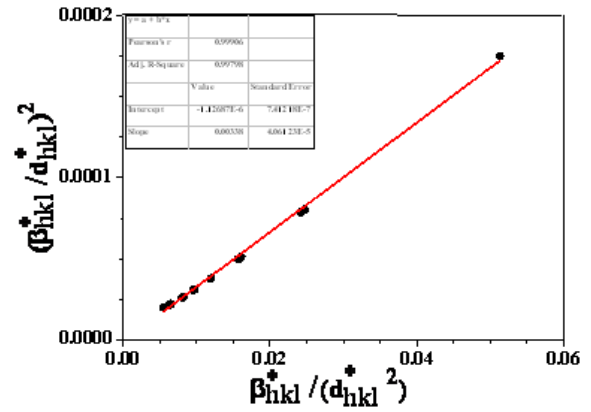


**Fig. 2.** Fitted curves of the Halder-Wagner analysis for  $x = 0$ . The y-intercept gives the mean value of the strain and the slope gives the crystallite size.

Therefore, for the perovskites with  $x < 0.50$ , the spectra corresponds to a rhombohedral structure with a great symmetry but for  $x > 0.50$ , a shoulder appears at  $550\text{ cm}^{-1}$  and is characteristic of a rhombohedral structure with a lower symmetry. The peak at  $410\text{ cm}^{-1}$  can be attributed to a lower symmetry in three samples  $x = 0.50, 0.75, 1.00$ . These results are in accordance with the unit cell parameter  $a$  obtained from the XRD analysis so that the larger  $a$ , shows a lower symmetry. The narrow band at  $1385\text{ cm}^{-1}$  might correspond to the  $\text{CO}_3^{2-}$  groups.

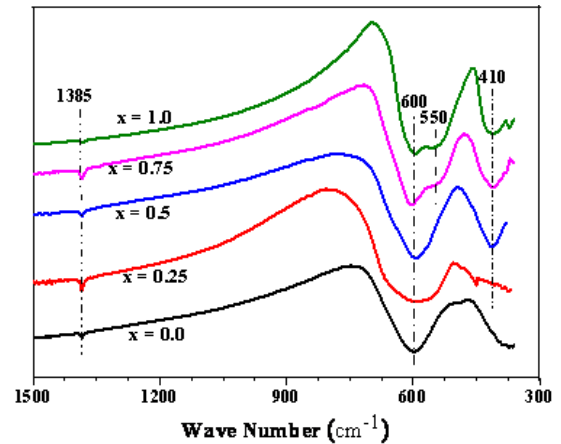


**Fig. 3.** FT-IR spectra for  $\text{LaMn}_{1-x}\text{Co}_x\text{O}_3$ .

A similar morphology is observed in SEM micrographs of the samples for  $\text{LaMn}_{1-x}\text{Co}_x\text{O}_3$  ( $x = 0.0, 1.0$ ) as shown in Fig. 4. The TEM micrographs and particle size distribution of samples at  $x = 0.0$  and  $1.0$  are shown in Fig. 4. Size distribution histograms are fitted by using a log-normal function as follow:

$$P(d) = \frac{1}{d\sigma_d\sqrt{2\pi}} \exp\left\{-\frac{1}{2\sigma_d^2} \ln^2\left(\frac{d}{d_{TEM}}\right)\right\}, \quad (6)$$

where  $\sigma_d$  is the standard deviation of the diameter and  $d_{TEM}$  is the mean diameter obtained from the

TEM results. The mean diameter was calculated to be 36 nm ( $x = 0.0$ ) and 50 nm ( $x = 1.0$ ), respectively. These results are different from the calculated crystallite sizes from the XRD line profile. The differences are related to the irregular shape of the nanoparticles with spherical and polygon morphologies which are observed in the TEM micrographs [8].

### Magnetic properties

The hysteresis loops of the  $\text{LaMn}_{1-x}\text{Co}_x\text{O}_3$  ( $x = 0.00, 0.25, 0.50, 0.75, 1.00$ ), shown in Fig. 5, are compared at 10 K, measured in a SQUID magnetometer (Quantum Design, Inc.). The curves of  $M_H$ , and S-shaped hysteresis loops show the coercivity field  $H_C$  (intersection with the x axis), remanance magnetization  $M_r$  (intersection with the y axis) and the saturation magnetization  $M_S$ . The values of  $H_C$ ,  $M_r$  and  $M_S$  as calculated are summarized in Table 3. The increase of  $H_C$  with cobalt content has been attributed to the increase of the magnetic domains. The  $M_r$  and  $M_S$  values for samples  $x \leq 0.50$  are larger than  $x > 0.50$ .

The temperature dependence of magnetization in the range 5-400 K under the applied magnetic field 0.1T for  $\text{LaMn}_{1-x}\text{Co}_x\text{O}_3$  ( $x = 0.00, 0.25, 0.50, 0.75, 1.00$ ) is shown in Fig. 6. The Curie temperature obtained from the critical point in the derivative of the M-T curves is mentioned in Table 3 that clearly displays a non-monotonic dependence of  $T_C$  with the Co doping level. In Co doped samples, the interval of  $T_C$  is about 50 K for each addition of 0.25 cobalt concentration. Firstly, the transition temperature,  $T_C$ , increases with  $x$  and then decreases as  $x$  increases. The compound  $\text{LaMn}_{0.5}\text{Co}_{0.5}\text{O}_3$  characterized by the presence of two ferromagnetic phases with  $T_C = 225$  and 150K is subject to the synthesis conditions [15]. The former magnetic phase is formed at 700 °C, whereas the latter phase can be obtained by quenching from 1300 °C. A high-spin order  $\text{Co}^{2+}$ - $\text{Mn}^{4+}$  valence state and low-spin disorder-nonmagnetic  $\text{Mn}^{3+}$ - $\text{Co}^{3+}$  ions were discovered for samples with higher and lower Curie temperatures, respectively. In addition, the  $\text{Co}^{2+}$  and  $\text{Mn}^{4+}$  ions are ferromagnetically aligned and the average ionic radii of  $\text{Mn}^{4+}$ - $\text{Co}^{2+}$  are larger than those of  $\text{Mn}^{3+}$ - $\text{Co}^{3+}$  and the high temperature samples  $\text{LaMn}_{0.5}\text{Co}_{0.5}\text{O}_3$  are characterized by a smaller volume [14].

The pure manganite  $\text{La}^{3+}\text{Mn}^{3+}\text{O}_2$  ( $x = 0$ ) is essentially antiferromagnetic [13] with an orthorhombic structure, while in our case, there is a ferromagnetic component with a low coercive field and large magnetization values. A recent study [16]

showed that stoichiometric  $\text{LaMnO}_3$  should be prepared in the absence of oxygen but sintering in ambient air results in nonstoichiometric  $\text{LaMnO}_{3+\delta}$  with the formation of  $\text{Mn}^{4+}$  ions larger than 20%.

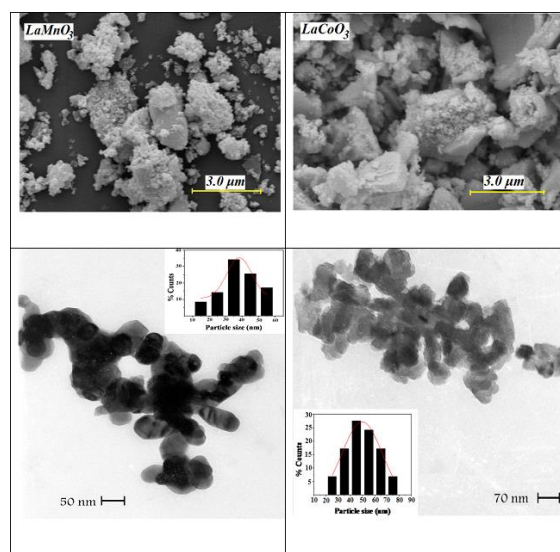


Fig. 4. SEM results, TEM micrographs and size distribution histograms for  $\text{LaMn}_{1-x}\text{Co}_x\text{O}_3$ .

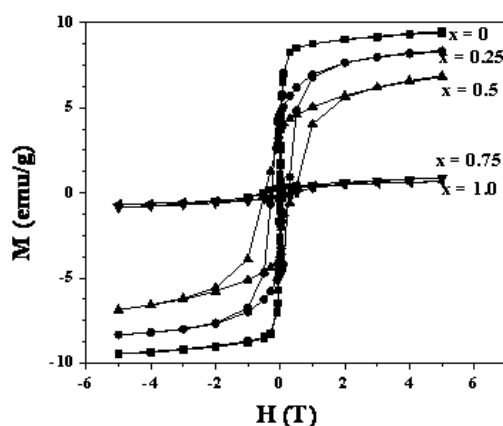


Fig. 5. The hysteresis loops (M-H) at 10 K for  $\text{LaMn}_{1-x}\text{Co}_x\text{O}_3$ .

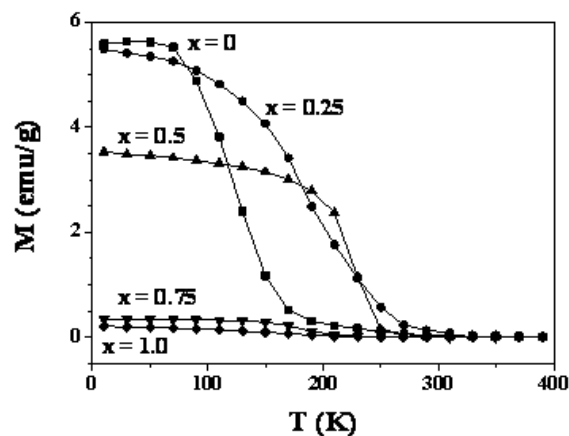


Fig. 6. The magnetization curves versus temperature measured under an applied magnetic field 0.1T for  $\text{LaMn}_{1-x}\text{Co}_x\text{O}_3$ .



For our sample  $\text{LaMnO}_3$  annealed in the presence of oxygen, the room temperature structure is rhombohedral and indicates the percentage of  $\text{Mn}^{4+}$  is larger than 20%. Therefore, the magnetization values observed in the studied  $\text{LaMnO}_3$  sample can be related to a double exchange of  $\text{Mn}^{4+}$ - $\text{Mn}^{3+}$ . In addition, all the samples are definitely ferromagnetic. The  $M_S$  values for  $x \leq 0.50$  are larger than  $x > 0.50$ . It is known that the interactions of  $\text{Co}^{2+}$ - $\text{Co}^{3+}$  and  $\text{Co}^{3+}$ - $\text{Mn}^{3+}$  are of the anti-ferromagnetic type and  $\text{Co}^{2+}$ - $\text{Mn}^{3+}$  and  $\text{Mn}^{4+}$ - $\text{Mn}^{3+}$  are ferromagnetic [6]. In accordance with the structural results, the large magnetization values for  $x \leq 0.50$  suggests a substitution of  $\text{Co}^{2+}$  with  $\text{Mn}^{3+}$  reaching a maximum at  $x = 0.50$ , for which the charge equilibrium equation is  $\text{La}^3\text{Mn}^{4+}_{0.5}\text{Co}^{2+}_{0.5}\text{O}^{2-}_3$ . While for  $x > 0.50$ , the magnetization decreases by several orders of magnitude, meaning that the ferromagnetic interactions of  $\text{Co}^{2+}$ - $\text{Mn}^{4+}$  are weaker (the quantity of Mn cations decreases), being progressively replaced by the less effective  $\text{Co}^{2+}$ - $\text{Co}^{3+}$  and  $\text{Mn}^{4+}$ - $\text{Co}^{3+}$  interactions. Therefore, again the hypothesis presented from structural calculations is confirmed by the magnetic data. Catalytic performance (%) curves of  $\text{C}_2\text{H}_6$  combustion and CO oxidation reactions for  $\text{LaMn}_{1-x}\text{Co}_x\text{O}_3$  with  $x = 0.00, 0.25, 0.50, 0.75$  and  $1.00$  are shown in Figs. 7, 8. Also, catalytic performance tests of  $\text{LaMn}_{1-x}\text{Co}_x\text{O}_3$  catalysts at 10%, 50% and 90% of  $\text{C}_2\text{H}_6$  combustion and CO oxidation are summarized in Table 4. The changes in the catalytic properties of  $\text{A}(\text{B}, \text{B}')\text{O}_3$  perovskite in substitution of cation B with B' can be classified in two categories: geometric and electronic structure of the cation B'. The effect of Co substitution on the geometric factors is considered in the calculation of factor  $t$  that should be related to the structural changes summarized in Table 1. It is suggested that

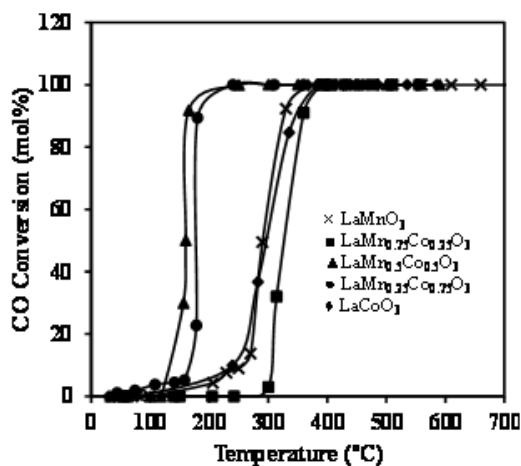


Fig. 7. Catalytic performance curves of  $\text{LaMn}_{1-x}\text{Co}_x\text{O}_3$  for CO oxidation.

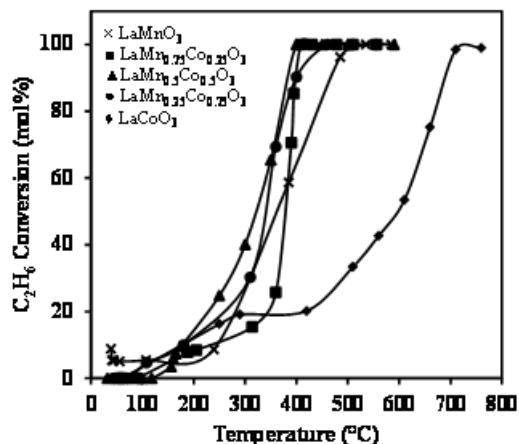


Fig. 8. Catalytic performance curves of  $\text{LaMn}_{1-x}\text{Co}_x\text{O}_3$  for the  $\text{C}_2\text{H}_6$  combustion.

### Catalytic Properties

the decrease in the tolerance factor will be lower than the  $B$ - $O$ - $B$  bond strength and promotes the formation of oxygen vacancies at the surface [7]. Therefore, it is expected that the samples  $x = 0.50, 0.75$  show a higher activity for  $\text{C}_2\text{H}_6$  combustion and CO oxidation reactions.

There is an inverse relationship between the crystallite size and the specific surface area of the samples. In addition, it is known that the higher activity should be related to the higher specific surface and lower crystallite sizes. Consequently, we can conclude that the higher activity of the samples  $x = 0.50, 0.75$  can be attributed to a lower crystallite size.

The band gap energies calculated for  $\text{LaMn}_{1-x}\text{Co}_x\text{O}_3$  compounds with  $x = 0.00, 0.25, 0.50, 0.75$ , and  $1.00$  are 1.58, 1.23, 0.98, 1.13, and 0.99, respectively. These values of the band gap energy show a semiconducting behavior of the samples. The low band gap energy of the compounds contributes to their high catalytic activities.

Also, the results of the catalytic characterization should be related to the electronic configuration which intervenes directly in the structural and magnetic changes formed. In  $\text{ABO}_3$  perovskites, a simple way of varying the oxidation state of the  $\text{B}^{3+}$  ion is by substitution of the  $\text{A}^{3+}$  ion by a different one with an oxidation state other than 3. For example, in  $(\text{La}, \text{M})\text{CoO}_3$  systems, the appearance of  $\text{Co}^{4+}$  ions by substitution with  $\text{M} = \text{Sr}$  decreases the rate, whereas the presence of  $\text{Co}^{2+}$  ions by introduction of  $\text{M} = \text{Ce}^{4+}$  enhances the rate of the oxidation reaction of CO and the hydrocarbons[5]. Therefore, the noticeable higher activity of  $x = 0.25, 0.50$  and  $0.75$  perovskites is attributed to the presence of  $\text{Co}^{2+}$ , as pointed out for hole doped  $(\text{La}, \text{M})\text{CoO}_3$  systems in reducing the atmosphere,

compared to pure cobaltite [5]. The larger  $\text{Co}^{2+}$  cation than  $\text{Co}^{3+}$  results in a shorter Co-O bond (see Fig. 3). Thus, lattice oxygens participate more easily in the redox process and therefore reduce the conversion temperature of  $\text{C}_2\text{H}_6$  combustion and CO oxidation. This behavior is explained considering that at high x values, the amount of unstable  $\text{Co}^{4+}$  ions and/or of oxygen vacancies increases, which favors the diffusion of lattice oxygen from the bulk to the surface, as charge compensators. As a consequence of the above discussions,  $\text{C}_2\text{H}_6$  combustion and CO oxidation take place at a lower temperature over the  $x = 0.50$  catalyst compared with the other samples.

Some reports have shown volcano-type dependence between the activity of  $\text{C}_2\text{H}_6$  combustion and CO oxidation and the electronic configuration of the transition metal ions B [5, 7]. According to crystal field theory, the octahedral environment of the  $\text{B}^{3+}$  ions splits into two lower and higher energy levels  $t_{2g}$  and  $e_g$ , respectively. The maximum activity in the volcano curves is attained for an occupation of the  $e_g$  levels of less than one electron whereas the  $t_{2g}$  levels remain half-filled or completely filled [5]. Also, the  $\text{Mn}^{4+}$  ion configuration in these manganites with the half filled  $t_{2g}$  orbitals and empty  $d_{z^2}$  orbitals shift the Fermi level towards the centre of the antibonding  $e_g$  orbitals at the surface, which promotes CO and  $\text{C}_2\text{H}_6$  chemisorptions at the surface leading to  $\text{C}_2\text{H}_6$  combustion and CO oxidation [7, 8]. Finally, we may conclude from the structural, magnetic, and catalytic variations of the sample at  $x = 0.50$  that the spin states of the  $\text{Co}^{2+}$  and  $\text{Mn}^{4+}$  ions may be in low spin  $t_{2g}^6 e_g^1$  and  $t_{2g}^3$ , respectively.

## CONCLUSIONS

The structural characterization of  $\text{LaMn}_{1-x}\text{Co}_x\text{O}_3$  ( $x = 0.00, 0.25, 0.50, 0.75, 1.00$ ) by X-ray powder diffraction and FTIR measurements is evidence for a monoclinic structure (P21/n space group) with  $x = 0.50$  and a rhombohedral structure (R-3c space group) for other samples without the presence of impurity phases. The unit cell volume obtained from the Rietveld method shows increasing and decreasing tendencies for the values  $x \leq 0.5$  and  $x > 0.5$ , respectively. The structural and magnetic results suggest  $\text{Co}^{2+}$  and  $\text{Co}^{3+}$  substitution with Mn ions for  $x \leq 0.50$  and  $x > 0.50$ , respectively. The results also show that the sample for  $x = 0.50$  has a lower symmetry, smaller crystallite size (bigger surface area) and a higher content of  $\text{Co}^{2+}$  than the other samples which make it the best catalyst for  $\text{C}_2\text{H}_6$  combustion and CO oxidation.

**Acknowledgment:** The authors wish to thank Frances Hellman, from the University of California-Berkeley for her help with the magnetic measurements.

## REFERENCES

1. P. Ciambelli, S. Cimino, S. De Rossi, L. Lisi, G. Minelli, P. Porta, G. Russo, *Appl. Catal. B.*, **29**, 239 (2001).
2. H. Tanaka, M. Misono, *Solid. State. Mater. Sci.*, **5**, 381 (2001).
3. C. Zener, *J. Phys. Rev.*, **81**, 440 (1951).
4. J. B. Goodenough, *J. Phys. Rev.*, **100**, 564 (1955).
5. M. A. Peña, J. L. G. Fierro, *Chem. Rev.*, **101**, 1981 (2001),
6. G. Pecchi, C. Campos, O. Peña, L. E. Cadus, *J. Mol. Catal. A: Chem.*, **282**, 158 (2008).
7. R.G. Shetkar, A.V. Salker, Electrical, *J. Mater. Sci. Technol.*, **26**, 1098 (2010).
8. E. Frozandeh-Mehr, A. Malekzadeh, M. Ghiasi, A. Gholizadeh, Y. Mortazavi, A. Khodadadi, *Catal. Commun.*, **28**, 32 (2012).
9. M. Khazaei, A. Malekzadeh, F. Amini, Y. Mortazavi, A. Khodadadi, *Cryst. Res. Technol.*, **45**, 1064 (2010).
10. A. Gholizadeh, *J. Adv. Mater. Process.*, **3**, 71 (2015).
11. A. Gholizadeh, N. Tajabor, *Mater. Sci. Semicond. Process.*, **13**, 162 (2010).
12. R. Groessinger, *Phys. Stat. Sol. (a)*, **66**, 665 (1981).
13. G. Pecchi, C. Campos, O. Peña, *Mater. Res. Bull.*, **44**, 846 (2009).
14. G.V. Bazuev, A.V. Korolyov, M.A. Melkozyorova, T.I. Chupakhina, *J. Magn. Magn. Mater.*, **322**, 494 (2010).
15. P. A. Joy, Y. B. Kholam, S. K. Date, *Phys. Rev. B*, **62**, 8608 (2000).
16. Y.D. Zhao, J. Park, R. J. Jung, H. J. Noh, S. J. Oh, *J. Magn. Magn. Mater.*, **280**, 404 (2004).

## СТРУКТУРНИ, МАГНИТНИ И КАТАЛИТИЧНИ СВОЙСТВА НА КОБАЛТ-ЗАМЕСТЕНИ МАНГАНТИНИ ПЕРОВСКИТИ

А. Голизаде<sup>1</sup>, А. Малекзаде<sup>2</sup>, М. Гиаси<sup>2</sup>

<sup>1</sup>Училище по физика, Университет Дамган, Дамган, И.Р. Иран

<sup>2</sup> Училище по химия, Университет Дамган, Дамган, И.Р. Иран

Постъпила на 4 август, 2015 г.; коригирана на 22 октомври, 2015 г.

(Резюме)

В тази работа са изследвани структурните, магнитните и каталитичните свойства на  $\text{LaMn}_{1-x}\text{Co}_x\text{O}_3$  ( $x = 0.00, 0.25, 0.50, 0.75, 1.00$ ). Структурното охарактеризиране на образците чрез прахова рентгено-структурна дифракция и с помощта на пакет от програми X'Pert и Fullprof доказва моноклинна структура (P21/n пространствена група) с  $x = 0.5$  и ромбодрична структура (R-3c пространствена група) за други проби. Тези резултати се потвърждават с FTIR-измервания. Магнитните характеристики на пробите са определени с измервания при различни температури и полета. Структурните и магнитните резултати показват, че феромагнитните взаимодействия  $\text{Co}^{2+}\text{-Mn}^{4+}$  при  $x \leq 0.5$  прогресивно се заменят с по-малко ефективните взаимодействия  $\text{Co}^{2+}\text{-Co}^{3+}$  и  $\text{Mn}^{4+}\text{-Co}^{3+}$  за  $x > 0.5$ . Каталитичната активност на  $\text{LaMn}_{1-x}\text{Co}_x\text{O}_3$  са оценени за реакциите на изгаряне на  $\text{C}_2\text{H}_6$  и окислението на CO. При сходни условия резултатите от катализата показват, че nano-перовскитът  $\text{LaMn}_{0.5}\text{Co}_{0.5}\text{O}_3$  е най-добрия катализатор за тези две реакции.

## Performance study of compartment-wise behaviour of modified anaerobic hybrid baffled (MAHB) reactor

S. R. Hassan<sup>1</sup>, N. Q. Zaman<sup>2,3</sup>, I. Dahlan<sup>3,4\*</sup>

<sup>1</sup>Faculty of Agro Based Industry, Universiti Malaysia Kelantan, Campus Jeli, 17600, Jeli, Kelantan, Malaysia

<sup>2</sup>School of Civil Engineering, Universiti Sains Malaysia, Engineering Campus, 14300 Nibong Tebal, Pulau Pinang, Malaysia.

<sup>3</sup>Solid Waste Management Cluster, Science and Engineering Research Centre, Universiti Sains Malaysia, Engineering Campus, Seri Ampangan, 14300 Nibong Tebal, Pulau Pinang, Malaysia

<sup>4</sup>School of Chemical Engineering, Universiti Sains Malaysia, Engineering Campus, 14300 Nibong Tebal, Pulau Pinang, Malaysia.

Received November 25, 2014, Revised November 2, 2015

A modified anaerobic hybrid baffled (MAHB) reactor was used to study its suitability for treatment of recycled paper mill effluent (RPME) and to establish the relationship between operational parameters and reactor design. The present study highlights the configuration of MAHB reactor, its start up, the effect of hydraulic retention time (HRT) on treatment efficiency and performance evaluation of MAHB reactor while treating RPME wastewater. The start-up process was carried out at HRT of 4 days. The MAHB reactor was run with constant feeding COD of 3000 mg L<sup>-1</sup> and HRT of 1, 3, 5 and 7 days. A start-up of 28 days was required for the MAHB reactor. Reactor performance evaluation of the compartment-wise profiles was carried out at different HRTs. Low pH of 6 – 6.2 and high volatile fatty acid concentration of 90 – 168 mg L<sup>-1</sup> were recorded in the first compartment for each HRT due to acidogenesis and acetogenesis processes. System pH and alkalinity showed an increment profile while VFA concentration decreased as it moves from compartment 1 to 5. Biogas volume was high ( 6.56 L at higher HRT) with a decreasing pattern of methane content from 96 – 35 % from compartment 1 to 5. Contrarily, at low HRT of 1 day, although the biogas volume was lower, the methane content showed an increment of 42 – 64 %. The results indicate that MAHB reactor was successfully operated in treating RPME wastewater.

**Keywords:** modified anaerobic hybrid baffled (MAHB) reactor, anaerobic digestion process, recycled paper mill effluent (RPME).

### INTRODUCTION

The application of anaerobic technology in treating industrial wastewaters highly depends on the performance of the reactor used. Thompson *et al.* [1] reported that about 80% COD removal efficiency was constantly achieved using anaerobic treatment, while Arshad and Hashim [2] obtained 58 % methane content with total organic carbon (TOC) and lignin removal efficiencies of 56 % and 51 %, respectively, at an OLR of 4.5 g TOC L<sup>-1</sup> per day and HRT of 18 h in treating the paper mill effluent. Another approach of treating paper mill effluent is by integrating two or more methods to take advantages of both processes. Shaw *et al.* [3] showed that a combination of aerobic reactor followed by anaerobic reactor is able to remove 66% of toxicity. From the survey, anaerobic baffled reactor (ABR) was one of the favorable systems in treating industrial waste. Although ABR were extensively used to treat different types of industrial waste, literature survey

shows that there is lack of data on the anaerobic treatment of recycled paper mill effluent (RPME) wastewater by a novel modified anaerobic hybrid baffled (MAHB) reactor.

This novel MAHB reactor consists of five compartments which are a combination of regular suspended growth and fixed biofilm systems. The most significant advantage of this design is the ability to nearly perfectly realize the staged multi-phase anaerobic theory, allowing different bacterial groups to develop under more favorable conditions, low costs and without the associated control problems. The MAHB bioreactor combines suspended growth and attached growth processes in a single reactor to take advantage of both biomass types [1][4].

With a less expensive, simple configuration and a background of successful performance and having been judged to perform well for industrial wastewater of conventional ABR, this hybrid novel MAHB reactor was assumed to give better performance in terms of COD removal and methane production. Keeping this as an observation, the present study was carried out to investigate the

\* To whom all correspondence should be sent:

E-mail: chirvan@usm.my

performance of the MAHB reactor treating RPME at different HRT in relationship of the compartmentalization behavior. The present study was also aimed to integrate various aspects like (a) performance of the reactor and compartment-wise variation of various parameters and (b) stable operation for a quite extended period in terms of COD removal efficiency, biogas production and performance of each different compartment of the MAHB reactor.

## METHODS

### Reactor configuration

A laboratory-scale modified anaerobic hybrid baffled (MAHB) reactor was fabricated using polypropylene. It consisted of 5 chambers (CH1–CH5) of equal size and volume, connected in series as shown in Fig 1.

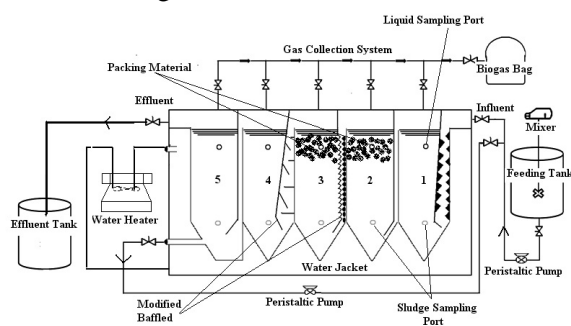


**Fig. 1.** Schematic diagram of 58 L capacity bench-scale continuous feed MAHB reactor.

The whole unit is square in shape with length to width ratio ( $l/w$ ) of 3.61 and  $l \times b \times h$  dimensions of 795 mm  $\times$  220 mm  $\times$  300 mm. To collect the biogas produced, five separate gas manifolds were provided and the biogas was finally led to the gas collection cum measurement assembly. The individual chamber was divided by a hanging baffle into five compartments, i.e., downcomer and upcomer. The volume of the downcomer was half that of the upcomer and the bottom portion of the baffle separating the two compartments was inclined at 45° and was stretched up to the center of the upcomer. The total volume of the modified anaerobic hybrid baffled (MAHB) reactor was 65 L with a net working volume of 58 L. The volume of the individual set of 5 compartments (CH1–CH5) was 11.6 L. The net volumes of the downcomer and the upcomer were 3.86 L and 7.74 L, respectively.

### Feed wastewater flow pattern

The wastewater was collected from Muda Paper Mill Bhd, Bandar Tasek Mutiara, Penang, Malaysia and refrigerated at 4°C. Prior to analysis, the

samples were warmed to room temperature ( $25 \pm 2^\circ\text{C}$ ). The collected samples were analysed for the required parameters such as pH, total dissolved solids (TDS), volatile suspended solids (VSS), total suspended solids (TSS), total solids (TS), alkalinity, ammonia, biological oxygen demand (BOD) and dissolved oxygen (DO) according to the Standard Methods of Analysis of Water and Wastewater [5] and were intermittently mixed to feed the reactor with a consistent quality.

**Table 1.** Physicochemical characteristics of recycled paper mill effluent.

Parameter	Concentration
pH	6.36
Alkalinity ( $\text{mg L}^{-1}$ as $\text{CaCO}_3$ )	94
TSS ( $\text{mg L}^{-1}$ )	645
VSS ( $\text{mg L}^{-1}$ )	850
TDS ( $\text{mg L}^{-1}$ )	3345
TS ( $\text{mg L}^{-1}$ )	5320
$\text{BOD}_5$ ( $\text{mg L}^{-1}$ )	669
COD ( $\text{mg L}^{-1}$ )	4328
VFA ( $\text{mg L}^{-1}$ )	501
Ammonia ( $\text{mg L}^{-1}$ )	0.4
DO ( $\text{mg L}^{-1}$ )	1.5

The wastewater was fed to the reactor with the help of a variable speed peristaltic pump. The MAHB reactor was operated at various hydraulic retention times (HRTs) by varying the flowrate of influent wastewater ( $Q_{inf}$ ), thereby varying the organic loading rate (OLR). The average composition of RPME wastewater is shown in Table 1. The wastewater flows from the downcomer to the upcomer, within an individual chamber through the sludge bed formed at the bottom of the individual chambers. After receiving treatment in the particular chamber, wastewater enters the next chamber from the top. Due to the specific design and positioning of the baffle, the wastewater is evenly distributed in the upcomer and the vertical upflow velocity ( $V_{up}$ ) could be significantly reduced. The treated effluent was collected from the outlet of CH5. The reactor was kept in a temperature controlled chamber maintained at 35°C.

### Sampling and Analysis

MAHB reactor was monitored every two days for COD, pH and biogas produced while volatile fatty acids (VFA) and alkalinity were measured weekly. Samples were taken for analysis from all five compartments of MAHB at HRT of 1, 3, 5 and 7 days as the system achieved its steady state. Biogas composition was determined using Shimadzu gas chromatograph with a flame ionization detector (GC-FID) with a propack N column. Carrier gas was helium set at a flow rate of 50 mL min<sup>-1</sup>, column temperature of 28°C, detector temperature of 38°C and injector temperature of 128°C. VFAs were measured using esterification methods. Triplicate samples were collected for each parameter reading to increase the precision of the results, and only the average value was reported throughout this study. Conventional parameters such as pH and alkalinity were measured according to the Standard Methods [5] while COD was measured using the spectrophotometer DR-2800 according to the reactor digestion method [6].

## RESULTS AND DISCUSSION

### Start-up of MAHB reactor

In this study, the MAHB reactor was filled with seed sludge taken from Malpom and allowed to rest for 12 days. Then, after 15 days, feeding of the RPME wastewater was resumed at a flow rate of 14.5 L per day at HRT of 4 days with a very low organic loading rate (OLR) of 0.1963 g COD L<sup>-1</sup> per day. The resumed wastewater feeding helped the development of the sludge bed at the bottom of the individual compartments of the MAHB reactor. The acclimatization curve for determination of the start-up period is shown in Fig. 2.

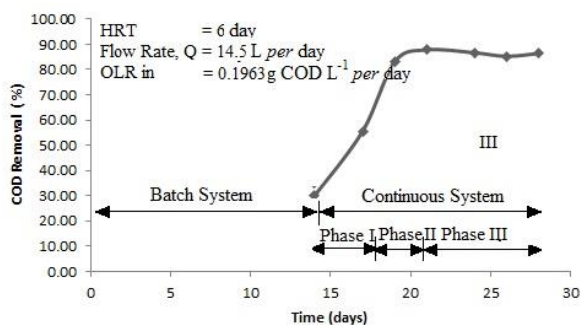


Fig. 2. Acclimatization curve for determination of the start-up period of MAHB reactor

S-shaped acclimatization curve with three distinct phases was demonstrated during the acclimatization period. During phase I of the acclimatization period of 16 days (from day 12 until day 17), the observed SS and COD removal

may be attributed to the interception of organics in the sludge bed. During the second phase of 5 days (17th – 21st day), a significant gain of up to 90% was observed in COD removal. The curve indicated that the COD reduction efficiency was related to the period of acclimatization. The steady state of increase in efficiency signified the adequate quantum of biosludge accumulation in the reactor [7]. The third phase of acclimatization lasted for 8 days (from day 21 until day 28). Last four consecutive observations revealed consistent COD removal efficiency of 85% and specific biogas yield of 0.25 L CH<sub>4</sub> per day. At this stage, the MAHB reactor was counted as matured or acclimatized. Therefore, the start-up period for the MAHB reactor was adjudicated to be 28 days. From previous studies, Lettinga *et al.* [8] took about 84 days for the start-up, whereas Kalogo *et al.* [9] required a period of 140 days of self-inoculated UASB. The anaerobic contact filter was started-up by feeding cow dung slurry and sewage sludge by Vijayaraghavan and Ramanujan [10] who needed 160 days to complete the start-up operation. The analysis of the requirements of start-up periods showed that the time consumed by the MAHB reactor was favorably comparable.

### Performance evaluation of MAHB reactor

#### Compartment-wise profile during HRT variation

Performance of MAHB reactor was subjected to four changes in HRT by increasing the feed flow rate. Figure 3 illustrates the COD removal efficiency and VFA concentration at different compartments of MAHB reactor. From the obtained results, it is seen that at each different HRT of 1, 3, 5 and 7 days, the COD removal efficiency shows an increasing pattern from compartment 1 to 5. COD removal efficiency was low at HRT of 1 day with an average of 50 – 92% from compartment 1 to 5.

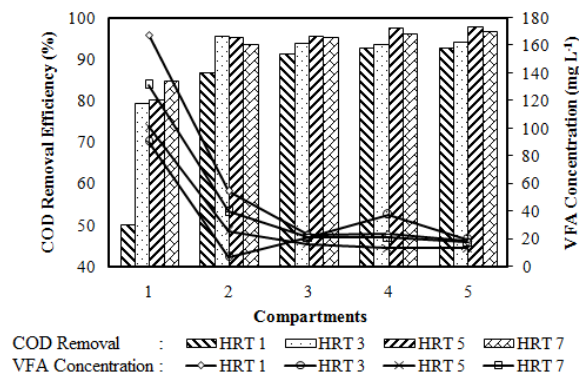


Fig. 3. COD removal and VFA concentration variation of each compartment of the MAHB reactor. Compartments are numbered in the sequence of flow pattern from compartment 1 to 5 at steady state.

From the obtained results it follows that at each different HRT of 1, 3, 5 and 7 days, the COD removal efficiency shows an increasing pattern from compartment 1 to 5. COD removal efficiency was low at HRT of 1 day with an average of 50 – 92% from compartment 1 to 5.

As the HRT was increased, the COD removal efficiency started to increase to a range of 79 – 94 %, 80 – 97 % and 84 – 96 % for HRT of 3, 5 and 7 days, respectively. This result shows that the retention times play an important role for the microbes inside to digest the substrate. Similar patterns were recorded by Krishna *et al.*[11], which indicates that COD removal efficiency of each compartment increased in the sequence of flow pattern from compartment 1 to 5. It is essential to note that as the HRT increased, the compartment-wise COD removal efficiency increased. In compartment 1, as the HRT increased, significant increase of COD removal efficiency was recorded. This shows that most of the organic matter was removed in the first compartment [12] while treating low-strength RPME wastewater using MAHB reactor.

In addition, VFA concentration tends to decrease with high HRT. The maximum VFA concentration achieved was 167 mg L<sup>-1</sup> in compartment 1 at HRT 1. As the wastewater moves from compartment 1 to 5, the concentrations of VFA decreased for all HRTs. This is a result of the conversion of VFA into final products such as hydrogen, carbon dioxide and acetate for methane production.

The VFA profile demonstrated that the main biochemical activities occurring in the first few compartments are hydrolysis and acidogenesis [13, 14]. For the last few compartments, methanogenesis appeared to be dominant. These observations implied that the MAHB reactor promoted a systematic selection in the different compartments in such a manner as to bring out phase separation. Wang *et al.* [15] also reported that the total VFA concentration decreased along the reactor from compartment 2 while treating high-strength wastewater using conventional ABR.

#### System pH and alkalinity for different compartments

The pH and alkalinity profiles for the MAHB reactor at different HRTs are shown in Figure 4. Slightly lower pH was noted in compartment 1 for each different HRT in a range of 6.1 to 6.3. As the wastewater moves towards the later compartments, a gradual increase in pH was achieved. The pH was found close to 7 (6.3 – 6.55) at the rear end of the

MAHB reactor. Similar patterns were also recorded by Dama *et al.* [16] who reported that earlier compartments had a lower pH as acidogenesis and acetogenesis take place in those compartments. It was also observed that during every shift to the next HRT, the pH in the first two chambers dropped rapidly, while other chambers (CH3–CH5) were found to be less affected.

This indicated that accumulation of fatty acids was restricted up to CH3 only, unaffacting the methanogenesis occurring in the rest of the chambers.

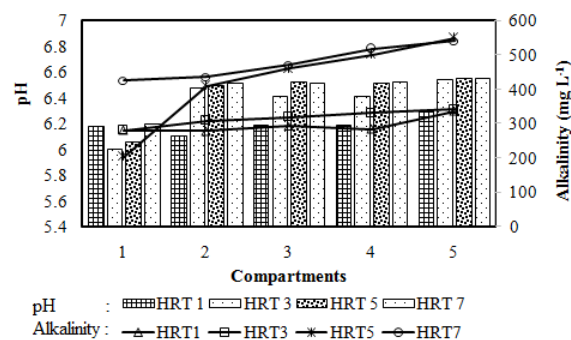


**Fig. 4.** pH and alkalinity variation of each compartment of MAHB reactor. Compartments are numbered in the sequence of flow pattern from compartment 1 to 5 at steady state.

This was due to the fact that hydrolysis, acidogenesis and acetogenesis occur in the initial chambers. Furthermore, degradation of VFA results in the increment of pH from compartment 1 to compartment 5 [17]. The distinct pH profile shows an indication of the degree of different phases created within the system. Similar alkalinity profiles were noted in the compartment-wise arrangement of the MAHB reactor.

#### Gas Production and Composition

Figure 5 illustrates the biogas volume and the methane content for each compartment at different HRTs. Overall, the biogas volume for HRT 3 was higher (range of 3 to 6.6 L per day) than for HRT 1 (range of 1.3 to 3.2 L per day) due to the longer hydraulic retention times which give enough time for the anaerobic process to take place in each compartment. For HRT 1 day, the total biogas volume increased from 2.2 to 3.2 L per day from compartment 1 to 3 but then decreased to 1.8 L per day in compartment 5 and *vice versa* for HRT 3. For longer HRTs, the travelling time to move up and down the compartment of the reactor is longer, which contributes to a larger biogas volume. However, most of the nutrients were already converted to methane in the first three

compartments. This explains the decrement of biogas volume at the last two compartments.

The methane content of the total biogas produced was determined every two days until it reached steady state. The order of the compartments from 1 to 5 shows that the methane content of the total biogas increased in sequence under HRT of 1 day (OLR = 3 g CODL<sup>-1</sup>per day) but decreased for HRT of 3 days (OLR = 1 g CODL<sup>-1</sup>per day). These results were in accordance with the conclusion of former studies by Uyanik [18] who indicated that acidogenic reactions were dominant in the earlier compartments of the MAHB reactor. However, at HRT of 3 days (with high OLR), the accumulation of VFA resulted in reduction of methane percentage through the rear of the reactor. The methane content, which can be a valuable indicator of the performance of the MAHB reactor shows a stepped up value from 42% to 64% as the HRT decreases under the average OLR of 3 g CODL<sup>-1</sup>per day. These results are in agreement with previous research by Liu *et al.* [19].

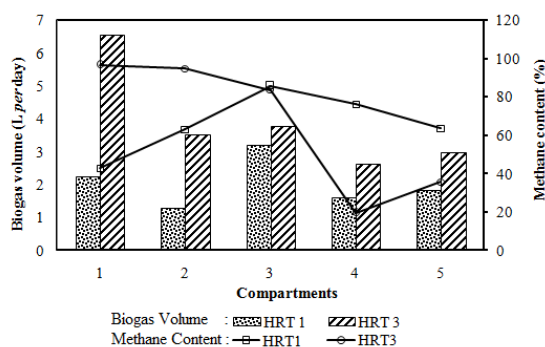


**Fig. 5.** Gas production variation of each compartment of the MAHB reactor at HRT of 1 day and 3 days.

Obviously, high methane content suggests high activity of methanogenic bacteria. The methanogenic bacteria can be divided into two main groups due to differences in substrate utilization - hydrogenotrophic and acetotrophic methanogens [20]. Hydrogenotrophic methanogens only use CO<sub>2</sub> and H<sub>2</sub> as their substrate. The partial pressure of hydrogen acts as a main indicator to describe disturbances and stability in AD. For that reason, hydrotrophic methanogens activity is crucial for the efficiency and stability of AD in processing of simple soluble types of substrates (i.e. ethanol, propionate, dextrose and acetate) and numerous types of wastewater. For acetotrophic methanogens, such as *Methanosarcinales* genus, they use simple compounds such as acetate as their substrate. More than 70% of biomethane are produced by acetate degradation. Methanogenic

bacteria that bind hydrogen are found to belong to *Methanobacteriaceae* family [21].

For cellulose (lignin) saccharification, the microbes that facilitate the process might consist of hydrolyzing and acid producing microorganisms. The primary route is the initial cleavage of ether-linked subunits followed by subsequent degradation of substituted aromatic rings where the derivatives of vanillic acid, cinnamic acid and syringic acid are the important constituents of lignin. For this AD process, fermenting bacteria (i.e., methanogenic bacteria) and acetogenic bacteria are responsible for breaking this ether-linked and aromatic ring bond [22].

## CONCLUSIONS

The present study revealed that HRT significantly influences the compartment-wise profile of MAHB reactor in terms of COD removal, VFA concentration, pH and alkalinity, methane content and biogas volume in treating RPME wastewater. The pH profile shows an increment within a range of 6.3 to 6.6 as the RPME wastewater moves towards the end of the MAHB reactor. Maximum alkalinity obtained was between 335 and 548 mg L<sup>-1</sup> in compartment 5 for each different HRT. The maximum methane content was 96.8 % with total biogas volume of 6.56 L per day at HRT of 3 days (OLR of 1 g CODL<sup>-1</sup>per day) in the MAHB reactor. High COD removal of 98.0% was achieved at HRT 5 of 0.6 g CODL<sup>-1</sup>per day. Therefore, the optimum HRT for anaerobic treatment of RPME in MAHB reactor was 5 days. Moreover, high COD removal and methane content was achieved in the MAHB reactor.

**Acknowledgement:** The authors acknowledge the financial support from the Universiti Sains Malaysia (RU-I A/C.1001/PJKIMIA/814148) and MyBrain15 Scholarship (KPM(B) 870204115782).

## REFERENCE

1. G.Thompson, J. Swain, M. Kay, C.F. Forster, *Bioresource Technology*, **77**, 275 (2001).
2. A. Arshad, N.H. Hashim. *International Journal of Environmental Research*, **6**, 1735 (2012).
3. C.B. Shaw, C.M. Carliell, A.D. Wheatley, *Water Research*, **36**, 1993 (2002).
4. S. R. Hassan, H. M. Zwain, I. Dahlan, *Journal Advance Science Research*, **4**, 07 (2013).
5. L.S. Clescerl, A.E. Greenberg, A.D. Eaton, eds. Standard methods for the examination of water and wastewater, American Public Health Association, American Water Works Association, Water Environment Federation, Washington, 1998.



6. S.R. Hassan, H. M.Zwain, N. Q. Zaman, I. Dahlan, *Environmental Technology*, **35**, 3(2013).
7. M. Hutnan, M. Drtil, L. Mrafkova, J. Derco, J. Buday, *Bioprocess Engineering*, **21**, 439 (1999).
8. G. Lettinga, J. Field, J. van Lier, G. Zeeman, L.W. HuishoffPol, *Water Science and Technology*, **35**, 5 (1997).
9. Y. Kalogo, J.H. MBouche, W. Verstraete, *Journal of Environmental Engineering*, **127**, 179 (2001).
10. K. Vijayaraghavan, T.K. Ramanujam, *Bioprocess Engineering*, **20**, 499 (1999).
11. G.V.T.G. Krishna, P. Kumar, P. Kumar, *Journal of Environmental Management*, **90**, 166 (2009).
12. C. Polprasert, P. Kemmadamrong, F.T. Tran, *Environmental Technology*, **13**, 857 (1992).
13. J.C. Akunna, M. Clark, *Bioresource Technology*, **74**, p? (2000).
14. M.I. Baloch, J.C. Akunna, *Journal of Environmental Technology*, **129**, 1015 (2003).
15. J. Wang, Y. Huang, X. Zhao, *Bioresource Technology*, **93**, 205 (2004).
16. P. Dama, J. Bell, K.M. Faxon, C.J. Brouckaert, T. Huany, C.A. Buckley, *Water Science Technology*, **26**, 263 (2002).
17. M.I. Baloch, J.C. Akunna, P.J. Collier, *Bioresource Technology*, **98**, 1849 (2007).
18. S.Uyanik, P.J. Sallis, G.K. Anderson, *Water Research*, **36**, 933 (2002).
19. X. Liu, N. Ren, Y. Yuan, *Bioresource Technology*, **100**, 104 (2009).
20. B. Demirel, P. Scherer, *Reviews in Environmental Science and Bio/Technology*, **7**, 173 (2008).
21. D.R. Boone, D.P. Chynoweth, R.A. Mah, P.H. Smith, A.C. Wilkie, *Biomass and Bioenergy*, **5**, 191 (1993).
22. J.J. Ko, Y. Shimizu, K. Ikeda, S.K. Kim, C.H. Park, S. Matsui, *Bioresource Technology*, **100**, 1622 (2009).

## ИЗСЛЕДВАНЕ НА СЕКЦИОННОТО ПОВЕДЕНИЕ НА МОДИФИЦИРАН АНАЕРОБЕН ХИБРИДЕН РЕАКТОР С ПРЕГРАДИ (МАНВ)

С.Р. Хасан<sup>1</sup>, Н.К. Заман<sup>1</sup>, И. Дахлан<sup>2\*</sup>

<sup>1</sup>Училище за строително инженерство, Саинс-университет в Малайзия, 14300 Нибонг Тебал, Пулау Пинанг, Малайзия

<sup>2</sup>Училище по химично инженерство, Саинс-университет в Малайзия 14300 Нибонг Тебал, Пулау Пинанг, Малайзия

Постъпила на 25 ноември, 2014 г.; коригирана на 2 ноември, 2015 г.

(Резюме)

Използван е модифициран анаеробен хибриден реактор с прегради (МАНВ) за изучаването на приложимостта му за третиране на отпадъчни води от рециклирането на хартия (RPME) и установяването на връзката между работните параметри и оформлението на реактора. Определени са конфигурацията на реактора, пускането му в действие и ефекта на времепребиваването (HRT) върху ефективността на пречистване и работата на реактора. Пусковият процес се зивършва при времепребиваване от 4 дни. МАНВ-реакторът работи с постоянно хранване с ХПК от 3000 mg L<sup>-1</sup> и времепребиваване HRT от 1, 3, 5 и 7 дни. Пусковият период е 28 дни. Работата на реактора се оценява по секционните профили за различни HRT. В първото отделение се наблюдават рН от 6 – 6.2 и високи концентрации на летливи мастни киселини от 90 до 168 mg L<sup>-1</sup> при всяко времепребиваване заради ацидогенезата и ацетогенезата. рН и алкалността на системата показва нарастване на профила по дължината на реактора, докато концентрациите на мастните киселини намалява от отделение 1 до отделение 5. Обемът на биогаза е голям ( 6.56 L при високи HRT) с намаляване на съдържанието на метан от 96 до 35 % от отделение 1 до 5. Обратно, при малки HRT (1 ден), въпреки че бемът на биогаз е малък, съдържанието на метан нараства от 42 до 64 %. Резултатите показват, че МАНВ-реакторът работи успешно за пречистването на отпадъчни води от рециклирането на хартия.

## Sorption capacity of oil sorbent for the removal of thin films of oil

D.A. Baiseitov, M.I. Tulepov, L.R. Sassykova\*, Sh.E. Gabdrashova, G.A. Essen, K.K. Kudaibergenov, Z.A. Mansurov

*Al-Farabi National University, Almaty, Kazakhstan*

Received May 4, 2015, Accepted July 27, 2015

The dependence of the sorption capacity of the sorbents on the amount of sorbent, sorption time, thickness of the oil film, as well as the number of cycles of use of the sorbent was investigated. The performed studies in this work demonstrated the potential use of the synthesized sorbents as adsorbents for the removal of thin oil films.

**Keywords:** oil sorbent, sorption capacity, thin oil film.

### INTRODUCTION

At present, the pollution of surface water bodies by petroleum hydrocarbons occurs not only under accident oil spills, but also during routine maintenance. The process of operative removal of oil pollution from the water surface is topical considering the increasing technogenic impact on the ecosystem. It is therefore particularly important to solve this problem. There is search of materials suitable for collecting oil from surface water and sewage industrial water.

Cleaning of the surface of water bodies from contamination involves the removal of the oil film by mechanical and (or) physical and chemical methods. Most promising and environmentally expedient is the method of removing oil film with the help of oil sorbents [1]. The materials used for the collection of oil and petroleum products from water, are commonly called oil sorbents, as well as collectors of oil and oil absorbers. One of the main problems when cleaning the surface of water bodies from pollution is the removal of a thin oil film having the ability to spread in the shortest terms over vast distances, violating the oxygen exchange [2-3].

For the production of oil sorbents various raw materials are applied [4]. By the mechanism of oil removal are distinguished the sorbents, for which physical surface adsorption dominates. Here, the collection of oil occurs due to adhesion to the surface of the sorbent particles. In this case, the amount of oil absorbed is determined by the specific surface area of the material and its properties (hydrophobic and oleophilic). Literature data show that such a mechanism for collecting of oil and petroleum products is realized for oleophilic

powders and granular materials with closed porous structure and materials in which the pores by size are not available for the molecules of the removable substances [5].

### EXPERIMENTAL

All experiments were carried out by the methods described in [6-8]. A Petri dish was filled with water and weighed, and then an oil slick was applied to the water surface so that it didn't touch the walls of the cup, followed by the cup reweighed. Then, on the oil slick a sample of sorbent was applied to complete absorption of the oil spill and the cup was reweighed. Gain of oil weight to the weight of the sorbent gave the value of the absorption capacity of the sorbent in water.

Weight of dry cup was 134.15 g and with water - 178.93 g. The weight of the oil slick was 0.4 g and the weight of the cup became 179.33 g. After the total absorption of the oil slick by a modified carbon sorbent with weight of 0.04 grams, the weight of the cup amounted to 179.37 g, and the sorption capacity was 10.0 g/g.

The weight of the cup with water was 173.44 g and 173.90 - with the oil spill, after applying the carbon sorbent of vegetable origin of weight 0.22 g, the oil spill was absorbed by the sorbent. The sorption capacity of the sorbent was 5, i.e. 1 g of sorbent could adsorb 5 g of oil.

After repeating the experiment with stirring of oil and sorbent, the total absorption of the oil slick was achieved with 0.05 g of modified carbon sorbent, i.e. the adsorbent capacity increased to 10.9 g/g.

For creation of an oil film into a Petri dish, about 40 ml of water with a salt concentration of 17-20 g/l (seawater) was poured and a few drops of oil were added. When the oil slick was formed, its diameter and thickness were determined.

\* To whom all correspondence should be sent:  
E-mail: larissa.rav@mail.ru

## RESULTS AND DISCUSSION

In the laboratory tests the medium viscous oil of Karazhanbas was used (Figure 1).

The dependence of the sorption capacity of the obtained carbonized sorbents based on rice husk (CRH) on the amount of sorbent, the sorption time, the thickness of the oil film, as well as the number of cycles of use of the sorbent was studied.

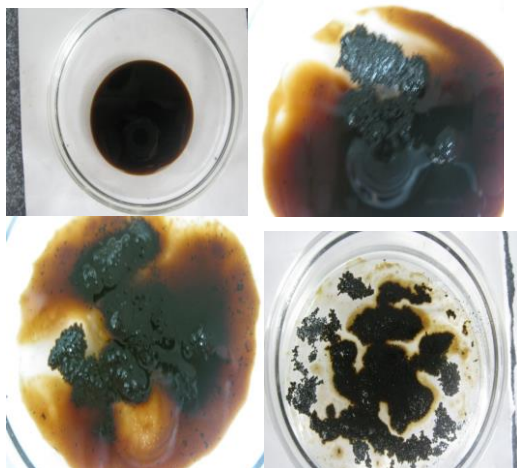


**Fig. 1.** Sorption of oil of Karazhanbas.

Figure 2 shows the sorption capacity of the sorbents on the sorption time. As can be seen from the presented data, the maximum sorption of oil is in the first minutes (~ 3-4 minutes), after which the sorbent based on foam rubber and sunflower husk carbonizate (FRCSH- 300) is able to retain the sorbed oil for two days, whereas the sorbents on the basis of polystyrene foam and carbonizate of rice husk PFCRH-400 and modified foam rubber (MFR-300) after active sorption gradually began to release it after 4 hours.

Such behavior of the sorbents may be due to the lower level of hydrophobicity and oleophilicity of the sorbents based on PFCRH-400 and MFR-300, and the different structure of the sorbents.

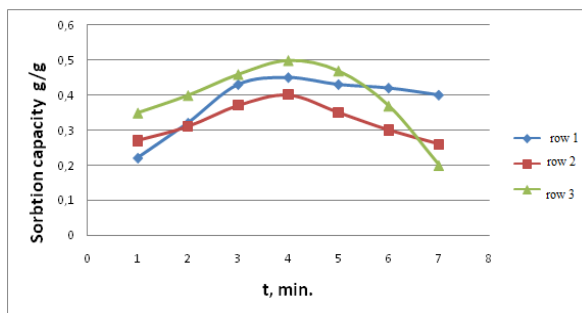


**Fig. 2.** Dependence of the sorptive capacity of the sorbents on the sorption time: 1 - Foam rubber + carbonizate of sunflower husk (FRCSH- 300) 2 - Foam polystyrene + carbonizate of rice husk (PFCRH-400) 3 - Modified foam rubber (MFR -300)

The sorption capacity of vegetable materials without polymers was studied as well. With the increase in mass of the sorbent amount, the sorbed by it oil gradually increased. After reaching the optimal sorption time (4 hours), the speed of active sorption markedly decreased, which may be explained, apparently, on the one hand by the oil saturation of the sorbents, and on the other hand, by the process of desorption (in the case of CRH-400 and -300).

The dependence of the sorption capacity of the sorbents on the thickness of the oil film was also studied (Fig.3).

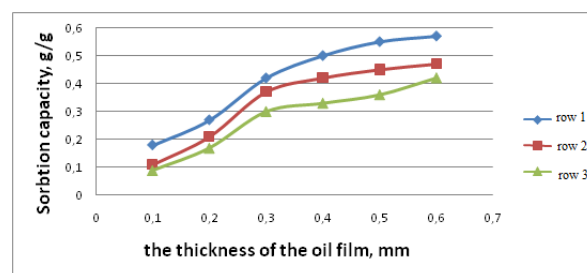


**Fig. 3.** - Dependence of the sorption capacity of the sorbent on the thickness of the oil film: row 1 - Foam rubber + carbonizate of sunflower husk (FRCRH- 300); row 2- Foam polystyrene + carbonizate of rice husk (PFCRH -400); row-3 modified foam rubber (MFR-300)

It is known that the maximum absorption capacity of the sorbent is exhibited with an excess amount of absorbed oil [9,10]. As seen in Fig.3, the increase in the thickness of oil film increases the oil absorption capacity of the sorbents.

The results of the studies of the dependence of the sorption capacity of the sorbents on the number of cycles used are shown in Table 1.

Regenerability of sorbents in one of the basic performance parameters. The obtained data illustrate the good regenerability of the sorbents and the possibility of their repeated use.

Regeneration of the sorbents was carried out by centrifugation by washing with a hydrocarbon solvent and followed air drying.

The data in Table 1 demonstrate the potential use of the sorbents synthesized by us as adsorbents for the removal of thin oil films.

We have also studied the maximum oil absorption of CKP-400, depending on the viscosity and the physical state of aggregation, i.e. the sorbed oil product was a petroleum oil, oil, gasoline and diesel fuel.

In the cases when the thickness of oil spill layer is less than the thickness of the sorbent the collection of oil from the water surface also occurs beyond the sorbent place. Table 2 shows that the sorbent absorbs oil «Mobil», to a higher extent than

gasoline and diesel. This is probably due to the higher affinity of the sorbent to the sorbed oil.

With increasing film thickness, the oil sorption capacity of the sorbent increases.

From the data of Table 2 it is clear that the collection of relatively low-viscosity products (gasoline and diesel) racking of their excesses and real-absorbing properties of the sorbent are characterized by oil absorption at the level of 30-40 g/g.

This sorbent is easily regenerated by simple squeezing of the absorbed oil. Despite of the high oil absorption of sorbent "CRH- 400" its application in dispersed form is not enough technological due to the significant time consuming

technical difficulties that arise at spraying of the sorbent on the surface oil spills and subsequent collection of the spent sorbent.

Since the performance of the sorbent heavily depends on the ambient temperature, for example, in winter conditions, we also investigated the effect of ambient temperature and volume weight of sorbents based on Apricot stone CAS-400 and rice husk CRH-400.

Table 3 represents the temperature dependence of the sorption capacity of sorbents (CAS - 400 with weight by volume of 50 g/cm<sup>3</sup> and CRH- 400 with weight by volume of 150 g/cm<sup>3</sup>) on oil and petroleum products in the temperature interval 10-50 °C.

**Table 1.** Dependence of the sorption capacity of the sorbents on the number of cycles used

Number of Cycles	Sorption Capacity, g/g		
	FRCRH-300	FPCRH-400	MFR -300
1	0.45	0.49	0.42
2	0.44	0.40	0.40
3	0.35	0.38	0.40
4	0.33	0.35	0.32

**Table 2.** Effect of the thickness of oil and oil products on the sorption capacity of the sorbent CRH-400, g/g

Collected oil product	Layer thickness, cm	Amount (g/g) of the sorbent on the collected oil product		Degree of squeezing, %
		absorbed	squeezed	
Oil field "Kumkol"	4.1	38-40	28	86
Oil "Mobil"	1.1	53-60	43	87
Motor car gasoline	3	32-33	25	78
Diesel fuel	4	24-30	19	77

**Table 3.** Influence of temperature of the medium and bulk density of sorbents on the sorption capacity on oil and petroleum products (g/g).

Weight by volume, g/cm <sup>3</sup>	Temperature of medium, °C	Sorption capacity of sorbents, g/g			
		Oil	Fuel oil	Diesel fuel	Gasoline
CAS-400 50 g/cm <sup>3</sup>	10	9.3	7.4	1.6	1.4
	15	12.4	11.5	2.4	2.1
	25	15.6	16.2	3.5	3.0
	30	17.4	17.3	3.5	2.4
	35	20.4	21.4	2.4	-
	40	22.5	24.2	1.0	-
CRH-400 150 g/cm <sup>3</sup>	10	4.0	2.2	8.3	7.2
	15	5.3	2.5	9.2	8.1
	20	5.4	2.6	10.3	9.1
	25	6.2	3.4	11.4	12.1
	30	8.1	5.2	12.5	12.1
	35	8.8	6.3	12.4	-
	40	10.2	7.2	12.0	-

Analyzing the data of Table 3, we can come to the following regularities: in the case of oil and fuel oil, temperature increase leads to a constant growth of the sorption capacity for oil and fuel oil of the sorbent CAS-400. In this case, the established temperature limit for the sorbents is not the limit of saturation of oil and fuel oil.

The maximum adsorption capacities of these sorbents are 22.5 and 24.2 g/g, respectively. In the case of gasoline and diesel fuel in the sorbent CAS-400 with weight by volume of 50 g/m<sup>3</sup> the maximum sorption of diesel fuel was achieved at a temperature of 30°C and was equal to 3.5 g/g. A further increase in the temperature of the medium causes a decrease in the sorption capacity of the sorbent on diesel fuel. This is due to the fact that the sufficiently large mesh size of the sorbent AS - 400 ensures that the forces of attraction between the sorbate molecules are higher than those between the sorbate and sorbent molecules, resulting in a liquid phase portion flowing from the cells of a solid sorbent during weighing [11].

In the same Table 3 the regularities of the changes of the sorption capacity of the sorbent CRH-400 with a bulk density of 150 g/m<sup>3</sup> with temperature are given. By analogy, in this case, regardless of the type of the sorbate, a regular increase of the temperature of sorption capacity was observed. This is due to the fact that with increasing temperature, the viscosity of oil and petroleum products is reduced, and thereby, the migration of sorbate to a diffusion region of fine-mesh macrostructure of the sorbents is accelerated. However, here, an opposite picture is observed: the sorption capacity for diesel fuel and gasoline is higher than that of oil and fuel oil. In this case, we are confronted with the specifics of selective sorption of sorbents and their ability to selectively perform the sorption of oil and petroleum products, depending on the size of the cells and bulk density. The studies revealed that the conducted studies allow to speak about potential use of the sorbents synthesized by us as adsorbents for the removal of thin oil films. On the basis of experimental data it was revealed that the maximum absorption of crude

oil is reached at equal proportions of the film thickness of dispersed sorbent and the thickness of layer of an oil spill, i.e. in the case of oil «Mobil» with a layer thickness of 1.1 cm the maximum adsorbed quantity of oil products is 53-60 g.

## CONCLUSION

It was found that irrespective of the type of oil and volume weight of the sorbent, with an increase of thickness of layer of oil from 1.0 to 7.0 mm there was a general tendency to increase the sorption capacity. It is interesting to note that the maximum sorption for each type of oil occurred on sorbents with definite values of bulk density.

## REFERENCES

1. F.A. Kamenshikov, E.I. Bogomolnii, Oil sorbents, M., Izhevsk, Institute of computer science, 2003, p. 268.
2. V. E. Ryabchikov, Modern methods of water preparing for industrial and domestic use, M., De Le print, 2004, p. 300.
3. F.A. Kamenshikov, E.I. Bogomolnii, Removal of oil products from the water surface and ground, M., Izhevsk, Institute of Computer Science, 2006, p.528.
4. G.I. Gorozhankina, L.I. Pinchukova, *Pipeline transport of oil*, **4**, 12 (2000).
5. V.V.Bordunov, E.O.Koval, I.A.Sobolev, *Oil and gas technologies*, **6**, 30 (2000).
6. J. Jandosov, Z.A. Mansurov, M.I. Tulepov, M.A. Biijsenbaev, Z.R. Ismagilov, N.V. Shikina, I.Z. Ismagilov, I.P. Andrievskaya, *Periodical of Advanced Materials Research*, **602-604**, 85 (2013).
7. K. Kudaibergenov, Y. Ongarbayev, Z. Mansurov, M. Tulepov, Y. Tileuberdi, *Applied Mechanics and Materials*, **446 – 447**, 1508 (2014).
8. K. Kudaibergenov, Y. Ongarbayev, M. Tulepov, Z. Mansurov, *Advanced Materials Research*, **893**, 478 (2014).
9. H. Luik, I. Johannes, V. Palu, L. Luik, K. Krwusement, *J. Anal. Appl. Pyrolysis*, **79**, 121 (2004).
10. R.-Q. Sun, L.-B. Sun, Y. Chun, Q.-H. Xu, *Carbon*, **46**(13), 1757 (2008).
11. Y.N. Kahramanly, *Refining and Petrochemistry*, **12**, 42 (2010).

## СОРБЦИОНЕН КАПАЦИТЕТ НА СОРБЕНТИ ЗА ОТСТРАНЯВАНЕ НА ТЪНКИ СЛОЕВЕ ОТ НЕФТ

Д.А. Байсейтов, М.И. Тулепов, Л.Р. Сасикова, Ш.Е. Габдрашова, Г.А. Есен, К.К. Кудайбергенов, З.А.  
Мансуров

*Национален университет „Ал-Фараби“, Алмати, Казахстан*

Постъпила на 4 май, 2015 г.; приета на 27 юли, 2015 г.

(Резюме)

Изследван е сорбционният капацитет на сорбенти в зависимост от количеството, времето, дебелината на нефтения филм, както и броя на циклите на употреба. Извършените изследвания демонстрират потенциалната полза от синтетични сорбенти за отстраняването на тънки филми от нефт.

## Influence of the carrier phase composition on the catalytic activity of copper-cobalt oxides deposited on slag glass-ceramics

I. K. Mihailova<sup>1\*</sup>, S. V. Dimitrova<sup>2</sup>, D. D. Stoyanova<sup>3</sup>, D. R. Mehandjiev<sup>3</sup>

<sup>1</sup> University of Chemical Technology and Metallurgy, 8, St. Kl. Ohridski Blvd., 1756 Sofia, Bulgaria

<sup>2</sup> University of Architecture, Civil Engineering and Geodesy, 1, H. Smirnenski Str. 1046 Sofia, Bulgaria

<sup>3</sup> Institute of General and Inorganic Chemistry, Bulgarian Academy of Sciences, Acad. Georgi Bonchev Str., bld. 11, 1113 Sofia, Bulgaria

Submitted May 20, 2015; Revised November 11, 2015

In order to check to what extent the slag based glass-ceramics may be used as carriers in the preparation of active supported catalysts, copper-cobalt oxide catalysts on different carriers (glass-ceramics obtained on the basis of blast furnace slag) were studied. The catalytic activity towards the complete oxidation of carbon monoxide was evaluated. The samples were characterized by X-ray diffraction (XRD), scanning electron microscopy (SEM) and BET analyses. Three main crystalline phases were present in varying proportions in the catalyst carriers: melilite, anorthite and pyroxene. The results of catalytic tests were interpreted with respect to the catalyst carrier phase composition. It was found that the catalytic activity and the formation of catalytically active complexes depend on the phase composition of the carrier. Among the crystalline phases present in the composition of the carriers, pyroxene contributes to the formation of the most efficient catalytically active complexes.

**Keywords:** Phase composition, supported catalysts, catalytic activity.

### INTRODUCTION

Regardless of its variable composition, blast furnace slag can be successfully used as an adsorbent or as a carrier for the preparation of catalysts for full oxidation. It has been found that this is possible because of the presence of crystalline phases of the melilite group. They determine the adsorption capacity of the slag to the ions of some heavy metals such as lead, copper and the like [1–8], whereas the inclusion of transition metal ions in the crystalline structure yields catalysts for the oxidation of CO and hydrocarbons [9, 10].

The preparation of catalysts, the active phase of which is deposited on a carrier, requires the synthesis to be conducted so that there are catalytically active complexes (CAC) on the surface of the carrier [11–14]. It is essential that the carrier and its chemical nature play an important role in CAC when there are deposited catalysts, since a variety of ions from the deposited phase, but also from the carrier may be involved in it [11–14]. Therefore, the same catalytically active phase deposited on different carriers has different catalytic activity in the same catalytic reaction. It is of interest to check to what extent the slag glass-ceramics obtained on the basis of blast furnace slag, may be used as carriers for the preparation of catalysts by depositing oxides of 3d-transition

metals. For slag glass-ceramics of this type, it has been shown that the crystal structure of the phases in them conditions the adsorption capacity to the ions of lead [15].

Therefore, the aim of this paper was to study the influence of phase composition of slag glass-ceramics which were used as a carrier of copper-cobalt oxides in reactions of CO oxidation.

### EXPERIMENTAL

#### *Synthesis of the carriers*

To obtain the carriers – slag glass-ceramics, kaolin, Al<sub>2</sub>O<sub>3</sub>, and TiO<sub>2</sub> were used, as well as granulated blast furnace slag with the following composition – CaO (40.5%), SiO<sub>2</sub> (35.2%), A<sub>2</sub>O<sub>3</sub> (9.3%), MgO (5.2%), BaO (3.2%), MnO (2.6%), S (1.2%), K<sub>2</sub>O (1.0%), Na<sub>2</sub>O (0.3%), FeO (1.0), Fe (0.7%). First, the parent glasses were prepared by melting at 1450–1470 °C for 60–90 min. Then the glasses were ground, pressed and heated at 1000 °C for 3 h. The method of synthesis of the samples is described in more detail in [16]. The choice of particular compositions and additives was based on our previous experimental data [17–19], which showed that high-strength glass-ceramics could be obtained from such compositions. Four sample carriers were obtained by changing the ratio of components with a view to the formation of different crystal phases. The carriers were designated as SC (a) with initial composition: 73.6% slag and kaolin 20.7%; SC (b) with initial

\* To whom all correspondence should be sent:  
E-mail: irena66@mail.bg

composition: slag 68.2%, kaolin 20.5%, Al<sub>2</sub>O<sub>3</sub> 5.7%; SC (c) with initial composition: slag 74.3% kaolin 12.0%, Al<sub>2</sub>O<sub>3</sub> 8.0% and SC (d) with initial composition: slag 79.9%, kaolin 12.2%, Al<sub>2</sub>O<sub>3</sub> 2.2%. In all batches, 5.7% of TiO<sub>2</sub> was added.

#### *Synthesis of the catalysts*

The obtained carriers were impregnated with a solution containing copper nitrate and cobalt nitrate with different concentrations, while maintaining the atomic ratio of Cu: Co = 1: 2. The procedure was carried out using a solution/carrier ratio of 5 (v/w) at a temperature of 90 °C for 1 h. Then the samples were left in the solution without heating for 24 h and the impregnation procedure was repeated once more. After impregnation and drying at 110 °C, the samples were heated in air at 350 °C for 3 h. The samples were labeled CAT (a), CAT (b), CAT (c) and CAT (d) and they were obtained from the respective carriers – SC (a), SC (b), SC (c) and SC (d).

#### *Experimental methods*

X-ray powder diffraction (XRD) analysis was applied for phase identification. An X-ray diffractometer Philips with Cu K $\alpha$  radiation ( $\lambda = 1.5418 \text{ \AA}$ ) was used in the range from 15° to 90° 2 $\theta$  (step size: 0.05°, counting time per step: 1 s). The crystalline phases were identified using the powder diffraction file cards № 35-0755, 41-1486 and 31-0249 from database JCPDS - International Centre for Diffraction Data PCPDFWIN v.2.2. (2001) ) [20].

The microstructure of the glass ceramic materials was investigated by SEM. Microscope JEOL JSM 5510 was used. The samples were coated with gold in an auto fine coater JEOL JFC-12200.

The concentration of the solutions used just after the procedure for the deposition of copper and cobalt phases was determined by ICP-OES analysis using Prodigy high-dispersion ICP-OES spectrometer from Teledyne Leeman Labs.

The measurement of the specific surface area of the samples was carried out by nitrogen adsorption at 77.4 K. Nitrogen adsorption isotherms were used to calculate the specific surface area using the BET equation.

The catalytic activity of the samples was measured in an isothermal plug-flow reactor enabling operation under steady-state conditions without any temperature gradients. The size of the catalyst particles (0.3 – 0.6 mm) was chosen taking into account the reactor diameter (6 mm) and the hourly space velocity (20 000 h<sup>-1</sup>). The gas feed

flow rate was 4.0 L/h, the catalyst bed volume was 0.2 cm<sup>3</sup>, and the mass of the charged catalyst was 0.50 – 0.55 g. The catalytic oxidation was performed within the temperature interval 200 – 400 °C, the oxidizing agent used being oxygen from the air (gas mixture: 21% O<sub>2</sub> and 79% N<sub>2</sub>). The preliminary treatment of the catalysts included heating in air flow at 120 °C for 1 h. The flow of CO was fed into the reactor by an Ismatex M62/6 pump (Switzerland). The initial concentration of carbon monoxide was 0.5 vol. %. The carrier gas was air (a mixture of 21% O<sub>2</sub> and 79% N<sub>2</sub>). A Maihak gas analyzer (O<sub>2</sub>, CO, CO<sub>2</sub>) was used to measure the CO and CO<sub>2</sub> concentrations with an accuracy of  $\pm 0.1$  ppm, whereas the oxygen measurement accuracy was  $\pm 100$  ppm.

## RESULTS AND DISCUSSION

Table 1 presents the results of the identified crystalline phases, for the given specific surface and for the deposited amounts of copper and cobalt. As seen from the Table, three main crystalline phases in varying proportions are present in the samples: melilite, anorthite and pyroxene [15, 16].

The quantification of the contents of each of these phases in the samples showed the following: the phase content of sample CAT (a) was anorthite accounting for slightly more than 50% of the crystalline phases. The compositions of CAT (b) and CAT (c) were characterized by a more significant participation of pyroxene in the phase content; 40-51% of the crystalline phases and melilite was the predominant crystal phase only in sample CAT (d).

From the data in Table 1 for specific surface area, it is obvious that the samples differ in this indicator; the highest one is that of CAT (d). The samples also differ in contents of the two metals, but the atomic ratio is preserved and is approximately equal to two. As noted before, the preparation of the catalysts was conducted so that there were CAC with ratio Co / Cu = 2 on the surface, for which it is known to have high activity in oxidation reactions [21].

The microscopic images of the samples showed that they had very suitable microstructure for carriers of catalysts. Fig. 1 shows a microscopic image of the specimen CAT (d).

Common micro-structural features were observed in all slag glass-ceramics [15, 16]. There was a good sintering of the initial powders. The obtained glass-ceramic materials had a finely dispersed crystalline structure showing microcrystals of  $\sim 3\text{-}4 \text{ \mu m}$ . Amorphous phase densely envelopes the crystals. Idiomorphic crystals



with a characteristic morphology that corresponds to anorthite, melilite and pyroxene, respectively, were identified in large rounded pores measuring up to 10-20  $\mu\text{m}$ . The pores observed in our study (Fig. 1) were typical intragranular induced crystallization pores. We consider it probable that these pores were formed as a consequence of the crystallization of glass. The crystals formed in the amorphous matrix had a higher density than the density of the amorphous mass, which led to shrinking of the sample and the formation of induced porosity.

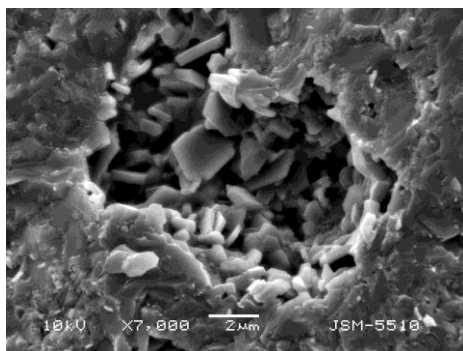


Fig. 1. SEM image of the sample CAT (d).

It was important to get information about the obtained crystalline structure containing copper and cobalt. Fig. 2 shows the X-ray-diffraction data for catalyst CAT (d), since according to chemical analysis, Table 1, this sample contains the highest amounts of the deposited phases and it is expected that this may have an impact on X-ray patterns.

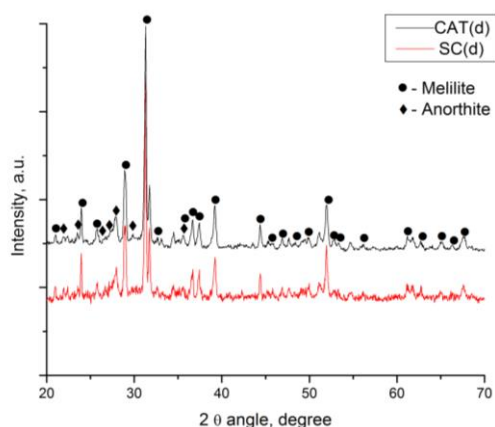


Fig. 2. X-ray diffraction data about catalyst CAT (d) and carrier SC (d)

For comparison, the X-ray pattern of the original sample used for obtaining the sample carrier SC (d) is shown. These diffraction patterns, as shown in Fig. 2, are almost identical, so unfortunately the newly formed copper- and cobalt-containing phases cannot be identified on the basis of XRD. The presence of the following crystalline phases is likely:  $\text{CuO}$ ,  $\text{Co}_3\text{O}_4$ ,  $\text{CuCo}_2\text{O}_4$ , but due to the small

quantities and the possibility of their most intense diffraction peaks to overlap with the peaks of the diffractogram of the carrier, they cannot be confirmed by XRD.

Figures 3 and 4 present the results of testing the catalytic activity of the catalysts. Fig. 3 shows data for the catalytic activity –  $\eta$  as a degree of CO oxidation in %. The catalytic activity given as an amount of oxidized CO per gram of catalyst – intensity ( $I_g$ ) is presented in Fig. 4.

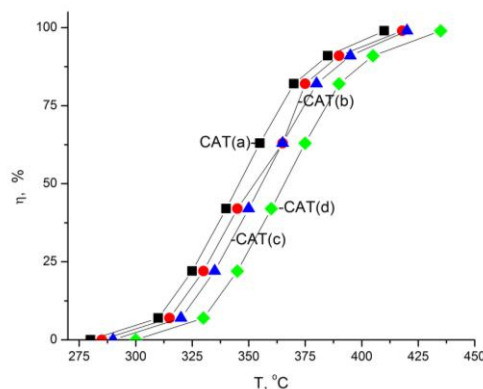


Fig. 3. Degree of conversion of CO [ $\eta$ , %] in dependence on temperature [ $T$ , °C].

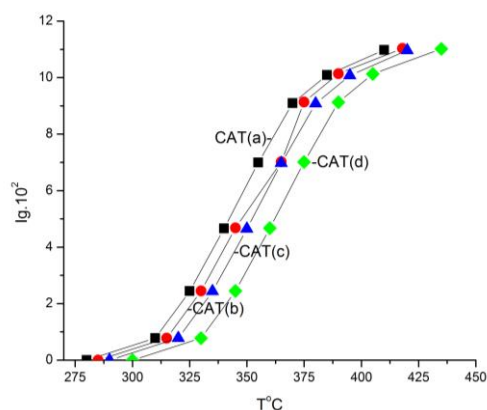
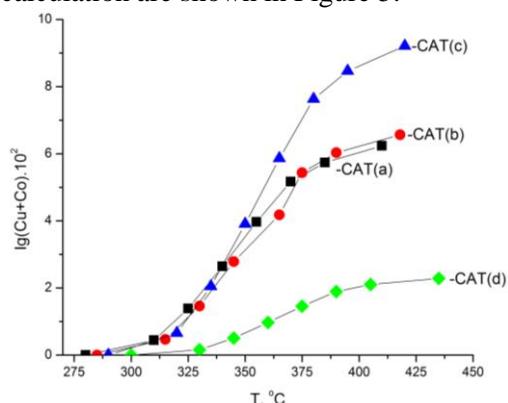


Fig. 4. Dependence of the amount of oxidized CO of 1 g catalyst for 1 hour [ $I_g$ ] on temperature [ $T$ , °C]

As it can be seen from the figures, the most active catalyst regarding both indicators is the catalyst CAT (a), and the least active one is the catalyst CAT (d). The difference in the activity of the catalysts is not huge, as it can be seen from Table 2, where the values for  $\eta$  and  $I_g$  at temperatures 365 °C are given. As the Table shows, the values for the parameter  $\eta$  are grouped in the range 76-49%. The same is true for the  $I_g$ . For CAT (a)  $I_g = 8.40 \cdot 10^{-2}$ , whereas for CAT (d)  $I_g = 5.45 \cdot 10^{-2}$ , despite the fact that the latter catalyst has the highest specific surface area (Table 1). This proves that this parameter – specific surface, is not decisive. The basic indicator must be the amount of the deposited oxide phases and their activity efficiency – namely, the activity of formed CAC. In

order to clarify how effectively the oxides of copper and cobalt are used, the intensity (I<sub>g</sub>) for one gram of total content of copper and cobalt in the catalysts (I<sub>gCu+Co</sub>) was estimated. The results of this calculation are shown in Figure 5.



**Fig. 5.** Dependence of the amount of oxidized CO of 1 g (Cu + Co) for 1 hour I<sub>g(Cu + Co)</sub> on temperature [T, °C]

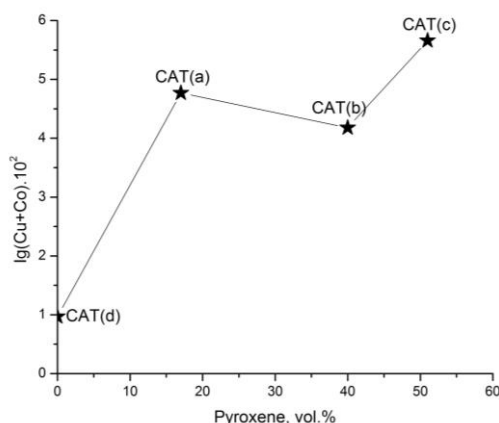


**Fig. 6.** Dependence of the intensity of the catalysts – I<sub>g(Cu + Co)</sub> at 365 °C on the content of pyroxene.

It can be seen from the figure that the sample CAT (d) again has the lowest activity. In this case the differences in activity are significant. According to this indicator, CAT (c) exhibits the highest activity, although the contents of copper and cobalt in it are the lowest (Table 1). Accordingly, not only the amount of the applied oxides, but also the phase composition is important for the formation of CAC – the amount and type of crystallized phases. If you compare the data presented in Table 1 and Table 2 it is immediately clear that in the least active

catalyst CAT (d), the phase pyroxene is missing. If we assume that this phase promotes the formation of more active CAC, i.e., it plays a significant role, it would be logical that with the increase of its amount, the activity of the catalysts would also increase. Fig. 6 presents data about I<sub>gCuCo</sub> depending on the content of the crystalline phase pyroxene. Activity actually increases with the increase of pyroxene in the catalysts. Therefore, this crystalline phase results in the formation of the most active CAC. Of course, the role of anorthite should not be ignored, since the catalysts are active even in the absence of pyroxene. On the basis of the obtained results, it is possible to make a conclusion that anorthite contributes to the formation of more efficient CAC than melilite. These crystal phases belong to two main structural silicate types and the CAC formed differ. These data confirm that the carrier and its nature play an important role in CAC formation.

**Table 2.** Data for the catalytic activity at 365 °C.

Samples	η, %	I <sub>g</sub> .10 <sup>2</sup>	I <sub>gCuCo</sub> .10 <sup>2</sup>
CAT(a)	75.7	8.40	4.77
CAT(b)	63.0	7.02	4.18
CAT(c)	63.0	6.97	5.66
CAT(d)	49.0	5.45	0.97

The activity of CAC depends on the generated Cu- and Co-containing phases; the formation of crystalline phases with spinel structure is desirable. The reason for the formation of more active CAC on carriers containing pyroxene is probably due to the ability of pyroxene to contribute to the heterogeneous nucleation of the spinel. An epitaxial relationship is widely observed in spinel exsolution lamellae within pyroxene [22, 23] facilitated by similar spacing and plane group symmetries of oxygen atoms of {010} pyroxene and {110} spinel. Hammer *et al.* [24], concluded that clustering and physical contact of pyroxene and spinel forming from melt develop from heterogeneous nucleation followed by epitaxial crystal growth. In the available literature we found no data on epitaxial relationships between spinel and anorthite or spinel and melilite.

**Table 1.** Phase compositions, BET surface area of the catalyst carriers and amount of copper and cobalt deposited

Sample	Crystalline phases, vol %			S <sub>0</sub> , m <sup>2</sup> /g	Content, weight %		Mol. ratio Cu/Co
	Melilite	Anorthite	Pyroxene		Cu	Co	
CAT(a)	32	51	17	17.7	0.62	1.14	1.90
CAT(b)	20	40	40	23.3	0.54	1.14	2.27
CAT(c)	26	23	51	31.2	0.40	0.79	2.13
CAT(d)	66	34	0	43.3	1.55	3.27	2.17

## CONCLUSIONS

Based on the experimentally obtained results for the catalytic activity of copper and cobalt oxides deposited on slag glass-ceramics, it can be concluded that the formation of catalytically active complexes (CAC) depends on the phase composition of the carrier. Among the crystalline phases present in the composition of slag glass-ceramics, pyroxene contributes to the formation of the most efficient CAC whereas the influence of anorthite and melilite is weaker.

## REFERENCES

1. S. V. Dimitrova, D. Mehandjiev, *Wat. Res.*, **32**, 3289 (1998).
2. S. Dimitrova, D. Mehandjiev, *Compt. rend. Acad. bulg. Sci.*, **52**, 33 (1999).
3. D. R. Mehandjiev, S. V. Dimitrova, *Bulg. Chem. Comm.*, **31**, 580 (1999).
4. S. V. Dimitrova, D. Mehandjiev, *Compt. rend. Acad. bulg. Sci.*, **53**, 49 (2000).
5. S. Dimitrova, V. Nickolov, D. Mehandjiev, *J. Mat. Sci.*, **36**, 2639 (2001).
6. E. Nehrenheim, J. P. Gustavson, *Biores. Technol.*, **99**, 1571 (2008).
7. A. Nakahira, H. Naganuma, T. Kubo, Y. Yamasaki, *J. Ceram. Soc. Jpn.*, **116**, 500 (2008).
8. Y. F. Zhou, R. J. Heines, *Water Air Soil Poll.*, **215**, 631 (2010).
9. S. Dimitrova, G. Ivanov, D. Mehandjiev, *Appl. Cat.*, **206**, 81 (2004).
10. S. Dimitrova, G. Ivanov, D. Mehandjiev, *Compt. rend. Acad. bulg. Sci.*, **55**, 79 (2002).
11. D. Mehandjiev, Proc. Inter. Symp. Heter. Cat., Varna, 2000, p. 19.
12. T. Tsoncheva, *Compt. rend. Acad. bulg. Sci.*, **53**, 49 (2000).
13. T. Tsoncheva, S. Vankova, D. Mehandjiev, *Fuel*, **82**, 755 (2003).
14. R. Nickolov, T. Tsoncheva, D. Mehandjiev, *Fuel*, **81**, 203 (2002).
15. S. V. Dimitrova, I. K. Mihailova, P. V. Vassileva, D. R. Mehandjiev, *Compt. rend. Acad. bulg. Sci.*, **65**, 1675 (2012).
16. Mihailova, I. K., P. R. Djambazki, D. Mehandjiev, *Bulg. Chem. Comm.*, **43**, 293 (2011).
17. I.T. Ivanov, I. Georgieva, F. Dipchikov, Proc. 11th Int. Conf. Glass and Ceramic, Varna, 1993, B. Samuneva. I. Gutzow, Y. Dimitriev, S. Bachvarov (eds.), Acad. Publ. House Marin Drinov, Sofia, 1994, p. 240.
18. I. Ivanov, I. Georgieva, F. Dipchikov, C. Ionchev, Proc. 12th Int. Conf. Glass Ceramics, Varna, 1996, B. Samuneva et al. (eds.), Acad. Publ. House Marin Drinov, Sofia, 1997, p. 200.
19. I. Georgieva - Mihailova, PhD Thesis, UCTM, Sofia, 1997.
20. JCPDS International Center for Diffraction Data, Powder Diffraction File, Swarthmore, PA.
21. S. Angelov, D. Mehandjiev, B. Piperov, V. Zarkov, A. Terlecki-Baricevic, D. Jovanovic, *Appl. Catalysis*, **16**, 431(1985).
22. M. Feinberg, H.-R. Wenk, P. Renne, and G. R., Scott, *American Mineralogist*, **89**, 462 (2004).
23. F. P. Okamura, I. S., McCallum, J. M. Stroh, and S., Ghose, Proc. 7th Lunar and Planetary Science Conference, **2**, 1976, p.1889.
24. I.E. Hammer, T. G. Sharp, *P. Wessel, Geology*, **38**, 367 (2010).

## ВЛИЯНИЕ НА ФАЗОВИЯ СЪСТАВ НА НОСИТЕЛЯ ВЪРХУ КАТАЛИТИЧНАТА АКТИВНОСТ НА МЕДНО-КОБАЛТОВИ ОКСИДИ НАНЕСЕНИ ВЪРХУ ШЛАКОСИТАЛИ

Ирена К. Михайлова<sup>1</sup>, Соня В. Димитрова<sup>2</sup>, Даниела Д. Стоянова<sup>3</sup>, Д. Р. Механджиев<sup>3</sup>

<sup>1</sup> Химикотехнологичен и металургичен университет, бул. „Св. Климент Охридски“ № 8, София 1756, България

<sup>2</sup> Университет по архитектура, строителство и геодезия, бул. „Христо Смирненски“ № 1, София 1046, България

<sup>3</sup> Институт по обща и неорганична химия – Българска академия на науките, ул. „Акад. Георги Бончев“ блок 11, София 1113, България

Постъпила на 20 май 2015 г.; коригирана на 11 ноември 2016 г.

(Резюме)

За да се провери доколко шлакосита̀ли могат да се използват като носители за получаване на активни нанесени катализатори, са изследвани катализатори, получени чрез нанасяне на медно-кобалтови оксиди на различни шлакосита̀ли. Каталитичната активност е изследвана по отношение окислението на въглероден оксид. Образците са охарактеризирани с помощта на рентгенодифракционен анализ, сканираща електронна микроскопия и ВЕТ-анализ. Установено е, че мелилит, пироксен и анортит в различни съотношения са основните кристални фази в тях. Резултатите от каталитичните тестове са интерпретирани във връзка с фазовия състав на носителите на катализаторите. Установено е, че каталитичната активност и формирането на каталитично активни комплекси зависят от фазовия състав на носителите. От кристалните фази в състава на носителите пироксенът допринася за образуване на най-ефективни каталитично активни комплекси.

## Validation of a TLC-densitometric method for quality control of Estradiol valerate in drug combinations

S. Ivanova, D. Tsvetkova\*

*Department of Pharmaceutical Chemistry, Faculty of Pharmacy, Medical University-Sofia*

Received January 28, 2016; Accepted February 25, 2016

The aim of the current study was the validation of a TLC-densitometric method for quality control of Estradiol valerate in drug combination dosage forms. The TLC conditions were: glass plates with silicagel G<sub>60</sub>F<sub>254</sub>; mobile phase: chloroform : water = 90 : 10 v/v. The TLC-densitometric method was validated with respect to the analytical parameters: linearity, LOD, LOQ, accuracy and precision (repeatability). Linear regression analysis was performed. The regression calibration curve was built. Linearity accordance between the concentration and spot area in range:  $5.10^{-4}$  g/ml ÷  $3.10^{-3}$  g/ml was proved by the regression equation:  $y = 28874286.x + 14290$ . LOD =  $3.15.10^{-4}$  mg/ml; LOQ =  $9.54.10^{-3}$  mg/ml.

For estimating the accuracy the recovery is presented in R [%] ± RSD [%] with the respective confidence interval: R[1.5 mg]: 95.92 % ÷ 103.98 %; R[2 mg]: 93.35 % ÷ 108.89 %; R[2.5 mg]: 95.37 % ÷ 103.77 %. Precision is estimated by standard deviation, relative standard deviation and confidence interval. All data for the obtained quantity correspond to the confidence interval: 1.88 mg ÷ 2.17 mg. The proposed validated TLC-densitometric method is appropriate for quality control of Estradiol valerate in commercially available tablets.

**Key words:** TLC-densitometry, Estradiol valerate, validation, linearity, accuracy.

### INTRODUCTION

Osteoporosis is a systemic skeletal disease, characterized by decreased bone mass and altered bone microarchitecture, leading to increased bone fragility and fracture risk in women [1] and men [2]. Estradiol valerate is used for treatment of symptoms of menopause (hot flashes, burning, irritation) and types of prostate cancer (androgen-dependent), for prevention of osteoporosis in postmenopausal women, replacement of estrogen in women with ovarian failure or other conditions that cause a lack of natural estrogen in the body. The risk of osteoporosis is increased in estrogen deficiency [3].

Estradiol valerate is included in combined dosage forms for contraception with Cyproterone acetate (Femilar) [4] and Dienogest [5, 6]. On the pharmaceutical market drug products are available for treatment of climacteric symptoms in postmenopausal women, containing Estradiol valerate 2 mg in combination with: Ciproterone acetate 1 mg (Climen tabl.) [4]; Dienogest 2 mg (Climodien tabl.) [7], Medroxyprogesterone acetate 10 mg (Divina, Farlutes) [8]; Levonogestrel 0.15 mg (Climonorm tabl.) [9].

The following methods for determination of Estradiol valerate in tablets are described: I) UV-spectrophotometry at  $\lambda = 280$  nm [10]; II) UV-

spectrophotometry - first derivative at  $\lambda = 270$  nm [11] and  $\lambda = 292$  nm [10]; III) fluorimetry after derivatization reaction with dansyl chloride [12]. For determination of Estradiol valerate in drug combinations containing other components in the tablets the following methods are developed:

I) UV-derivative spectrophotometry:

1) Estradiol valerate and Cyproterone acetate [13]

2) 2nd derivative spectrophotometry: at  $\lambda = 297.4$  nm for Estradiol valerate and at  $\lambda = 273.4$  for Medroxyprogesterone acetate [14]

II) chemiluminescence method: inhibition of luminol luminescence by Estradiol valerate [15]

III) HPLC with UV-detection:

1) Estradiol valerate/Dienogest: stationary phase: ACE C<sub>8</sub>, mobile phase: ammonium nitrate: acetonitrile = 30 : 70 v/v, flow rate: 2 ml/min,  $\lambda = 280$  nm, internal standard: Cyproterone acetate [16]

2) Estradiol valerate/Medroxyprogesterone acetate: stationary phase: C<sub>18</sub>, mobile phase: ammonium nitrate: acetonitrile = 30 : 70 v/v,  $\lambda = 280$  nm [17]

IV) GC/MS: Estradiol valerate and Medroxyprogesterone acetate [18]

V) electrochemical method: carbon electrode modified with iron tetrapyridinoporphyrazine: 17 $\beta$ -Estradiol valerate in injections [19].

The aim of the current study is to validate the TLC-densitometric method for quality control of Estradiol valerate with respect to the analytical

\* To whom all correspondence should be sent:  
E-mail: dobrinka30@abv.bg

parameters: selectivity, linearity, accuracy, precision.

## MATERIALS AND METHODS

### Materials

I) Reference standard: Estradiol valerate

II) Reagents with analytical grade quality: chloroform (Sigma Aldrich, N: SZBD 074SV UN 1888); 99.98 % ethanol (Sigma Aldrich, N: SZBD 0500V UN 1170), distilled water

III) TLC glass plates precoated with silicagel G<sub>60</sub>F<sub>254</sub>, 20 cm × 20 cm (Sigma Aldrich, N: 2364681).

### Method: TLC-densitometry.

I) Instrumentation: densitometer VILBER LOURMAT CN-15.LC Serial:16263; sample applicator 10 µl micropipette (Hamilton, Bonaduz, Switzerland, N:18005701); TLC chamber (22 cm × 12 cm × 22 cm); stationary phase: Silicagel G<sub>60</sub>F<sub>254</sub>; mobile phase: chloroform : distilled water = 90 : 10 v/v, detection at λ = 254 nm.

II) Preparation of solution of RS for linearity check.

Accurately weighed quantities of the reference standard Estradiol valerate: 0.005 g, 0.01 g, 0.015 g, 0.02 g, 0.025 g, 0.03 g were dissolved in separate volumetric flasks of 10.0 ml in 99.98 % ethanol to obtain solutions with concentrations correspondingly:  $5.10^{-4}$  g/ml;  $1.10^{-3}$  g/ml;  $1.5.10^{-3}$  g/ml,  $2.10^{-3}$  g/ml,  $2.5.10^{-3}$  g/ml,  $3.10^{-3}$  g/ml.

III) Preparation of model mixtures for accuracy check.

Accurately weighed quantities equivalent to 0.015 g, 0.020 g, 0.025 g of the reference standard Estradiol valerate were dissolved in separate volumetric flasks of 10.0 ml in 99.98 % ethanol to obtain 3 samples from 3 different model mixtures with contents equivalent to 80 % (1.5 mg/ml, I), 100 % (2 mg/ml, II) and 120 % (2.5 mg/ml, III) of the theoretical concentration in the tablets (2 mg).

IV) Preparation of model mixtures for precision (repeatability) check.

Accurately weighed quantities equivalent to 0.02 g of the reference standard Estradiol valerate were dissolved in 6 separate volumetric flasks of 10.0 ml in 99.98 % ethanol to obtain 6 model mixtures with Estradiol valerate content equivalent to 100 % (2 mg/ml) of the theoretical concentration in the tablets (2 mg).

## RESULTS AND DISCUSSION

The TLC-densitometric method was validated for the analytical parameters: selectivity, linearity, accuracy and precision.

### 1) Selectivity

A "placebo" solution without the active substance Estradiol valerate was prepared in the same manner like the solution of the reference standard. The selectivity of the applied TLC-densitometric method was proved by the fact, that on the chromatograms with "placebo" solutions there were no spots with R<sub>f</sub>, corresponding to the R<sub>f</sub> of Estradiol valerate (0.92).

### 2) Linearity

Linearity accordance between the concentration and spot area in the range:  $5.10^{-4}$  g/ml ÷  $3.10^{-3}$  g/ml was proved by the regression equation:  $y = 28874286.x + 14290$ . (Fig. 1.). LOD =  $3.15.10^{-4}$  mg/ml; LOQ =  $9.54.10^{-3}$  mg/ml.

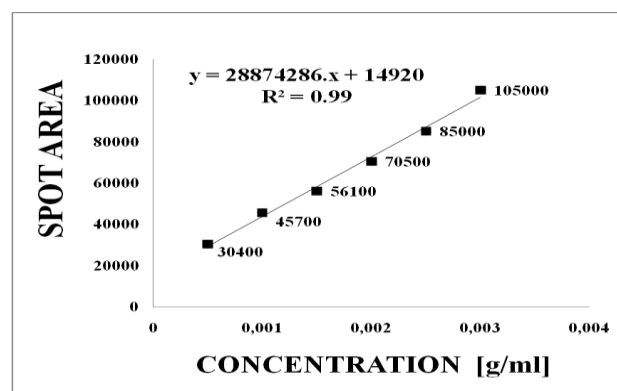


Fig. 1. Linearity for Estradiol valerate

### 3) Test for system suitability

The suitability of the system was confirmed by the lack of a statistically significant difference between the values of the chromatographic mobility parameter relative to the front (R<sub>f</sub>) in the analysis of 6 samples of Estradiol valerate: R<sub>f</sub>: 0.43, 0.43, 0.43, 0.43, 0.44, 0.44 ( $0.43 \div 0.005$ , SD = 1.4).

### 4) Accuracy

For the estimation of accuracy, in Table 1 are summarized data for the spot area (A), obtained by the method of calibration curve for model mixtures, the quantity [C] and the recovery [RC] of Estradiol

valerate, arithmetical mean ( $\bar{X}$ ); standard deviation (SD) and relative standard deviation (RSD) (%);

$S\bar{X}$  – mean quadratic error; P – confidence possibility (%)

;  $t$  – Student's coefficient;  $\bar{X} \div t.S\bar{X}$  – confidence interval; E – relative error. Accuracy is presented by the recovery R (%) and RSD [20].

**Table 1.** Data for spot area (A), quantity [C] and degree of recovery [RC] for Estradiol valerate in model mixtures – estimation of accuracy.

N:	A	[C <sub>1.5</sub> ] [mg]	R [C <sub>1.5</sub> ] [%]	A	[C <sub>2</sub> ] [mg]	R [C <sub>2</sub> ] [%]	A	[C <sub>2.5</sub> ] [mg]	R [C <sub>2.5</sub> ] [%]
1.	56000	1.42	97.73	68000	1.84	96.84	84000	2.39	97.55
2.	57900	1.49	99.33	71500	1.96	100.51	86200	2.47	98.80
3.	60700	1.59	102.58	76200	2.12	106.0	90300	2.61	102.35
$\bar{X} \pm SD$	58200	1.5 ± 0.09		71900	1.97 ± 0.14		86833	2.49 ± 0.11	
$\bar{R} [\%] \pm$ RSD[%]			99.95 ± 2.39			101.12 ± 4.56	3197		99.57 ± 2.5
SD	2364	0.09	2.39	4115	0.14	4.61	3.68	0.11	2.49
RSD [%]	4.06	6.0	2.39	5.72	7.11	4.56		4.42	2.5
$S \bar{X}$		0.05	1.38		0.08	2.66		0.06	1.44
P [%]		90.0	90.0		90.0	90.0		90.0	90.0
t		2.92	2.92		2.92	2.92		2.92	2.92
t.S $\bar{X}$		0.15	4.03		0.23	7.77		0.18	4.2
$\bar{X} \pm$ t.S $\bar{X}$		1.35 ÷ 1.65	95.92 ÷ 103.98		1.74 ÷ 2.2	93.35 ÷ 108.89		2.31 ÷ 2.67	95.37 ÷ 103.77
E [%]		3.33	1.38		4.06	2.63		2.41	1.45

**Table 2.** Data for spot area (A), quantity [C] and degree of recovery [RC] for Estradiol valerate in model mixtures – estimation of precision.

N:	C	A	U A	[C]	R [C] [mg/l]	U [C]
1.	1.95	69900	1.14	1.90	97.44	1.22
2.	1.95	70300	0.99	1.92	98.46	1.00
3.	2.00	71900	0.36	1.97	98.50	0.44
4.	2.00	73500	0.27	2.03	101.50	0.22
5.	2.05	75200	0.93	2.09	101.95	0.89
6.	2.05	76100	1.29	2.12	103.41	1.22
$\bar{X} \pm SD$		72817 ± 2584		2.01 ± 0.09		
$\bar{R} [\%] \pm$ RSD[%]					100.21 ± 2.39	
SD		2584		0.09	2.38	
RSD [%]		3.51		4.48	2.39	
$S \bar{X}$				0.04	0.98	
P [%]				98.0	98.0	
t				3.37	3.37	
t.S $\bar{X}$				0.13	3.30	
$\bar{X} - t.S \bar{X} \div$ $\bar{X} + t.S \bar{X}$				1.88 ÷ 2.17	96.91 ÷ 103.51	
E [%]				1.99	0.98	

All results are within the respective confidence interval: R[1.5 mg]: 95.92 % ÷ 103.98 %; R[2 mg]: 93.35 % ÷ 108.89 %; R[2.5 mg]: 95.37 % ÷ 103.77 %.

#### 5) Precision (repeatability)

Precision is estimated by the uncertainty of the result, determined by standard deviation (SD), relative standard deviation (RSD) and confidence

interval ( $\bar{X} \div t.S \bar{X}$ ). Table 2 presents: C – added content of Estradiol valerate in model mixtures, [C] – content obtained by the method of the calibration curve, [RC] – degree of recovery, U[A] – Chauvenet criterion for area, U[C] – Chauvenet criterion for the obtained content. All data for the obtained quantity of Estradiol valerate correspond to the confidence interval: 1.88 mg ÷ 2.17 mg (SD = 0.05).

### CONCLUSIONS

Estradiol valerate is available on the market in drug combinations with: Ciproterone acetate, Dienogest, Medroxyprogesterone acetate, Levonogestrel. The obtained quantities by the applied method correspond to the relevant confidence interval: 1.88 mg ÷ 2.17 mg. The proposed validated TLC-densitometric method is appropriate for quality control of Estradiol valerate in commercially available tablets.

**Acknowledgements:** This article was prepared with the financial support from DP N:13/2015, Medical University-Plovdiv, Bulgaria.

### REFERENCES

1. S. Sanders, S. A. Geraci, *South Med. J.*, **106**(12), 698 (2013).
2. S. Khosla, S. Amin, E. Orwoll *Endocr. Rev.*, **9**(4), 441 (2008).
3. V. B. Popat, K. A. Calis, V. H. Vanderhoof, G. Cizza, J. C. Reynolds, N. Sebring, J. F. Troendle, L. M. Nelson, *J. Clin. Endocrinol. Metab.*, **94**(7), 2277 (2009).
4. J. T. Jensen, J. Bitzer, M. Serrani, *J. Contracept.*, **4**(1), 39 (2013).
5. A. Graziottin, *Minerva Ginecol.*, **66**, (5), 479 (2014).
6. J. W. Kiley L. P. Shulman, *Int. J. Womens Health.*, **3**(1), 281 (2011).
7. T. Gräser T. Römer, K. D. Wiedey, A. Janaud, *Climacteric.*, **4**(4), 332 (2001).
8. C. Egarter P. Geurts, E. Boschitsch, P. Speiser, J. Huber, *Acta Obstet. Gynecol. Scand.*, **75**(4), 386 (1996).
9. D. B. Georgiev, S. Golbs, A. Goudev, *Methods Find. Exp. Clin. Pharmacol.*, **23**(4), 197(2001).
10. B. Yilmaz, *Int. J. Pharm. Sci. Rev. Res.*, **1**(2), 112 (2010).
11. A. S. L. Mendez, L. Deconto, C. V. Garcia, *Química nova São Paulo*, **33**(4), 981 (2010).
12. S. Fishman, *J. Pharm. Sci.*, **64**(4), 674 (1975).
13. E. Dinç, C. Yücesoy, I. M. Palabiyik, O. Ustündağ, F. Onur, *J. Pharm. Biomed. Anal.*, **32**(3), 539 (2003).
14. M. I. Toral, C. Soto, P. Richter, A. E Tapia, *J AOAC Int.*, **85**(4), 883 (2002).
15. W. Liu L. Xie, H. Liu, S. Xu, B. Hu, W. Cao, *Luminescence*, **28**(3), 407 (2013).
16. M. G. Çağlayan I. M. Palabiyik, F. Onur, *J. AOAC Int.*, **93**(3), 862 (2010).
17. A. Segall, F. Hormaechea, M. Vitale, V. Perez, M. T. Pizzorno, *J. Pharm. Biomed. Anal.*, **19**(5), 803 (1999).
18. B. Yilmaz, *Anal. Sci.*, **26**(3), 391 (2010).
19. I. V. Batista, M. R. Lanza, I. L. Dias, S. M. Tanaka, A. A. Tanaka, M. D. Sotomayor, *Analyst*, **133**(12), 1692 (2008).
20. N. P. Dimov, In: Chromatography in Pharmaceutical Analysis Dimov (ed. N. P. Dimov), Sofia, Chemical Pharmaceutical Research Institute (NIHFI), 1999, p. 205.

## ВАЛИДИРАНЕ НА TLC-ДЕНЗИТОМЕТРИЧЕН МЕТОД ЗА КОНТРОЛ НА КАЧЕСТВОТО НА ESTRADIOL VALERATE В ЛЕКАРСТВЕНИ КОМБИНАЦИИ

С. Иванова, Д. Цветкова\*

*Катедра по фармацевтична химия, Фармацевтичен факултет, Медицински университет-София*

Получена 28 януари, 2016 г., приета 25 февруари, 2016 г.

(Резюме)

Целта на настоящото изследване е валидирането на TLC-дензитометричен метод за контрол на качеството на Estradiol valerate в комбинирани дозирани лекарствени форми. Условието на TLC са: стъклени плаки: Silicagel G<sub>60</sub>F<sub>254</sub>; подвижна фаза: хлороформ : вода = 90 : 10 v/v. TLC-дензитометричният метод е валидиран по отношение на аналитичните параметри: линейност, LOD, LOQ, точност и прецизност (повторяемост). Проведен е линеен регресионен анализ. Построена е калибрационна права. Линеината зависимост между концентрацията и площта на петната в интервала: 5.10<sup>-4</sup> g/ml ÷ 3.10<sup>-3</sup> g/ml се доказва от уравнението на регресия:  $y = 28874286.x + 14290$ . LOD = 3.15.10<sup>-4</sup> mg/ml; LOQ = 9.54.10<sup>-3</sup> mg/ml.

За оценка на аналитичния параметър точност, е представен аналитичният добив в R [%] ± RSD [%], като резултатите отговарят на съответния доверителен интервал: R[1.5 mg]: 95.92 % ÷ 103.98 %; R[2 mg]: 93.35 % ÷ 108.89 %; R[2.5 mg]: 95.37 % ÷ 103.77 %. Прецизността е оценена чрез изчисляване на стандартно отклонение, относително стандартно отклонение и доверителен интервал. Всички данни за получените количества съответстват на доверителния интервал: 1.88 mg ÷ 2.17 mg.. Предложеният валидиран TLC-дензитометричен метод е подходящ за контрол на качеството на Estradiol valerate valetate в таблетки.



## Synthetic cannabimimetics detected in smoking blends on the Bulgarian territory – toxicological significance

P. A. Gateva<sup>1\*</sup>, V. T. Angelova<sup>2</sup>, R. T. Georgieva-Nikolova<sup>3</sup>, T. R. Veselinov<sup>4</sup>, V. H. Nankova<sup>4</sup>,  
M. M. Nikolova<sup>5</sup>, R. K. Hadjiolova<sup>6</sup>, M. P. Slavova<sup>7</sup>

<sup>1</sup> - Department of Pharmacology and Toxicology, Faculty of Medicine, Medical University of Sofia, Sofia, Bulgaria

<sup>2</sup> - Department of Chemistry, Faculty of Pharmacy, Medical University of Sofia, Sofia, Bulgaria

<sup>3</sup> - Department of Chemistry and Biochemistry, Faculty of Medicine, Medical University of Sofia, Sofia, Bulgaria

<sup>4</sup> - Research Institute of Forensic Science and Criminology, Sofia, Bulgaria

<sup>5</sup> - Middlesex University, School of Health and Education – London, United Kingdom

<sup>6</sup> - Department of Pathophysiology, Faculty of Medicine, Medical University of Sofia, Sofia, Bulgaria

<sup>7</sup> - Department of Biotechnologies, University of Chemical Technology and Metallurgy, Sofia, Bulgaria

Submitted June 10, 2015; Accepted July 15, 2015

Synthetic cannabimimetics are some of the most aggressively marketed narcotic drugs. Most often they are added to herbal incenses or are sold in powder as “bath salts”, “research chemicals/not intended for human consumption”, “plant foods”, etc. In our country for the period of 2010-2013 in herbal incenses were identified JWH-018, JWH-073, MAM-2201, UR-144и STS-135. Analysis of the information about their effects after human’s consumption reveals that they are psychoactive substances often with stronger effects than the marijuana itself. The time of their appearance on the market coincides with their worldwide distribution and almost always precedes their inclusion into the List of forbidden substances. Our legislative system attempts to include the new designer drugs under regulation as quickly as possible.

**Keywords:** cannabimimetics, JWH-018, JWH-073, MAM-2201, UR-144, STS-135

### INTRODUCTION

Synthetic cannabinoids and cannabimimetics are amongst the most aggressively marketed narcotic drugs. To this day, more than a hundred substances of this kind have been synthesized. Synthetic cannabinoids are substances structurally similar to  $\Delta^9$ -tetrahydrocannabinol (THC) – the active component of marijuana. The chemical structure of cannabimimetics does not bear any resemblance to THC, but produces similar pharmacological/physiological effects on the body. Although the two terms are often used as synonyms, it is important from a judicial point of view to distinguish them; as, according to the legislation of many countries cannabinoids are illegal from the moment of their production, unlike cannabimimetics, the regulation of which comes into effect months, and sometimes years, after they have been synthesized.

Around 2004, herbal smoking blends (‘herbal incense’ or ‘spice’) appeared in Europe as an alternative to cannabis. At first it was thought that their cannabis-like effects were herb-induced; however, it was soon rightly suspected that they also had synthetic substances added to them. Synthetic cannabinoids and cannabimimetics are

commonly added to dried narcotic herbs that, when smoked, produce psychopharmacological effects: *Salvia divinorum*, *Mitragyna speciosa* (Kratom), *Turnera aphrodisiaca* (Damiana), *Leonotis leonurus* (Lion’s ear), *Pedicularis densiflora* (Indian Warrior), *Rosa canina* (Dog Rose, rosehip), *Althaea officinalis* (marshmallow), etc. to produce the so called ‘synthetic marijuana’. Synthetic cannabimimetics are first dissolved in acetone or ethanol, which the herbs are sprayed with and dried, producing various concentrations of these potentially toxic substances [1]. They usually come in small packages, wrapped in foil, with attractive labels.

According to our country’s *National Focal Point for Narcotics and Addiction*, during the last few years there has been a steady trend in the use of synthetic cannabinoids and cannabimimetics.

We present our experience with newly-discovered cannabimimetics in our country – the subject of forensic medicine reports for the period 2010-2013. The subjects for analysis are dried herbal blends, reported to the Center for Expert Forensic Analysis and Trials – Research Institute of Forensic Science and Criminology – Ministry of Interior, Sofia, for the purpose of determining their significance in forensic toxicology.

\* To whom all correspondence should be sent:  
E-mail: pandreevagateva@yahoo.com

## METHODS

The following techniques were used for analysis:

1. Visual and microscopic analysis, weighing analysis – conducted on a Sartorius MC 210-S weighing balance, class I accuracy according to The Bulgarian Institute for Standardization (BDS) EN 45501:2001, max – 210 g; min-0.02 g, scale interval (d) 0.0001. The balance has a calibrating certificate from the accredited calibration laboratory Kalibra Bulgaria ltd.

2. Thin-layer chromatography (TLC): TLC plate with adsorbent: silica gel; solvent: chloroform:methanol (9:1); solvent front: 10 cm; developing material: iodine platinate.

3. The following analytical methods were used for measuring the respective proportion of each of the components in the analyzed blends:

a) Gas chromatography: Thermo Finnigan GC Ultra Gas Chromatograph, quartz capillary column EC-5 (30 m × 0.32 mm × 0.25 μm), injector at 270 °C, flame ionization detector at 300 °C, with temperature programming from 160 °C to 290 °C (10 min) with a heating rate of 30°C/min, carrier gas: nitrogen 1.3 ml/min.

b) Gas chromatography: Hewlett Packard 6890 Gas Chromatograph, injector at temperature of 270 °C, quartz capillary column EC™ 20 /15 m × 0.25 mm/ with temperature programming from 100 °C to 290 °C with a heating rate of 15 °C/min, carrier gas: nitrogen 1.5 ml/min. Flame ionization detector with hydrogen 35 ml/min at 300 °C.

4. Gas chromatography was used for identifying the substances in the analyzed samples – mass spectrometry (GC-MS) – Thermo Finnigan Trace GC/MS Gas Chromatograph – column: AT-5MS (30 m × 0.25 mm × 0.25 μm) by Alltech. Temperature programming: 60 °C/4min/ - 15 °C – 290 °C /10min/. Carrier gas: helium at flow rate: 1.0 ml/min. Split injector at split ratio: 1:20 at 270 °C. Interface at 280 °C and ionization chamber at 250 °C. Scan range: 40-460 amu. Ionization mode: electron ionization (EI).

Identification of the obtained mass spectra was done by their comparison with two mass spectral libraries by using computer software.

## RESULTS AND DISCUSSION

The active components were isolated from the vegetal matter using methanol. The procedure is easy to perform and gives fixed results, which is most likely due to the substances being added to the vegetal matter, and therefore not having to be isolated from cell components.

As expected, none of the extracts cross-reacted with the cannabinoid panel of our immunological screening laboratory test (Randox Evidence).

By using the above-described analytical methods and by doing comparison with a database and the existing body of literature, we identified the following compounds: JWH-018, JWH-073, MAM-2201, UR-144 and STS-135. As Bulgarian legislation forbids the use of narcotics, regardless of their effects and the level of impact, the precise concentrations were not further discussed.

### *JWH-018 and JWH-073*

In samples analyzed in 2010 and 2011, JWH-018 (see Table 1), and its butyric analog - JWH-073 (see Table 2) were determined. The literature search revealed that these substances were synthesized at the end of the past century [2], with a high affinity for the endocannabinoid receptors CB1 and CB2. In December 2008, two laboratories – THC Pharma (Germany) and AGES PharmMed (Austria), independently determined the presence of JWH-018 in smoking blends [3]. The same results were obtained in other laboratories across Europe and Japan [4, 5]. A direct link was discovered between JWH-018 and the psychotropic effects of smoking blends in which it was present [6].

Before JWH-018 was made illegal in Western Europe at the beginning of 2009, JWH-073 was found in predominantly low concentrations in smoking blends. Blends that possessed it were mostly regarded as impure [7].

However, after the ban, JWH-073 fully replaced JWH-018 (before its ban in 2011).

The effects of JWH-018 and JWH-073 were tested on animals, and it was found that they are similar to those produced by THC – the classic ‘cannabinoid tetrad’ was observed, which includes hypothermia, analgesia, catalepsy, and locomotion suppression [8, 9]. Moreover, the effects of JWH-073 and, to a greater degree those of JWH-018, were much more clearly expressed than the ones produced by THC.

No systemic research has been done on the effects of JWH-018 and JWH-073 on humans. Information about them is mostly found on Internet forums. The most common mode of use of synthetic cannabinoids is smoking, although peroral use is also possible. The contents of JWH-018 and JWH-073 in smoking blends vary between 2.3 mg/g and 35.9 mg/g, and between 5.8 and 22.9 mg/g, respectively [4, 7].

In humans, the effects usually occur either instantaneously, or in 1 to 10 min after smoking. In different individuals, these last 20 min to 4-6 h, and

they resemble those produced by marijuana: high spirits and euphoria; antistressor effect; creative, philosophical, abstract mental activity; increased sense of hearing, smell, taste, vision; altered body sensations; altered perception of time; analgesia; reduced nausea and increased appetite. Adverse effects: increased heart rate (palpitations); eye redness; dry mouth; impaired short term memory; impaired motor coordination; delayed reactions. Although not well documented, excessive use has been found to produce effects not typically observed in marijuana users – agitation and vomiting [10]. There is a reported case of addiction to Spice Gold (a smoking blend containing JWH-018) (after daily consumption of 3 g for several months, followed by the development of withdrawal syndrome, similar to the one produced by hard drugs [11]). There is also a reported case of acute intoxication with seizures and tachycardia, leading to hospitalization [12]. A recently published systematic literature review on psychopathological events resulting from the use of synthetic cannabinimimetics summarized the results of 223 trials, leading to its authors coining the term ‘spicephrenia’ [13]. Although there is currently no scientific evidence, these substances have been

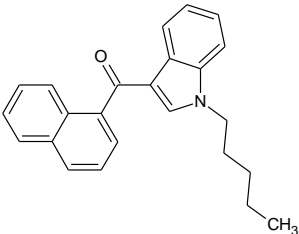
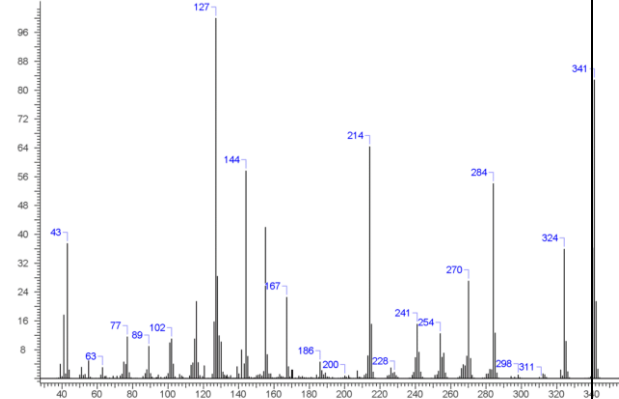
found to trigger acute psychosis in susceptible individuals, and/or exacerbate psychotic episodes in individuals with established psychosis.

A literature search revealed that in February 2011, JWH-018 and JWH-073 were included in the list of “Plants and chemicals with high degree of risk for social health because of the harmful effect of their abuse, prohibited for putting in practice in human and veterinary medicine”.

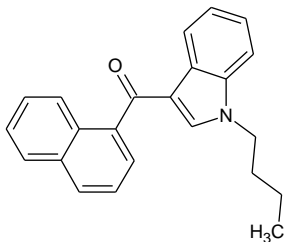
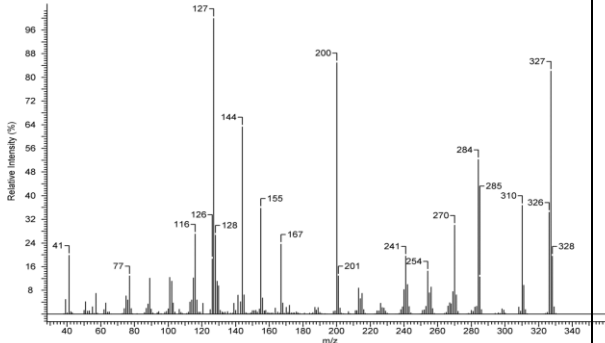
#### MAM-2201

In samples we analyzed in 2012, we established the presence of a substance called MAM-2201 (see Table 3), which is thought to act as a powerful agonist of the cannabinoid receptors. It was first isolated in laboratories in Germany and Netherlands in June 2011, as a component of synthetic cannabinimimetic smoking products [14]. MAM-2201 is a new substance developed by ‘research chemical’ suppliers of grey-market recreational drugs. Structurally, MAM-2201 is a hybrid of two known cannabinoids, JWH-122 and AM-2201, which were used as active components of cannabinoid smoking blends, before being internationally banned. MAM-2201 was banned in New Zealand in July 2012.

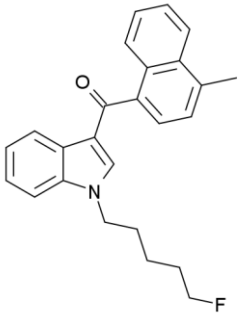
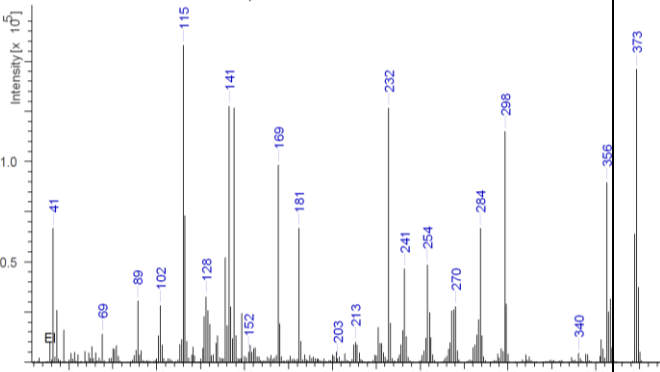
**Table 1.** JWH-018 – general, physical and analytical data

 <p style="text-align: center;">JWH-018</p>	<p>IUPAC name</p> <p>Synonyms</p> <p>Molecular weight</p> <p>Chemical formula</p> <p>Appearance</p> <p>Melting point (°C)</p> <p>GC-MS spectral data</p>	<p>Naphthalen-1-yl-(1-pentylindol-3-yl)methanone</p> <p>AM678, pentyl-3-(1-naphthoyl)indole</p> <p>341.189 g/mol</p> <p>C<sub>24</sub>H<sub>23</sub>NO</p> <p>White to grey powder</p> <p>51.9</p> <p>(Principal GC-MS ions)</p> <p>127.1, 214.2, 270.2, 284.2, 324.3, (341.3 [M<sup>+</sup>])</p> 
--	--	---

**Table 2.** JWH-073 – general, physical and analytical data.

 <p style="text-align: center;">JWH-073</p>	<p>IUPAC name Synonyms Molecular weight Chemical formula Appearance Melting point (°C) GC-MS spectral data</p>	<p>Naphthalen-1-yl-(1-butylindol-3-yl)methanon - 327.16 g/mol C<sub>23</sub>H<sub>21</sub>NO White powder 99.8</p> <p style="text-align: center;">(Principal GC-MS ions) 127.1, 144.1, 200.2, 284.2, 310.3, (327.3 [M<sup>+</sup>])</p> 
--	--	--

**Table 3.** MAM 2201 – general, physical and analytical data.

 <p style="text-align: center;">MAM 2201</p>	<p>IUPAC name Synonyms Molecular weight Chemical formula Appearance Melting point (°C) GC-MS spectral data</p>	<p>(1-(5-Fluoropentyl)-1H-indol-3-yl)(4-methyl-1-naphthalenyl)-methanone AM 2201 4-methylnaphthyl analog; JWH-122 N-(5-fluoropentyl) analog 373.462 g/mol C<sub>25</sub>H<sub>24</sub>FNO White powder 109.4</p> <p style="text-align: center;">(Principal GC-MS ions) 115.2, 141.1, 169.3, 181.1, 232.2, 284.2, 298.1, 356.2, 373.1 [M<sup>+</sup>]</p> 
---	--	---

Internet forum testimonies of herbal incense smokers claim that MAM-2201 does not cause chest tightness, its taste is not very appealing but its effect is stronger and longer-lasting than that of cannabinoids. The minimal effective dose is 500 µg, and the dose-response curve is very steep. In

some cases, panic attacks and vomiting are observed. There is a lack of clinical data for MAM-2201.

In medical literature, several cases of MAM-2201 intoxication can be found. One of them is that of a 31 year-old man of Japanese origin who, after

smoking 300 mg smoking incense through a bong, falls into a transitory acute psychotic state with agitation, aggression, anxiety and vomiting, with a comorbid sympathomimetic syndrome (arterial hypertension, tachycardia, hyperglycemia) [15]. His condition required immediate hospitalization. One hour after smoking, his blood contained 49 mg/ml MAM-2201. His psychological state recovered 1.5 hours after smoking.

Another case is that of a 59 year-old man, with a fatal outcome [16]. The forensic medical report, done on the 4<sup>th</sup> day *post mortem*, established the presence of MAM-2201 in the blood and in a number of tissues; its concentration in the adipose tissue being 124 times higher than that in the blood.

There is also a case of an intranasal ingestion of the powdered substance, paired with the local anesthetic benzocaine, by a 20 year-old individual; who was urgently admitted to the emergency room 6 hours later with agitation, xerostomia, chest pain, severe dyspnea, tachycardia, and hypertonia. These effects are thought to be due to the noradrenalin secretion – one of the supposed mechanisms of the cannabinoid receptor agonists [12].

There is a reported case of seizures and death of a 36 year-old man after a simultaneous intake of several synthetic cannabinoids through smoking blends, including MAM-2201 and UR-144, and amphetamines [17].

At the time we identified MAM-2201 in smoking blends (2012), it was not included in the list of “Plants and chemicals with high degree of risk for social health because of the harmful effect of their abuse, prohibited for putting in practice in human and veterinary medicine”. However, its analog AM-2201 was included, which justified the undertaking of legal action.

#### *UR-144*

In smoking blends analyzed in 2012-2013, the substance UR-144 or KM-X1 (see Table 4) was also identified. Apart from the compound itself, its main pyrolysis product-artefact was also found in the samples; which is due to the molecular rearrangement caused by the high temperature in the GC injector port.

The chemical structure of UR-144 is very similar to that of JWH-018, the first synthetic cannabinoid. The presence of UR-144 in herbal incense was first reported in Korea in 2012, and it quickly spread throughout Europe and New Zealand [18]. The substance was found in Russia, Croatia, Sweden, Germany, Finland, Norway, Hungary, Japan, and the USA.

UR-144 is a clinical candidate developed by Abbott Laboratories, which acts as a full agonist of the peripheral cannabinoid receptors CB2, but with a much lower affinity for the psychoactive CB1 receptors [19]. The CB2 receptors play a role in the perception of pain, and therefore similar compounds are of medical interest. Despite the relatively low affinity of UR-144 to the CB1 receptors, Internet forum reviews of users of this substance show that it is popularly sought-after for its psychoactive activity.

UR-144 is mainly distributed as a research chemical, in quantities of 0.25 to 100 g. Although it is labeled as ‘unfit for human consumption’, UR-144 is usually smoked like a joint (mixed with tobacco, St. John’s worth, and other herbs). New UR-144-smokers usually start with doses of 0.5-2 mg, and often reach doses of up to 2.5-20 mg (its contents in cigarettes is 0.05%-0.4%). Some users take several doses at a time in order to prolong the effect, which leads to the intake of several tens of mg of the substance in one smoke.

The effect occurs 0.5-2 min after smoking, reaches its peak 3-5 min later, and wears off after 1-2 hours (after 4 hours at high doses). Its users compare its effect to the ones produced by JWH-122, AM-2201, and marijuana. At inhaling, it produces a cocaine-like euphoric and aphrodisiacal effect that comes with an opiate-like tidal feeling, which slowly subsides after 35-40 minutes. During the effect, euphoria, uplifted mood, relaxation, drowsiness, hallucinations, and increased appetite are observed. Most commonly reported adverse effects include anxiety, paranoia, attention deficit, depression and hallucinations, which can last for several days. At high doses, especially during the first few minutes, the hallucinogen effect is very intensive. Overdosing causes tachycardia, nausea, disorientation, dysphoria, blurred vision, inability to communicate, extreme hallucinations, and loss of consciousness. UR-144 tolerance can be developed, compelling the users to increase the doses they take over time. There is one reported case of an epileptic fit after smoking UR-144 [3].

In 2012, UR-144 was the most commonly found synthetic cannabinoid in laboratories in Russia and Poland. It was the most popular synthetic cannabinoid for 2012. In 2013, two UR-144 analogs were released to the market. In many countries, including the UK, Russia and New Zealand, UR-144 was banned in 2012. At the time we discovered this substance in smoking blends, it was not yet banned in Bulgaria. In 2013, it was included in the list of “Plants and chemicals with high degree of risk for social health because of the

harmful effect of their abuse, prohibited for putting in practice in human and veterinary medicine”.

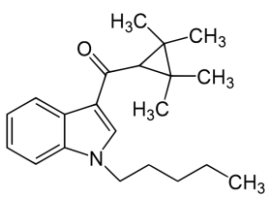
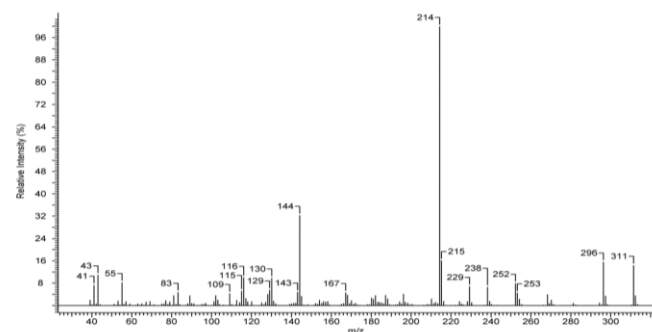
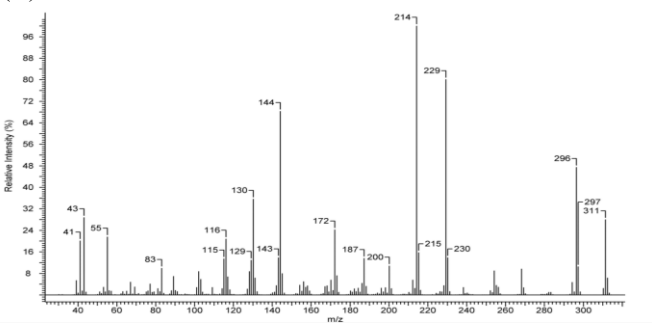
### STS-135

STS-135 is a designer synthetic cannabinoid, which acts as a full powerful agonist to the CB1 and CB2 receptors (see Table 5).

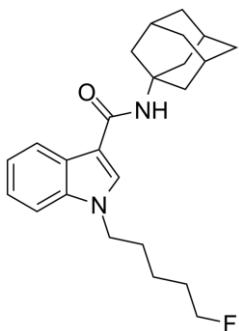
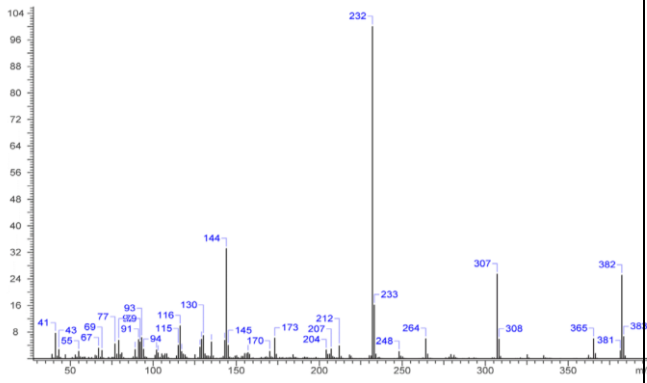
This compound has a unique carboxamide bond between the adamantyl side chain and the indole ring, which allows for it to circumvent regulation. STS-135 has a 5-fluoropentyl side chain, which is a commonly found modification in the aminoalkylindole series of designer drugs. It is known that the adamantoyl group is a selective CB1 agonist; the adamantyl carboxamide group is

described in literature and may possess higher affinity for CB2 receptors in the periphery. Similar compounds include AB-001 (1-pentyl-3-(1-adamantoyl) indole), JWH-018 adamantyl carboxamide, AM1248, AKB48, and AKB48-N-(5-fluoropentyl) analogs. The origins of the name of STS-135 are unknown, but it is thought that it is derived from the name of the last US space mission; a metaphor for the psychoactive activity of the substance. There are reported cases of abuse of compounds with the adamantoyl structure, and unpublished reports about the presence of STS-135 in synthetic cannabinoid samples.

**Table 4.** UR-144 – general, physical and analytical data of the compound (A) and its main pyrolysis product (B)

 <p style="text-align: center;">UR-144</p>	<p>IUPAC name</p> <p>Synonyms</p> <p>Molecular weight</p> <p>Chemical formula</p> <p>Appearance</p> <p>Melting point (°C)</p> <p>GC-MS spectral data of UR-144 (A) and its main pyrolysis product (B)</p>	<p>(1-Pentylindol-3-yl)-(2,2,3,3-tetramethylcyclopropyl)methanone</p> <p>KM-X1</p> <p>311.461 g/mol</p> <p>C<sub>21</sub>H<sub>29</sub>NO</p> <p>White powder</p> <p>68.0</p> <p style="text-align: center;">(Principal GC-MS ions)</p> <p>116.2, 130.1, 144.1, 214, 229.1, 296.0, 311.1[M<sup>+</sup>]</p> <p>(A)</p>  <p>(B)</p> 
--	---	---

**Table 5.** General, physical and analytical properties of STS-135

 <p>STS-135</p>	<p>IUPAC name N-adamantyl-1-fluoropentylindole-3-carboxamide</p> <p>Synonyms 5F-APICA 5-fluoro-APICA</p> <p>Molecular weight 382.51 g/mol</p> <p>Chemical formula C<sub>24</sub>H<sub>31</sub>FN<sub>2</sub>O</p> <p>Appearance White powder</p> <p>Melting point (°C) 138.6</p> <p>GC-MS spectral data (Principal GC-MS ions) 116.2, 130.1, 144.1, 173.1, 232.1, 307.0, 365.1, 382.3[M<sup>+</sup>]</p>
	

There are no official statements on the pharmacological profile of STS-135 as of yet. The only information available is on Internet forums, provided by users of the substance: there are short-term panic attacks of 10-15 minutes. During smoking and evaporating, the substance gives off an unpleasant smell. The effect is pleasant, but less euphoric than that of cannabis. Some report a ‘bipolar effect’ – exaltation, followed by depression. It also causes a certain hallucinogenic effect.

### CONCLUSION

The manufacturing, distribution and use of illegal drugs and chemical substances has seen dynamic changes over the last few years, as, together with the wide distribution of explosives, the so-called ‘designer drugs’ or ‘legal highs’ have had an unprecedented success. These are uncontrolled substances whose effects are similar to the controlled ones. Manufactured in semi-legal or illegal laboratories, widely marketed on the Internet, and with misleading labels such as ‘research chemicals/unfit for human consumption’, or as ‘smoking blends’, ‘bath salts’, ‘plant food’, etc., they are either structural analogs of controlled substances, or have different structure but similar effects. Laws for the regulation of these substances are too slow to come into effect, compared to the

speed with which the substances are distributed on the market. Since 2010, designer synthetic cannabinimimetics are categorized by the World Anti-Doping Agency as ‘banned substances prohibited in sport’.

Most of these substances were originally developed by scientists researching the CB1 and CB2 receptors in the human body. Often, the newly-synthesized cannabinoids and cannabinimimetics prove to be more powerful than THC. Therefore it is difficult, and in the case of the cannabinimimetics – downright impossible, to be detected by standard marijuana screening tests. That and the uncontrolled status of synthetic cannabinimimetics at their initial release to the market, is the reason behind the mass consumption of ‘synthetic marijuana’.

### REFERENCES

1. W. E. Fantegrossi, J. H. Moran, A. Radominska-Pandya, P. L. Prather, *Life Sci.*, **97**, 45, (2014).
2. J. L. Wiley, D. R. Compton, D. Dai, J. A. Lainton, M. Phillips, J. W. Huffman, B. R. Martin, *J. Pharmacol. Exp. Ther.* **285**, 995, (1998).
3. A. Grigoryev, P. Kavanagh, A. Melnik, S. Savchuk, A. Simonov, *J. Anal. Toxicol.*, **37**, 265, (2013).
4. N. Uchiyama, R. Kikura-Hanajiri, J. Ogata, Y. Goda, *Forensic Sci Int.*, **198**, 31, (2010).

5. V. Auwärter, S. Dresen, W. Weinmann, M. Müller, M. Pütz, N. Ferreirós, *J. Mass Spectrom.*, **44**, 832, (2009).
6. K. Atwood, J. W. Huffman, A. Straiker, K. Mackie., *Br. J. Pharmacol.*, **260**, 585, (2010).
7. R. Lindigkeit, A. Boehme, I. Eiserloh, M. Luebbecke, M. Wiggermann, L. Ernst, T. Beuerle, *Forensic Sci. Int.*, **191**, 58, (2009).
8. J. L. Poklis, D. Amira, L. E. Wise, J. M. Wiebelhaus, B. J. Haggerty, A. Poklis, *Forensic Sci. Int.*, **220**, 91, (2012).
9. R. Marshall, T. Kearney-Ramos, L. K. Brents, W. S. Hyatt, S. Tai, P. L. Prather, W. E. Fantegrossi, *Pharmacol Biochem Beha*, **124C**, 40, (2014).
10. A.Y. Hopkins, B. L. Gilchrist, *J. Emerg. Med.*, **45**, 544, (2013).
11. U. S. Zimmermann, P. R. Winkelmann, M. Pilhatsch, J. A. Nees, R. Spanage, K. Schulz, *Dtsch. Arztebl. Int.*, **106**, 464, (2009).
12. J. Lapoint, L. P. James, C. L. Moran, L. S. Nelson, R. S. Hoffman, J. H. Moran, *Clin. Toxicol. (Phila)*, **49**, 760, (2011).
13. D. Papanti, F. Schifano, G. Botteon, F. Bertossi, J. Mannix, D. Vidoni, M. Impagnatiello, E. Pascolo-Fabrizi, T. Bonavigo, *Hum. Psychopharmacol.*, **28**, 379, (2013).
14. K Simolka, R Lindigkeit, HM Schiebel, U Papke, L Ernst, T Beuerle, *Anal. Bioanal. Chem.*, **404**, 157, (2012).
15. A. Derungs, A. E. Schwaninger, G. Mansella, R. Bingisser, R. Kraemer, M. E., Liechti *Forensic Toxicol.* **31**, 164, (2013).
16. T. Saito, A. Namera, N. Miura, S. Ohta, S. Miyazaki, M. Osawa, S. Inokuchi, *Forensic Toxicol.*, **31**, 333, (2013).
17. N. Schaefer, B. Peters, D. Bregel, S. Kneisel, V. Auwärter, V. Schmidt, A. H. Ewald, *Toxicchem. Krimtech.*, **80**, 248, (2013).
18. H. Choi, S. Heo, E. Kim, B. Y. Hwang, C. Lee, J. Lee, *Forensic Toxicol.*, **31**, 86, (2013).
19. J. M. Frost, M. J. Dart, K. R. Tietje, T. R. Garrison, G. K. Grayson, A. V. Daza, O. F. El-Kouhen, L. N. Miller, L. Li, B. B. Yao, G. C. Hsieh, M. Pai, C. Z. Zhu, P. Chandran, M. D. Meyer, *J. Med. Chem.*, **51**, 1904, (2008).

## СИНТЕТИЧНИ КАНАБИМИМЕТИЦИ, УСТАНОВЯВАНИ В СМЕСКИ ЗА ПУШЕНЕ НА ТЕРИТОРИЯТА НА БЪЛГАРИЯ– ТОКСИКОЛОГИЧНО ЗНАЧЕНИЕ

П. А. Гатева<sup>1\*</sup>, В. Т. Ангелова<sup>2</sup>, Р. Т. Георгиева-Николова<sup>3</sup>, Ц. Р. Веселинов<sup>4</sup>, В. Х. Нанкова<sup>4</sup>, М. М. Николова<sup>5</sup>, Р. К. Хаджиолова<sup>6</sup>, М. П. Славова<sup>7</sup>

<sup>1</sup>Катедра по фармакология и токсикология, Медицински факултет, Медицински университет - София  
България

<sup>2</sup>Катедра по химия, Фармацевтичен факултет, Медицински университет-София, София България

<sup>3</sup>Катедра по химия и биохимия, Медицински факултет, Медицински университет – София, София, България

<sup>4</sup>Научен институт по съдебна медицина и криминология, София, България

<sup>5</sup>Middlesex University, School of Health and Education – London, United Kingdom

<sup>6</sup>Катедра по патофизиология, Медицински факултет, Медицински университет - София България

<sup>7</sup>Катедра по биотехнологии, Химикотехнологичен и металургичен университет, София, България

Получена на 10 юни 2015 г., приета на 15 юли 2015 г.

(Резюме)

Синтетичните каннабимиметици са едни от най-агресивно налагащите се на пазара наркотични вещества. Най-често те се добавят към растителни смеси за пушене или се продават под формата на прах като „соли за вана“, „химикали за анализ, непредназначени за употреба от хора“, „растителни храни“ и др. В нашата страна за периода от 2010 до 2013 г. в смеси за пушени са идентифицирани JWH-018, JWH-073, MAM-2201, UR-144 и STS-135. Анализът на информацията относно ефектите им след консумирането им от хора показва, че те са психоактивни субстанции, често с по-силни ефекти от самата марихуана. Времето на тяхната поява на пазара съвпада със световното им разпространение и почти винаги предшества включването им в Списъка със забранени вещества. Нашата правна система се стреми да включва колкото се може по-бързо новите дизайнерски дроги в регулация.



## Hydrogen sorption of magnesium plates deformed by surface mechanical attrition treatment

Á. Révész<sup>1\*</sup>, C. Szilágyi<sup>1</sup>, T. Spassov<sup>2</sup>

<sup>1</sup>Department of Materials Physics, Eötvös University, Budapest, H-1518, P.O.B. 32, Budapest, Hungary

<sup>2</sup>Faculty of Chemistry and Pharmacy, University of Sofia “St. Kl. Ohridski”, 1 J. Bourchier Str., 1164 Sofia, Bulgaria

Received June 26, 2015; Revised December 1, 2015

Surface modification attrition treatment was carried out on commercial magnesium disks in a SPEX 8000 shaker mill. Morphological and microstructural evolution during the severe plastic deformation process have been investigated by scanning electron-microscopy and X-ray diffraction line profile analysis, respectively. Complementary hydrogen absorption experiments in a Sieverts'-type apparatus revealed that hydrogen kinetics and the microstructural parameters exhibit correlation.

**Keywords:** Hydrogen storage; Mg-based; Microstructure; Severe plastic deformation; Surface modification by attrition treatment.

### INTRODUCTION

Magnesium attracts high interest in solid state hydrogen storage due to its remarkable gravimetric storage capacity, lightness and moderate cost [1, 2]. Unfortunately, the relatively high stability of the hydride phase and the poor  $\text{Mg} \leftrightarrow \text{MgH}_2$  kinetics retain the wide-spread application of commercial  $\text{MgH}_2$  [3]. In order to overcome these obstacles, magnesium is extensively subjected to severe plastic deformation (SPD) by different technical routes [4, 5]. Among them high energy ball milling (HEBM) is applied, since this technique leads to the most effective particle-size and crystallite-size reduction [3, 6-8], which significantly enhance the hydrogen sorption kinetics due to the increased volumetric density of grain boundaries and lattice defects [9, 10]. Moreover, the addition of metal or metal-oxides catalyst powders to magnesium [9, 11, 12] results in the thermo-dynamical destabilization of  $\text{MgH}_2$  [8]. Notwithstanding that HEBM exhibits several advantages, drawbacks are also present due to powder processing, i.e. surface oxidation, large energy consumption, the necessity of an inert atmosphere, a potential fire risk and the difficulty of industrial level production.

These disadvantages of HEBM have extensively been eliminated very recently by novel bulk SPD techniques, including high-pressure torsion (HPT) [13-16], cold rolling [17-19] and equal-channel angular pressing [20-23]. These bulk methods have numerous benefits, i.e. the process is less intensive than HEBM, scaling up to larger quantities at a lower cost has a larger potential, impurity

concentration is lower and causes less safety concerns [20].

Recently, an alternative SPD method was invented by Lu and coworkers by modifying the surface layer of a bulk material by mechanical attrition [24, 25]. Conventional surface-modified techniques usually involve chemical reactions resulting in an optimized mechanical, tribological or chemical structure of the surface layer in order to improve the general performance of the end-product. Nevertheless, the change of the surface microstructure by decreasing the grain size of the top-most layer of the bulk material can also accelerate the different reactions. Namely, the surface mechanical attrition treatment (SMAT) technique involves repeated multidirectional impacts by flying balls to induce severe plastic deformation in the surface layer of a target sample accompanied with large grain boundary misorientation, formation of dislocation blocks and surface nanocrystallization [26]. This nanocrystalline surface layer becomes chemically active, promoting the effectiveness of subsequent treatments such as nitriding [24] and chromizing [27]. Examination of the Mg alloy subjected to SMAT indicated an improved wear resistance of the surface nanocrystalline layer with an average grain size of  $30 \pm 5$  nm [28, 29]. As a result of the SMAT process, the micro-hardness of a biodegradable Mg-alloy has increased considerably in the near-surface region, however, the high dislocation density and abundant grain boundaries have severely weakened the corrosion resistance [30]. Cross sectional structural investigations revealed that the SMAT affected layer can be subdivided into three zones, i.e. an ultrafine grain zone at the top surface, a subsurface transition zone and

\* To whom all correspondence should be sent:  
E-mail: reveszadam@ludens.elte.hu

a deformed zone where the initial grains are only plastically deformed [31]. The enhanced hardening achieved by the non-uniform deformation and grain-size gradient microstructure during the SMAT technique can satisfactorily be correlated by the physical model of Li et al. [32].

In the present experiment, we applied the SMAT technique on commercial Mg disks for different treatment times to generate a different microstructure in the severely deformed top layer. We demonstrate the correlation of hydrogen absorption kinetics and the microstructure obtained by applying the Convolutional Whole Profile Fitting (CMWP) algorithm of X-ray line profiles.

## EXPERIMENTAL

### *SMAT processing*

The mechanical treatment by the SMAT technique was carried out on commercial magnesium specimens (Goodfellow #MG007918) in a SPEX 8000 mixer mill. The conventional end cap of the container was replaced by a well-attached Mg disk target (50 mm in diameter and 5 mm in thickness). In order to ensure an approximately homogeneous distribution of the impacts, the stainless steel vial was filled with plenty hardened steel balls. Based on preliminary experiments [33], we applied 40 balls with a diameter of 6.35 mm and 12 balls with a diameter of 12.5 mm for different treatment times (15 min, 30 min and 90 min). The whole SMAT process was carried out in air. It is noted that the use of a few balls can lead to a non-uniform distribution of the impact points, while too many balls result in many ball-to-ball collisions and a reduced impact velocity.

### *Microstructural characterization*

Microstructural characterization of the surface of the SMATed disks was performed by X-ray powder diffraction (XRD) with Cu-K $\alpha$  radiation on a Philips X'pert powder diffractometer in  $\theta$ -2 $\theta$  geometry. The instrumental pattern was measured on NIST SRM660a LaB6 peak profile standard material.

The recorded X-ray diffraction patterns have been evaluated by the CMWP fitting procedure developed by prof. T. Ungár and co-workers [34]. Briefly, the CMWP analysis incorporates the direct fit of the whole of the X-ray diffractogram as measured by summing up the background, theoretically constructed profile functions and measured instrumental profile. These profile functions are calculated for each Bragg-reflection

as the inverse Fourier transform of the product of the size and strain of Fourier coefficients and the Fourier coefficients of the corresponding measured instrumental profile [35]. In the simplest version of the CMWP analysis it is assumed that the crystallites are spherical and obey lognormal size distribution:

$$G(x) = (2\pi)^{-1/2} \sigma^{-1} x^{-1} \exp[-(\ln(x/m))^2/2\sigma^2], \quad (1)$$

where  $\sigma$  and  $m$  are the variance and median of the distribution, respectively. Besides the microstructure size parameters, the line profile analysis provides the strain parameters, the average dislocation density ( $\rho$ ) and effective outer cut-off radius of dislocations ( $R_e$ ). From the available data, the average coherently scattering crystallite size can be determined [34] as:

$$\langle D \rangle = m \exp(2.5\sigma^2), \quad (2)$$

More details of the fitting algorithm and its systematic application to ball-milled Mg-based powders can be found elsewhere [10, 35, 36].

The morphology was studied on a FEI QUANTA 3D dual beam scanning electron microscope (SEM). The local composition was quantitatively determined by energy dispersive X-ray (EDX) analysis.

### *Hydrogen sorption kinetics*

Hydrogenation kinetic curves of the SMAT processed Mg samples were measured by a Sieverts'-type apparatus (PCT) at 573 K. The initial hydrogen pressure was set as 1 MPa. For details, see [15].

## RESULTS AND DISCUSSION

The microstructural variations associated with the SMAT process of commercial Mg disks can be monitored in Fig. 1. The diffractograms carried out on the topmost surface of all treated states are evidently characterized by the peaks of hexagonal Mg (JCPDS 35-0821). As the milling commences, the breadth of the Bragg-peaks changes slightly, indicating a variation of lattice strain and average grain-size induced by the severe plastic deformation during the surface modification. In addition, faint diffraction peaks corresponding to the MgO phase emerge at the end of the treatment process. As a result of the surface treatment, one might expect some evolving anisotropy, nevertheless the relative intensities of the Mg-peaks change only negligibly, contrary to other different SPD-processed Mg-alloys [15, 23]. An example of the CMWP fitting procedure is presented in Fig. 2, where the measured diffractogram corresponding to

the sample SMATed for 15 min, the fitted pattern and the difference plot between the measured and fitted patterns are presented. An obvious correlation between the measured and fitted pattern is clear, however slight differences occur at the high intensity peak centers.

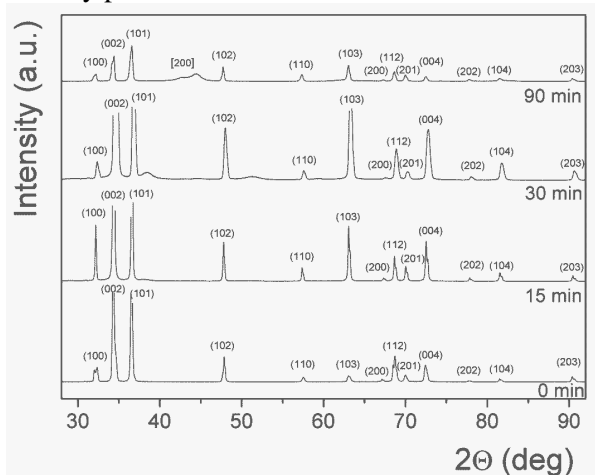


**Fig. 1.** XRD patterns taken from the surface of the Mg plates treated for different times. The brackets (...) and [...] denote the Bragg-peaks of hexagonal Mg and MgO, respectively.

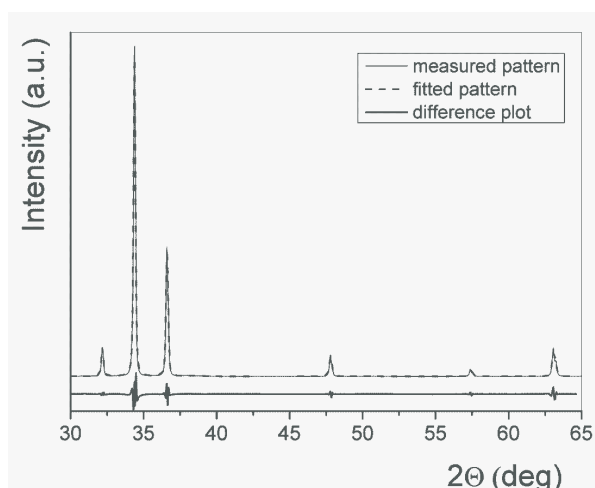


**Fig. 2.** Measured XRD pattern of the Mg disk SMATed for 15 min, the function fitted by the CMWP method and the difference between the measured and fitted data.

The median and the variance of the magnesium crystallite-size distribution as a function of the SMAT procedure time determined by the CMWP procedure can be realized in Fig. 3. As seen, the  $m$  value decreases continuously from the initial value of 29 nm to 18.5 nm at the early stages of the treatment time, however, a remarkable increase up to 32.4 nm is noticed after 90 min. At the same time,  $\sigma$  gradually decreases for up to 30 min from 0.74 to 0.58 and then obeys a subsequent increase (0.81) at the end of the SMAT treatment. From the calculated data of  $m$  and  $\sigma$ , the corresponding

normalized log-normal distribution functions can be plotted, see Fig. 4. A simultaneous shift of the distribution maxima to lower values and a significant narrowing of the histograms up to 30 min of SMAT treatment are evidenced from the curves, indicating that not only a crystallite-size reduction occurs in the uppermost layers of the Mg disks, but a homogenization on the nanoscale also takes place. Surprisingly, these phenomena do not continue until the end of the SMAT process, on the contrary, longer treatment time exhibits a wider distribution of the crystallite size referring to a relatively more inhomogeneous microstructure. Moreover, the right-hand sidetail of the distribution function becomes more pronounced, corresponding to the formation of larger crystallites.

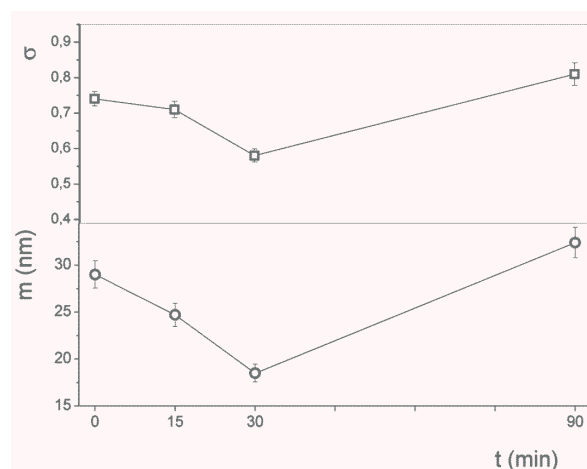


**Fig. 3.** Variation of the median ( $m$ ) and the variance ( $\sigma$ ) as a function of treatment time.

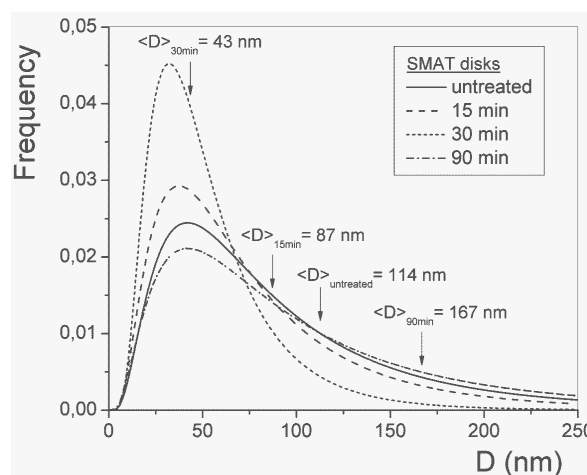


**Fig. 4.** Crystallite size distribution functions of the Mg disks. The volume averaged crystallite size ( $\langle D \rangle = m \exp(2.5\sigma^2)$ ) for each treatment time is also denoted.

The calculated volume averaged crystallite size values ( $\langle D \rangle$ ) are plotted in Fig. 5. As one can conclude, the SMAT process changes the microstructure of the top deformed layer considerably,  $\langle D \rangle$  decreases by a factor of 3 (to 43

nm) after 30 min of treatment. Thereafter some kind of recrystallization takes place, reaching a final value of  $\langle D \rangle = 167$  nm. As described above, the CMWP analysis provides also the strain parameters, in our case the average lattice defect density, i.e. the dislocation density plays a crucial role. Fig. 5 also presents the variation of  $\rho$  as a function of the surface treatment time. A roughly linear increase can be noticed reaching a maximum value of  $\rho = 2.5 \cdot 10^{13} \text{ m}^{-2}$  after finishing the SMAT process. This value is slightly lower than that as found for ball-milled Mg powder [35] and an Mg-alloy processed by equal channel angular pressing [37]. Despite the large defect density, the obtained average defect distance  $L \geq 200$  nm ( $L = \rho^{-1/2}$ ) exceeds the average crystallite size  $\langle D \rangle$  at any treated state. Consequently, a significant portion of the crystallites can be considered as defect-free. In addition, as obtained from the analysis, the severe plastic deformation during SMAT favors the formation of  $\langle a \rangle$ -type dislocations with a Burgers' vector  $b = \frac{1}{3} \langle \bar{2}110 \rangle$ , exhibiting the lowest formation energy among the possible types of dislocations. The relative fraction of  $\langle a+c \rangle$  and  $\langle c \rangle$ -type of dislocations is negligible.

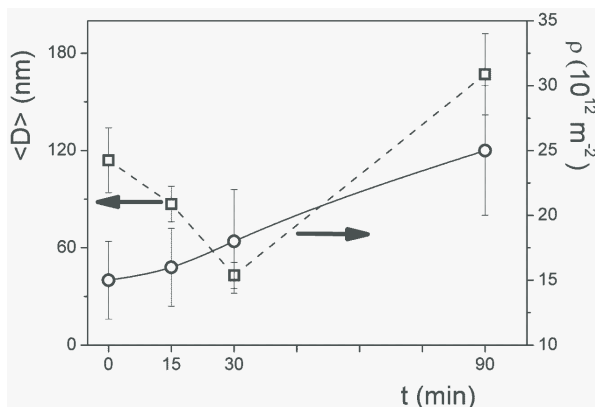


**Fig. 5.** Variation of the average crystallite size ( $\langle D \rangle$ ) and the average dislocation density ( $\rho$ ) as a function of the SMAT treatment time.

SEM images taken on the cross-section of the sample SMATed for the longest treatment time (90 min) explain some aspects of the relevant XRD pattern and exhibit several interesting features concerning the morphology of the severely deformed top layer (Fig. 6). As the low magnification micrograph (250x) indicates, the surface of the treated sample is uneven, clear signs of surface shearing and folding are visible and can be divided up into well-separated areas of different contrast. In some areas the formation of a non-contiguous bright surface layer is observed. One might also notice that cracks perpendicular to the surface, which are favorable for accelerated

hydrogen diffusion, penetrate into the bulk regions. At higher magnification (1000x) it is clear that the surface layer is not uniform, its thickness spans over a wide range with an average value of  $22 \mu\text{m}$ . The results of the EDS elemental analysis carried out on three different regions (denoted by rectangles) can be found in Table 1.

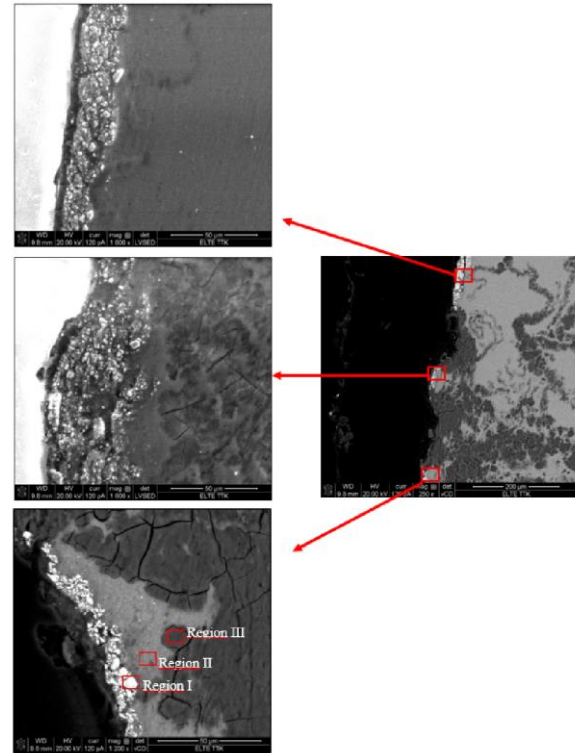


**Fig. 6.** SEM images taken on different parts of the cross section of the disk treated for 90 min.

**Table 1.** Elemental concentrations of the three different regions obtained on the cross section of the Mg disk treated for 90 min of SMAT.

Element	Region I	Region II	Region III
	Atomic percent		
Mg	76,41	99,10	99,75
Fe	20,93	0,33	0,14
Ni	1,85	0,10	0,04
Nb	0,66	0,23	0,07
Al	0,15	0,24	0,00

Concentrations averaged for the brightest white area (Region I) are significantly enriched in iron. Regions II and III are abundant in magnesium, the contrast difference may originate from the different iron and trace element content. At first glance, the detected high iron content at some positions of the surface layer is surprising, since no elemental Fe could be identified on the corresponding XRD pattern (see Fig. 1). Henceforth, it is assumed that iron is dissolved in the Mg-lattice and on the grain boundaries among the individual crystallites, even though Fe is immiscible in Mg according to the

equilibrium phase diagram [38]. Nevertheless, the extreme severe plastic deformation occurring at the contact points between the target and the balls may result in highly non-equilibrium processes that can promote some solubility of iron in Mg. The detected significant amount of iron presumably originates from the milling media, i.e. the steel vial and the balls. During the initial stages of the SMAT process the bombarded Mg-targets become harder and physically active. After a certain amount of processing time, the abundant ball-to-target collisions can induce some removal of hardened Mg particles (chips) from the top layer. Later on these particles are mixed with iron debris in the milling container due to the ball-to-ball collisions. As a final step, this powder mixture is re-deposited onto some parts of the fresh and active surface of the target disk forming the observed non-contiguous iron-rich top surface layer.

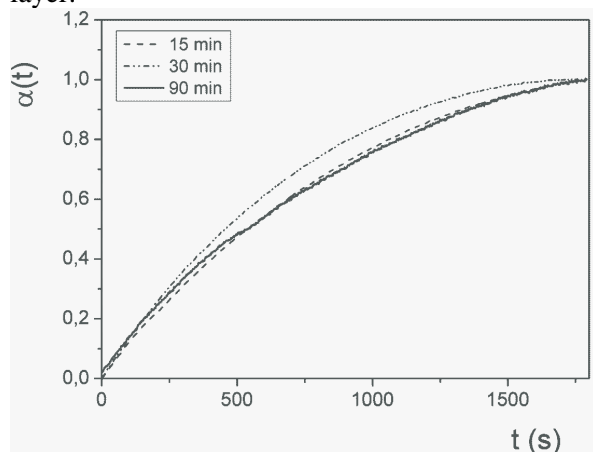


**Fig. 7.** Normalized hydrogen kinetic absorption curves of the Mg plates, treated for different SMAT times.

Normalized hydrogen absorption kinetic data ( $\alpha$ ) for the different Mg plates obtained at 573 K are presented in Fig. 7. All the specimens absorb hydrogen almost without activation, as the maximum capacity is reached after the first full absorption-desorption cycle. The detectable maximum capacity of the disks increases gradually with the SMAT treatment time, confirming the fact that Mg or Mg-based alloys processed by SPD under air are able to absorb hydrogen [39]. As one will also notice, the initial absorption kinetics is fast for all samples, reaching 50% of hydriding within 500s. As the CMWP results indicate (see Figs. 4 and 5), the specimen treated for the longest time (90 min) suffers a recrystallization of the nanocrystalline Mg-grains, however, it exhibits the largest defect density. Henceforth, the observed increase in the maximum H-capacity can be attributed mainly to the lattice defects (dislocations)

generated during the heavy shear deformation during the SMAT process which can act as hydrogen absorption sites in the grain interiors by enhancing the diffusion of the H atoms, while the role of the grain boundaries and particle surfaces is remarkably less important. In a recent paper we have shown that abundant lattice defects have a crucial role in the creation of new and easily accessible hydrogen sites in Mg-Ni alloys produced by HPT [15]. Moreover, Horita and co-workers demonstrated noticeable hydrogen storage performance in coarse-grained MgNi<sub>2</sub> processed by HPT due to the intense anisotropic strain, although this compound possesses no measurable capacity under equilibrium conditions [13].

The normalized absorption curves for all treatment times can satisfactorily be fitted by the contracting volume function (CV) [40]. In brief, this model is valid when the nucleation starts at the surface of the particle and growth takes place from the surface into the bulk and the growth of the new phase occurs with a constant interface velocity. The kinetics can then be described by:

$$\alpha_{CV}(t, R) = 1 - (1 - k_{CV}t)^n, \quad (3)$$

where  $k_{CV}$  is a reaction constant and can be given as  $k_{CV} = u/R$ , where  $u$  is the velocity of the hydride metal interface motion and  $R$  is the average crystallite radius.  $n$  depends on the dimensionality of the growth, with  $n = 3$  for three-dimensional and  $n = 2$  for two-dimensional growth. The parameters obtained from the CV fits are listed in Table 2. As realized, the dimensionality parameter increases monotonously with the treatment time referring to a more isotropic hydride formation. The  $u$  value is significantly the greatest for the disk processed for 90 min of SMAT, indicating that the growth velocity of the hydride phase is the largest for this specimen, in accordance with the above findings, i.e. despite the larger average crystallite size, the abundant lattice defects account for the observed H-storage performance. In addition, we can further assume that iron as a catalyst can also influence the hydrogenation of the Mg-disks processed by the SMAT technique.

**Table 2.** Fitting parameters of the CV-model for different times.

Treatment time (min)	$k_{CV} \left(\frac{1}{s}\right)$	$n$	$u \left(\frac{nm}{s}\right)$
15	$(4,686 \pm 0,010) \cdot 10^{-4}$	$2,378 \pm 0,007$	$0,020 \pm 0,024$
30	$(4,997 \pm 0,009) \cdot 10^{-4}$	$2,669 \pm 0,006$	$0,003 \pm 0,014$
90	$(4,112 \pm 0,033) \cdot 10^{-4}$	$2,798 \pm 0,029$	$0,082 \pm 0,027$

## CONCLUSIONS

In this study commercial Mg disks were subjected to intense plastic deformation by SMAT. The CMWP analysis of X-ray line profiles revealed that the uppermost layer of the disks undergoes significant microstructural changes, i.e. the volume averaged coherent crystallite size reaches a minimum of  $\langle D \rangle = 43$  nm after 30 min of SMAT treatment, while a significant recrystallization takes place after that ( $\langle D \rangle = 167$  nm). During this process, the removal of hardened Mg particles from the top layer occurs which are mixed with iron debris in the milling container later on. As a final step, this powder mixture is re-deposited onto the target disk forming a non-contiguous iron-rich top surface layer. Combined XRD and SEM experiments confirmed that iron forms a non-equilibrium solid solution in the Mg-lattice. At the same time the average lattice defect obeys a roughly linear increase up to a final value of  $\rho = 2.5 \cdot 10^{13} \text{ m}^{-2}$ . The hydrogen absorption curves of all the SMAT processed samples can satisfactorily be fitted by the CV function. By analyzing the fitting parameters, we found that the growth velocity of the hydride phase is the largest for the disk treated for 90 min, indicating that lattice defects (dislocations) generated during the SMAT process can act as hydrogen absorption sites in the grain interiors, while the role of the grain boundaries and particle surfaces is remarkably less important.

**Acknowledgements:** Á.R. is indebted for the János Bolyai Research Scholarship of the Hungarian Academy of Sciences. T.S. is grateful to the FP7 project Beyond Everest. The authors appreciate the support of G. Varga in the SEM experiments. We acknowledge the support of the COST Action MP1103.

## REFERENCES

1. E.C.E. Rönnebro, E.H. Majzoub, *MRS Bull.*, **38**, 452(2013).
2. L. Schlapbach, A. Züttel, *Nature*, **414**, 353(2001).
3. R.A. Varin, T. Czujko, Z.S. Wronski, *Nanomaterials for Solid State Hydrogen Storage*, Springer Science, New York, 2009.
4. R.Z. Valiev, R.K. Ishlamgaliev, I.V. Alexandrov, *Prog. Mater. Sci.*, **45**, 103(2000).
5. Y. Estrin, A. Vinogradov, *Acta Mater.*, **61**, 782 (2013).
6. L. Zaluski, A. Zaluska, P. Tessier, J.O. Ström-Olsen, R. Schulz, *Mater. Sci. Forum*, **225**, 853 (1996).
7. D. Fátay, Á. Révész, T. Spassov, *J. Alloys Compd.*, **399**, 237(2005).
8. W. Oelerich, T. Klassen, R. Bormann, *J. Alloys Compd.*, **315**, 237 (2001).

9. Á. Révész, D. Fátay, T. Spassov, *J. Alloys Compd.*, **434-435**, 725(2007).
10. D. Fátay, T. Spassov, P. Delchev, G. Ribárik, Á. Révész, *Int. J. Hydrogen Energy*, **32**, 2914 (2007).
11. X. Zhao, S. Han, Y. Zhu, X. Chen, D. Ke, Z. Wang, T. Liu, Y. Ma, *J. Solid State Chem.*, **221**, 441 (2015).
12. X. Zhu, L. Pei, Z. Zhao, B. Liu, S. Han, R. Wang, *J. Alloys Compd.*, **577**, 64 (2013).
13. Y. Kusadome, K. Ikeda, Y. Nakamori, S. Orimo, Z. Horita, *Scripta Mater.*, **57**, 751(2007).
14. K. Edalati, A. Yamamoto, Z. Horita, T. Ishihara, *Scripta Mater.*, **64**, 880 (2011).
15. Á. Révész, Zs. Kánya, T. Verebélyi, P.J. Szabó, A.P. Zhilyaev, T. Spassov, *J. Alloys Compd.*, **504**, 83 (2010).
16. T. Hongo, K. Edalati, H. Iwaoka, M. Arita, J. Matsuda, E. Akiba, Z. Horita, *Mater. Sci. Engineering A*, **618**, 1 (2014).
17. S.D. Vincent, J. Lang, J. Huot, *J. Alloys Compd.*, **512**, 290 (2012).
18. J. Bellemare, J. Huot, *J. Alloys Compd.*, **512**, 33 (2012).
19. D.R. Leiva, H.C. de Almeida Costa, J. Huot, T.S. Pinheiro, A.M. Jorge, T.T. Ishikawa, W.J. Botta, *Mater. Res.*, **15**, 813 (2012).
20. V.M. Skripnyuk, E. Rabkin, Y. Estrin, R. Lapovok, *Acta Mater.*, **52**, 405 (2004).
21. V.M. Skripnyuk, E. Rabkin, Y. Estrin, R. Lapovok, *Int. J. Hydrogen Energy*, **34**, 6320 (2009).
22. A.M. Jorge, E. Prokofiev, G.F. de Lima, E. Rauch, M. Veron, W.J. Botta, M. Kawasaki, T.G. Langdon, *Int. J. Hydrogen Energy*, **38**, 8306 (2013).
23. Á. Révész, M. Gajdics, L.K. Varga, Gy. Krállics, T. Spassov, *Int. J. Hydrogen Energy*, **39**, 9911 (2014).
24. W.P. Tong, N.R. Tao, Z.B. Wang, J. Lu, K. Lu, *Science*, **299**, 686 (2003).
25. X. Wu, N. Tao, Y. Hong, G. Liu, B. Xu, J. Lu, K. Lu, *Acta Mater.*, **53**, 681(2005).
26. N.R. Tao, Z.B. Wang, W.P. Tong, M.L. Sui, J. Lu, K. Lu, *Acta Mater.*, **50**, 4603 (2002).
27. Z.B. Wang, J. Lu, K. Lu, *Acta Mater.*, **53**, 2081 (2005).
28. H.Q. Sun, Y.N. Shi, M.X. Zhang, *Surf. Coat. Technol.*, **202**, 2859 (2008).
29. H.Q. Sun, Y.N. Shi, M.X. Zhang, K. Lu, *Surf. Coat. Technol.*, **202**, 3947 (2008).
30. N. Li, Y.D. Li, Y.X. Li, Y.H. Wu, Y.F. Zheng, Y. Han, *Mater. Sci. Engineering C*, **35**, 314 (2014).
31. Y. Samih, B. Beausir, B. Bolle, T. Grosdidier, *Mater. Charact.*, **83**, 129 (2013).
32. J. Li, S. Chen, X. Wu, A.K. Soh, *Mater. Sci. Engineering A*, **620**, 16 (2015).
33. Á. Révész, L. Takacs, *J. Alloys Compd.*, **441**, 111 (2007).
34. G. Ribárik, J. Gubicza, T. Ungár, *Mater. Sci. Engineering A*, **387-389**, 343 (2004).
35. Á. Révész, D. Fátay, *J. Power Sources*, **195**, 6997 (2010).
35. Á. Révész, M. Gajdics, T. Spassov, *Int. J. Hydrogen Energy*, **38**, 8342 (2013).
36. J. Gubicza, K. Máthis, Z. Hegedűs, G. Ribárik, A.L. Tóth, *J. Alloys Compd.*, **492**, 166 (2010).

37. A. A. Nayeb-Hashemi, J. B. Clark, L. J. Swartzendruber, *Bulletin of Alloy Phase Diagrams*, **6**, 235 (1985).
38. J. Huot, S.D. Vincent, *J. Alloys Compd.*, **509**, L175 (2011).
39. P.W.M Jacobs and F.C Tompkins: Classification and theory of solid reactions, in *Chemistry of the Solid State*, W.E. Garner (ed.), Butterworth, London, 1955, p.184..

## СОРБЦИЯ НА ВОДОРОД В МАГНЕЗИЕВИ ПЛАСТИНИ ДЕФОРМИРАНИ ЧРЕЗ ПОВЪРХНОСТНО МЕХАНИЧНО ИЗТРИВАНЕ

А. Ревеш<sup>1</sup>, Ц. Силаги<sup>1</sup>, Т. Спасов<sup>2</sup>

<sup>1</sup>Факултет по физика на материалите, Йотвош университет, Будапеща, Н-1518, Р.О.В. 32, Унгария

<sup>2</sup>Факултет по химия и фармация, Софийски университет "Св. Кл. Охридски", 1 Дж. Баучер, 1164 София, България

Получена на 26 юни 2015 г., коригирана на 1 декември 2015 г.

(Резюме)

Търговски магнезиеви дискове са модифицирани чрез повърхностно механично изтриване в мелница тип SPEX 8000. Морфологичните и микроструктурни промени по време на процеса на пластична деформация са изследвани с помощта съответно на сканираща електронна микроскопия и рентгеново дифракционен линеен профилен анализ. Водородно-абсорбционни експерименти с апарат на Сиверт показват наличие на корелация между кинетиката на водородна сорбция и микроструктурните параметри на материала.

## Chemical composition of *Limonium thouinii* (viv.) kuntze (Plumbaginaceae) and the DPPH free radical scavenging activity

M. Lefahal<sup>1</sup>, M. Benahmed<sup>2</sup>, L. Djarri, N. Zaabat<sup>1</sup>, A. E Hay<sup>3</sup>, M. Kamel<sup>1</sup>, M.G. Dijoux Franca<sup>3</sup>, H. Laouer<sup>4</sup>, S. Akkal<sup>1\*</sup>

<sup>1</sup>Université de Constantine1, Unité de Recherche Valorisation des ressources naturelles Molécules bioactives et Analyses Physico-Chimiques et Biologiques, Département de Chimie, Facultés des Sciences exactes, Algérie.

<sup>2</sup>Université Larbi Tébessi Tébessa Laboratoire des molécules et applications, Algérie.

<sup>3</sup>UMR 5557 CNRS-UCBL – Ecologie Microbienne, CESN, ISPB, 8 Avenue Rockefeller, F69373 Lyon cedex, France

<sup>4</sup>Université Ferhat Abbas Sétif 1, laboratoire de valorisation des ressources naturelles biologiques. le département de biologie et d'écologie végétales, Algérie.

Received July 8, 2015, Accepted October 2, 2015

The present work considers the phytochemical investigation and DPPH free radical-scavenging activity of the aerial parts of *Limonium thouinii* (Viv.) Kuntze (Plumbaginaceae). The aerial parts of *Limonium thouinii* (Viv.) Kuntze allow the isolation of four flavonoids: Quercetin, Vitexin, Isoorientin and Cannabiscitrin. Their structures were elucidated on the basis of spectroscopic analysis, including UV, MS and NMR techniques. The DPPH free radical-scavenging activity was evaluated on crude extracts (MeOH, EtOAc and n-BuOH extracts).

**Keywords:** Plumbaginaceae; *Limonium thouinii*; Flavonoids; Free DPPH radical scavenging activity.

### INTRODUCTION

The genus *Limonium* Miller belongs to the Plumbaginaceae family [1]. This genus is represented by 350 species which are growing throughout the world [2]. The flora of Algeria contains 20 species of *Limonium* among which 8 are endemic [3]. Many *Limonium* species were well known in folk medicine for their cure proprieties, such as *L. wrightii* species which is used for the treatment of fever or arthritis [4], the roots of *L. gmelinii* are used in folk medicine as an astringent and for acute gastrointestinal diseases [5]. Furthermore, *L. brasiliense* are employed as an antioxidant medicinal herb [6], whereas *L. sinense* exhibits antiviral activity [7]. Previous phytochemical studies of *Limonium* revealed the presence of different classes of flavonoids such as flavanes, aurones, flavonols and flavonol glycosides [8-14]. Furthermore, it is observed that *Limonium thouinii* has been tested as an inhibitor of corrosion [15]. The present study was aimed to investigate, for the first time, the constituent aerial parts of *L. thouinii*. The fractionation, isolation and structural elucidation yielded four compounds, which are shown in Fig. 1. The crude extracts were evaluated for their DPPH free radical-scavenging activity. Flavonoids are a group of polyphenolic compounds with known properties which include free radical scavenging, due to the presence of the

hydroxyl group in their chemical structures [16].

### RESULTS AND DISCUSSION

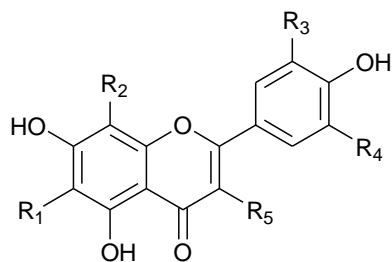
Structures elucidation compounds 1-4 (fig.1) were identified by means of spectral data as quercetin (**1**), Apigenin 8-C-glucoside (**2**), Luteolin 6-C-glucoside (**3**) and Myricetin-3'-O-glucoside (**4**). These compounds are identified by spectral data, co-chromatography with authentic sampling when possible and confirmed by comparison with data from the literature [16-20]. Compound 1 was identified by spectroscopic techniques (UV-visible and mass spectroscopy), while 2, 3 and 4 were identified by UV-visible and <sup>1</sup>H, <sup>13</sup>C NMR spectra and mass spectroscopy.

Quercetin **1**. UV ( $\lambda_{max}$ , nm), MeOH: 255-368. Mass spectrum (IE) m/z: 302 [M]<sup>+</sup>, 153 [A1 + H], 137 [B2]. [17].

Vitexin (Apigenin 8-C-glucoside) **2**. UV ( $\lambda_{max}$ , nm), MeOH: 266-336. Mass spectrum (ES) m/z : 433 [M+H].  $\delta$  <sup>1</sup>H NMR (300 MHz, DMSO-d<sub>6</sub>): 6.71 (1H, s, H-3), 6.21(1H, s, H-6), 8 (2H, d, J= 8.6 Hz, H-2', H-6'), 6.9 (2H, d, J= 8.6 Hz, H-5', H-3'), 4.75 (1H, d, J= 9.9 Hz, H-1''), sugar protons (3.5- 4), 13.13 (1H, s, OH-5).  $\delta$  <sup>13</sup>C NMR (75 MHz, DMSO-d<sub>6</sub>): 163.8 (C-2), 102.4 (C-3), 182.0 (C-4), 161.2 (C-5), 98.3 (C-6), 163.2 (C-7), 104.6 (C-8), 156.0 (C-9), 104.6 (C-10), 121.6 (C-1'), 128.9 (C-2'), 115.8 (C-3'), 160.4 (C-4'), 115.8 (C-5'), 128.9 (C-6'), 73.4 (C-1''), 70.9 (C-2''), 78.7 (C-3''), 70.5 (C-4''), 81.8 (C-5''), 61.3 (C-6''). [18].

\* To whom all correspondence should be sent:  
E-mail: salah4dz@yahoo.fr





	R1	R2	R3	R4	R5
1	H	H	OH	H	OH
2	H	Glu	H	H	H
3	Glu	H	OH	H	H
4	H	H	OH	O-glu	OH

Fig. 1. Chemical structures of compounds 1-4.

Isoorientin (*Luteolin 6-C-glucoside*) 3. UV ( $\lambda_{max}$ , nm), MeOH: 266-336. Mass spectrum (ES)  $m/z$ : 447 [M-H].

$\delta$  <sup>1</sup>H NMR (300 MHz, CD<sub>3</sub>OD): 6.57 (1H, s, H-3), 6.52(1H, s, H-8), 7.39(1H, d, J= 2.2 Hz, H-2'), 7.41 (1H, dd, J= 2.2; 8.6 Hz, H-6'), 6.93(1H, d, J= 8.6 Hz H-5'), 4.92 (1H, d, J= 9.9 Hz ,H-1"). Sugar protons (3.5- 3.9).  $\delta$  <sup>13</sup>C NMR (75 MHz, CD<sub>3</sub>OD): 166.3 (C-2), 103.9 (C-3), 184.0 (C-4), 162.0 (C-5), 109.2 (C-6), 165.0 (C-7), 95.2 (C-8), 158.7 (C-9), 105.2 (C-10), 123.5 (C-1'), 114.1 (C-2'), 147.0 (C-3'), 151.0 (C-4'), 116.8 (C-5'), 120.3 (C-6'), 72.5 (C-1"), 75.3 (C-2"), 80.1 (C-3"), 71.7 (C-4"), 82.6 (C-5"), 62.8 (C-6"). [19].

Cannabiscitrin (*Myricetin-3'-O-glucoside*) 4, UV ( $\lambda_{max}$ , nm), MeOH: 254-371. Mass spectrum (ES)  $m/z$ : 479 [M-H], 317[M-H-162].  $\delta$  <sup>1</sup>H NMR (300 MHz, CD<sub>3</sub>OD): 6.18 (1H, d, J= 2.2Hz, H-6), 6.44 (1H, d, J= 2.2Hz, H-8), 7.57 (1H, d, J= 2.2 Hz, H-2'), 7.73 (1H, d, J= 2.2 Hz, H-6'), 4.93 (1H, H1"). Sugar protons (3.5- 3.96).  $\delta$  <sup>13</sup>C NMR (75 MHz, CD<sub>3</sub>OD): 147.2 (C-2), 138.6 (C-3), 177.3 (C-4), 162.0 (C-5), 99.3 (C-6), 165.7 (C-7), 94.5 (C-8), 158.0 (C-9), 104.4 (C-10), 123.3 (C-1'), 109.9 (C2'), 146.9 (C-3', C-5'), 138.6 (C-4'), 111.6 (C-6'), 104.4 (C1"), 74.8 (C-2"), 77.6 (C-3"), 71.2 (C-4"), 78.4 (C-5"), 62.4 (C-6"). [20, 21].

#### DPPH free radical-scavenging activity

The anti-radical activity extracts of *L. thouinii* was evaluated through the ability to scavenge DPPH radicals. The results are represented in Table 1.

The results shown in table1 indicate that all extracts present a weak DPPH free radical-scavenging activity compared to Trolox (TEAC<sub>MeOH</sub> = 0.119, TEAC<sub>n-BuOH</sub> = 0.081, TEAC<sub>EtOAc</sub> = 0.037).

Table 1. DPPH free radical-scavenging activity of *L. thouinii* extracts

	IC <sub>50</sub> ( $\mu$ g/ml)	ARP	TEAC
Trolox	0.106	9.43	1
MeOH	0.89	1.13	0.119
EtOAc	2.87	0.354	0.037
n-BuOH	1.30	0.77	0.081

#### CONCLUSIONS

The phytochemical investigation of *Limonium thouinii* (Viv.) Kuntze revealed the presence of flavonol (Quercetin), two C-glucoside flavones (Vitexin, Isoorientin) and one O-glucoside flavonol (Cannabiscitrin), these four flavonoids are identified for the first time in this species, but Cannabiscitrin is a new compound in the Plumbaginaceae family. The tested extracts of the plant showed a weak DPPH free radical scavenging activity. We have also found the relationship of total flavonoids contents in these extracts with antioxidant activity, may be the hydroxyl group in these chemical structures.

#### EXPERIMENTAL SECTION

The aerial parts of *Limonium thouinii* (Viv.) Kuntze (Plumbaginaceae) was collected during the flowering period, from Setif in the east of Algeria and identified by Prof. H. Laouer (biology and plant ecology department, University of Setif, Algeria). A voucher specimen was deposited in the Herbarium of our laboratory. Voucher specimens of the plant material are deposited in the Herbarium at the department of biology and ecology vegetal, University of Setif (UFAS).

#### Extraction and isolation

Air dried aerial parts of *L. thouinii* (300 g) were soaked in methanol solvent (70%) at room temperature for 72 hours. The residue was filtered and concentrated under reduced pressure to dryness and the residue was dissolved in hot water and kept in the cold overnight. After filtration the aqueous solution was successively extracted with ethyl acetate and n-BuOH. The n-BuOH extract (5g) was subjected to a column polyamide MN SC6 and eluted with a gradient of Toluene-MeOH with increasing polarity to give ten fractions (F1-F10). The fractions F5 and F6 were applied to a preparative PC on Watman n°3 paper using acetic acid 15%, then by preparative TLC on polyamide DC6 to yield compounds: 1 (10mg), 2 (8mg), 3 (30mg) and 4 (11mg).The structures of the isolated compounds were elucidated by spectral analysis

mainly MS, UV, H 1 NMR and C 13 NMR as well as by comparing their spectroscopic data with those reported in the literature.

#### DPPH free radical-scavenging activity

The free radical scavenging capacity of the *L. thouinii* extracts were determined by using DPPH• (1, 1-diphenyl-2-picryl-hydrazyl), according to the method of Brand-Williams [22]. Five concentrations of each extract were prepared from the stock solution, added in equal volume, to the methanolic solution of DPPH on 96 well micro plates. After an incubation of 30 min at room temperature, the absorbance was determined at 515 nm. Trolox was used as a standard control.

The percentage inhibition of the DPPH free radical was calculated as per the following formula:

$$\% \text{ inhibition of DPPH radical} = \frac{(\text{DO control} - \text{DO sample})}{\text{DO control}} \times 100$$

The IC50 value was defined as the concentration of antioxidant necessary to decrease the initial DPPH concentration by 50% [23] and determined from the results by linear regression analysis. The lower IC50 values designate the greater antiradical activity. The antiradical power (ARP) was calculated as 1/IC50: the highest ARP values indicate the greater DPPH scavenging effect. The evaluation of free radical-scavenging activity was performed by the Trolox Equivalent Antioxidant Capacity (TEAC). The TEAC value is based on the ability of the antioxidant to scavenge the DPPH radical and was calculated by the following formula:

$$\text{TEAC} = \frac{\text{ARP (compound)}}{\text{ARP (Trolox)}}$$

**Acknowledgments:** This work was supported by the National Basic Research Program of Algeria Project (E00920120008).

#### REFERENCES

1. T.G. Tutin, V.H. Heywood, N.A. Burges, D. M. Moore, D. H. Valentine, S. M. Walter, D. A. Webb, *Flora Europaea*, 3rd ed. Cambridge University Press, 1972, p. 29.
2. M. Dolores Liedo, M. Erben, M. B. Crespo, Myriolepis, *Taxon*, **52**, 67 (2003).
3. P. Quezel, S. Santa, *New flora of Algeria and the southern régions*. 2nd ed., Paris : CNRS, 1963, p. 731.
4. F. Medini, R. Ksouri, H. Falleh, W. Megdiche, N. Trabelsi, C. Abdelly, *Journal of Medicinal Plants Research*, **5**(31), 6719 (2011).
5. L. M. Korul'kina, G. E. Zhusupova, E. E. Shul'ts, K. B. Erzhanov, *Chemistry of Natural Compounds*, **40**(5), 417 (2004).
6. D. Saidana, S. Mahjoub, O. Boussaada, J. Chriaa, A. Mahjoub, I. Chéraif, M. Daami, Z. Mighri, A. N. Helal, *J Am Oil Chem Soc.*, **85**(9), 817 (2008).
7. K. Yuh-Chi, L. Lie-Chwen, T. Wei-Jern, C. Cheng-Jen, K. Szu-Hao, H. Yen-Hui, *Antimicrob Agents Chemother*, **46**(9), 2854 (2002).
8. G. E. Zhusupova, S. A. Abilkaeva, *Chemistry of Natural Compounds*, **42**(1), 112 (2006).
9. L. Zhang, G.Zou, *Chemistry of Natural Compounds*, **40**(6), 602 (2004).
10. S. Asen, J. R. Plimmer, *Phytochemistry*, **11**, 2601 (1972).
11. J. I. Lee, C. Kong, M. E. Jung, S. Y. Lim, Y. Seo, *Biotechnology and Bioprocess Engineering*, **16**, 992 (2011).
12. L. M. Korul'kina. E. E. Shul'ts, G. E. Zhusupova, Zh. A. Abilov, K. B. Erzhanov, M. I. Chaudri, *Chemistry of Natural Compounds*, **40**(5), 465 (2004).
13. F. E. Kandil, Kh. M. Ahmed, H. A. Hussieny, A. M. Soliman, *Chemistry of Natural Compounds*, **41**(3), 417 (2005).
14. I. S. Movsumov, E. A. Garaev, *Chemistry of Natural Compounds*, **41**(3), 417 (2005).
15. M. Benahmed, M. Lafhal, N. Djeddi, H. Laouer, S. Akkal, *Advances in Environmental Biology*, **12**(6), 4052 (2012).
16. F. Pourmorad, S. J. Hosseinimehr, N. Shahabimajd. *African Journal of Biotechnology*, **5**(11), 1142 (2006).
17. M. A. Aderogba, A. O. Ogundaini, J. N. Eloff, *Afr J Trad CAM*, **3**(4), 59 (2006).
18. L. Yun-Lian, K. Yueh-Hsiung, S. Ming-Shi, C. Chien-Chih, O. Jun-Chih, *Journal of the Chinese Chemical Society*, **47**(1), 253 (2000).
19. R. N. Yadava, S. Khan, *Int J Pharm Sci Res.*, **3**(10), 3932 (2012).
20. L. Xian-yin, Z. Yu-ying, H. Liang, *China Journal of Chinese Materia Medica*, **31**(19), 1597 (2006).
21. L. Chun-mei, W. Tao, Z. Yi, G. Xiu-mei, L. Tianxiang, *Journal of Shenyang Pharmaceutical University*, **27**(9), 711 (2010).
22. W. Brand-Williams, M. E. Cuvelier, C. Berset, *LW T- Food Sci Control*, **28**(1), 25 (1995).
23. S. Azzouzi, N. Zaatat, K. Medjroubi, S. Akkal, K. Benlabed, F. Smati, M.G. Dijoux-Franca, *Asian Pac J trop med.*, **7**(1), S481 (2014).

## ХИМИЧЕН СЪСТАВ НА *Limonium thouinii* (viv.) kuntze (Plumbaginaceae) и DPPH-АКТИВНОСТТА ЗА ОТСТРАНЯВАНЕ НА СВОБОДНИ РАДИКАЛИ

М. Лефахал<sup>1</sup>, М. Бенахмед<sup>2</sup>, Л. Джари, Н. Заабат<sup>1</sup>, А.Е. Хай<sup>3</sup>, М. Камел<sup>1</sup>, М.-Г. Дижу Франка<sup>3</sup>, Х. Лауе<sup>4</sup>, С. Аккал<sup>1</sup>

<sup>1</sup>Университет в Константин, Група по изследване на оползотворяването на природни ресурси, биоактивни молекули, физико-химични и биологични анализи, Департамент по химия, Факултет по точни науки, Алжир

<sup>2</sup>Университет Ларби Тебеси, Алжир

<sup>3</sup>Университет в Лион 1, Департамент по микробиология, Вийорбан, Франция

<sup>4</sup> Университет Ферхат Абас Сетиф 1, Лаборатория по оползотворяване на биологични ресурси, Департамент по биология и екология на растителните ресурси, Алжир.

Постъпила на 8 юли, 2015 г.; приета на 2 октомври, 2015 г.

(Резюме)

Настоящата работа разглежда фитохимичните изследвания и DPPH-отстраняващата активност към свободните радикали на надземните части на растението *Limonium thouinii* (Viv.) kuntze (Plumbaginaceae). Надземните части на това растение позволяват да се изолират четири флавоноида: кверцетин, витексин, изо-ориентин и канабисцитрин. Тяхната структура се определя на базата на спектроскопски анализи, включващи УВ, МС и ЯМР – техники. Способността им да отстраняват DPPH свободни радикали е определяна върху сурови екстракти в метанол, етилацетат и n-бутанол.

## Evaluation of the drying methods and conditions with respect to drying kinetics, colour quality and specific energy consumption of thin layer pumpkins

O. İsmail<sup>1\*</sup>, Ö. G. Kocabay<sup>1,2</sup>

<sup>1</sup>*Department of Chemical Engineering, Faculty of Chemical and Metallurgical Engineering, Yildiz Technical University, Davutpaşa Campus, 34210 İstanbul, Turkey*

<sup>2</sup>*T.R. Ministry of Culture and Tourism, Directorate of Central and Laboratory for Restoration and Conservation, İstanbul, Turkey*

Received August 3, 2015, Revised September 21, 2015

In this study, the effects of dry air temperature and power levels when drying pumpkin (*Cucurbita pepo* L.) slices by five different methods was investigated experimentally. Pumpkin slices were dehydrated by five different drying methods: open-sun, vacuum, microwave, infrared and hot air drying. In particular, the experiments were carried out at two different microwave power levels (90 and 180 W), infrared power levels (83 and 125 W) and hot air temperatures (50 and 70 °C) to investigate the effects of these factors on the microwave, infrared and hot-air drying, respectively. The vacuum drying experiment was carried out in one vacuum oven dryer at a constant temperature of 50 °C and a pressure of 0.1 kPa. The experimental moisture data was fitted to some models (namely Lewis, Henderson and Pabis, Page, Logarithmic, Aghbashlo et al., Verma et al. and Midilli et al. models) available in the literature and according to the results, the Midilli et al. model is superior to the others in explaining the drying behavior of pumpkin slices. The energy efficiency and diffusion coefficients increased with the increase in microwave power. In terms of colour criteria the best values were obtained by the hot-air and open-sun drying methods.

**Keywords:** colour, drying models, mathematical models.

### INTRODUCTION

In accordance with the botanical classification Cucurbitaceae is part of the Dicotyledoneae class, Cucurbitales team, Cucurbitaceae genus. Approximate 118 kinds and 825 species are present in the Cucurbitaceae genus. In the genus of Cucurbitaceae, *Cucurbita pepo* L. is a species with a high economic value [1].

Pumpkin (*Cucurbita pepo* L.) is one of the most important vegetables grown in Turkey. In 2012, pumpkin's world production reached 24616115 tons meanwhile in Turkey its production was 395986 tons. The five major pumpkin producing countries in the world are China, India, Ukraine, Egypt and the United States [2].

Pumpkins, which grow in the different regions of Turkey, are a seasonal crop and for this reason a processing step is often used to preserve pumpkin products. Depending upon the processing possibilities, inadequateness of seasonal fresh vegetables and fruits, Turkey as well as in many countries are experiencing big economic losses. It was reported that in the developing countries approximately 30 to 40 percent of the seasonal fresh vegetables and fruits are cast away due to spoilage [3].

The excess quantity of agricultural produce can't be consumed immediately and its life span is too short. These products can be kept fresh after special processing. Great numbers of preserving techniques such as freezing, heat treatment, drying etc. are used to increase the endurance of foodstuffs. In food products with respect to protection of the vitamin value, maintenance of a good outward appearance, taste preservation, the emergence of a decreasing mass advantage, the improvement of storage and transportation facilities, drying is the most appropriate method [4, 5].

The most common drying method used for drying fruits and vegetables in the world and in Turkey is open-sun and outdoors drying. Because the solar energy is renewable, clean and cheap, open-sun drying is carried out commonly in the tropical countries. As there are no energy requirements and a maintenance expense, open-sun drying is a cost-effective method. The only disadvantages of drying under the sun in accordance with other processes are that the drying rate is slow and the time is prolonged [6].

Convective drying by hot air is a widely used drying method in the literature. In these kinds of dryers specific, air speed is practiced by product, the product has a short drying time. Having a simple design, manufactured locally, having a small maintenance and operational cost, drying different

\* To whom all correspondence should be sent:  
E-mail: ismail@yildiz.edu.tr

products according to the season, are among the advantages of these drying systems [7, 8]. During both conventional drying processes, considerable loss in food content takes place. To reduce the food content losses, to preserve the quality of the dried food and to shorten the drying time at low temperatures, the vacuum drying process is successfully applied instead of the conventional methods [9].

Microwave and infrared technology, which has become common in recent years, takes its place in the food industry by shortening the drying time associated with providing quality food. Using microwave driers in combination with hot air live driers increases product quality and energy efficiency [10]. The fundamental principle of microwave heating is provided with the conversion of electromagnetic energy to thermal energy by affecting the polar molecules in the material [11]. Microwave heating systems are successful drying systems for fruits, cereal crops and many food products which have a high moisture content. In brief, drying with microwaves has the characteristics of 4 important properties; fast processing, energy efficiency, low cost and a high quality of the dried product [12].

As stated in [13], various infrared heat sources could be used for drying applications. IR energy is a form of electromagnetic energy or heat energy. The penetration properties of IR radiation into a given material directly increases the energy flux without burning the material's surface and so the required heating time of the conventional heating method decreases. The advantages of infrared heating by conventional heating can be listed as follows: providing regular heating in a short time, decreasing deterioration and nutritional loss, the equipment has simple and flexible usage areas and considerably economizes the energy consumption.

Drying is also the most energy consuming process in the food industry. New drying methods and dryers must be designed and investigated to minimise the energy cost of the drying process [14].

Although there are some investigations focused on the drying characteristic of the pumpkin, there is too much information on the drying characteristics of the *Cucurbita pepo* L., which is a subgroup of pumpkin. The objectives of this study are to evaluate and compare the drying kinetics, product quality and specific energy consumption during the drying of pumpkin slices (*Cucurbita pepo* L.) by five drying methods: (1) hot-air convection drying, (2) open-sun drying (3) the vacuum drying process, (4) IR drying and (5) microwave drying. Two different drying conditions were applied for the

microwave, IR and hot-air drying methods. In addition to this, to obtain the best model for the drying kinetics of pumpkin slices; Lewis, Henderson & Pabis, Page, Logarithmic, Aghbashlo et al., Verma et al. and Midilli et al. models were fitted to the experimental data. Also effective moisture diffusivity values were calculated.

## MATERIALS AND METHODS

### *Material*

Fresh pumpkin (*Cucurbita pepo* L.) samples were obtained from a local supermarket in İstanbul, Turkey and stored in a chamber at 15–20 °C until processing. The initial moisture content of the fresh pumpkin samples was determined using the drying oven (Memmert UM-400, Germany) at 105 °C for 24 h [15]. These experiments were run thrice to obtain a reasonable average. The average initial moisture content of the pumpkins was found to be 92 % w.b. Before the drying process the pumpkin samples were washed, their top and bottom parts were cut and then the pumpkin samples were cut into  $0.5 \pm 0.03$  cm sized cylindrical slices using a knife.

### *Drying equipment and IR drying procedure*

Drying experiments were carried out in a moisture analyzer with a 250 W halogen lamp (Snijders Moisture Balance, Snijders b.v., Tilburg, Holland). During the infrared drying process, a sample was separated over the entire pan evenly and homogeneously. The power level was set in the control unit of the equipment. The drying experiment was performed at the infrared power levels of 83 W and 125 W. The pumpkin samples (approximately  $40 \pm 0.2$  g) were taken from the dryer at 30 min time intervals during the drying process and their weights were measured with a digital balance (Precisa, model XB220A, Precisa Instruments AG, Dietikon, Switzerland) with an accuracy of 0.001 g. When the samples' moisture content reached approximately 0.08 g water/g of dry matter (dry basis) the drying process was terminated.

### *MW*

The drying experiments were carried out in a Robert Bosch Hausgerate GmbH (Germany) model microwave oven which has a maximum output power of 800 W at 2450 MHz. The microwave oven has the capability of operating at different microwave stages while its power range is 90 to 800 W. The area subjected to microwave drying is 530 mm x 500 mm x 322 mm in size and consists

of a rotating glass plate which is 300 mm in diameter at the base of the oven.

The adjustment of the microwave output power and processing time was done with the aid of a digital control apparatus located on the microwave oven. The drying experiments were set at two different microwave power levels of 90 W and 125 W. During drying, the experiments were carried out using the sliced pumpkins known weight of approximately  $34 \pm 2$  g with the thin layer placed on the rotatable plate fitted inside the microwave oven cabin. The rotating glass plate was removed from the oven every 2 min during the drying period and the moisture loss was determined by weighing the plate using a digital balance. The microwave drying process continued until the moisture content reduced to approximately 0.09 g water/g of dry basis of the initial moisture content.

#### *Cabinet dryer*

The drying experiments were performed in a cabinet type dryer (APV & PASILAC Limited of Carlisle, Cumbria, UK). It was made up of stainless steel sheets and it consisted of a rectangular tunnel 0.54 m x 1.4 m x 1.02 m in size. The dryer consisted of a centrifugal fan to supply the air flow, an electrical heater and an air filter. The dryer is operated at dry bulb temperatures of 0–200 °C. The desired drying air temperature was attained by electrical resistance and controlled by the heating control unit. The velocity of the air passed through the system was measured by an anemometer in the range of 0.4–30  $\text{ms}^{-1}$  (model AM-4201, Lutron Electronic, Taipei, Taiwan). The air flow was measured directly in the drying chamber. The samples were dried in the perforated square chamber, which had a flow cross-section of 30 cm x 30 cm. Weight loss of the samples was recorded by using a digital balance (Mettler-Toledo AG, Grefensee, Switzerland, model BB3000) with a sensitivity of 0.01 g.

The pumpkin slices of about 100g were distributed uniformly as a single layer at the sample tray and then were dried in the hot air dryer. The hot air drying was carried out by drying the pumpkin samples at 50°C and 70°C air temperatures and with a constant air velocity of 1 m/s. Pumpkin samples' moisture loss was measured by a balance and recorded at 30 min intervals. The drying process was finished when the moisture content of the samples achieved approximately 0.07 g water/g of dry matter.

#### *Open air-sun drying*

To clean the samples from dust and foreign materials, the selected pumpkin samples were

washed with tap water. Open air - sun drying experiments were carried out during the month of August 2014 (from 08.00 a.m. to 20.00 p.m.) in Greece. The pumpkin slices of about 50 g were distributed uniformly as a single layer on the sample tray and then were exposed to sunlight for 12 hours daily. Moisture loss and the ambient air's temperature was measured by a portable digital balance during the drying process at 30 min intervals (Alfais, I2000-1, which has 0–300 g measurement range with an accuracy of  $\pm 0.1$  g). When the drying time took more than 12 h to reduce the effect of the increase in moisture content, samples were packed overnight. The ambient air's temperature during the drying experiments was between 36 to 49 °C. The highest air temperature was reached between 10:30 a.m. and 14:30 p.m. The drying process continued until the sample reached the desired moisture level of 9 % (w.b.). The dried samples were packed in low density polyethylene bags.

#### *Vacuum drying oven*

Vacuum drying treatment was performed in the laboratory type vacuum oven (Nuve EV 0180, Turkey) with the technical features ~220 V, 50 Hz, 3.5 A and 800 W. The vacuum oven's temperature, which has a sensitivity of 1°C, is a maximum of 250°C. The area of vacuum drying was 30 cm x 20 cm x 25 cm in size. A laboratory type vacuum pump (Carpanelli MMDE80B4, Italy) was used in the vacuum drying operation. Its operating conditions were ~220/240 V, 50/60 Hz and 5.1/4.8 A. The adjustment of the vacuum value and processing temperature was done with the aid of a digital control facility located on the vacuum drying oven. In the drying experiments pumpkin slices' with a weight approximately of  $30 \pm 2$  g and a constant temperature of 50 °C and pressure of 0.1 kPa were used in the vacuum oven dryer. The moisture loss in the pumpkin slices was measured with a balance and it was recorded at 30 min intervals. Good results as a consequence of drying of the pumpkin slices by vacuum drying were not achieved.

#### *Mathematical modelling*

##### *Moisture ratio*

The moisture ratio (*MR*) and drying rate were calculated using the following equations:

$$MR = \frac{M_t - M_e}{M_o - M_e}, \quad (1)$$

where *MR* is the moisture ratio,  $M_t$ ,  $M_o$  and  $M_e$  are the moisture content (g water/g dry matter) on a dry

basis at any time, initial and equilibrium, respectively. The equilibrium moisture content ( $M_e$ ) was assumed to be zero for microwave, infrared drying etc. and the  $MR$  equation (Equation 1) was simplified as Equation 2 [16]:

$$MR = \frac{M_t}{M_o}, \quad (2)$$

*Drying Rate*

The drying rate during the experiments was calculated using the following formula:

$$\frac{dM}{dt} = \frac{M_{t+dt} - M_t}{dt}, \quad (3)$$

where  $t$  is the drying time (min),  $M_t$  and  $M_{t+dt}$  are the moisture content at  $t$  and  $t + dt$  (g water/g dry matter) respectively.

*Effective moisture diffusivity*

The effective moisture diffusivity is therefore calculated by the following equation [17]:

$$MR = \frac{M_t - M_e}{M_o - M_e} = \frac{8}{\pi^2} \sum_{n=0}^{\infty} \frac{1}{(2n+1)^2} \exp\left[-\frac{(2n+1)^2 \cdot \pi^2 \cdot D_{eff} \cdot t}{4L^2}\right] \quad (4)$$

where,  $D_{eff}$  is the effective moisture diffusivity ( $m^2/s$ );  $L$  is the half-thickness of the slab in the samples (m); and  $n$  is a positive integer. In practice, only the first term of Eq. (4) is used to yield [18]:

$$MR = \frac{M_t - M_e}{M_o - M_e} = \frac{8}{\pi^2} \exp\left[-\frac{\pi^2 D_{eff} t}{4L^2}\right], \quad (5)$$

The effective moisture diffusivity ( $D_{eff}$ ) was also typically calculated by using the slope of Eq. (5). A straight line with a slope of  $k_o$  was obtained when  $\ln(MR)$  was plotted versus the time:

$$k_o = \frac{\pi^2 D_{eff}}{4L^2}, \quad (6)$$

Using the slope value of (Eq. 6), the effective moisture diffusivity could be determined.

*The statistical modelling procedure*

In order to determine the moisture ratio as a function of drying time, seven different thin-layer drying models, namely Lewis, Henderson & Pabis, Page, Logarithmic, Aghbashlo et al., Verma et al. and Midilli et al. models were used (Table 1).

*Statistical analysis*

The statistical analysis of the experimental data was determined using the STATISTICA computer program. Three criteria of statistical analysis were used to evaluate the adjustment of the experimental data to the different models; the coefficient of determination ( $R^2$ ), reduced chi-square ( $\chi^2$ ) and root – mean-square error (RMSE). The parameters can be calculated as follow:

$$\chi^2 = \frac{\sum_{i=1}^N \left( MR_{exp,i} - MR_{pre,i} \right)^2}{N - z}, \quad (7)$$

$$RMSE = \left[ \frac{1}{N} \sum_{i=1}^N \left( MR_{pre,i} - MR_{exp,i} \right)^2 \right]^{1/2}, \quad (8)$$

where  $MR_{exp,i}$  and  $MR_{pre,i}$  are the experimental and predicted dimensionless MR, respectively,  $N$  is the number of the data values and  $z$  is the number of constants of the models. Higher  $R^2$ , smaller  $\chi^2$  and RMSE values indicated a better fit of the experimental data to the model [26].

**Table 1.** List of models.

Model name	Model	Reference
Lewis	$MR = \exp(-kt)$	[19]
Henderson and Pabis	$MR = a \exp(-kt)$	[20]
Page	$MR = \exp(-kt^n)$	[21]
Logarithmic	$MR = a \exp(-kt) + c$	[22]
Aghbashlo et al.	$MR = \exp\left(-\frac{k_1 t}{1 + k_2 t}\right)$	[23]
Verma et al.	$MR = a \exp(-kt) + (1-a) \exp(-gt)$	[24]
Midilli et al.	$MR = a \exp(-kt^n) + bt$	[25]

*Colour measurement*

The sample colour before and after the drying process was measured using a Chromameter CR - 400 (Minolta, Japan). For the dried samples three parameters L, a and b, which indicate the brightness (on a lightness–darkness scale), greenness-redness and blueness-yellowness respectively, were used to study the changes in colour. The Chroma was determined using the following equation [27].

$$C^* = \sqrt{a^2 + b^2} \text{ , (9)}$$

*Energy consumption*

*Energy consumption in the infrared*

In the IR dryer, sum of the energy was consumed by the IR lamp to dry the pumpkin samples.

$E_t$  is the total energy consumption during the infrared drying that is calculated using the following equation (10).

$$E_t = P * t \text{ , (10)}$$

where  $E_t$  is the total energy consumption (kWh), P is the infrared power level (kW), t is the drying time (h).

*Energy consumption in the microwaves*

The energy consumption value required for drying pumpkin slices in the microwaves was calculated with Equation (11) [28].

$$E_t = P * t \text{ , (11)}$$

where  $E_t$  is the total energy consumption (kWh), P is the microwave power output (kW), t is the drying time (h).

*Energy consumption in the hot air*

In hot air drying, the total energy consumption was due to the drying and blowing of air by an electric heater and fan, respectively. The total energy consumption value was calculated from Equation (12) [29]:

$$E_t = \rho_a A v c_p \Delta T * D_t \text{ , (12)}$$

where  $E_t$  is the total energy consumption (kWh),  $\rho_a$  is the air density ( $\text{kg/m}^3$ ), A is the cross sectional area of the container ( $\text{m}^2$ ), herein a sample is placed, v is the air velocity (m/sec),  $c_p$  is the specific heat ( $\text{kJ/kg } ^\circ\text{C}$ ),  $\Delta T$  is a temperature difference between the air inlet and outlet of the

dryer ( $^\circ\text{C}$ ),  $D_t$  is the total drying time of each sample (h).

*Calculation of the specific energy consumption*

The total energy consumption of the drying process was evaluated through the Specific Energy Consumption (SEC). Electrical energy was consumed during the drying process. The specific energy consumption, which is a measure of the energy needed to evaporate a unit mass of water from the product, was calculated using the following equation [30]:

$$Q_s = \frac{Q_t}{m_w} \text{ , (13)}$$

where  $Q_s$  is the specific energy consumption in  $\text{kWh *kg}^{-1}[\text{H}_2\text{O}]$ ,  $Q_t$  is the consumed energy in kWh,  $m_w$  is the mass of vaporized water in kg  $[\text{H}_2\text{O}]$ .

RESULTS AND DISCUSSION

*Drying curves*

Figure 1 shows the moisture ratio as a function of drying time for the different drying methods and conditions.

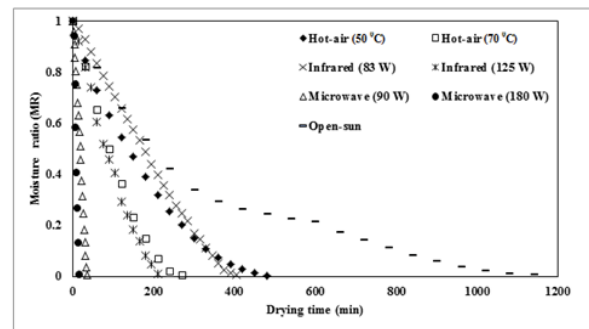


**Fig. 1.** Drying curves of pumpkin slices at different drying methods and conditions.

As seen from Figure 1, the drying time was quite different for four drying methods to reach the final moisture ratio. The drying time of the dried pumpkin slices with different drying methods ranged from 14 to 1140 minutes. The drying curves are typical and similar to fruits and vegetables. In Fig. 1 it is discerned that the increase in the microwave power level [31, 32], air temperature [33, 34] and infrared power level [35] shortened the drying period in microwave drying, air-drying and infrared drying, respectively. The moisture ratio decreases gradually with the increases in drying time, exhibiting a downward curve. The figure also indicates that the drying time for microwave drying is much shorter than the hot air, infrared and open-sun drying. The time required to reduce the



moisture ratio from 1 to 0.006 ranged between 14 and 36 min at two power levels with microwave drying, while it ranged between 270 and 480 min at two temperatures with hot air drying, while it ranged between 210 and 405 min at two power levels with infrared drying. To reach the desired final moisture content, 14 minutes drying time indicated the high efficiency of the microwave drying method (180 W), which was about 82 times faster than open-sun drying. The drying time of pumpkin slices dried under the sun was determined as 19 h.

The drying time was much faster than for the other drying methods as compared to the conditions by microwave drying of pumpkin slices. For this reason, the drying rate (g water)/(g dry matter\*min) curves are shown in the two different figures as Figure 1 and 2 in order to clearly see the drying rate curves.

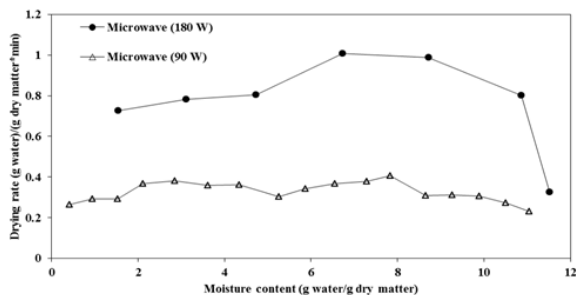


**Fig. 2.** Drying rate versus moisture content of pumpkin slices at two different microwave power levels.

Since the initial moisture content of the pumpkin slices was relatively constant (11.5 g water/g dry matter), the difference in the drying time requirements was considered mainly due to the difference in the drying rates. The drying rate curves for pumpkin slices dried at two microwave output power levels (90 to 180 W) are given in Figure 2. Depending on the drying conditions, the

average drying rates of pumpkin slices ranged from 0.407 to 1.008 (g water)/(g dry matter\*min) for the output power between 90 and 180 W, respectively. The moisture content of the pumpkin (92% w.b.) was very high during the initial phase of the drying process which resulted in a higher absorption of microwave power level and higher drying rates due to the higher moisture diffusion. As the drying time progressed, the moisture loss in the product caused a decrease in the absorption of microwave power and resulted in a fall in the drying rate. Higher drying rates were determined at higher microwave output power levels. Thus, the microwave output power level had a crucial effect on the drying rate. The variation of drying rate with moisture content for the different drying conditions of hot air, infrared and open-sun drying are shown in Figure 3.

As expected, the drying rate would decrease as the moisture content decreases. As can be seen from these figures, no constant rate period exists. All the drying processes occurred in the falling rate period. In the infrared drying experiments (83 and 125 W) initially rising but after a while falling the drying rate period is present. The experiment, in which the infrared power level is 125 W, the rising drying rate period is clear by far. During the falling drying rate period, the predominant mechanism is the internal mass transfer. The open sun drying experiment lasted for approximately 19 h. Consequently, a small rising drying rate period formed in the figure that originated as a result of the drying process continued the next day. Similar results were reported by [36, 14, 37].

#### Mathematical Modelling of Drying Data

The values of  $R^2$ ,  $\chi^2$  and RMSE were calculated and given in Table 2.

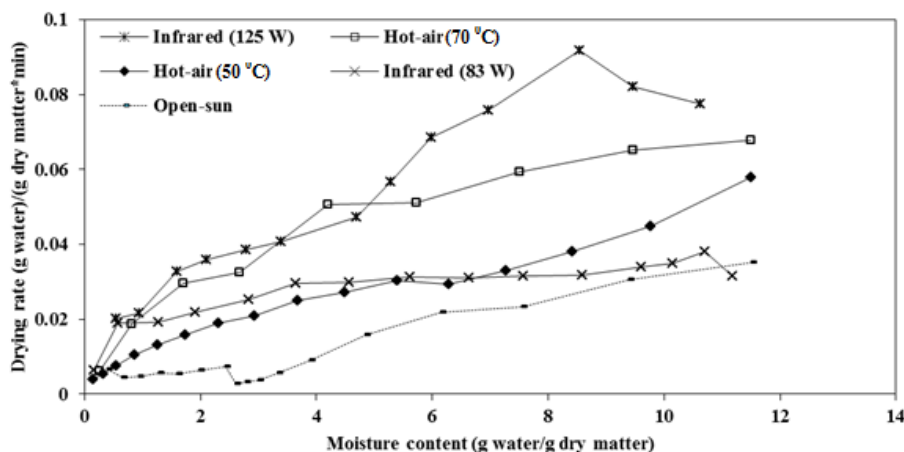


**Fig. 3.** Drying rate versus moisture content of pumpkin slices at different drying methods and conditions.

**Table 2.** Statistical results obtained from the selected models.

Models	Drying methods	Drying conditions	R <sup>2</sup>	χ <sup>2</sup>	RMSE
Lewis	Infrared	83 W	0.9304	0.007238	0.083527
	Infrared	125 W	0.9563	0.004683	0.066081
	Microwave	90 W	0.8991	0.010951	0.101825
	Microwave	180 W	0.8982	0.013873	0.110176
	Sun	36 to 49 °C	0.9864	0.001048	0.031551
	Hot - air	50 °C	0.9826	0.001724	0.040277
	Hot - air	70 °C	0.9673	0.004022	0.060163
Henderson & Pabis	Infrared	83 W	0.9803	0.005327	0.070318
	Infrared	125 W	0.9676	0.003731	0.056838
	Microwave	90 W	0.9247	0.008652	0.087956
	Microwave	180 W	0.9211	0.012548	0.097011
	Sun	36 to 49 °C	0.9876	0.001007	0.030106
	Hot - air	50 °C	0.9846	0.001626	0.037867
	Hot - air	70 °C	0.9728	0.003757	0.054825
Page	Infrared	83 W	0.9912	0.000947	0.029651
	Infrared	125 W	0.9937	0.000719	0.024955
	Microwave	90 W	0.9907	0.000754	0.025974
	Microwave	180 W	0.9946	0.000854	0.025309
	Sun	36 to 49 °C	0.9904	0.000780	0.026491
	Hot - air	50 °C	0.9937	0.000664	0.024207
	Hot - air	70 °C	0.9959	0.000562	0.021209
Logarithmic	Infrared	83 W	0.9982	0.000193	0.013117
	Infrared	125 W	0.9974	0.000318	0.015943
	Microwave	90 W	0.9973	0.000324	0.016517
	Microwave	180 W	0.9932	0.001284	0.028329
	Sun	36 to 49 °C	0.9878	0.001048	0.029848
	Hot - air	50 °C	0.9989	0.000118	0.009865
	Hot - air	70 °C	0.9970	0.000474	0.018212
Aghbashlo et al.	Infrared	83 W	0.9304	0.007516	0.083527
	Infrared	125 W	0.9563	0.005044	0.066081
	Microwave	90 W	0.8991	0.011595	0.101825
	Microwave	180 W	0.8982	0.016185	0.110176
	Sun	36 to 49 °C	0.9903	0.000785	0.026586
	Hot - air	50 °C	0.9825	0.001839	0.040277
	Hot - air	70 °C	0.9673	0.004524	0.060163
Verma et al.	Infrared	83 W	0.9583	0.004685	0.064667
	Infrared	125 W	0.9780	0.002743	0.046818
	Microwave	90 W	0.9758	0.002956	0.049879
	Microwave	180 W	0.9868	0.002509	0.039598
	Sun	36 to 49 °C	0.9890	0.000944	0.028327
	Hot - air	50 °C	0.9866	0.001510	0.035258
	Hot - air	70 °C	0.9847	0.002419	0.041154
Midilli at al.	Infrared	83 W	0.9994	0.000070	0.00775
	Infrared	125 W	0.9984	0.000216	0.012588
	Microwave	90 W	0.9991	0.000113	0.009452
	Microwave	180 W	0.9986	0.000315	0.012555
	Sun	36 to 49 °C	0.9924	0.000692	0.023526
	Hot - air	50 °C	0.9987	0.000151	0.010758
	Hot - air	70 °C	0.9990	0.000170	0.010089

**Table 3.** Colour parameters of fresh and dried pumpkin slices.

Drying methods	Drying conditions	Colour parameters			C*
		L	a	b	
	Fresh	67.75	11.06	21.77	24.41
Infrared	83 W	49.73	12.80	10.66	16.65
	125 W	47.75	14.42	10.74	17.98
Microwave	90 W	67.19	0.59	27.28	27.28
	180 W	57.11	3.89	26.31	26.59
Hot - air	50 °C	68.95	11.91	25.65	28.28
	70 °C	68.68	11.58	26.75	29.15
Open - sun	31 - 46 °C	70.63	11.12	24.2	26.63

**Table 4.** Effective moisture diffusivity values for the various drying methods.

Drying methods	Drying conditions	D <sub>eff</sub> (m <sup>2</sup> s <sup>-1</sup> )
Infrared	83 W	3.24 x 10 <sup>-10</sup>
	125 W	6.09 x 10 <sup>-10</sup>
Microwave	90 W	0.85 x 10 <sup>-7</sup>
	180 W	2.48 x 10 <sup>-7</sup>
Hot - air	50 °C	2.78 x 10 <sup>-10</sup>
	70 °C	9.38 x 10 <sup>-10</sup>
Open - sun	31 – 46 °C	2.96 x 10 <sup>-11</sup>

Thin-layer drying models, in other words the Lewis, Henderson and Pabis, Page, Logarithmic, Aghbashlo et al., Verma et al. and Midilli et al. were used to describe the drying process during the drying of pumpkin slices.

In order to describe the moisture ratio as a function of drying time with different drying methods, 7 different drying models were fitted to the experimental data and their coefficient of determination (R<sup>2</sup>), reduced chi-square (χ<sup>2</sup>) and root-mean-square error (RMSE) were calculated. R<sup>2</sup>, RMSE and χ<sup>2</sup> statistical data with respect to 7 different drying models are given in the Table 2. The grade of fitting was determined by the lowest χ<sup>2</sup> and RMSE and the highest R<sup>2</sup> values.

From Table 2, the statistical data with respect to 7 different drying models used for explaining the drying circumstance occurred in the falling rate drying period was examined individually and using the Midilli et al. model and provided the minimum error for a separable moisture rate. At drying the process of pumpkin slices' standard error (RMSE) of prediction conducted by this model ranged from 0.00775 to 0.023526. In addition to this as seen from the table, the chi-square (χ<sup>2</sup>) values ranged from 0.000070 to 0.000692 which are close to zero.

Adequacy of modelling ranged from 0.9994 to 0.9924.

*Effect of drying methods and conditions on the colour of pumpkin slices*

Before and after the drying process, the L (lightness), a (greenness), b (yellowness) and C\* (Chroma) values of pumpkin slices were measured and these results are given in Table 3.

One of the quality of the parameters of food and agricultural product is the colour parameter. Too much colour changes influence the marketing negatively by affecting the quality of the product. It is an index of the inherent good qualities of a food and the association of colour with the acceptability of a food is universal. Among the several basic quality characteristics of dried pumpkin slices the colour is an important one which indicates the effect levels of different drying methods or conditions. As stated previously, the L term stands for brightness, the a term is for a green-red balance, the b term is for a blue-yellow balance, the Hunter colour ratio and the chroma are measures for the colour purity. Values for the L, a, b and chroma (C\*) coordinates of the fresh pumpkin slices were 67.75, 11.06, 21.77 and 24.41, respectively.

In general, the infrared drying at 83 and 125 W produced no remarkable changes in the colour parameters of the pumpkin slices as compared with the fresh pumpkin. However, the increase of power level from 83 W to 125 W caused an increase of the a and b values and a decrease of the L value. The microwave irradiation drying at 90 W allowed the obtaining of a product which was more similar to the fresh sample when the lightness was considered since the L value varied only from 67.75 to 67.19. When comparing the values obtained for the opposing colour parameters between the fresh sample and the pumpkin slices dried at 90 W, the a decreased from 11.06 to 0.59, showing that the red colour decreased with the drying process. As for the b, it increased slightly from 21.77 to 27.28, the dried samples were more yellow. These observations are corroborated with the increase from 24.41 to 27.28 in the value of the chroma. The dried pumpkin at 180 W turns into the final product as much lighter, much less red and more yellow with L, a and b values for which the values are 57.11, 3.89 and 26.31, respectively. The colour criteria obtained from the air drying experiments using 50 and 70 °C temperatures are given in Table 3. According to this the colour is closest to the fresh product when the air drying process's temperature is 50°C and 75°C. When the drying air temperature increased from 50 to 75 °C; the L, a values decreased and b values increased. These results were consistent with the observations made by different authors on the drying of pumpkin (*Cucurbita pepo* L.) slices [38, 39]. As seen from Table 3, the best colour values were achieved during the open sun drying and these values are the closest to the fresh material. This is followed by hot air-drying, microwave drying and infrared drying successively. Similar findings are also available in the literature [40, 41].

#### *Determination of Effective Moisture Diffusivity*

The effective moisture diffusivity was calculated using the method of slopes. Effective diffusivities are typically determined by plotting the experimental drying data in terms of  $\ln(MR)$  versus time. From the Eq. (6), a plot of  $\ln(MR)$  versus time gives a straight line with a slope ( $k_0$ ). This slope is the measure of the diffusivity. The effective diffusivity values for various drying methods and conditions are presented in Table 4.

Among the four drying methods, microwave drying offered the highest values of  $D_{\text{eff}}$  for microwave power levels of 90 and 180 W. In microwave drying, the  $D_{\text{eff}}$  values increased with

the increasing drying microwave power. If samples were dried at higher microwave power, increased heating energy would increase the activity of the water molecules leading to a higher moisture diffusivity. The value of  $D_{\text{eff}}$  for infrared and hot-air drying was slightly higher than the open sun drying. In drying pumpkin slices by the infrared and hot-air drying methods, the effective moisture diffusivity value increases with increasing power and temperature. In foods the effective moisture diffusivity values are in the range of  $10^{-12}$  to  $10^{-6}$   $\text{m}^2/\text{s}$  and the accumulation of values is in the region  $10^{-10}$  to  $10^{-8}$   $\text{m}^2/\text{s}$  (75%) [42, 43]. In the literature there is no study associated with the drying of pumpkin slices (*Cucurbita pepo* L.) with infrared and open sun drying. Some studies dealing with the drying of pumpkin slices with microwaves are available in the literature but data about the effectiveness of moisture diffusivity does not exist.

The  $D_{\text{eff}}$  value of pumpkin slices (*Cucurbita pepo* L.) [8] undergoing hot-air drying at 50 and 60 °C was in the range of  $3.38 \times 10^{-10}$  to  $9.38 \times 10^{-10}$   $\text{m}^2/\text{s}$ , respectively.

#### *Energy consumption*

The energy consumption values obtained in the drying trials carried out with three different drying methods are given in Figure 4.

When three different drying methods were compared with the energy consumption values, the lowest energy consumption occurred in the microwave drying method and this was followed by the infrared and hot-air drying methods. Energy consumption is zero for the open sun drying so this drying method isn't accounted for in Figure 4. As seen in Figure 4, the total energy consumption decreases with the increasing air temperature and power level. The best result with regard to energy consumption was obtained for microwave drying at the 180 W power level. The energy consumption at this level was 0.042 kWh. Among all the drying methods the highest value with respect to the energy consumption was obtained for the hot-air drying process at a temperature of 50°C and 1.35 kWh. The energy consumption was 0.042–0.054, 0.44–0.56 and 0.75–1.35 kWh for microwave, infrared and hot-air drying, respectively. As a result, the energy consumption in the drying processes carried out at low temperature and power levels which yielded a longer drying period was determined to be at higher rates. These results agree with the observations of previous researchers [44, 45].

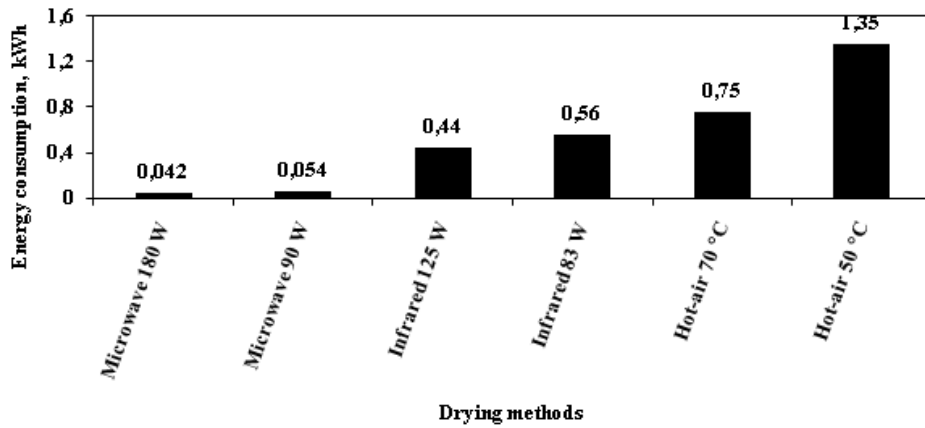


Fig. 4. Energy consumption versus different drying methods of pumpkin slices during the drying process.

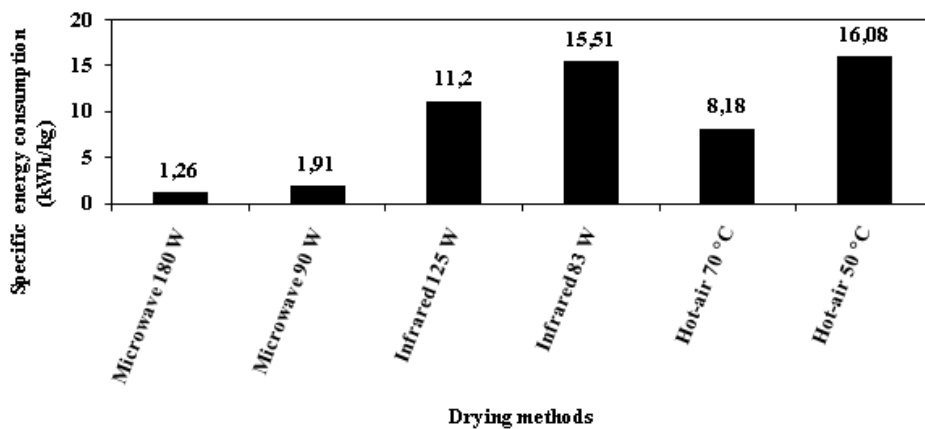


Fig. 5. Specific energy consumption versus different drying methods and conditions for drying of 1 kg wet product.

#### Specific energy consumption

The specific energy consumption was determined by considering the total energy supplied to dry pumpkin samples from an initial moisture content of about 11.5 g water/g dry matter to a final moisture content of approximately 0.05 to 0.10 g water/g dry matter in all three dryers.

The specific energy consumption of the drying process under the different drying methods and conditions was calculated by Equation (13) and this graph is given in Figure 5.

As can be understood from Figure 5, a minimum heat energy (1.26 kWh/kg) is needed by the microwave drying method to dry 1 kg of pumpkin slices. The maximum energy (16.08 kWh/kg) is needed for the hot-air drying method. Because of a minimum of heat energy consumption (1.26 kWh/kg) and less drying time (14 min) it can be said from Figure 5 that the microwave drying method must be selected for drying the fresh pumpkin samples. Again as seen from Figure 5, reducing the specific energy consumption was observed by the increase in power level and

temperature. These results are similar to those reported by the researchers for the other products [46, 47, 28, 48].

#### CONCLUSION

The pumpkin (*Cucurbita pepo* L.) has an important place for our country's vegetable production. Obtaining new products by drying pumpkin slices will increase the income gained from pumpkin production/processing and this situation will allow for the consumption of pumpkin all the year round. Researchers were motivated to prospect using different combinations of drying technologies because of the increasing trends in energy cost, product quality and product quantity.

Based on the conducted experiments, we can draw the following conclusions. The vacuum drying process is not suitable for the drying of pumpkin slices. The best result based on the drying period, coefficient of diffusion and specific energy consumption was obtained by the microwave drying method at the 180 W output power level.

In drying pumpkin slices by this method, the drying period was found to be 14 min, the coefficient of diffusion was  $2.48 \times 10^{-7} \text{ m}^2\text{s}^{-1}$ , the energy consumption was found to be 0.042 kWh and the specific energy consumption was found to be 1.26 kWh/kg.

For the foodstuffs high “L”, “b” and low “a” values are important parameters.

The measured colour parameters of the dried samples compared to fresh, the best colour quality was obtained in the pumpkin slices dried by the hot-air and open-sun drying methods.

The experimental data was obtained as a consequence of drying pumpkin slices by five different drying methods and the conditions were modelled with seven different thin layer drying models available in the literature. The Midilli et al. model, which will be used for determining the changing of the product’s moisture content, has a high modelling efficiency. Therefore it is possible to obtain results very close to the experimental values.

The opinion is that the microwave drying method can be easily applied industrially and offers uniform high quality products to the consumer.

#### REFERENCES

1. R.W. Robinson, D.S. Decker-Walters, Cucurbits, CAB International, New York, NY, (1997).
2. FAO, FAO Statistical Database (2012), available from: <http://www.fao.org>
3. M.A. Karim, M.N.A. Hawlader, *Int. J. Heat Mass Transfer.*, **48**, 4914 (2005).
4. D. Arslan, M.M. Ozcan, *LWT-Food Sci and Technol.*, **43**, 1121 (2010).
5. M. Zielinska, M. Markowski, *Chem Eng Process.*, **49**, 212 (2010).
6. D.B. Jadhav, G.L. Visavale, N. Sutar, *Drying Technol.*, **28**, 600 (2010).
7. F.M. Berruti, M. Klaas, C. Briens, F. Berruti, *J Food Eng.*, **92**, 196 (2009).
8. İ. Doymaz, *J Food Eng.*, **79**, 243 (2007).
9. A. Arevalo-Pinedo, F.E.X. Murr, *J Food Eng.*, **80**, 152 (2007).
10. G.P. Sharma, S. Prasad, *J Food Eng.*, **50**, 99 (2001).
11. R. Vadivambal, D.S. Jayas, *Biosyst Eng*, **98**, 1 (2007).
12. M. Zhangz, J. Tang, A. J. Majumdar, S. Wang, *Trends Food Sci Tech.*, **17**, 524 (2006).
13. C. Strumillo, T. Kudra, *Drying: Principles, Applications and Design.*, Topics in Chemical Engineering. R.Hughes (ed.), Vol. 3. New York; Gordon and Breach Science Publishers, p. 371, (1986).
14. H. Kocabiyik, D. Tezer, *Int J Food Sci Tech.*, **44**, 953 (2009).
15. AOAC., Official method of analysis, Arlington, USA, (1990).
16. R.A. Chayjan, M. Kaveh, S. Khayati, *J Food Process Preserv.*, **1745**, 4549 (2014).
17. J. Crank, *The Mathematics of Diffusion*, second ed. Oxford University Press, London, UK, (1975).
18. K. Sacilik, *J. Food Eng.*, **79**(1), 23 (2007).
19. J.S. Roberts, D.R. Kidd, O. Padilla-Zakour, *J. Food Eng.*, **89**, 460 (2008).
20. S.M. Henderson, S. Pabis, *J Agr Eng Res.*, **6**, 169 (1961).
21. G. Page, [M.S. thesis], Factors influencing the maximum rates of air-drying shelled corn in thin layer, Department of Mechanical Engineering, Purdue University, West Lafayette, IN. 1949.
22. R.P. Kingsly, R. K. Goyal, M. Manikantan, S. M. Ilyas, *Int J Food Sci Tech.*, **42**, 65 (2007).
23. M. Aghbashlo, M.H. Kianmehr, S. Khani, M. Ghasemi, *Int Agrophys.*, **23**, 313 (2009).
24. L.R. Verma, R.A. Bucklin, J.B. Endan, F.T. Wratten, *TASAE*, **28**, 296 (1985).
25. A. Midilli, H. Kucuk, Z. Yapar, *Drying Technol.*, **20**(7), 1503 (2002).
26. K.O. Falade, O.S. Ogunwolu, *J. Food Process.*, **38**, 373 (2014).
27. S. Phoungchandang, S. Saentaweek, *Food Bioprod Process.*, **89** (4), 429 (2011).
28. A. Motevali, S. Minaei, M. H. Khoshtagaza, *Energ Convers Manage.*, **52**(2), 1192 (2011).
29. M. Aghbashlo, M.H. Kianmehr, H. Samimi-Akhijahani, *Energ Convers Manage.*, **49**, 2865 (2008).
30. W. Jindarat, P. Rattanadecho, S. Vongpradubcha, *Exp Therm Fluid Sci.*, **35**(4), 728 (2011).
31. L.V. Mana, T. Orikasa, Y. Muramatsu, A. Tagawa, *J Food Process Technol.*, **3**, 10 (2012).
32. J. Wang, J.S. Wang, Y. Yu, *Int J Food Sci Tech.*, **42**, 148 (2007).
33. T.Y. Tunde-Akintunde, G. O. Ogunlakin, *J Food Sci Tech.*, **50** (4), 705 (2013).
34. P.K. Wankhade, R.S. Sapkal, V. S. Sapkal, *Procedia Eng.*, **51**, 371 (2013).
35. İ. Doymaz, *J. Agric. Sci.*, **19**, 44 (2013).
36. D. Evin, *Food Bioprod Process.*, **90**, 323 (2012).
37. J. Wang, K. Sheng, *LWT.*, **39**, 247 (2006).
38. T. Rakcejeva, R. Galoburda, L. Cude, E. Strautniece, *Procedia Food Sci.*, **1**, 441 (2011).
39. M. Shafafi Zenoozians, H. Feng, S. M. A. Razavi, F. Shahidi, H.R. Pourreza, *J Food Process Pres*, **32**, 88 (2008).
40. I. Alibas, *LWT.*, **40**, 1445 (2007).
41. R.P.F. Guine, S. Pinho, M. J. Barroca, *Food Bioprod Process.*, **89**, 422 (2011).
42. Z. Erbay, F. Icier, *Crit Rev Food Sci Nutr.*, **50** (5), 441 (2010).
43. P.S. Madamba, R.H. Driscoll, K. A. Buckle, *J. Food Eng.*, **29**(1), 75 (1996).
44. I. Alibas, *Biosystems Eng.*, **96**(4), 495 (2007).
45. H.S. El-Mesery, G. Mwithiga, *Afr. J. Agric. Res.*, **7**(31), 4440 (2012).
46. A.R. Celma, F.L. Rodriguez, F. C. Blazquez, *Food Bioprod Process.*, **87**, 247 (2009).
47. I. Das, S.K. Das, S. Bal, *J Food Eng.*, **62**, 9 (2004).
48. G.P. Sharma, S. Prasad, *Energy.*, **31**, 1921 (2006).

## ОЦЕНЯВАНЕ НА МЕТОДИТЕ И УСЛОВИЯТА НА СУШЕНЕ СПОРЕД КИНЕТИКАТА, КАЧЕСТВАТА НА ЦВЕТОВЕТЕ И СПЕЦИФИЧНАТА ЕНЕРГИЯ НА СУШЕНЕ НА ТЪНКИ СЛОЕВЕ ОТ ТИКВА

О. Исмаил<sup>1</sup>, Й.Г. Коджабай<sup>1,2</sup>

<sup>1</sup>*Департамент по химично инженерство, Факултет по химично и металургично инженерство, Кампус „Давут паша“, Технически университет „Йилдиз“, 34210 Истанбул, Турция*

<sup>2</sup>*Регионална лаборатория по възстановяване и консервация в Истанбул, Турция*

Постъпила на 3 август 2015 г.; коригирана на 21 септември 2015 г.

(Резюме)

В тази работа са изследвани експериментално температурата на сушене на резени от тиква (*Cucurbita pepo* L.) и нивата на мощността. Образците са дехидратирани по пет различни метода: на открито, под вакуум, микровълни, инфрачервени лъчи и горещ въздух. Две нива на мощността са изпитани както следва: микровълни (90 и 180 W), инфрачервени лъчи (83 и 125 W) и горещ въздух (50 и 70 °C), за да се изследва ефекта на тези методи. Вакуумното сушене е изследвано при постоянна температура от 50 °C и налягане от 0.1 kPa. Опитните данни за влагата са обработени по различни модели, известни в литературата (на Lewis, Henderson & Pabis, Page, логаритмичен, Aghbashlo и др., Verma и др. и Midilli и др.). Според тези резултати моделът на Midilli и др. превъзхожда останалите в хода на сушенето на образците. Енергийната ефективност и дифузионните коефициенти нарастват с нарастване на мощността на микровълните. От цвetoва гледна точка най-добри резултати се получават при сушене с горещ въздух и на открито.

## Preparation, characterization and fluorescence of two cadmium compounds with different extended structures

Z.-L. Yao<sup>2</sup>, Y.-P. Pei<sup>1</sup>, Z.-Y. Luo<sup>1</sup>, R.-H. Hu<sup>1</sup>, Y.-X. Yang<sup>1</sup>, Wen-Tong Chen<sup>1\*</sup>

<sup>1</sup>*Institute of Applied Chemistry, School of Chemistry and Chemical Engineering, Jiangxi Province Key Laboratory of Coordination Chemistry, Jingtangshan University, Ji'an, Jiangxi 343009, China*

<sup>2</sup>*Biology and Chemistry Engineering Department, Fuqing Branch of Fujian Normal University, Fuqing, Fujian 350300, P.R. China*

Received August 6, 2015, Revised August 19, 2015

Two cadmium compounds,  $[\text{Cd}_2\text{Cl}_4(2,2'\text{-bipy})]_n$  (**1**) and  $[\text{CdCl}_2(2,2'\text{-bipy})]_n$  (**2**) (bipy = bipyridine) with different extended structures, have been obtained from hydrothermal reactions and structurally characterized by X-ray single-crystal diffraction. Compound **1** is characterized by a three-dimensional (3D) structure and the cadmium ion is coordinated by three chloride ions and one nitrogen atom to yield a tetrahedron. Differently, compound **2** features a one-dimensional (1D) structure and the cadmium ion is coordinated by four chloride ions and two nitrogen atoms to yield an octahedron. Fluorescence investigation shows that compound **1** displays an emission in the ultraviolet region, while compound **2** exhibits an emission in the green region.

**Keywords:** crystal, cadmium, extended structure, fluorescence, hydrothermal reaction

### INTRODUCTION

Because of the intrinsic aesthetic appeal and the various applications, metal halide bipyridine compounds have recently gained more and more interest [1-23]. The pyridyl rings of the bipyridine are characteristic of a delocalized  $\pi$ -system. Therefore, bipyridine is a useful ligand for preparing light emitting compounds which can be applied in many fields such as organic light emitting diodes, chemical sensors and solar energy conversion. To our knowledge, a large amount of metal halide bipyridine compounds have been reported so far [1]. However, the group-12 (IIB) metal halide bipyridine compounds are still relatively rare. Actually, the IIB metal halide bipyridine compounds can usually exhibit useful fluorescence and photoelectric properties. Furthermore, 2,2'-bipyridine is a bifunctional ligand and it can act as a bidentate ligand to coordinate the metal ions. Our recent efforts in synthesizing IIB metal halide bipyridine compounds are mainly aimed at the systems containing the 2,2'-bipyridine. In this paper, we report the preparation, crystal structures and fluorescence of two cadmium compounds  $[\text{Cd}_2\text{Cl}_4(2,2'\text{-bipy})]_n$  (**1**) and  $[\text{CdCl}_2(2,2'\text{-bipy})]_n$  (**2**) (bipy = bipyridine) which are synthesized from hydrothermal reactions. It is noteworthy that both compounds show totally different extended structures, although they have similar molecular formula.

### EXPERIMENTAL

#### Materials and instrumentation

All chemicals and reagents employed are purchased and used as received without purification. Fluorescence studies are performed with solid state samples at room temperature on a computer-controlled JY FluoroMax-3 spectrometer.

#### Synthesis of $[\text{Cd}_2\text{Cl}_4(2,2'\text{-bipy})]_n$ (**1**).

A mixture of  $\text{CdCl}_2$  (1 mmol, 183 mg) and 2,2'-bipy (0.5 mmol, 78 mg) are stirred and dissolved in 1 mL ethanol and 9 mL distilled water at an ambient temperature. Then, the mixture is heated at 180 °C for 10 days in a 25 mL teflon-lined stainless steel autoclave. Colorless block crystals of compound **1** are obtained and dried in air.

#### Synthesis of $[\text{CdCl}_2(2,2'\text{-bipy})]_n$ (**2**).

This compound is prepared by mixing  $\text{CdCl}_2$  (1 mmol, 183 mg), 2,2'-bipy (1 mmol, 156 mg), 3 mL ethanol and 7 mL distilled water in a 25 mL Teflon-lined stainless steel autoclave and heated at 180 °C for 10 days. After being slowly cooled down to room temperature at 6 K/h, colorless crystals are collected.

#### X-ray structure determination.

The X-ray single-crystal data set of both compounds are measured on a Rigaku Mercury CCD X-ray area detector with graphite monochromatic Mo- $K\alpha$  radiation ( $\lambda = 0.71073 \text{ \AA}$ ). Their data reduction and empirical correction

\* To whom all correspondence should be sent:  
E-mail: cwtqq@aliyun.com



absorption are performed with the CrystalClear software. Crystal structures for both compounds are solved by the direct methods and refined by full-matrix least-squares techniques against  $F^2$  with the Siemens SHELXTL™ Version 5 crystallographic software package. Non-hydrogen atoms are found based on the difference Fourier maps, while the hydrogen atoms are symmetrically generated and allowed to ride on the parent atoms. The crystal data and structural refinement parameters are presented in Table 1. Selected bond lengths and angles are given in Table 2. CCDC No. 1416689 (**1**) and 1416690 (**2**).

## RESULTS AND DISCUSSION

The ORTEP figure displaying the molecular structure of compound **1** is shown in Figure 1.

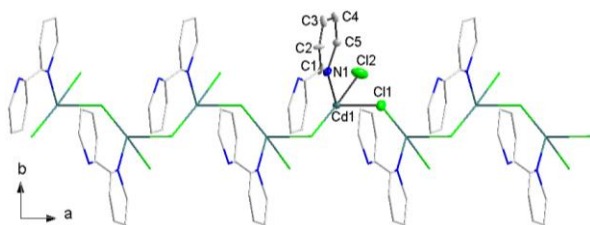


**Fig. 1.** An ORTEP figure showing the molecular structure of compound **1** (hydrogen atoms were omitted for clarity)

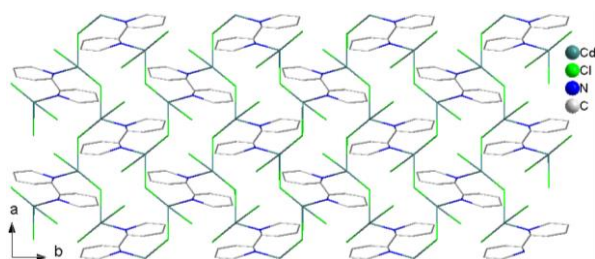
The X-ray single-crystal diffraction results reveal that the molecular structure of compound **1** is characterized by a three-dimensional (3D) structure. All of the crystallographically independent atoms are located on the general positions. The cadmium ion is coordinated by three chloride ions and one nitrogen atom to yield a tetrahedron. The bond length of Cd-N is 2.208(2) Å, while the Cd-Cl bond lengths are between 2.5185(16) Å and 2.6722(13) Å. These bond lengths are normal and comparable with those previously reported [1-8]. The bond angle of N-Cd-N is 69.18(7)°. The bond angles of N-Cd-Cl and Cl-Cd-Cl are in the wide range of 85.70(6)°–160.069(12)° and 84.35(8)°–178.694(2)°, respectively. The result of the bond valence calculation reveals that the cadmium ion is in the +2 oxidation state (Cd1: 1.7) [1]. The pyridyl rings of 2,2'-bipy are perfectly coplanar with the nitrogen atoms pointing in opposite directions. The 2,2'-bipy of compound **1** acts as a bidentate ligand binding to two cadmium(II) ions. The deviation of the atoms of the pyridyl rings is -0.099 Å – +0.081 Å apart from their average ring plane. The molecules of compound **1** interlink two neighboring ones via the chloride ions to form an infinite chain running along the *a* axis (Figure 1). The chains further interconnect together to yield a three-dimensional (3D) framework, as given in Figure 2.

**Table 1.** Crystallographic data and structural refinement parameters for **1** and **2**

Compound	<b>1</b>	<b>2</b>
Empirical formula	C10 H8 Cd2 Cl4 N2	C10 H8 Cd Cl2 N2
Color and Habit	colorless block	colorless block
Crystal Size (mm)	0.14 0.10 0.08	0.12 0.08 0.05
Crystal system	monoclinic	monoclinic
Space group	<i>I</i> 2/ <i>a</i>	<i>C</i> 2/ <i>c</i>
<i>a</i> (Å)	7.1691(4)	17.52(2)
<i>b</i> (Å)	9.3087(5)	9.290(10)
<i>c</i> (Å)	16.4175(12)	7.165(9)
$\beta$ (°)	93.1810(10)	110.897(14)
<i>V</i> (Å <sup>3</sup> )	1093.93(12)	1090(2)
Formula weight	522.78	339.48
<i>Z</i>	4	4
Theta range (°)	5.41 – 25.02	4.98 – 25.00
Reflections collected	1734	3455
Independent, observed reflections ( <i>R</i> <sub>int</sub> )	526, 513 (0.0196)	884, 433 (0.0577)
Density(cal.) (g/cm <sup>3</sup> )	3.174	2.665
Absorption coefficient (mm <sup>-1</sup> )	4.838	5.405
Temperature(K)	296(2)	296(2)
<i>F</i> (000)	984	790
<i>R</i> 1, <i>wR</i> 2	0.0695, 0.1642	0.0866, 0.1353
Goodness-of-fit	1.018	0.645
Largest and Mean Delta/Sigma	0, 0	0.004, 0
$\Delta\rho$ (max, min) (e/Å <sup>3</sup> )	1.265, -0.858	1.779, -0.872

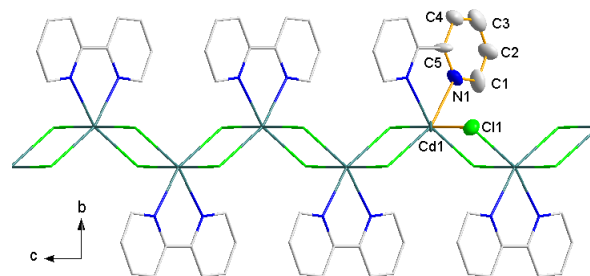
**Table 2.** Some bond lengths (Å) and angles (°)

Compound 1			
Cd(1)-N(1)	2.208(2)	N(1)-Cd(1)-Cl(1)	89.56(7)
Cd(1)-Cl(1)	2.5877(13)	Cl(2)-Cd(1)-Cl(1)	177.39(5)
Cd(1)-Cl(1)#1	2.6722(13)	N(1)-Cd(1)-Cl(1)#1	82.65(7)
Cd(1)-Cl(2)	2.5185(16)	Cl(2)-Cd(1)-Cl(1)#1	84.91(6)
N(1)-Cd(1)-Cl(2)	88.21(7)	Cl(1)-Cd(1)-Cl(1)#1	96.15(4)
Symmetry codes: #1 $x-1/2, -y+2, z$ .			
Compound 2			
Cd(1)-N(1)	2.3220(18)	Cl(1)-Cd(1)-Cl(1)#1	103.40(8)
Cd(1)-N(1)#1	2.3220(18)	N(1)-Cd(1)-Cl(1)#2	95.38(6)
Cd(1)-Cl(1)	2.5422(17)	N(1)#1-Cd(1)-Cl(1)#2	85.70(6)
Cd(1)-Cl(1)#1	2.5422(17)	Cl(1)-Cd(1)-Cl(1)#2	94.83(8)
Cd(1)-Cl(1)#2	2.752(2)	Cl(1)#1-Cd(1)-Cl(1)#2	84.35(8)
Cd(1)-Cl(1)#3	2.752(2)	N(1)-Cd(1)-Cl(1)#3	85.70(6)
N(1)-Cd(1)-N(1)#1	69.18(7)	N(1)#1-Cd(1)-Cl(1)#3	95.38(6)
N(1)-Cd(1)-Cl(1)	160.069(12)	Cl(1)-Cd(1)-Cl(1)#3	84.35(8)
N(1)#1-Cd(1)-Cl(1)	94.61(7)	Cl(1)#1-Cd(1)-Cl(1)#3	94.83(8)
N(1)-Cd(1)-Cl(1)#1	94.61(7)	Cl(1)#2-Cd(1)-Cl(1)#3	178.694(2)
Symmetry codes: #1 $-x+1, y, -z+3/2$ ; #2 $x, -y+1, z+1/2$ ; #3 $-x+1, -y+1, -z+1$ .			

**Fig. 2.** A packing figure of compound 1 viewed down along the  $c$  axis.

Compound 2 crystallizes in the space group  $C2/c$  of the monoclinic system, while compound 1 crystallizes in the monoclinic  $I2/a$  space group. The Cd(II) ion of compound 2 is located in a special position, while other crystallographically independent atoms reside at general positions. The crystal structure of compound 2 is characteristic of a one-dimensional (1D) chain-like motif comprising of  $\text{CdCl}_2(2,2'\text{-bipy})$  building blocks. As depicted in Figure 3, the cadmium ion of compound 2 is coordinated by four chloride ions and two nitrogen atoms to yield an octahedron. The equatorial plane of this octahedron yields two nitrogen atoms and two chloride ions, while both apical positions are occupied by another two chloride ions. The result of the bond valence calculation reveals that the cadmium ion is in the +2 oxidation state (Cd1: 2.1). Different from compound 1, both nitrogen atoms of the pyridyl rings of compound 2 point in the same direction and both of them are coordinated to the same cadmium ion. The bond lengths of Cd–N and Cd–Cl in the equatorial plane are 2.3220(18) Å and 2.5422(17) Å, respectively. The bond lengths of the apical Cd–Cl are 2.752(2) Å. The bond distances of Cd–N and Cd–Cl in the coordination sphere of the

cadmium ion are normal and comparable with those reported in the references [1, 2, 3, 4]. Each cadmium(II) ion interconnects two neighboring ones through two  $\mu_2$ -chloride ions to form an infinite 1-D chain-like motif, as displayed in Figure 3. The 2,2'-bipy of compound 2 is a bidentate ligand chelating one cadmium(II) ion, while that of compound 1 acts as a bidentate ligand binding to two cadmium(II) ions. The dihedral angle between the pyridyl rings of the 2,2'-bipy molecule of compound 2 is 7.024(23)°. The 1-D chains stack together via the van der Waals interaction to give a 3-D packing figure, as shown in Figure 4. The reason for the 3D structure and 1D chain in compounds 1 and 2, respectively, should be ascribed to different coordination modes of the 2,2'-bipy ligand. In compound 1, two nitrogen atoms of one 2,2'-bipy point to opposite directions that allow the 2,2'-bipy to bind to two different cadmium(II) ions and yield a 3D structure. However, in compound 2, both nitrogen atoms of one 2,2'-bipy point to the same direction and both of them are coordinated to one same cadmium ion and only form a 1D chain.

**Fig. 3.** An ORTEP figure showing the molecular structure of compound 2 (hydrogen atoms were omitted for clarity).

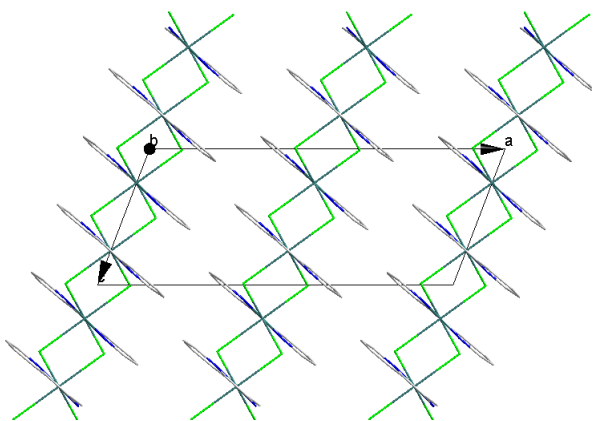


**Fig. 4.** A packing figure of compound **2** viewed down along the *b* axis

To our knowledge, the 2,2'-bipy and the cadmium ion can generally display fluorescence [5, 6, 7]. Based on this consideration, we deduced the fluorescence spectra for both compounds by using solid-state samples at an ambient temperature. As presented in Figure 5, the excitation spectra of compound **1** shows that the effective energy absorption is dominantly found in the ultraviolet region of 300–350 nm.

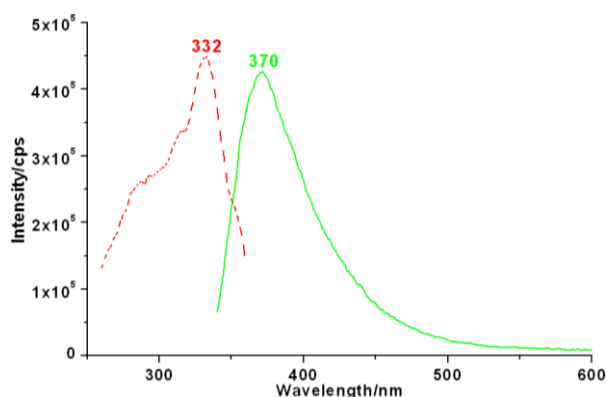


**Fig. 5.** Solid-state fluorescence spectra of compound **1** under room temperature with the dashed and solid lines representing excitation and emission spectra, respectively.

Excitation at 370 nm yields a strong band at 332 nm. The peak at 332 nm, is an intensive emission in the ultraviolet region. As for compound **2**, we also measured its fluorescence spectra and the result is shown in Figure 6. As depicted in Figure 6, the excitation spectra of compound **2**, exhibits the effective energy absorption mainly in the ultraviolet region of 350–400 nm. The excitation spectra under the emission of 522 nm display a strong band at 391 nm. By virtue of the excitation peak of 391 nm, we also measured the emission spectra of compound **2** and the result shows an intensive emission peak in the green region with a maximum value of 522 nm.

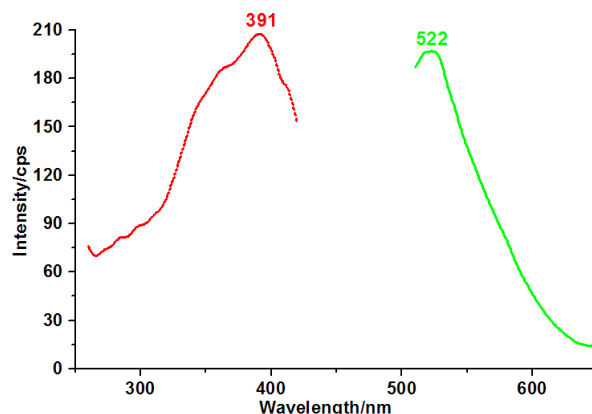


**Fig. 6.** Solid-state fluorescence spectra of compound **2** under room temperature with the dashed and solid lines representing excitation and emission spectra, respectively.

In summary, two cadmium compounds with different extended structures have been synthesized through hydrothermal reactions and structurally characterized by X-ray single-crystal diffraction. Compound **1** features a 3D structure, while compound **2** is characterized by a 1D motif. The coordination environments of the cadmium ions and the binding modes of the 2,2'-bipy ligand in both compounds are different, which yields different extended structures of the title compounds. Fluorescence investigation shows that the compounds display different fluorescence spectra.

**Acknowledgements:** We acknowledge the financial support of the NSF of China (21361013), the science and technology project of Jiangxi Provincial Department of Education (GJJ14554), the NSF of Jiangxi Province (20132BAB203010), and the open foundation (No. 20150019) of the State Key Laboratory of Structural Chemistry, Fujian Institute of Research on the Structure of Matter, Chinese Academy of Sciences.

## REFERENCES

1. C. K. Prier, D. A. Rankic, D. W. C. MacMillan. *Chem. Rev.*, **113**, 5322 (2013).
2. C. Riplinger, M. D. Sampson, A. M. Ritzmann, C. P. Kubiak, E. A. Carter. *J. Am. Chem. Soc.*, **136**, 16285 (2014).
3. T. R. Cook, Y.-R. Zheng, P. J. Stang. *Chem. Rev.*, **113**, 734 (2013).
4. A. O. Surov, A. A. Simagina, N. G. Manin, L. G. Kuzmina, A. V. Churakov, G. L. Perlovich. *Crystal Growth Des.*, **15**, 228 (2015).
5. Z. Yao, W. Chen, R. Hu. *Indian J Chem, Sec A*, **54**, 489 (2015).
6. H. F. Chen, M. J. Zhang, M. S. Wang, W. B. Yang, X. G. Guo, C. Z. Lu. *Inorg. Chem. Commun.*, **23**, 123 (2012).
7. R. Hu, W. Chen, Q. Y. Luo, Y. Xu, X. Zhang. *Asian J.*

- Chem.*, **27**, 2339 (2015).
8. W. Chen. *Journal of Jingtangshan University (Natural Science)*, **35**(5), 38 (2014).
9. Z. H. Lei, X. Li. *J. Coord. Chem.*, **64**, 2450 (2011).
10. W.-T. Chen, Z.-L. Yao, H.-M. Kuang, H.-L. Chen, Z.-G. Luo. *Synth. React. Inorg. M.*, **45**, 952 (2015).
11. Z. Ma, B. Liu, H. Yang, Y. Xiang, M. Hu, J. Sun. *J. Coord. Chem.*, **62**, 3314 (2009).
12. B. Machura, I. Nawrot, K. Michalik. *Polyhedron*, **31**, 548 (2012).
13. W. Chen. *Synth. React. Inorg. M.*, **45**, 315 (2015).
14. I. D. Brown, D. Altermat. *Acta Crystallogr. B.*, **41**, 244 (1985).
15. X.-H. Jin, J.-K. Sun, L.-X. Cai, J. Zhang. *Chem. Commun.*, **47**, 2667 (2011).
16. W. Chen, R. Hu, X. Yi, Y. Wang, Z. Luo, H. Fu, J. Liu, H. Chen. *Asian J. Chem.*, **26**, 4865 (2014).
17. C. Hu, Q. Li, U. Englert. *CrystEngComm.*, **5**, 519 (2003).
18. W. Chen, R. Hu, Z. Luo, H. Chen, X. Zhang, J. Liu. *Indian J Chem, Sec A*, **53**, 294 (2014).
19. M. S. Henry, M. Z. Hoffman. *J. Am. Chem. Soc.*, **99**, 5201 (1977).
20. M. S. Henry, M. Z. Hoffman. *J. Phys. Chem.*, **83**, 618 (1979).
21. H. J. Zhao, D. Jia, J. H. Li, G. J. Moxey, C. Zhang. *Inorg. Chim. Acta*, **432**, 1 (2015).

## ПРИГОТВЯНЕ, ОХАРАКТЕРИЗИРАНЕ И ФЛУОРЕСЦЕНЦИЯ НА ДВЕ КАДМИЕВИ СЪЕДИНЕНИЯ С РАЗЛИЧНИ РАЗГЪНАТИ СТРУКТУРИ

Ж.-Л. Яо<sup>2</sup>, И.-П. Пей<sup>1</sup>, Ж.-И. Луо<sup>1</sup>, Р.-Х. Ху<sup>1</sup>, И.-С. Яанг<sup>1</sup>, Уен-Тонг Чен<sup>1\*</sup>

<sup>1</sup>Институт по приложна химия, Колеж по химия и химично инженерство, Ключова лаборатория по координационна химия в провинция Янгси, Университет Джингангшан, Джсиан, Янгси 343009, Китай  
<sup>2</sup>Департамент по химично и биоинженерство, Клон Фуджин на Университета във Фуджиян, Фуджиян 350300, Китай

Постъпила на 6 август 2015 г.; коригирана на 19 август 2015 г.

(Резюме)

Две кадмиеви съединения  $[\text{Cd}_2\text{Cl}_4(2,2'\text{-bipy})]_n$  (**1**) и  $[\text{CdCl}_2(2,2'\text{-bipy})]_n$  (**2**) (bipy = бипиридил) с различни разгънати структури са получени при хидротермални реакции и са структурно охарактеризирани с рентгеноструктурен анализ чрез дифракция на един кристал. Съединение **1** се характеризира с три-измерна (3D) структура, а кадмиевият йон се координира от три хлоридни йона и един азотен атом с получаването на тетраедър. Съединение **2** се характеризира с едно-измерна (1D) структура, а кадмиевият йон се координира с четири хлоридни йона и та азотни атома с получаването на октаедър. Флуоресцентните изследвания показват, че съединение **1** дава емисии в ултравиолетовата област, докато съединение **2** проявява емисии в зелената област на спектъра.

## Non-Darcy effect on non-Newtonian Bingham fluid with heat transfer between two parallel plates

W. Abbas<sup>1</sup>, Hazem Ali Attia<sup>2</sup>, Mostafa A. M. Abdeen<sup>3\*</sup>

<sup>1</sup>Basic and Applied Science Department, College of Engineering and Technology, Arab Academy for Science, Technology, and Maritime Transport, Cairo, Egypt

<sup>2</sup>Department of Engineering Mathematics and Physics, Faculty of Engineering, El-Fayoum University, El-Fayoum-63514, Egypt

<sup>3</sup>Department of Engineering Mathematics and Physics, Faculty of Engineering, Cairo University, Giza-12211, Egypt

Submitted August 13, 2015; Accepted September 15, 2015

The non-Darcy model for the Bingham fluid has a wide range of applications in energy systems and magnetic material processing. This work investigated the effect of unsteady non-Darcy flow on the velocity and temperature distributions for non-Newtonian Bingham fluid between two infinite parallel porous plates with heat transfer considering the Hall Effect. A constant pressure gradient is applied in the main axial direction and an external uniform magnetic field and uniform suction and injection are applied in the direction perpendicular to the plates. The dimensionless governing coupled momentum and energy equations taking the Joule and viscous dissipations into consideration are derived and solved numerically using the finite difference approach. The effect of porosity of the medium, Hartmann, and Hall current parameters on the velocity and temperature distributions with a Reynolds number fixed at 10 (For  $R_e \geq 10$ , non-Darcy model is sufficient) is investigated. It is found that the porosity and inertial effects have a marked effect on decreasing the velocity distribution in an inverse proportionality manner. Furthermore, increasing the non-Darcian parameter decreases the temperature values for each value of the porosity.

**Keywords:** Non-Newtonian fluid, Bingham model, Non-Darcyflow, Heat transfer, Hall current.

### INTRODUCTION

Recently, Researchers have considerable interest in the study of flow phenomenon between two parallel plates because of its possible applications in many branches of science and technology, as its occurrence in rheumatic experiments to determine the constitutive properties of the fluid, in lubrication engineering, and in transportation and processing encountered in chemical engineering, etc. [1]. On the other hand, Couette flow of an electrically conducting viscous incompressible fluid under the action of a transverse magnetic field has many applications in magneto-hydrodynamic (MHD) power generators, aerodynamics heating, pumps, polymer technology, petroleum industry, and fluid droplets-sprays [2]. Bharali and Borkakati [3], studied the effect of Hall currents on magneto hydrodynamic (MHD) flow of an incompressible viscous electrically conducting fluid between two non-conducting porous plates in the presence of a strong uniform magnetic field. The steady flow of an electrically conducting, viscous, incompressible fluid bounded by two parallel infinite insulated horizontal plates and the heat transfer was studied

by Attia and Kotb [4]. Joaquín et al. [5], studied numerically the variations with velocity of suction, hall effect, Reynolds and Hartmann number, particle concentration and Eckert number on the unsteady MHD Couette Flow and heat transfer of a dusty and electrically conducting fluid between parallel plates in the presence of an external uniform magnetic field and uniform suction and injection. The transient hydromagnetic flow through a porous medium between two infinite parallel porous plates with heat transfer considering the Hall effect and the temperature dependent physical properties under constant pressure gradient was studied by Attia et al. [6]. Also, other research work concerning the flow between two parallel plates has been obtained under different physical effects [7-12].

A non-Newtonian fluid is a fluid that does not obey Newton's law of viscosity (viscosity is variable based on applied stress or force). The non-Newtonian fluid is a classical problem that has many industrial applications such as cement, drilling mud, sludge, grease, granular suspensions, aqueous foams, slurries, paints, food products, plastics and paper pulp exhibit a yield stress  $\tau_0$  to allow for the motion of the fluid. Many non-Newtonian fluids, encountered in chemical engineering processes, are known to follow the so-

\* To whom all correspondence should be sent:  
E-mail: [mostafa\\_a\\_m\\_abdeen@hotmail.com](mailto:mostafa_a_m_abdeen@hotmail.com)

called ‘‘Bingham model’’ which have a linear shear stress/shear strain relationship and require a finite yield stress before they begin to flow (the plot of shear stress against shear strain does not pass through the origin). Several examples are clay suspensions, drilling mud, toothpaste, mayonnaise, chocolate and mustard. Many authors have studied the flow of a Bingham fluid under different physical effects and geometries, Walton and Bittleston [13], described analytical and numerical solutions for the flow of a Bingham plastic in an eccentric annulus. The magneto-hydrodynamic unsteady flow of an electrically conducting viscous incompressible non-Newtonian Bingham fluid bounded by two parallel non-conducting porous plates was studied with heat transfer considering the Hall effect by Yang and Zuh [14]. Rees and Bassom [15], presented an unsteady free convection flow of a Bingham fluid when it saturates a porous medium and the flows was induced by suddenly raising the constant temperature of a vertical bounding surface.

Fluid flow in porous media is important in many areas of reservoir engineering, such as petroleum, environmental and ground water hydrology[16]. According to previous work, Darcy’s law depicts fluid flow behavior in porous media. The Darcy law is sufficient in studying small rate flows where the Reynolds number is very small ( $Re < 10$ ) [17]. For larger Reynolds numbers the Darcy law is insufficient and several models have been adopted to correct the Darcy law. Based on a review of previous work, the Darcy-Forchheimer model is probably the most popular modification to Darcy flows. In 1901, Philippe Forchheimer assumed that Darcy’s law is still valid, but an additional term must be added to account for the increased pressure drop and represent the microscopic inertial effect [18]. Recent contributions are the interesting studies considered in the references [19-24].

In the present paper, an extension has been made to the study in [25], to assess the influence of Non-Darcy porous media on unsteady non-Newtonian Bingham fluid between two infinite horizontal porous plates, by heat transfer and the Hall Effect. The fluid is acted upon by a constant pressure gradient, a uniform suction from above and a uniform injection from below while it is subjected to a uniform magnetic field perpendicular to the plates. The inclusion of the porosity effect and inertial effects as well as the velocity of suction or injection leads to some interesting effects, on both the velocity and temperature distributions to be investigated.

### MATHEMATICAL MODEL

In the present model, two infinite horizontal plates located at the  $y = \pm h$  planes and extended from  $x = 0$  to  $\infty$  and from  $z = 0$  to  $\infty$  have been considered and filled with incompressible, non-Newtonian fluid obeying the Bingham model and electrically conducting fluid through a porous medium. The characteristics of the porous medium in this study obey the Darcy-Forchheimer model. The fluid flows between the two plates under the influence of a pressure gradient  $dp/dx$  in the  $x$ -direction which is constant with time. The two plates are porous, insulated and kept at two constant but different temperatures  $T_1$  for the lower plate and  $T_2$  for the upper plate ( $T_2 > T_1$ ). The upper plate moves with a uniform velocity  $U_0$  whereas the lower plate is kept stationary. A uniform suction from above and injection from below, with velocity  $v_0$ , are applied impulsively at  $t = 0$ . A uniform magnetic field  $B = (0, B_0, 0)$  is applied parallel to the  $y$ -axis which is normal to the planes of the plates in the positive direction. The effect of the Hall current is considered which results in a new component for the velocity in the  $z$ -direction.

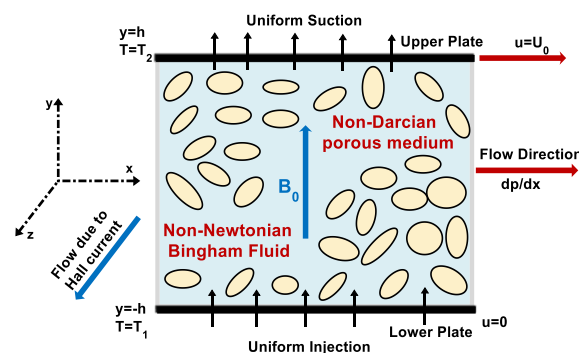


Fig. 1. Schematic diagram of the problem

From the geometry of the problem and due to the infinite dimensions in the  $x$  and  $z$  directions, it is evident that the physical quantities do not change in these directions ( $\partial/\partial x = \partial/\partial z = 0$  for all quantities). The flow in the porous medium deals with the analysis in which the differential equation governing the fluid motion is based on the Darcy-Forchheimer law which considers the drag exerted by the porous medium. The fluid motion starts from rest at  $t = 0$ , and the no-slip condition at the plates implies that the fluid velocity has neither a  $z$  nor an  $x$ -component at  $y = \pm h$ . The initial temperature of the fluid is assumed to be equal to  $T_1$  as the temperature of the lower plate. Figure 1 represents a schematic diagram of the proposed problem.

The governing equations of this study are based on the conservation laws of mass, linear momentum and energy for both phases.

The generalized Ohm's law including the Hall current is given in the form [26]:

$$\vec{j} = \sigma \left[ \vec{E} + \vec{v} \times \vec{B} - \frac{1}{en_e} (\vec{j} \times \vec{B}) \right], \quad (1)$$

Where  $\vec{j}$  is the electric current density vector,  $\sigma$  is the electric conductivity of the fluid,  $\vec{v}$  is the velocity vector,  $\vec{E}$  is the intensity vector of the electric field,  $\vec{B}$  is the induced magnetic vector,  $e$  is the charge of an electron and  $n_e$  is the number density of electrons.

The fluid velocity vector is given by:

$$\vec{v}(y, t) = u(y, t)\vec{i} + v_0\vec{j} + w(y, t)\vec{k}, \quad (2)$$

By neglecting the polarization effect, we get the electric field vector equal to zero ( $\vec{E}=0$ ). The generalized Ohm's law equation (1) gives  $J_y = 0$  everywhere in the flow. The current density components  $J_x$  and  $J_z$  are given as:

$$J_x = \frac{\sigma B_0}{1+m^2} (mu - w), \quad (3a)$$

$$J_z = \frac{\sigma B_0}{1+m^2} (u + mw), \quad (3b)$$

where,  $m$  is the Hall parameter,  $m = \frac{\sigma B_0}{en_e}$ .

The vector equation of motion for the fluid is governed by the momentum equation together with the generalized Ohm's law and non-Darcy's resistance and can be written as:

$$\rho \frac{D\vec{v}}{Dt} = -\nabla p + \nabla \cdot (\mu \nabla \vec{v}) + \vec{j} \times \vec{B} - \frac{\mu}{K} \vec{v} - \frac{\lambda \rho}{K} |\vec{v}| \vec{v}, \quad (4)$$

where,  $\rho$  is the density of the fluid,  $D/Dt$  is a differential operator,  $t$  is the time,  $K$  is the Darcy permeability,  $\lambda$  is the inertial coefficient, and  $\mu$  is the apparent viscosity.

The two components of the momentum equation (4) in the x and z-direction become:

$$\rho \frac{\partial u}{\partial t} + \rho v_0 \frac{\partial u}{\partial y} = \frac{-\partial p}{\partial x} + \frac{\partial}{\partial y} \left( \mu \frac{\partial u}{\partial y} \right) - \frac{\sigma B_0^2}{1+m^2} (u + mw) - \frac{\mu}{K} u - \frac{\lambda \rho}{K} u^2, \quad (5)$$

$$\rho \frac{\partial w}{\partial t} + \rho v_0 \frac{\partial w}{\partial y} = \frac{\partial}{\partial y} \left( \mu \frac{\partial w}{\partial y} \right) - \frac{\sigma B_0^2}{1+m^2} (w - mu) - \frac{\mu}{K} w - \frac{\lambda \rho}{K} w^2, \quad (6)$$

where,  $u$  and  $v$  are velocity components in the x- and z-directions.

The energy equation describing the temperature distribution for the fluid and Joule dissipations is given by Attia et al.[25]:

$$\rho c_p \frac{\partial T}{\partial t} + \rho c_p v_0 \frac{\partial T}{\partial y} = k \frac{\partial^2 T}{\partial y^2} + \mu \left[ \left( \frac{\partial u}{\partial y} \right)^2 + \left( \frac{\partial w}{\partial y} \right)^2 \right] + \frac{\sigma B_0^2}{1+m^2} (u^2 + w^2) \quad (7)$$

where,  $c_p$  and  $k$  are the specific heat capacity and the thermal conductivity of the fluid, respectively and  $T$  denotes the temperature. The second and third terms on the right side represent, respectively, the viscous and Joule dissipations. We notice that each of these terms has two components. This is because the Hall effect leads to an additional velocity component  $w$  in the z-direction.

The shear stress  $\tau$  of the Bingham fluid model can be written as follows[25]:

$$\tau = \tau_0 + K_B \dot{\gamma} \quad \text{for } |\tau| > \tau_0 \\ \dot{\gamma} = 0 \quad \text{for } |\tau| \leq \tau_0$$

where,  $\dot{\gamma} = \sqrt{\left( \frac{\partial u}{\partial y} \right)^2 + \left( \frac{\partial w}{\partial y} \right)^2}$  is the shear rate,  $\tau_0$  is the yield stress,  $K_B$  is the plastic viscosity of the Bingham fluid. Thus, the apparent viscosity is given by:

$$\mu = K_B + \frac{\tau_0}{|\dot{\gamma}|}, \quad (8)$$

Owing to provides no information about the stress field whenever  $\tau < \tau_0$ , and is discontinuous. In order to avoid this discontinuity, Papanastasiou [27] proposed a modified model with a growth rate parameter  $m$  which controls the exponential growth of stress. Thus the Bingham model can be rewritten by using Papanastasiou modification as follows:

$$\tau = \tau_0 [1 - e^{-\delta \dot{\gamma}}] + K_B \dot{\gamma} \quad \text{for all } \dot{\gamma}, \quad (9)$$

The parameter  $m$  controls the stress growth, such that the yield stress  $\tau_0$  a finite stress is allowed to vanish, therefore this model is valid for all regions [28]. For sufficiently the parameter  $\delta > 100$  in the above equation mimics the Bingham plastic model [28]. Thus, the scalar viscosity is given by:

$$\mu = K_B + \frac{\tau_0 [1 - e^{-\delta |\dot{\gamma}|}]}{|\dot{\gamma}|}, \quad (10)$$

The initial and boundary conditions of both the flow and heat problems are, respectively, given by:

$$\text{At } t \leq 0: u = w = 0; T = T_1, \quad (11a)$$

$$\text{At } t > 0: u = w = 0; T = T_1 \\ \text{at } y = -h, \quad (11b)$$

$$\text{At } t > 0: u = U_0; w = 0; T = T_2 \\ \text{at } y = h. \quad (11c)$$

The following non-dimensional variables will be introduced into equations (5)-(7) and (10)-(11):

$$x^* = \frac{x}{h}, y^* = \frac{y}{h}, z^* = \frac{z}{h}, t^* = \frac{t U_0}{h}, \\ u^* = \frac{u}{U_0}, w^* = \frac{w}{U_0}, p^* = \frac{p}{\rho U_0^2}, \\ T^* = \frac{T - T_1}{T_2 - T_1}, \mu^* = \frac{\mu}{K_B}$$

The non-dimensional conservation equations will be in the following forms:

Momentum conservation in the x-direction:

$$\frac{\partial u^*}{\partial t^*} + s \frac{\partial u^*}{\partial y^*} = \frac{-\partial p^*}{\partial x^*} + \frac{1}{R_g} \frac{\partial}{\partial y^*} \left( \mu^* \frac{\partial u^*}{\partial y^*} \right) - \frac{Ha^2}{R_g(1+m^2)} (u^* + mw^*) - \beta \mu^* u^* - \gamma u^{*2} \quad (12)$$

Momentum conservation in the z-direction:

$$\frac{\partial w^*}{\partial t^*} + s \frac{\partial w^*}{\partial y^*} = \frac{1}{R_g} \frac{\partial}{\partial y^*} \left( \mu^* \frac{\partial w^*}{\partial y^*} \right) - \frac{Ha^2}{R_g(1+m^2)} (w^* - mu^*) - \beta \mu^* w^* - \gamma w^{*2} \quad (13)$$

Energy conservation:

$$\frac{\partial T^*}{\partial t^*} + s \frac{\partial T^*}{\partial y^*} = \frac{1}{R_g Pr} \frac{\partial^2 T^*}{\partial y^{*2}} + \frac{E_c \mu^*}{R_g} \left[ \left( \frac{\partial u^*}{\partial y^*} \right)^2 + \left( \frac{\partial w^*}{\partial y^*} \right)^2 \right] + \frac{E_c Ha^2}{R_g(1+m^2)} (u^{*2} + w^{*2}) \quad (14)$$

The apparent viscosity:

$$\mu^* = 1 + \frac{\tau_D \left[ 1 - \eta \sqrt{\left( \frac{\partial u^*}{\partial y^*} \right)^2 + \left( \frac{\partial w^*}{\partial y^*} \right)^2} \right]}{\sqrt{\left( \frac{\partial u^*}{\partial y^*} \right)^2 + \left( \frac{\partial w^*}{\partial y^*} \right)^2}}, \quad (15)$$

The dimensionless initial and boundary conditions of both the flow and heat problems are, respectively, given by:

$$\text{At } t^* \leq 0: u^* = w^* = 0; T^* = 0, \quad (16a)$$

$$\text{At } t^* > 0: u^* = w^* = 0; T^* = 0$$

$$\text{at } y = -1, \quad (16b)$$

$$\text{At } t^* > 0: u^* = 1; w^* = 0; T^* = 1$$

$$\text{at } y = 1, \quad (16c)$$

where,  $R_g = \frac{\rho U_0 h}{K_B}$  is the Reynolds number representing the ratio of inertial forces to viscous forces,  $Ha^2 = \frac{\sigma B_0^2 h^2}{K_B}$  is the Hartmann number squared which represents the ratio of electromagnetic force to the viscous force,  $Pr = \frac{\mu C_p}{k}$  is the Prandtl number which dimensionless number defines the ratio of the momentum diffusivity (kinematic viscosity) to thermal diffusivity,  $\tau_D = \frac{\tau_0 h}{K_B U_0}$  is the dimensionless yield stress,  $S = \frac{V_0}{U_0}$  is the suction parameter representing the mass of the fluid passing through the lower plate and exiting through the upper plate (when  $S > 0$  the suction at the upper plate and injection at the lower plate),  $E_c = \frac{U_0^2}{c_p (T_2 - T_1)}$  is the Eckert number which defines the ratio of the kinetic energy of the flow to the enthalpy difference,  $\beta = \frac{h^2}{R_g K}$  is the porosity parameter,  $\gamma = \frac{\lambda h}{K}$  is the dimensionless non-Darcy parameter, and  $\eta = \frac{\delta U_0}{h}$  is the dimensionless growth parameter.

## NUMERICAL SOLUTION

There are many numerous methods available for the solution of the differential equation system. In the present work the finite difference method is used to solve the coupled non-linear partial differential equation systems (12)–(15) under conditions (16a), (16-b), and (16-c). The computational domain is discretized with a uniform grid of dimension  $\Delta t$  and  $\Delta y$  in time and space respectively as shown in Figure 2. A finite difference scheme for coupled partial differential equation systems (12)–(15) is created using the Crank-Nicolson implicit method which can be achieved by doing an average of the central difference schemes at time levels  $n$  and  $n+1$ .

To solve for the  $n+1$ <sup>th</sup> time step, where we know already the  $n$ <sup>th</sup> time step, we consider our scheme as if we were standing at the  $n+0.5$  time step and then take the average of the forward half time step and backward half time step. So the discretized equations would be of the form:

x-direction momentum equation:

$$\begin{aligned} & \frac{u_i^{n+1} - u_i^n}{\Delta t} + s \left( \frac{u_{i+1}^{n+1} - u_{i-1}^{n+1} + u_{i+1}^n - u_{i-1}^n}{4\Delta y} \right) = -C + \\ & \frac{1}{R_g} \left( \frac{\mu_{i+1}^{n+1} - \mu_{i-1}^{n+1} + \mu_{i+1}^n - \mu_{i-1}^n}{4\Delta y} \right) \left( \frac{u_{i+1}^{n+1} - u_{i-1}^{n+1} + u_{i+1}^n - u_{i-1}^n}{4\Delta y} \right) + \\ & \frac{1}{R_g} \left( \frac{\mu_i^{n+1} + \mu_i^n}{2} \right) \left( \frac{u_{i+1}^{n+1} - 2u_i^{n+1} + u_{i-1}^{n+1}}{2\Delta y^2} + \right. \\ & \left. \frac{u_{i+1}^n - 2u_i^n + u_{i-1}^n}{2\Delta y^2} \right) - \\ & \frac{Ha^2}{R_g(1+m^2)} \left( \frac{u_i^{n+1} + u_i^n}{2} + m \frac{w_i^{n+1} + w_i^n}{2} \right) - \\ & \beta \left( \frac{\mu_i^{n+1} + \mu_i^n}{2} \right) \left( \frac{u_i^{n+1} + u_i^n}{2} \right) - \gamma \left( \frac{u_i^{n+1} + u_i^n}{2} \right)^2 \end{aligned} \quad (17)$$

y-direction momentum equation:

$$\begin{aligned} & \frac{w_i^{n+1} - w_i^n}{\Delta t} + s \left( \frac{w_{i+1}^{n+1} - w_{i-1}^{n+1} + w_{i+1}^n - w_{i-1}^n}{4\Delta y} \right) = \\ & \frac{1}{R_g} \left( \frac{\mu_{i+1}^{n+1} - \mu_{i-1}^{n+1} + \mu_{i+1}^n - \mu_{i-1}^n}{4\Delta y} \right) \left( \frac{w_{i+1}^{n+1} - w_{i-1}^{n+1} + w_{i+1}^n - w_{i-1}^n}{4\Delta y} \right) + \\ & \frac{1}{R_g} \left( \frac{\mu_i^{n+1} + \mu_i^n}{2} \right) \left( \frac{w_{i+1}^{n+1} - 2w_i^{n+1} + w_{i-1}^{n+1}}{2\Delta y^2} + \right. \\ & \left. \frac{w_{i+1}^n - 2w_i^n + w_{i-1}^n}{2\Delta y^2} \right) - \\ & \frac{Ha^2}{R_g(1+m^2)} \left( \frac{w_i^{n+1} + w_i^n}{2} - m \frac{u_i^{n+1} + u_i^n}{2} \right) - \\ & \beta \left( \frac{\mu_i^{n+1} + \mu_i^n}{2} \right) \left( \frac{w_i^{n+1} + w_i^n}{2} \right) - \gamma \left( \frac{w_i^{n+1} + w_i^n}{2} \right)^2 \end{aligned} \quad (18)$$



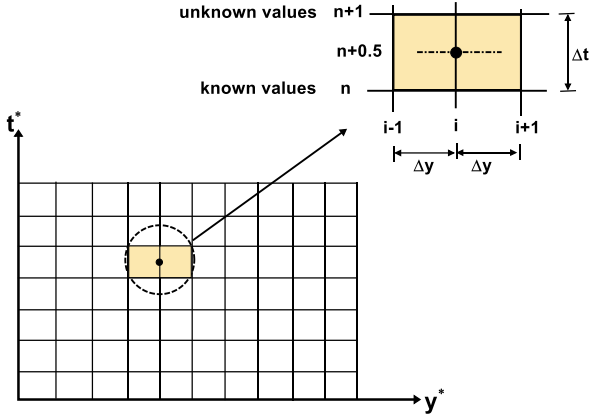


Fig. 2. Mesh layout for the Crank-Nicolson implicit method.

Similarly, the Crank-Nicolson approximation to the Energy equation is:

$$\begin{aligned} & \frac{T_i^{n+1} - T_i^n}{\Delta t} + S \left( \frac{T_{i+1}^{n+1} - T_{i-1}^{n+1} + T_{i+1}^n - T_{i-1}^n}{4\Delta y} \right) = \\ & \frac{1}{Pr Re} \left( \frac{T_{i+1}^{n+1} - 2T_i^{n+1} + T_{i-1}^{n+1}}{2\Delta y^2} + \frac{T_{i+1}^n - 2T_i^n + T_{i-1}^n}{2\Delta y^2} \right) + \\ & \frac{Ec}{Re} \left( \frac{\mu_i^{n+1} + \mu_i^n}{2} \right) \left( \left( \frac{u_{i+1}^{n+1} - u_{i-1}^{n+1} + u_{i+1}^n - u_{i-1}^n}{4\Delta y} \right)^2 + \right. \\ & \left. \left( \frac{w_{i+1}^{n+1} - w_{i-1}^{n+1} + w_{i+1}^n - w_{i-1}^n}{4\Delta y} \right)^2 \right) + \\ & \frac{Ec Ha^2}{Re(1+m^2)} \left( \left( \frac{u_i^{n+1} + u_i^n}{2} \right)^2 + \left( \frac{w_i^{n+1} + w_i^n}{2} \right)^2 \right) \end{aligned} \quad (19)$$

Finally, the resulting block tri-diagonal system is solved using the generalized Thomas-algorithm. All calculations are carried out for the non-dimensional variables and parameters given by,  $\frac{\partial p^*}{\partial x^*} = C = -5$ . Grid-independence studies show that the computational domain  $0 < t < \infty$  and  $1 < y < 1$  is divided into intervals with step sizes  $\Delta t = 0.0001$  and  $\Delta y = 0.005$  for time and space respectively.

## RESULTS AND DISCUSSION

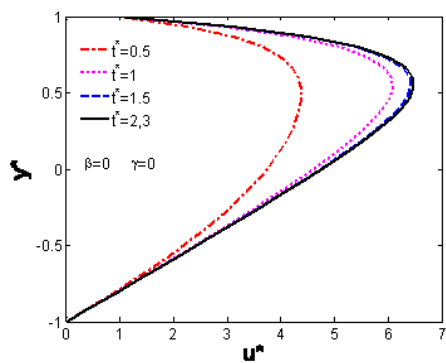
Figures 3-5 show the evolution of dimensionless velocities  $u^*$  and  $w^*$  and temperature distribution  $T^*$  with time  $t^*$  for various Darcy and non-Darcy parameters ( $\beta$  and  $\gamma$ ) at  $Ha=3$ ,  $m=3$ ,  $S=1$ ,  $Re=10$ ,  $Pr=1$ ,  $Ec=0.2$  and  $\tau_D = 0.1$ . Figures 3 and 4 show the effect of Darcy and non-Darcy parameters ( $\beta$  and  $\gamma$ ) on the time development of  $u^*$  and  $w^*$ . It is obvious that increasing the Darcy parameter  $\beta$  decreases  $u^*$  and  $w^*$  and its steady state time as a result of increasing the resistive damping porosity force on  $u^*$  and  $w^*$ . On the other hand, increasing the non-Darcy parameter  $\gamma$  for each value of  $\beta$  decreases the velocity  $u^*$  and  $w^*$  and its steady state

time which reflects the expected resistance because of the inertial effects.

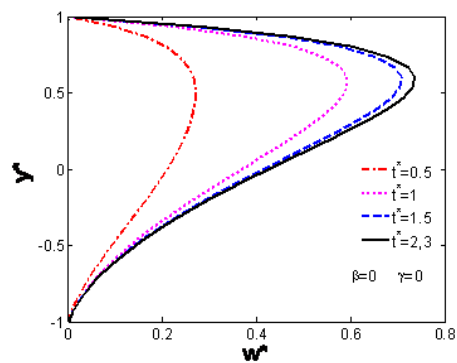
Also, it is observed that the charts of the velocity  $u^*$  are asymmetric about the  $y = 0$  plane because of the suction. Figure 5 shows the effect of Darcy and non-Darcy parameters on the time progression of the temperature  $T^*$ . It is observed that the increase of the Darcy parameter  $\beta$  and non-Darcy parameter  $\gamma$  decreases  $T^*$  and its steady state time. The increasing  $\beta$  and  $\gamma$  decreases  $u^*$  which in turn decreases the viscous dissipation and  $T^*$ . Also, increasing the non-Darcy parameter  $\gamma$  for each value of  $\beta$  further decreases the temperature and its steady time because of the additional resistive inertial effects. Figures 3-a, 4-a, and 5-a, indicate the unsteady non-Newtonian Bingham fluid case where the plates and medium are non-porous ( $\beta=0$  and  $\gamma=0$ ) obtaining the highest velocity and temperature distributions, which were considered earlier by Attia [25]. In addition, we mean a flow without additional inertial effects and the Darcy case where  $\beta=1$  and  $\gamma=0$  as shown in figures 3-b, 4-b and 5-b, obtained to provide an easier quick path for the fluid flow and temperature values.

Figure 6 presents the profiles of the velocity component  $u^*$  and  $w^*$  and temperature distribution  $T^*$  at the center of the channel ( $y^* = 0$ ) with time  $t^*$  for various non-Darcy parameters  $\gamma$  and for  $\tau_D = 0.01$  and  $0.1$  at  $Ha=3$ ,  $m=3$ ,  $S=1$ ,  $Re=10$ ,  $Pr=1$ ,  $Ec=0.2$ . The figures show that, with increasing the yield stress  $\tau_D$  decreases the velocity components  $u^*$  and  $w^*$  and temperature profile  $T^*$ , the time at which they reach their steady state values also decreases as a result of increasing the viscosity. It is obvious that increasing the non-Darcy parameter  $\gamma$  decreases  $u^*$ ,  $w^*$ ,  $T^*$  and its steady state time as a result of increasing the resistive damping porosity force on  $u^*$  and  $w^*$ . Also, it is observed that the velocity component  $u^*$  reaches the steady state faster than  $w^*$  which, in turn, reaches the steady state faster than  $T^*$ . This is expected as  $u^*$  is the source of  $w^*$ , while both  $u^*$  and  $w^*$  act as sources for the temperature.

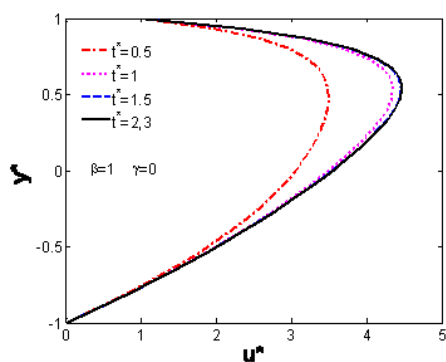
The influence of the non-Darcy parameter  $\gamma$  on the velocity components  $u^*$ ,  $w^*$  and temperature distribution  $T^*$  with time  $t^*$  for various Hartmann numbers  $Ha$  are shown in figure 7 at the center of the channel ( $y^* = 0$ ). It is clear that, with increasing the value of the non-Darcy parameter  $\gamma$  ( $\gamma = 0.1, 2$ ), there is a marked decrease in the velocity components  $u^*$  and  $w^*$ , i.e. the flow is accelerated strongly with the decrease in the non-Darcy parameter, owing to a simultaneous increase in the inertial force in equation (12)  $-\gamma u^{*2}$  and in equation (13)  $-\gamma w^{*2}$ .



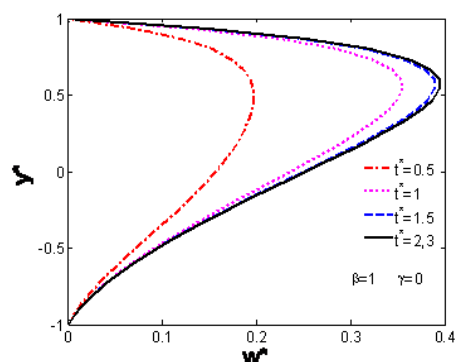
(a)



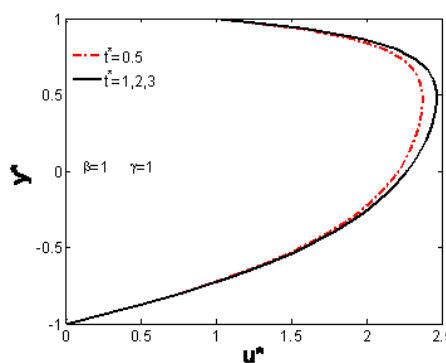
(a)



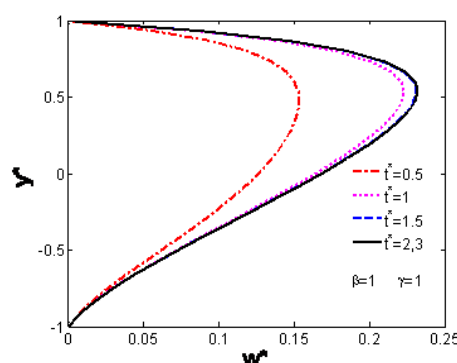
(b)



(b)



(c)



(c)

**Fig. 3.** Time variation of the profile of  $u^*$  for various values of  $\gamma$  and  $\beta$ . (a)  $\beta=0$  and  $\gamma=0$ ; (b)  $\beta=1$  and  $\gamma=0$ ; (c)  $\beta=1$  and  $\gamma=1$ .

Figure 7-a shows that, with an increase of the Hartmann number  $Ha$ , the magnitude of the velocity component  $u^*$  is reduced because the hydromagnetic drag force in equation (12),  $\frac{-Ha^2}{R_2(1+m^2)}(u^* + mw^*)$  is proportional to the square of  $Ha$  and remains with a negative sign. Therefore, by increasing the Hartmann number  $Ha$  creates a larger negative force. On the other hand, figure 7-b indicates the increase in the velocity component  $w^*$  with a rise in the Hartmann number because the hydromagnetic force in (13)  $\left(\frac{-Ha^2}{R_2(1+m^2)}(w^* - mu^*)\right)$  has two components, positive

**Fig. 4.** Time variation of the profile of  $w^*$  for various values of  $\gamma$  and  $\beta$ . (a)  $\beta=0$  and  $\gamma=0$ ; (b)  $\beta=1$  and  $\gamma=0$ ; (c)  $\beta=1$  and  $\gamma=1$ .

$u^* \left(\frac{Ha^2}{R_2(1+m^2)} mu^*\right)$  and negative  $w^* \left(\frac{-Ha^2}{R_2(1+m^2)} w^*\right)$ , so the collective effect is markedly boosted with a rise in the Hartmann number. The temperature  $T^*$  is also increasing substantially with increasing the Hartmann number  $Ha$  indicating that the regime is cooled by stronger magnetic fields.

Figure 8 presents the influence of the non-Darcy parameter  $\gamma$  on the velocity components  $u^*$ ,  $w^*$  and the temperature distribution  $T^*$  with time  $t^*$  for the Hall parameter  $m$  at  $\beta = 1, S=1, Ha=3, R_e=10, P_r=1, E_c=0.2, \tau_D=0.1$ . It is clear that by increasing the non-Darcy parameter  $\gamma$  (inertial effect),  $u^*$ ,  $w^*$  and  $T^*$  decrease. Figure 8-a, indicates that the velocity of component  $u^*$  increases by increasing the Hall

parameter  $m$  which can be attributed to the fact that an increment in  $m$  decreases the resistive force. Figure 8-b shows that the velocity component  $w^*$  decreases with the increasing Hall parameter  $m$  which can be attributed to the fact that an increment in  $m$  increases the resistive force. Figure 8-c shows that  $T^*$  decreases with the increasing Hall parameter  $m$  for all values of time as a result of an increase in the Hall current parameter  $m$ , will decrease the contribution from the Joule dissipation term.

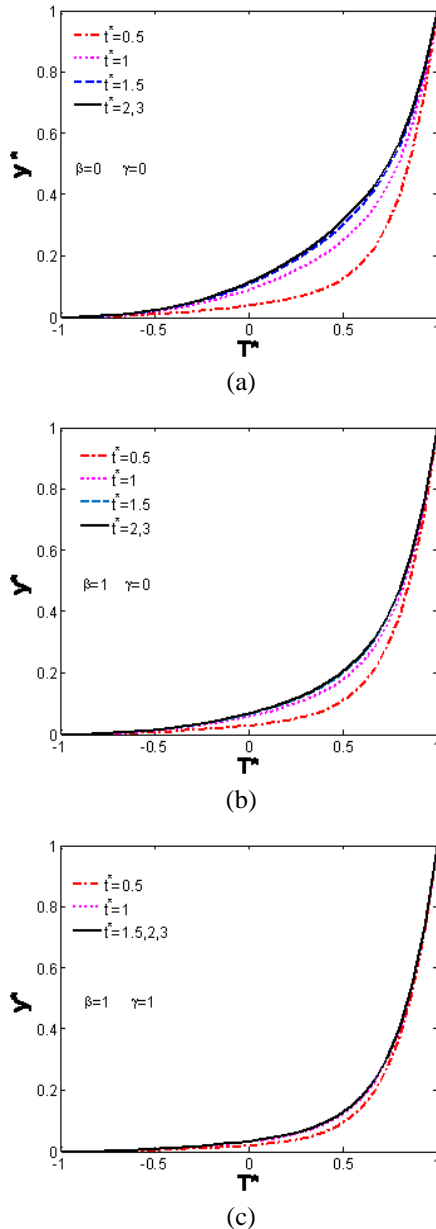


**Fig. 5.** Time variation of the profile of  $T^*$  for various values of  $\gamma$  and  $\beta$ . (a)  $\beta=0$  and  $\gamma=0$ ; (b)  $\beta=1$  and  $\gamma=0$ ; (c)  $\beta=1$  and  $\gamma=1$ .

### CONCLUSIONS

The unsteady couette flow of non-Newtonian Bingham fluid between two parallel porous plates containing a non-Darcy porous medium has been

studied with heat transfer and the Hall effect in the presence of uniform suction and injection.

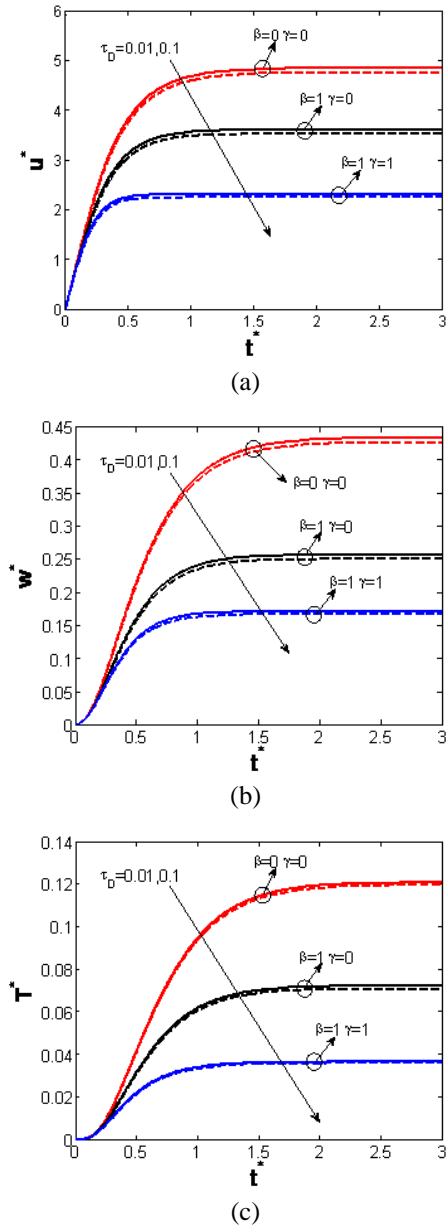


**Fig. 6.**  $u^*$ ,  $w^*$ , and  $T^*$  versus  $t^*$  at channel center ( $y^* = 0$ ) for various values of  $\gamma$  and  $\beta$  and various values  $\tau_D$ . (a)  $u^*$ ; (b)  $w^*$ ; (c)  $T^*$  Profile.

The governing momentum and energy equations are solved numerically using the finite difference approximations. Through the numerical results the following can be concluded:

- The effects of the resistive porosity force and the inertial force (Darcy and non-Darcy parameters  $\beta$  and  $\gamma$ ) on the velocity components and temperature distribution have been investigated. The increase in  $\beta$  and  $\gamma$  will decrease the velocity and temperature.
- The yield stress  $\tau_D$  has a remarkable effect on the velocity components and temperature distribution. An increase occurred in  $\tau_D$

accompanied by a decrease in the velocity and temperature as well as their steady state time.

- The effects of the Hartmann number  $Ha$  on the velocity components and temperature distribution have been studied. By increasing  $Ha$  the x-component of the velocity will decrease, while the z-component of the velocity and temperature will increase.
- The effect of the Hall parameter  $m$  on the velocity components and temperature distributions has been assessed. The Hall parameter  $m$  is directly proportional to the x-component of the velocity while it is inversely proportional to the z-component of the velocity and temperature distribution.

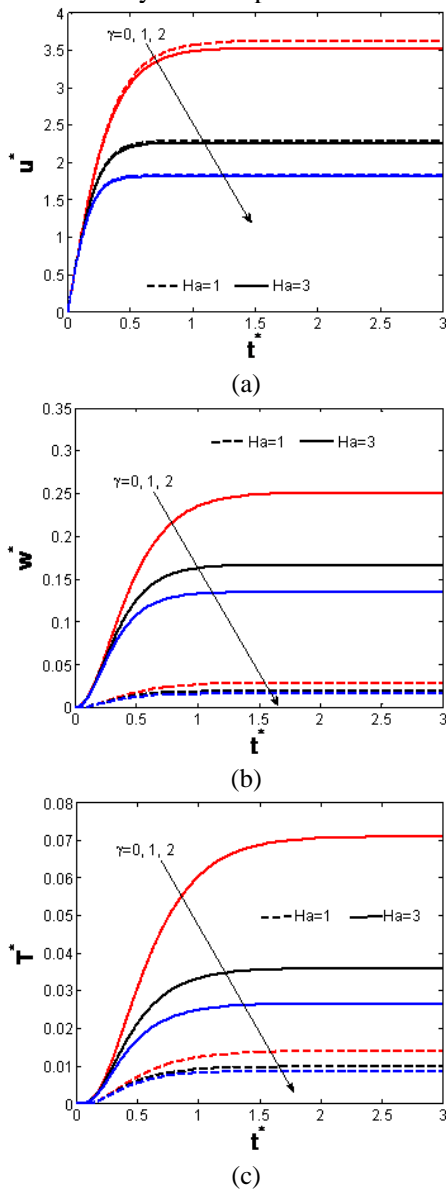


**Fig. 7.** Effect of the non-Darcian parameter  $\gamma$  on  $u^*$ ,  $w^*$ , and  $T^*$  profiles at the channel center for low and high Hartmann number  $Ha$ . (a)  $u^*$ ; (b)  $w^*$ ; (c)  $T^*$  Profile

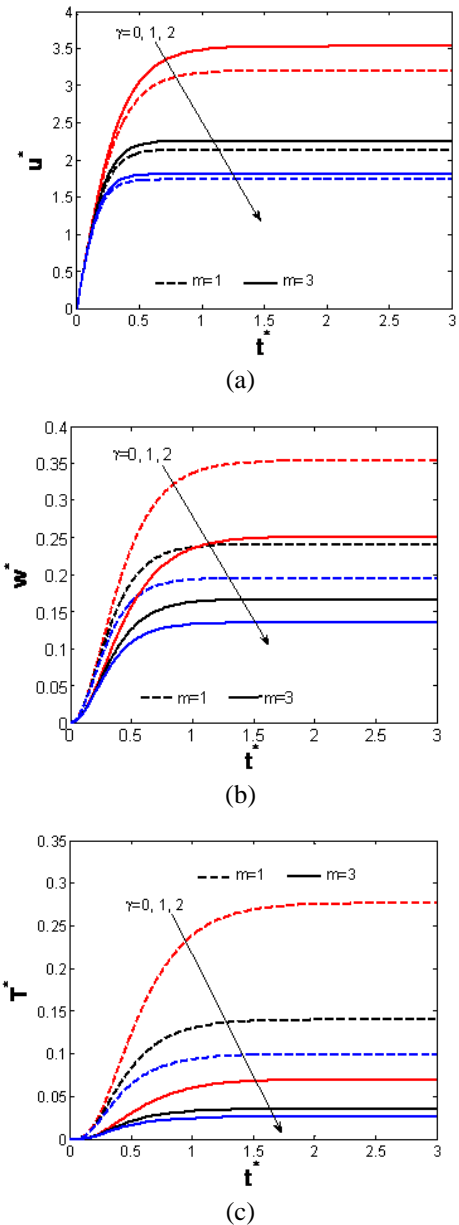


**Fig. 8.** Effect of the non-Darcian parameter  $\gamma$  on  $u^*$ ,  $w^*$ , and  $T^*$  profiles at channel center for various values of the Hall parameter  $m$ . (a)  $u^*$ ; (b)  $w^*$ ; (c)  $T^*$  Profile

## REFERENCES

1. B. Devika, P. V. Narayana, S. Venkataramana, *International Journal of Engineering Science Invention*, **2**, 26(2013).
2. H. A. Attia, W. Abd El-Meged, W. Abbas, M. A. M. Abdeen, *International Journal of Civil Engineering*, **12**, 277 (2014).
3. A. Bharali and A. K. Borkakati, *Applied Scientific Research*, **39**, 155 (1982).
4. H. A. Attia, N. A. Kotb, *Actamechanica*, **117**, 215 (1996).
5. Z. Joaquín, E. Pablo, G. Enrique, L. M. José, A. B. Osman, *Int. Comm. Heat and Mass Trans.*, **37**, 1432 (2010).
6. H. A. Attia, W. Abbas, M. A. M. Abdeen, A. E.-D. Abdin, *Blug. Chem. Commun.*, **46**, 535 (2014).

7. E. Sweet, K. Vajravelu, R. A. Van Gorder, I. Pop, *Commun Nonlinear Sci Numer Simulat*, **16**, 266 (2011).
8. H. A. Attia, W. Abbas, M. A. M. Abdeen, M. S. Emam, *European Journal of Environmental and Civil Engineering*, **18**, 241 (2014).
9. H. A. Attia, W. Abbas, M. A. M. Abdeen, A. A. M. Said, *Sadhana*, **40**(1), 183 (2015).
10. H. A. Attia, W. Abbas, A. El-Din Abdin, M. A. M. Abdeen, *High Temperature*, **53**, 891 (2015).
11. C-C. Liu, C-Y. Lo, *International Communications in Heat and Mass Transfer*, **39**, 1354 (2012).
12. H. A. Attia, W. Abbas, M. A. M. Abdeen, *Journal of the Brazilian Society of Mechanical Sciences and Engineering*, in press, Available online 11 February, 2015.
13. I. C. Walton, S. H. Bittleston, *J. Fluid Mech.*, **222**, 39 (1991).
14. S. Yang, K. Zhu, *J. Non-Newtonian Fluid Mech.*, **138**, 73 (2006).
15. D. A. S. Rees, A. P. Bassom, *International Journal of Heat and Mass Transfer*, **82**, 460 (2015).
16. Z. Zeng, R. Grigg, *Transport In Porous Media*, **63**, 57 (2006).
17. O.A. Bég, J. Zueco, H.S. Takhar, *Communications in Nonlinear Science and Numerical Simulation*, **14**, 1082 (2009).
18. A. Matthew, M. Sc. Thesis, Texas Tech University, Lubbock, Texas, United States, 2006.
19. Y. J. Kim, *International Journal of Engineering sciences*, **38**, 833 (2000).
20. D. Pal, B. Talukdar, *International Journal of Appl. Math. and Mech.*, **7**, 58 (2011).
21. S. S. Das, M. Maity, J. K. Das, *International Journal of Energy and Environment*, **1**, 109 (2012).
22. A.A. Moniem, W. S. Hassanin, *Applied Mathematics*, **4**, 694 (2013).
23. A. Afify, *Transport in Porous Media*, **66**, 391 (2007).
24. O. A. Bég, J. Zueco, R. Bhargava, H. S. Takhar, *International Journal of Thermal Sciences*, **48**, 913 (2009).
25. H. A. Attia, M. E. Sayed-Ahmed, *Applied Mathematical Modelling*, **28**, 1027 (2004).
26. Abdeen M. A. M., Attia H A, Abbas W, Abd El-Meged W, *Indian Journal of Physics*, **87**, 767 (2013).
27. T. C. Papanastasiou, *J. Rheol.*, **31**, 385 (1987).
28. E. Mitsoulis, *The British Society of Rheology*, **135**, 135 (2007).

## ОТКЛОНЕНИЯ ОТ ЗАКОНА НА ДАРСИ ПРИ НЕНЬУТОНОВИ БИНГАМОВИ ФЛУИДА С ТОПЛОПРЕНАСЯНЕ МЕЖДУ ДВЕ УСПОРЕДНИ ПЛОСКОСТИ

У. Аббас<sup>1</sup>, Х. Али Атия<sup>2</sup>, М.А.М. Абдийн<sup>3</sup>

<sup>1</sup>Департамент по основни и приложни науки, Колеж по инженерство и технологии, Арабска академия за наука, технологии и морски транспорт, Кайро, Египет

<sup>2</sup>Департамент по инженерство, математика и физика, Инженерен факултет, Университет Ел-Фаюм, Ел-Фаюм - 63514, Египет

<sup>3</sup>Департамент по инженерство, математика и физика, Инженерен факултет, Университет в Кайро, Гиза-12211, Египет

Постъпила на 13 август 2015 г.; приета на 15 септември 2015 г.

(Резюме)

Моделът на не-Дарси'ев поток за Бингамови флуиди има широк кръг от приложения в енергийните системи и обработката на магнитни материали. Тази работа изследва ефекта на не-Дарси'ево течение върху разпределението на скоростите и температурата за не-нютонув Бингамов флуид между две безкрайни успоредни поръзни плоскости с топлопренасяне отчитайки ефекта на Хол. По главното надлъжно направление се прилага постоянен градиент на налягането, перпендикулярно на плоскостите се прилага постоянно външно магнитно поле, както и равномерно всмукване и впръскване в същото направление. Изведения са и числено са решени безизмерните уравнения на движението и енергията, отчитащи механичната и вискозната дисипация на енергията. Изследвани са ефектите на поръзността на средата, на Хартман и Хол, на скоростта и разпределението на температурата за число на Рейнолдс равно на 10 (за  $Re_e \geq 10$  не-Дарси'евият модел е достатъчен). Намерено е, че поръзността и инерционните ефекти имат забележимо влияние върху разпределението на скоростите. Освен това, нарастването на не-Дарси'евия параметър понижава температурата при всяка поръзност.

## Convective heat transfer of viscous fluid over a stretching sheet embedded in a thermally stratified medium

T. Mahmood<sup>1</sup>, J. Ahmed<sup>2\*</sup>, A. Shahzad<sup>2</sup>, R. Ali<sup>3</sup>, Z. Iqbal<sup>1</sup>

<sup>1</sup>Department of Mathematics, Faculty of Sciences, HITEC University, Taxila Cantt, Pakistan

<sup>2</sup>Department of Basic Sciences, University of Engineering and Technology, Taxila 47050, Pakistan

<sup>3</sup>University of Central Asia, 722920, Naryn, Kyrgyzstan

Received August 17, 2015; Accepted September 7, 2015

In this article we have investigated the heat transfer of an electrically conducting viscous fluid over a porous stretching sheet in a thermally stratified medium. The governing non-linear partial differential equations are reduced to ordinary differential equations using appropriate similarity transformations. The resulting ordinary differential equations are then solved in the form of a confluent hyper-geometric function for an exact solution. The developed exact solutions of the velocity and temperature fields are graphically sketched and examined for various values of pertinent parameters including the Prandtl number, stratification parameter, suction/injection parameter and the magnetic parameter. The skin friction coefficient and the local Nusselt number are tabulated and thoroughly discussed.

**Keywords:** Convective heat transfer; Suction/Injection; Exact solution

### INTRODUCTION

The study of the boundary layer flow on a stretching sheet has been done by a large number of researchers during the last few decades with the aid of significant applications of industrial and technological processes. To name a few; these applications include manufacturing of glass fiber, drawing plastic films and wires, the condensation process, crystal growing polymer extrusion and others. These processes are highly dependent on the subject of heat transfer of stretching surfaces. In his ground breaking work, Sakiadis [1] presented the studies on the boundary flow layer over continuously moving surfaces and obtained the numerical solution. Natarja et al. [2] obtained the closed form solution for the boundary layer flow of walters' B-type fluid, over a stretching sheet for the heat transfer and obtained the coefficients of skin friction. Meanwhile, Crane [3] provided the closed form solution for the boundary layer flow of a stretching sheet. The heat transfer in hydrodynamic flow of viscoelastic fluid over a stretching sheet was analyzed by Char [4]. Liao [5] studied the analytic solution of unsteady boundary layer flows caused by an impulsively stretching plate. Khan and Sanjayanand [6] presented the analytic solution for the heat transfer of visco-elastic boundary layer flow with viscous dissipation. Devi and Ganga [7] bring into account the non-linear MHD flow in a porous medium over a stretching porous surface including the effects of viscous dissipation. Abel et al. [8] have

investigated the heat transfer over a stretching surface for second grade fluid through porous medium with viscous dissipation and a non-uniform heat source/sink. Cortell [9] investigated the flow and heat transfer through a porous medium over a stretching surface with heat generation/absorption and suction/blowing. Hayat et al. [10] provided the analytic solution for the axi-symmetric flow and heat transfer of second grade fluid past over a stretching sheet. Xu and Liao [11] considered the unsteady MHD flows of non-Newtonian fluids over impulsively a stretching plate. In another related article Cortell [12] studied MHD flow heat transfer of visco-elastic fluid by considering the effects of viscous dissipation.

Thermally stratified flows are of significant interest because of their importance in thermo-hydraulics, volcanic flows, geothermal systems and also in industrial thermal processes. Stratification of a medium arises due to temperature variation which results in density variation of the medium. Stratification may also arise due to the presence of different fluids so that a stable situation arises when the lighter fluid lies over the denser one. Keeping in view these applications of stratified mediums several studies have been carried out. Hayat et al. [13] studied the thermally stratified flow of third grade fluid over a stretching sheet including radiation. Kandasamy and Khamis [14] discussed the effect of thermal stratification on heat transfer across a porous vertical stretching sheet. Ishak et al. [15] studied the mixed convection flow to a vertical plate in a thermally stratified medium. Mukhopadhyay and Ishak [16] examined mixed convection flow along a stretching cylinder in a

\* To whom all correspondence should be sent:  
E-mail: j.ahmedqau@gmail.com

thermally stratified medium. MHD boundary layer flow and heat transfer over an exponentially stretching sheet in a thermally stratified medium have also been investigated by the same author Mukhopadhyay [17].

It is clear that the suction/injection of fluid can play a significant role in changing the flow field. Roughly speaking, suction tends to enhance the skin friction, whereas injection acts in the opposite manner. These processes have great importance in many engineering activities like the design of thrust bearing and radial diffusers, thermal oil recovery and many more.

In manufacturing processes the properties of the final product highly depend on the rate of cooling. In this scenario, an electrically conducting fluid proves to be beneficial for industrial application. The applied magnetic field may play a key role in heat transfer and momentum of the boundary layer flow. Keeping all these facts in view, recently Chen [18] examined the analytic solution of MHD flow and heat transfer for two types of visco-elastic fluid over a stretching sheet, also bring under consideration the energy dissipation, internal heat source and thermal radiation. Liu [19] presented an analytic solution for heat transfer of second grade MHD flow subject to the transverse magnetic field across a stretching sheet with power law surface heat flux. Shahzad and Ali [20, 21] contributed a couple of articles on an approximate solution for MHD flow of a non-Newtonian Power law fluid over a vertical stretching sheet with convective boundary conditions and radiation effects, respectively. Kar et al. [22] studied the heat and mass transfer effects on dissipative and radiative visco-elastic MHD flow over a stretching porous sheet.

The exact solution for the flow problem with heat transfer is highly demanding in many research areas. The exact solutions are handy to compare with the numerical counter parts in the study of several flow problems. The purpose of the present study is, to give the exact solution of fluid flow and heat transfer of an electrically conducting viscous fluid over a stretching sheet in a thermally stratified medium with suction/injection. We derived a closed form analytic solution in the form of a confluent hyper-geometric function for non-dimensional velocity and temperature profiles. The skin friction coefficient and heat flux at the wall with a constant wall temperature are brought into account. The influence of different non-dimensional parameters like the Prandtl number, magnetic number, stratification parameter and the surface suction/injection are graphically discussed with respect to velocity and temperature profiles.

## MATHEMATICAL FORMULATION

We consider the steady two-dimensional boundary layer flow of an incompressible electrically conducting viscous fluid, which is passed over a stretching sheet in the presence of a magnetic field coinciding with the plane  $y = 0$ . The flow is generated due to linearly stretching of sheet by applying two equal and opposite forces along the  $x$ -axis keeping the origin fixed as observed in figure (1). A variable magnetic field  $B_o$  is applied normal to the sheet. It is assumed that the surface temperature of the sheet is  $T_w(x) = T_0 + a(\frac{x}{l})^2$  and is embedded in a thermally stratified medium of a variable ambient fluid temperatures  $T_\infty = T_0 + b(\frac{x}{l})^2$  where  $T_w > T_\infty$ ,  $T_0$  is the reference temperature,  $a > 0$ ,  $b \geq 0$  are constants.

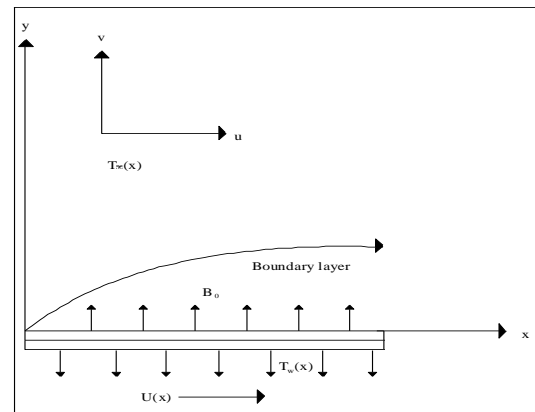


Fig. 1. Sketch of the physical problem.

Under these assumptions the steady state boundary layer equations governing the flow and heat transfer of viscous fluid are

$$\frac{\partial u}{\partial x} + \frac{\partial v}{\partial y} = 0, \quad (1)$$

$$u \frac{\partial u}{\partial x} + v \frac{\partial u}{\partial y} = \nu \frac{\partial^2 u}{\partial y^2} - \frac{\sigma B_o^2 u}{\rho}, \quad (2)$$

$$u \frac{\partial T}{\partial x} + v \frac{\partial T}{\partial y} = \frac{k}{\rho c_p} \frac{\partial^2 T}{\partial y^2}, \quad (3)$$

where  $x$  and  $y$  are the directions along and perpendicular to the sheet respectively, with  $u$  and  $v$  the velocity components along the  $x$  and  $y$  directions, respectively,  $T$  the temperature of the fluid,  $\nu$  the kinematic viscosity,  $\rho$  the density of the fluid,  $\sigma$  the electrical conductivity,  $B_o$  the applied magnetic field and  $c_p$  is the specific heat at constant pressure. The corresponding boundary conditions for the momentum equation are

$$u = U = Ex \quad v = -v_0 \quad \text{at } y = 0, \quad (4)$$

$$u \rightarrow 0 \text{ as } y \rightarrow \infty,$$

where  $E > 0$  is called stretching rate,  $v_0 > 0$  is the velocity of suction and  $v_0 < 0$  is the velocity of injection. To facilitate the analysis we introduce the following transformations:

$$u = Uf'(\eta), \quad v = -\sqrt{Ev}f(\eta), \quad \eta = \sqrt{\frac{E}{\nu}}y, \quad (5)$$

clearly  $u$  and  $v$  satisfy Eq. (1), here  $f(\eta)$  is the dimensionless stream function,  $\eta$  is the similarity variable and denote the differentiation with respect to  $\eta$ . Making use of Eq. (5) in Eq. (2) the following third order non-linear differential equation is obtained:

$$f''' - f'^2 + ff'' - M_n f' = 0, \quad (6)$$

where  $M_n = \frac{\sigma B_0^2}{\rho E}$ , is the Magnetic parameter.

Similarly the boundary conditions in Eq. (4) can be written as:

$$f'(\eta) = 1, \quad f(\eta) = S \quad \text{at } \eta = 0, \quad (7)$$

$$f'(\eta) \rightarrow 0 \text{ as } \eta \rightarrow \infty,$$

where  $S = \frac{v_0}{\sqrt{Ev}} > 0$  (or  $< 0$ ) is the suction (or injection) parameter.

Lawrence and Rao [23] presented a general method and obtained an all non-unique solution of the modified Eq. (6). Recently Taha et al. [24] have discussed a unified compatibility method for the exact solutions of non-linear flow models of Newtonian and non-Newtonian fluids, we consider the following solution:

$$f(\eta) = S + \frac{1}{\beta}(1 - \exp[-\beta\eta]), \quad (8)$$

where  $\beta = \frac{S + \sqrt{S^2 + 4(1 + M_n)}}{2}$  with  $S^2 + 4(1 + M_n) \geq 0$ .

The physical quantities of interest are the skin friction coefficient  $C_f$  and the local Nusselt number  $N_u$  defined as:

$$C_f = \frac{\tau_w}{\frac{\rho}{2}U^2}, \quad N_u = \frac{xq_w}{k(T_w - T_0)}, \quad (9)$$

where  $\tau_w = \mu\left(\frac{\partial u}{\partial y}\right)_{y=0}$  is the wall shear stress and  $q_w = -k\left(\frac{\partial T}{\partial y}\right)_{y=0}$  the wall heat flux. In terms of dimensionless variables defined in Eq. (5), we can write:

$$\text{Re}^{1/2} C_f = f''(0), \quad \text{Re}^{-1/2} N_u = -\theta'(0), \quad (10)$$

where  $\text{Re} = \frac{xU}{\nu}$  is the local Reynolds number.

## SOLUTION OF THE HEAT TRANSFER EQUATION

In order to solve the governing heat transport Eq. (3), we consider the boundary with a prescribed surface temperature (PST). In this case we employ the following surface boundary conditions on temperature:

$$T = T_w(x) = T_0 + a\left(\frac{x}{l}\right)^2 \quad \text{at } y = 0, \quad (11)$$

$$T = T_\infty(x) = T_0 + b\left(\frac{x}{l}\right)^2 \quad \text{as } y \rightarrow \infty,$$

where  $T_w$  and  $T_\infty$  are the temperatures at the wall and far away from the wall, respectively and  $T_0$  is the reference temperature. In order to obtain the similarity solution we define the non-dimensional temperature variables as:

$$\theta(\eta) = \frac{T - T_0}{T_w - T_0}. \quad (12)$$

Making use of the transformations (5) and (12), we obtain the following non-dimensional form of temperature Eq. (3) as:

$$\theta'' + \text{Pr}(f\theta' - 2f'\theta) = 2St \text{Pr} f', \quad (13)$$

where in the non-dimensional parameters  $\text{Pr} = \frac{\rho C_p \nu}{k}$  the Prandtl number and  $St = \frac{b}{a}$  is the stratification parameter. We note that  $St > 0$  for a stably stratified environment and  $St = 0$  corresponds to an unstratified environment.

The non-dimensional form of the boundary conditions in Eq. (11) is:

$$\theta = 1 - St \quad \text{at } \eta = 0, \quad (14)$$

$$\theta \rightarrow 0 \quad \text{as } \eta \rightarrow \infty.$$

Following the introduction of a new variable  $\xi = -\frac{\text{Pr}}{\beta^2} \exp(-\beta\eta)$ , Eq. (13) becomes:

$$\xi \frac{d^2\theta}{d\xi^2} + (1 - \text{Pr}^* - \xi) \frac{d\theta}{d\xi} + 2\theta = -2St, \quad (15)$$

and the boundary conditions presented in Eq. (14) reduce to:

$$\theta(\xi) = 1 - St \quad \text{at } \xi = -\text{Pr}^*, \quad (16)$$

$$\theta(\xi) = 0 \quad \text{at } \xi = 0,$$

where  $\text{Pr}^* = \frac{\text{Pr}}{\beta^2}$  is the modified Prandtl number.

Equations (15) and (16) constitute a non-homogenous boundary value problem. Let us decompose the temperature  $\theta(\xi)$  into two parts:

$$\theta(\xi) = \theta_c(\xi) + \theta_p(\xi), \quad (17)$$



where  $\theta_c(\xi)$  stands for the complementary solution and  $\theta_p(\xi)$  is a particular solution. The closed form particular solution is given by:

$$\theta_p(\xi) = -St. \tag{18}$$

The complementary factor  $\theta_c(\xi)$  can be written in the form of a confluent hyper-geometric function [25] as:

$$\theta_c(\xi) = AM[-2, 1 - Pr^*, \xi] + B\xi^{Pr^*} M[-2 + Pr^*, 1 + Pr^*, \xi] \tag{19}$$

where  $M$  is the Kummer's function defined as:

$$M(a_o, b_o, z) = 1 + \sum_{n=1}^{\infty} \frac{(a_o)_n z^n}{(b_o)_n n!}, \tag{20}$$

$$(a_o)_n = a_o(a_o + 1)(a_o + 2) \cdots (a_o + n - 1),$$

$$(b_o)_n = b_o(b_o + 1)(b_o + 2) \cdots (b_o + n - 1).$$

The solution of Eq. (15), subject to the boundary conditions of Eq. (16) is determined to be:

$$\theta(\xi) = StM[-2, 1 - Pr^*, \xi] + \left\{ \frac{1 - StM[-2, 1 - Pr^*, -Pr^*]}{(-Pr^*)^{Pr^*} M[-2 + Pr^*, 1 + Pr^*, -Pr^*]} \right\} \xi^{Pr^*} M[-2 + Pr^*, 1 + Pr^*, \xi] - St. \tag{21}$$

The temperature profile in term of  $\eta$  is given by

$$\theta(\eta) = StM[-2, 1 - Pr^*, -Pr^* \exp(-\beta\eta)] + \left\{ \frac{1 - StM[-2, 1 - Pr^*, -Pr^*]}{M[-2 + Pr^*, 1 + Pr^*, -Pr^*]} \right\} \times \exp(-\beta Pr^* \eta) M[-2 + Pr^*, 1 + Pr^*, -Pr^* \exp(-\beta\eta)] - St. \tag{22}$$

The derivative of the Kummer's function  $M(a_o, b_o, z)$  with respect to  $z$  is given by:

$$\frac{d^n}{dz^n} M[a_o, b_o, z] = \frac{(a_o)_n}{(b_o)_n} M[a_o + n, b_o + n, z].$$

The dimensionless wall temperature gradient is obtained from Eq. (22)

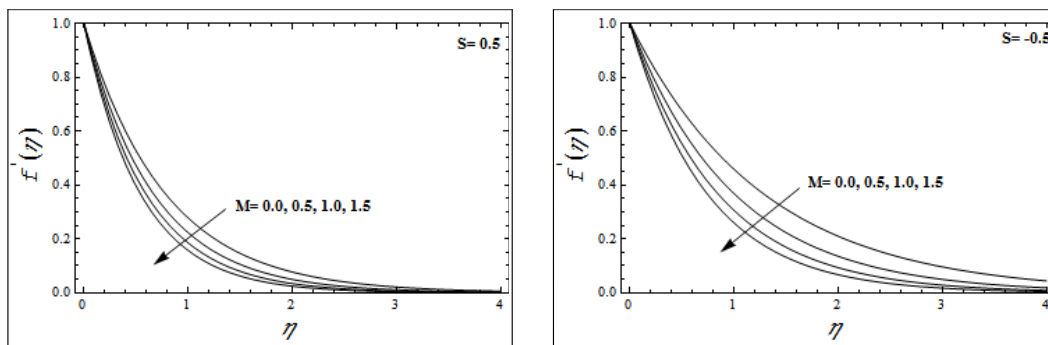
$$\theta'(0) = \frac{-2St\beta Pr^*}{1 - Pr^*} M[-1, 2 - Pr^*, -Pr^*] - \left\{ \frac{1 - StM[-2, 1 - Pr^*, -Pr^*]}{M[-2 + Pr^*, 1 + Pr^*, -Pr^*]} \right\} \times \left\{ -\frac{\beta Pr^* (-2 + Pr^*)}{1 + Pr^*} M[-1 + Pr^*, 2 + Pr^*, -Pr^*] + \beta Pr^* M[-2 + Pr^*, 1 + Pr^*, -Pr^*] \right\}. \tag{23}$$

### GRAPHICAL RESULTS AND DISCUSSION

Momentum and heat transfer in a boundary layer flow of a viscous fluid over a stretching sheet in a thermally stratified medium have been discussed in

this article. The governing non-linear partial differential equations have been reduced to a set of non-linear ordinary differential equations. The exact solutions are developed for the reduced problem in terms of the Kummer's function. In order to have a clear insight of a physical problem, the influence of various pertinent parameters on velocity and temperature profiles are shown graphically through figures (2–9). Figures (2a, 2b) depict the influence of the magnetic parameter  $M$  on the velocity profile  $f'(\eta)$  for both suction/injection  $S$  cases. It is observed that the velocity profile  $f'(\eta)$  decreases with an increase in the values of the magnetic parameter  $M$  for both suction/injection parameters  $S$ . The boundary layer thickness also decreases here. The variation of suction/injection parameter  $S$  on the velocity profile  $f'(\eta)$  is shown in figures (3a, 3b). The velocity profile  $f'(\eta)$  decreases in the case of the suction parameter ( $S > 0$ ), while the opposite behavior is noticed in case of injection ( $S < 0$ ). Figures (4a, 4b) are plotted to see the effects of the Prandtl number  $Pr$  on the temperature profile  $\theta(\eta)$  in the presence of suction/injection parameter  $S$ . It is obvious from these figures that an increase in the Prandtl number  $Pr$  results in a decrease in the temperature profile  $\theta(\eta)$  for both cases suction ( $S > 0$ ) and injection ( $S < 0$ ), however this decrease in the temperature profile  $\theta(\eta)$  is more prominent in the case of suction ( $S > 0$ ). The influence of the suction /injection parameter  $S$  on the temperature profile  $\theta(\eta)$  is displayed in figures (5a, 5b). These figures show that by increasing the suction parameter ( $S > 0$ ) the temperature profile  $\theta(\eta)$  increases while an adverse behavior is observed in the case of injection ( $S < 0$ ).

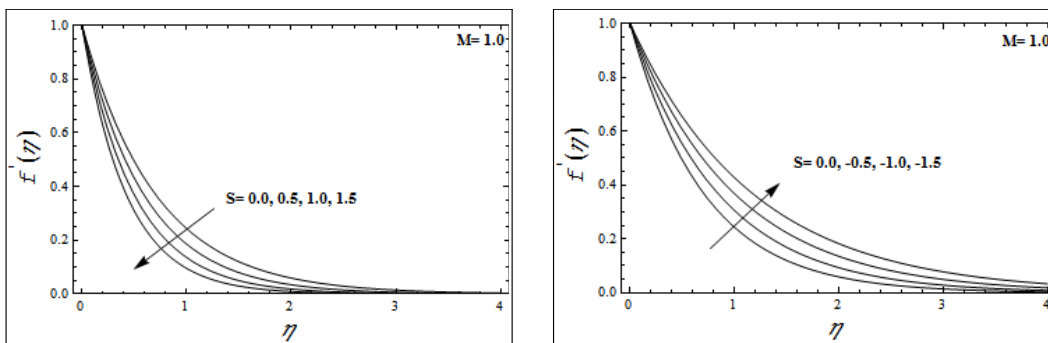
In order to see the effects of the stratified medium  $St$  on the temperature profile  $\theta(\eta)$  in the presence of the suction/injection parameter  $S$  figures (6a, 6b) are plotted. These figures illustrate that the temperature profile  $\theta(\eta)$  decreases as the stratification parameter  $St$  increases for both suction/injection parameters  $S$ . As the increase in the stratification medium  $St$  implies an increase in ambient fluid temperature or a decrease in the surface temperature, which results in a decrease of the thermal boundary layer thickness.



2a

2b

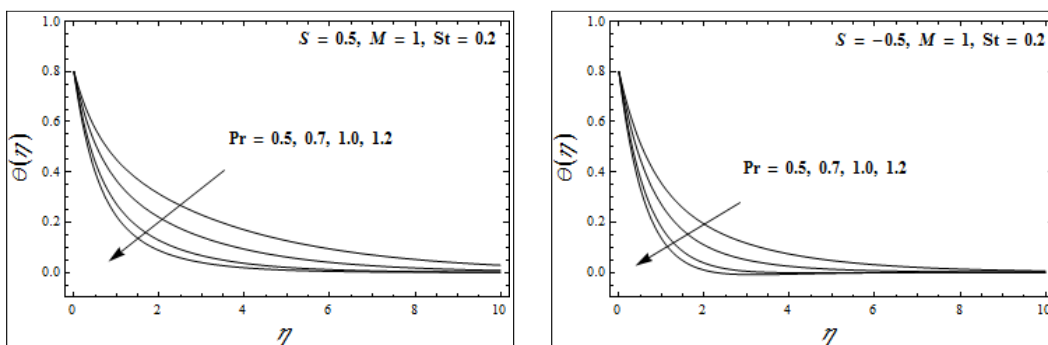
**Fig.2.** Variation of velocity profile  $f'(\eta)$  with  $\eta$  for several values of magnetic parameter  $M$  in the presence of the suction/injection parameter  $S$ .



3a

3b

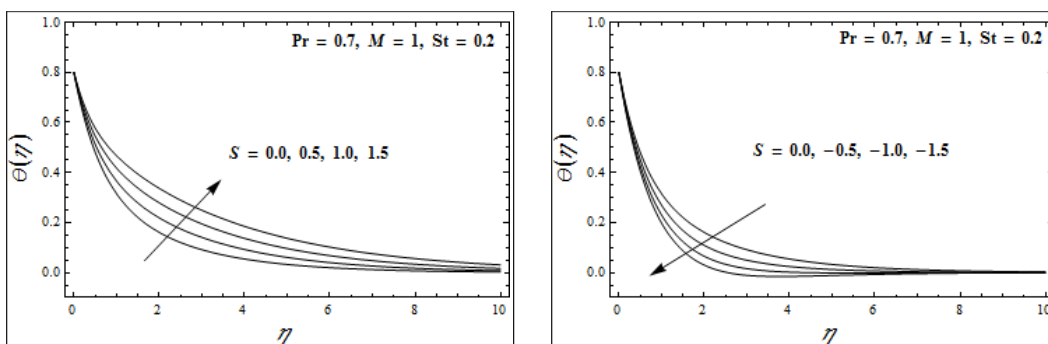
**Fig. 3.** Variation of the velocity profile  $f'(\eta)$  with  $\eta$  for several values of the suction/injection parameter  $S$ .



4a

4b

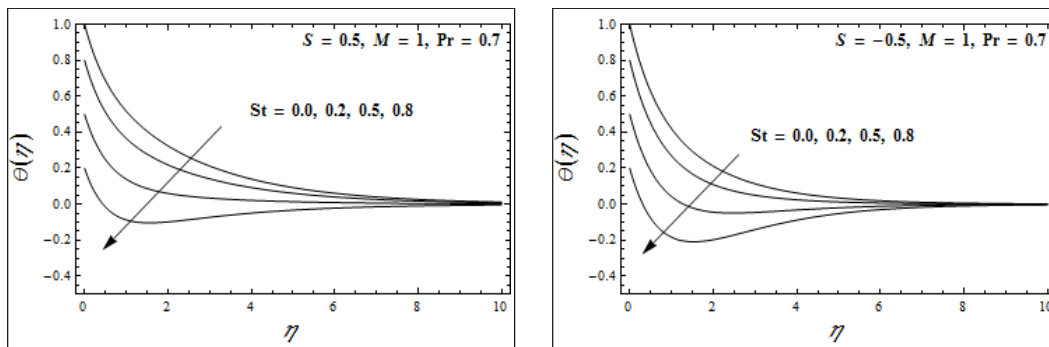
**Fig. 4.** Variation of the temperature profile  $\theta(\eta)$  with  $\eta$  for several values of the Prandtl number  $Pr$ .



5a

5b

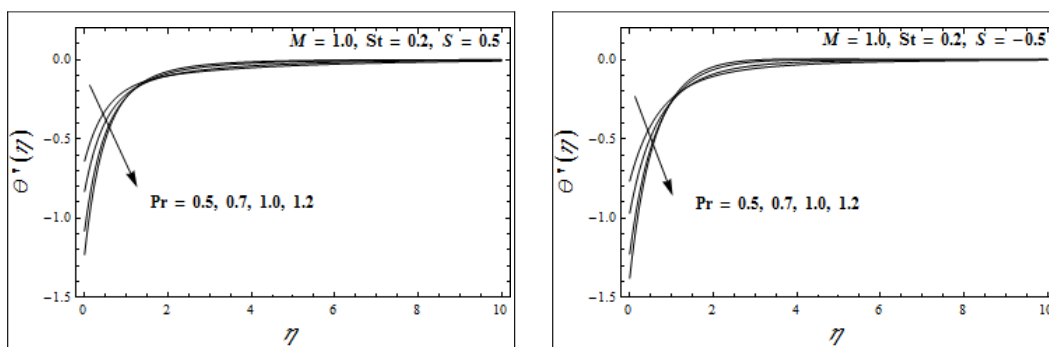
**Fig. 5.** Variation of the temperature profile  $\theta(\eta)$  with  $\eta$  for several values of the suction parameter  $S$ .



6a

6b

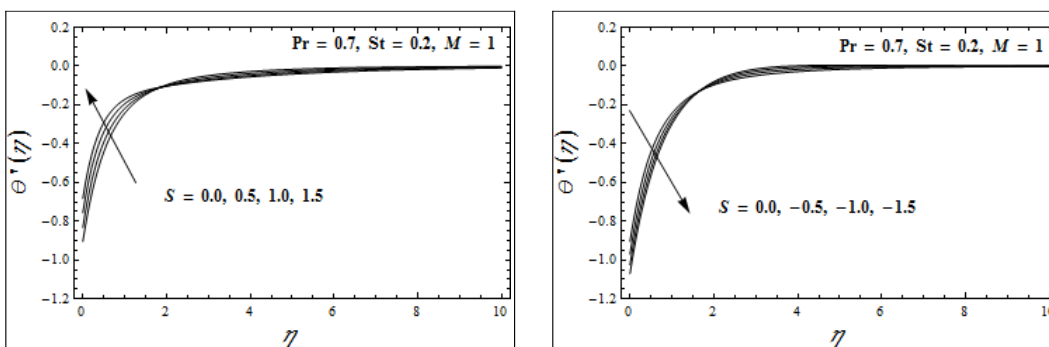
Fig. 6. Variation of the temperature profile  $\theta(\eta)$  with  $\eta$  for several values of the thermal stratification parameter  $St$  in the presence of suction/injection  $S$ .



7a

7b

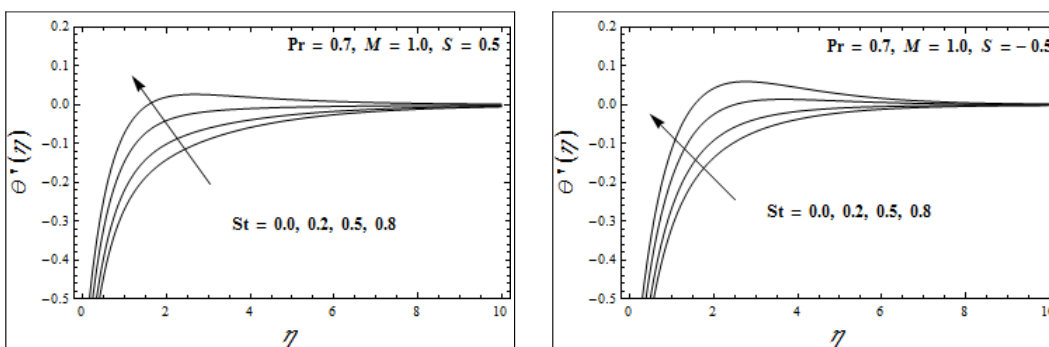
Fig. 7. Variation of the temperature gradient  $\theta'(\eta)$  with  $\eta$  for several values of the Prandtl number  $Pr$ .



8a

8b

Fig. 8. Variation of the temperature gradient  $\theta'(\eta)$  with  $\eta$  for several values of the suction/injection parameter  $S$ .



9a

9b

Fig. 9. Variation of the temperature gradient  $\theta'(\eta)$  with  $\eta$  for several values of the thermal stratification parameter  $St$ .

The influence of the Prandtl number  $Pr$  on the temperature gradient  $\theta'(\eta)$  in the presence of suction/injection  $S$  is displayed in figures (7a,7b).

From these figures it is observed that initially an increase in the Prandtl number  $Pr$  results in a decrease in the temperature gradient  $\theta'(\eta)$ . It is also observed that the temperature gradient  $\theta'(\eta)$  starts increasing after a certain distance  $\eta$  from the surface. Moreover this effect is more prominent in the case of injection ( $S < 0$ ). From figures (8a,8b) it can be seen that by increasing the suction parameter ( $S > 0$ ) the temperature gradient  $\theta'(\eta)$  increases up to a certain distance from the surface and then decreases. Quite the opposite behavior is observed in the case of injection ( $S < 0$ ). To analyze the effect of the stratification parameter  $St$  on the temperature gradient the figures (9a,9b) are plotted. It is noticed that the temperature gradient  $\theta'(\eta)$  increases with an increase in the stratification parameter  $St$  for both suction and the injection parameter  $S$ . Furthermore, it is also observed that this increase is more prominent in the case of injection ( $S < 0$ ).

**Table 1.** Values of the skin friction coefficient  $C_f$   $Re^{1/2} = f''(0)$  for several values of the material parameters.

$M$	$S$	$-f''(0)$
0.0	0.5	1.28078
0.5		1.50000
1.0		1.68614
0.5	-1.0	0.822876
	-0.5	1.00000
	0.0	1.22474
	0.5	1.50000
	1.0	1.82288

Table 1 is displayed in order to see the effect of the magnetic parameter  $M$  and the suction/injection parameter  $S$  on the skin friction coefficient. We can see that by increasing the values of the magnetic parameter  $M$  and the suction/injection parameter  $S$ , the values of the skin friction coefficient increase. Table 2 shows the effect of the Prandtl number  $Pr$ , suction/injection  $S$  and stratification parameter  $St$  on the dimensionless heat transfer rate at the wall. It has been observed that the increase in the Prandtl number

$Pr$  and stratification parameter,  $St$  results, an increase in the dimensionless heat transfer rate at the wall. While increasing values of suction/injection parameter  $S$  decreases the dimensionless heat transfer rate at the wall.

**Table 2.** Values of the Nusselt number  $N_u$   $Re^{-1/2} = -\theta'(0)$  for several values of the material parameters for  $M = 1$ .

$Pr$	$S$	$St$	$-\theta'(0)$
0.5	0.5	0.2	0.640382
0.7			0.831958
1.0			1.08195
0.7	0.5	0.0	0.87966
		0.2	0.831958
		0.5	0.760405
0.7	-1.0	0.2	1.02462
	-0.5		0.969256
	0.0		0.904259
	0.5		0.831958
	1.0		0.756596

### CONCLUDING REMARKS

In this contribution, we have articulated the exact solutions of a viscous fluid over a stretching sheet in a thermally stratified medium in the presence of a magnetic field. The modeled non-linear partial equations were transformed into a system of non-dimensional ordinary differential equations using appropriate transformations. The exact solutions were found in the form of confluent hyper-geometric functions (Kummer's function). The influence of pertinent parameters on the velocity and temperature profiles were shown graphically and discussed in details. Numerical values concerning the skin friction coefficient and Nusselt numbers with several respective parameters were provided in tabular form.

### REFERENCES

1. B. C. Sakiadis, *AICHE J.*, **7**, 26 (1961).
2. H. R. Natarja, M. S. Sarma, B. N. Rao, *Acta Mech.*, **128**, 259 (1998).
3. L. J. Crane, *Z. Angew. Math. Phys.*, **21**, 645 (1970).
4. M. I. Char, *J. Math. Anal. Appl.*, **186**, 674 (1994).
5. S. J. Liao, *Commun. Nonlin. Sci. Numer. Simul.*, **11**, 326 (2006).
6. S. K. Khan, E. Sanjayanand, *Int. J. Heat Mass Transf.*, **48**, 1534 (2005).
7. S. P. A. Devi, B. Ganga, *Ind. J. Appl. Math.*, **5**, 45 (2009).

8. M. S. Abel, M. M. Nandeppanavar, S. B. Malipatla, *Int. J. Heat Mass Transf.*, **53**, 1788 (2010).
9. R. Cortell, *Fluid dyn. Res.*, **37**, 231 (2005).
10. T. Hayat, M. Sajid, *Int. J. Heat Mass Transf.*, **50**, 75 (2007).
11. H. Xu, S. J. Liao, *J. Non-Newton. Fluid Mech.*, **159**, 46 (2005).
12. R. Cortell, *Phys. Lett. A.*, **357**, 298 (2006).
13. T. Hayat, S. A. Shehzad, M. Qasim, S. Asghar, A. Alsaedi, *J. Thermophy. Heat Transf.*, **28**, 155 (2014).
14. R. Kandasamy and A. Khamis, *Int. J. Appl. Mech. Eng.*, **12**, 47 (2007).
15. A. Ishak, R. Nazar, I. Pop, *Int. J. Heat Mass Transf.*, **51**, 3693 (2008).
16. S. Mukhopadhyay, A. Ishak, *J. Appl. Math.* (2012), Article ID 491695.
17. S. Mukhopadhyay, *MHD Alex. Eng. J.*, **52**, 259 (2013).
18. C. H. Chen, *Int. J. Heat Mass Transf.*, **53**, 4264 (2010).
19. I. C. Liu, *Int. J. Heat Mass Transf.*, **47**, 4427 (2004).
20. A. Shahzad, R. Ali, *Walailak J. Sci. Tech.*, **10**, 43, (2013).
21. A. Shahzad, R. Ali, *Canad. J. Appl. Sci.*, **2**, 202 (2012).
22. M. Kar, S. N. Sahoo, P. K. Rath, G. C. Dash, *Arab. J. Sci. Eng.*, **39**, 3393 (2014).
23. P. S. Lawrence, B. N. Rao, *Acta Mech.*, **112**, 223, (1995).
24. T. Aziz, F. M. Mahomed, D. P. Mason, *Int. J. Non-linear Mech.*, **78**, 142 (2016).
25. Abramowitz, L. A. Stegun, *Handbook of mathematical functions*, National Bureau of standards/Amer. Math. Soc. Providence, RI., 1972, p.55.

## КОНВЕКТИВНО ТОПЛОПРЕНАСЯНЕ ВЪВ ВИСКОЗЕН ФЛУИД НАД РАЗТЕГНАТ ЛИСТ, ПОСТАВЕН В ТЕРМИЧНО ЕДНОРОДНА СРЕДА

Т. Махмуд<sup>1</sup>, Дж. Ахмед<sup>2\*</sup>, А. Шахзад<sup>2</sup>, Р. Али<sup>3</sup>, З. Икбал<sup>1</sup>

<sup>1</sup>Департамент по математика, Научен факултет, Университет НИТЕС, Таксила Кант, Пакистан

<sup>2b</sup>Департамент по основни науки, Технологично-инженерен университет, Таксила 47050, Пакистан

<sup>3</sup>Централно-азиатски университет, Бишкек, Киргизстан

Постъпила на 19 август, 2015 г.; приета на 7 септември, 2015 г.

(Резюме)

В тази статия ние изследвахме топлопренасянето в електропроводящ вискозен флуид над разтегнат поръзен лист в термично еднородна среда. Не-линейните частни диференциални уравнения на преноса са сведени до обикновени с помощта на автомоделни трансформации. Получените обикновени диференциални уравнения са решени точно във вид на изродени хипергеометрични функции. Получените точни решения за скоростното и температурното поле са представени графично и са изследвани за различни съществени параметри на течението, включвайки числото на Прандтл, параметъра на стратификация, параметъра за всмукване/впръскване и за магнитните свойства. Табулирани са и подробно са обсъдени коефициента на триене и числото на Нуселт.